UNIVERSITY OF CALIFORNIA
RIVERSIDE

Plume Rise and Dispersion of Emissions from Low Level Buoyant Sources in Urban Areas

A Dissertation submitted in partial satisfaction
of the requirements for the degree of

Doctor of Philosophy

in

Mechanical Engineering

by

Sam Pournazeri

June 2012

Dissertation Committee:

Dr. Marko Princevac, Chairperson
Dr. Akula Venkatram
Dr. Guillermo Aguilar

The Dissertation of Sam Pournazeri is approved:

_____

_____

_____

Committee Chairperson

University of California, Riverside

ACKNOWLEDGEMENTS

First, I would like to acknowledge my advisor Professor Marko Princevac. Without his help, this journey would have become impassable. His endless supports and encouragements throughout the course of this study are appreciable. His generosity, easy-going personality, and strong management skills make him not only perfect as an adviser, but someone who can act as a role-model for the future life. The way he looks at the life is fantastic. I truly believe that this dissertation would not have been possible without his help and support.

I would like to thank my co-advisor, Professor Akula Venkatram for his perpetual helps and supports and for serving on my committee. His infinite knowledge in the field of air quality modeling is valuable and I truly believe without his comments, and extraordinary ideas, this dissertation could not reach to the desired quality. I would like to thank Prof. Venkatram, for always having an open door to questions that led to significant improvements of the dissertation. I owe my intense interest to this field to him.

I would like to thank Professor Guillermo Aguilar for serving on my committee and being my teaching assistant advisor for spring 2009. I am thankful to him for his help and support throughout my PhD study. I would also like to thank Prof. Chris Dames who expand my knowledge in the field of thermal fluid science. Although Prof. Dames did not directly impact my research at UC Riverside, however, his distinct way of approaching

the research problems, and transferring the knowledge to the audience was a great lesson to me.

During the past four year, many other people were helping and supporting me throughout the development of this dissertation: Mr. Christian Bartolome, who helped and supported me throughout every seconds of this study without any expectations; Dr. Hansheng Pan, who taught me how to do the laboratory experimentations, her patience and kindness in teaching is valuable; Dr. Qiguo Jing, who helped me a lot throughout the plume rise field study and AERMOD simulations; Mr. Trevor Maynard, who provided a lot of support for the revision of my journal articles, his comments significantly improved these articles. I would also like to thank Mr. Karim Alizad, Ms. Si Tan, Mr. Nico Schulte, Mr. Senyeung Shu, and Mr. Eric Gutierrez for their help in the field and laboratory studies. Special thanks go to the City of Palm Springs for their support of this study. Field assistance from Mr. Steven Vinci and logistic assistance from Mr. Jan Anderson of the City of Palm Springs, Department of Facilities were invaluable.

In addition to the people helped me with the realization of this dissertation, there are many other friends who helped me with different aspect of my PhD life: Shaahin Amini, Haamun Kalantari, Arman Haghighi, Dr. Maryam Shafahi, Melina Roshandel, Amin Akbari, and Sara Rostami.

At the end I would like to thank my girlfriend Ms. Yasaman Samei who has been a great source of motivation and inspiration during the last 4 years and great thanks go to my families: my lovely mother and father, Shahrzad and Bahram Pournazeri, and my

wonderful sister and brother, Shaghayegh and Mohammad, who supported me throughout my whole life.

My research was supported by the California Energy Commission (Grant # CIEE MAQ-07-03).

Dedicated to my lovely mother and father, Shahrzad and Bahram

ABSTRACT OF THE DISSERTATION

Plume Rise and Dispersion of Emissions from Low Level Buoyant Sources in Urban Areas

by

Sam Pournazeri

Doctor of Philosophy, Graduate Program in Mechanical Engineering
University of California, Riverside, June 2012
Dr. Marko Princevac, Chairperson

The projected increase in distributed power generation (DG) has given rise to the concerns on the air quality impact of small power plants located in urban areas. In order to estimate this impact, there is a need for a model that can treat plume rise and dispersion of a buoyant release in an inhomogeneous urban boundary layer whose structure is governed by complex surface characteristics. Such a model requires three essential ingredients: 1) a realistic treatment of the interaction between the highly turbulent urban canopy layer and the turbulent plume spread, 2) a plume rise model that can accounts for the flow modifications caused by buildings, and 3) an appropriate estimate of the height of the nocturnal urban boundary layer.

Comprehensive laboratory and field studies were conducted to investigate each of these elements separately. Ground level concentrations (GLC) associated with a modeled DG were measured inside the water channel under different surrounding building geometries. Results from these measurements indicated that surrounding buildings induce vigorous vertical mixing which increase the near source GLC. Further investigations focused on the plume rise from these sources. The results from plume rise measurements

suggested that plume exiting the DG stack can be significantly impacted by the flows induced by surrounding buildings. In addition to dispersion and plume rise measurements, a field study was conducted in Riverside, CA and the structure of the nocturnal urban boundary layer was investigated over three different nights. Results from these measurements helped us to develop a semi-empirical model that can predict the height of the stable boundary layer.

Although we were able to reasonably understand and develop models to predict the micrometeorology as well as plume rise and spread; we concluded that simple Gaussian dispersion models have limited performance in predicting the concentrations associated with urban sources due to the substantial complexity involved with the urban dispersion process.

TABLE OF CONTENTS

LIST OF FIGURES

LIST OF TABLES

1 INTRODUCTION

Air pollution mainly from vehicles, industries, and power plants, raises the chances of variety of health problems in people exposed to it long, and even short term. Numerous epidemiological studies have shown that long-term exposure to outdoor air pollution increases the risk of respiratory diseases, birth defects, premature mortality, cardiovascular disease, and cancer (McConnell et al., 2006; Wilhelm and Ritz, 2003; Jerrett et al., 2005; Peters et al., 2004; Harrison et al., 1999). In addition, the short term impacts of air pollution such as irritation to the eyes, nose and throat, and upper respiratory infections such as bronchitis and pneumonia can have significant negative impact on the life quality. Short-term air pollution can also exaggerate the medical conditions of individuals with asthma and emphysema. As an example toward the impact of short time exposure to pollutants, during the great "Smog Disaster" in London in 1952, almost four thousand people died in a few days due to the very high ground level concentrations. These Pollutants historically originate from traffic and more recently from small power generators.

A study by United Nation Environment Programme (UNEP) showed that more than 1 billion people are exposed to outdoor air pollution. This study revealed that problems associated with the urban air pollution cost almost equal to 2% of GDP in developed countries and 5% in developing countries. Following a report published in the Guardian newspaper on April 2, 2007, it has been mentioned that the health impact of urban air

pollution can be even more destructive than the radiation in the exclusion zone around the Chernobyl power plant straight after the accident.

These major negative impacts followed by the rapid increase in the trend of urbanization, motivated many of the recent studies to investigate the dispersion of toxic materials in urban areas. In 1950, only 42% of world populations were living in urban areas, this number has been increased to 72% in 1990. This rapid increase in urban population, introduces rapid increase in ground level pollutant concentrations, as a result of higher demands for energy and transportation. Therefore, air quality scientists started to investigate the dispersion problems inside urban areas mostly associated with pollutants originated from traffic. One of the main concerns associated with these kinds of pollutants is the close proximity of the source to recipients and the fact that these releases are happening close to the ground. Thus, most literatures in last 20 years were mainly focused on the dispersion from line sources and surface releases inside urban areas (Berkowicz, 2000; Berkowicz et al., 2002; Mensink et al., 2006; Vardoulakis et al., 2007; Kumar et al., 2009; Pan, 2011).

On the other hand, over many years, the central power plants were most dominant provider of the electricity for residential and industrial users. The produced electricity from these centralized power plants were transmitted over the traditional distribution grids to load centers and then to consumers. The major benefit of these power plants was the lower cost in the energy since the power generation at smaller scales close to user could have resulted in high costs. These high costs were originated from the expensive cost of transportation of fuel, and generating technologies. However, starting from 1970,

centralized power plants were not able to provide considerably cheaper energy to the users, since the capital cost of these power plants per energy unit were comparable to that of small power generators. Thus, the main driver of the energy cost was the grid distribution system. Therefore, economic wise, industries moved toward the distributed power generation also called on-site power generation which are referred to small power plants (<10 MW) located in the vicinity of the user (≈100m). The western U.S energy crisis in 2000 and 2001 expedited this process. Thus, schools, businesses and hospitals moved toward the independency from central power plants by installing on site small scale power generators, known as distributed power generators (DGs). From January 2001 through May 2002, the power capacity from DGs has been increased by 400MW (Heath et al., 2005). Distributed generation (DG) has the potential to meet a significant portion of increased power demand because of the following advantages: 1) reduction in electricity transmission losses since DG units are located in the area they service, 2) flexibility in size tailored to local power demand; 3) increase in efficiency and decrease in emissions by replacing boilers by Combined Heat and Power (CHP) systems. It may serve a single home, neighborhood, or business more efficiently and reliably than a centrally located power plant, and at a lower cost (Allison and Lents, 2002). These benefits and the continuing concerns about the power reliability, quality, costs, and evolving technology have all contributed to the use of DG. Although DGs were beneficial for local industries by providing power independency and lower cost, they have significant effect on air quality in urban areas especially in neighborhood (up to 1 or 2 km) and street scale (less than ~100 to 200 m) (Britter and Hanna, 2003). Exhausts from

DGs are hot and highly buoyant; however, as they are released within the city, in vicinity of businesses, schools, restaurants and hospitals, they can be captured in the wake produced by surrounding buildings. The process of dispersion of these kinds of pollutants is complicated and mostly affected by the complex geometry of the buildings in urban area which requires a thorough understanding of the street-scale flow and turbulence. Therefore, it is significantly important to have a detailed understanding of flow and dispersion in built environments in order to improve air quality of urban areas where more than 70% of population lives.

Several studies have examined specifically the impact of DG on air quality at urban and regional scales. Hadley and Vandyke (2003) have shown that replacing Centralized power plants with DGs can reduce the total emissions and this effect can become greater when DGs are used as both heat and electricity generators (formerly known as co-generation). However the study by Iannucci et al. (2000) indicates that DGs with diesel engines have higher emission per unit energy than existing power generators. Iannucci et al. (2000) showed that, for the year of 2002, if DGs were about to produce 976MW of powers, the total NO_x emissions could exceed to 1256 tons vs. 13 tons for centralized power plants. In another study, Allison and Lents (2002) analyzed the tradeoff between the increase in emissions associated with urban DGs emissions and the decrease in emissions by replacing heating plants with waste heat generated from DGs. They found that emissions associated with realistic DG scenarios with the lowest emission and high waste heat recovery is nearly comparable to that in the central generated power plants. Their relatively simple analysis focused on total emissions and did not investigate the

impact of these emissions on the air quality. Following the study by Greene and Hammerschlag (2000), DGs have been reported to have larger environmental impact than centralized power generators as 1) they are less efficient in turning fuel into heat comparing to large power plants 2) centralized power plants have strict regulations and are constantly monitored for efficiency and emission control 3) DG emission are in close proximity to its recipient, people. Heath et al. (2006) have also examined the air quality impact of DG units relative to central generating stations. They found that the air quality impact of DG units, quantified in terms of intake factors (dimensionless number representing the ratio between the amount pollutants inhaled by population to the amount of pollutants released), could be as much as 20 times that of central generating (CG) stations because a) the ground-level concentrations from the elevated emissions of a CG plant are much smaller than those associated with the near surface emissions from DG units (An analysis of air quality impact of CG plants have shown that reducing the CG stack height to zero can increase their intake fraction up to an order of magnitude) b) CG plants are likely to be located far from urban centers, while DG units are located in urban areas in close proximity to energy consumers. However, this study has been limited to the pollutants released directly into the atmosphere and did not account for the atmospheric chemistry.

A detailed examination of the impact of DG emissions on ambient ground level concentrations of both primary and secondary pollutants in the South Coast Air Basin (SoCAB) using CIT Airshed model (Three dimensional model that predicts air pollutants concentration accounting for chemical reactions, depositions and transport) has been

done by Rodriguez et al. (2006). They have shown that although the use of DGs is increasing substantially, the emission from DGs has little effect on secondary pollutants such as ozone and $PM_{2.5}$ concentrations. In addition to this study, Vutukuru et al. (2011) investigated the future impact of distributed power generation on the ground level concentration in the San Joaquin Valley of California. They focused on market penetration of distributed power generation in the year of 2023. Using a three dimensional Eulerian grid model, they have shown that the impacts of DGs are small as a result of stringent regulation made by California Air Resources Board on the emissions from DGs in the year of 2007. Although these studies provide an insight through the problem, however, they mostly focused on the regional impact of these sources and none of them directly addressed the impact of DG emissions on ambient ground level concentrations in short distances from the source which can be orders of magnitudes higher than the background pollutant concentrations. Motivated by this need the air quality modeling group at UC Riverside conducted several field and laboratory studies to address this question that: How DGs modify the ground level concentration pattern in urban areas at distances of 100 m from the stack?

The results of the passive tracer experiment (Venkatram et al., 2004a) at the Center for Environmental Research and Technology (CE-CERT) indicated that existing dispersion models, such as AERMOD (Cimorelli et al., 2005), do need improvement and can overestimate maximum concentrations as the downwash model used in them do not accounts for lateral meandering and underestimate area-wide concentrations in urban

areas. Although this model is widely used, it has not been validated for use in real urban areas due to the lack of field data.

Following this problem, a tracer field study has been conducted in Palm Springs in summer 2008 around a gas fired 650 kW DG unit (Jing et al., 2009). We will briefly explain the field study and associated results in this dissertation. However, the main message from this field study was that the currently used dispersion models such AERMOD are not able to describe the ground level concentrations from the low level buoyant sources in urban areas especially during night time. The reason to these limitations is that the formulation of plume rise, turbulence governed plume spreads and the micrometeorological parameters in these models are designed primarily for large power plants without any building in the vicinity and cannot perform satisfactory considering the inhomogeneity of urban geometries. Therefore, there is a need to develop and apply methods to estimate the air quality impact of distributed generation at source-receptor distances of tens and hundreds of meters by developing new models for plume rise and dispersion from low level sources such as DGs. However, due to the high costs and site- specific results of field studies, results from field experiments can be supplemented with results from laboratory measurements to provide a thorough insight into the problem.

This dissertation has been motivated by the need for a better understanding on the dispersion and plume rise of pollutants from low-level buoyant sources such as DGs. In the process of this research, we conducted several field as well as laboratory experiments. In Section 2, a brief overview on the structure of the atmospheric boundary layer,

relevant micro-meteorological and dispersion parameters will be given. The most commonly used Gaussian dispersion models will be explained. The derivation of well-known Briggs plume rise model will be shown as well. In section 3, we discuss the tracer field study conducted in Palm Springs, CA on July 2008 in detail. The observations will be analyzed and a different model approaches to explain the measured ground level concentrations will be discussed. As explained earlier, this study utilized both field and laboratory study to provide adequate information for modeling purposes. The laboratory setup will be explained in section 4.

In order to be consistent between the two different scales of measurements (i.e. field vs. laboratory), we developed a scaling method for dispersion and plume rise in urban areas. This scaling method will be explained in section 5. Following the correct scaling of plume rise and dispersion, laboratory measurements of ground level concentrations associated with a modeled DG in the water channel will be discussed in section 6. Section 7 will deliberate a detailed investigation on the plume rise from DG sources through both the field and laboratory measurements.

Section 8 will present the results from a field study on the structure of the nocturnal boundary layer. The motivation for this study was that the results from the Palm Springs tracer field study in 2008 shows that the highest concentrations occurred during the night even though the emissions were highly buoyant (Jing et al., 2011). The ability to explain these concentrations was limited by the uncertainty in describing the structure of the stable boundary layer (SBL) over an urban area. In order to provide further information on the structure of nighttime boundary layer, we conducted a field study in Riverside,

CA, to investigate the urban nocturnal boundary layer height and possible methods to predict it. The details of this study are given in Section 8. Following this chapter we will provide a brief overview on the different sections of dissertation along with conclusions in Section 9.

2 BACKGROUND

In order to have a better understanding on air quality models, adequate knowledge on the structure of these models is required. Thus, in this section we will outline the important features of the structure of the atmospheric boundary layer, the basis of the well-known Gaussian dispersion model, and the Briggs plume rise model. This chapter will provide the basis for our further air quality analysis in chapters 3 through 8 on the impact of distributed power generators. Most of the contents of this chapter are obtained from "Air Pollution Dispersion Modeling" book, authored by Akula Venkatram and Sam Pournazeri. This book is under preparation, and will be published by Springer.

2.1 Vertical Structure of Atmospheric Boundary Layer

The lower part of the atmosphere where wind speed, temperature and mixing ratio profiles are significantly influenced by the earth's surface is known as the atmospheric boundary layer (ABL). The height of this boundary layer is highly variable with time and ranges from tens of meters at nights to thousands during daytime (Stull, 1988). The responding time scale of this layer to the shear / convective forces induced by the ground is in the order of an hour (Stull, 1988). One of the main characteristics of the ABL is the presence of relatively high turbulence near the ground. Pollutants emitted in this layer are dispersed in both horizontal and vertical direction as a result of turbulence and eventually become well mixed throughout this layer. As a result of this mixing, the height of this layer can strongly influence the ground level concentrations especially during nighttime where boundary layer is relatively shallow.

The surface boundary layer refers to the lowest tenth of the atmospheric boundary layer. Over the past decade, this layer has been studied extensively, and many attempts have been made to characterize the behavior of this layer (Businger, 1973; Wyngaard, 1973; Venkatram 1980a; Sorbjan, 1986; Stull, 1988). This characterization is facilitated by the fact that the surface boundary layer can be assumed to be in quasi-steady equilibrium with the underlying surface. Another representation of the surface boundary layer in urban areas is made by Grimmond and Oke (2002) through two distinct regions, roughness sub-layer (RSL) and inertial sub-layer (ISL). The ISL refers to the layer that is about 1 to 3 times the average building height where the flow can be considered to be in equilibrium with the underlying rough surface. The RSL lies below the ISL, and corresponds to the lowest layer that is governed by the spatially averaged properties of the urban surface. Fluxes of momentum, energy, and moisture vary with height in the RSL. The shear stress and local friction velocity, reach a maximum at the bottom of the ISL.

As the wind flow over an urban area a layer with high turbulent intensities forms. This layer is called urban boundary layer (UBL). The increase in the roughness length over an urban area and the urban heat island (Oke, 1982; Bornstein, 1987; Stull, 1988) are the key parameters increasing the turbulence levels over an urban surface. The bottom part of the urban boundary layer is called the urban canopy layer which lies below the average buildings height in the urban area. This layer is part of the RSL layer, and is primarily formed by micro-scale effects of site characteristics (Pan, 2011). Surrounding buildings and structures are the key controlling parameters of thermal and turbulent shear

processes within this layer. The flow and turbulence structure are generally very complex and cannot be explained through the classical similarity theories. A simple representation of all layers of the atmospheric boundary layer explained above is shown in Figure 2-1(from Grimmond and Oke, 2002).

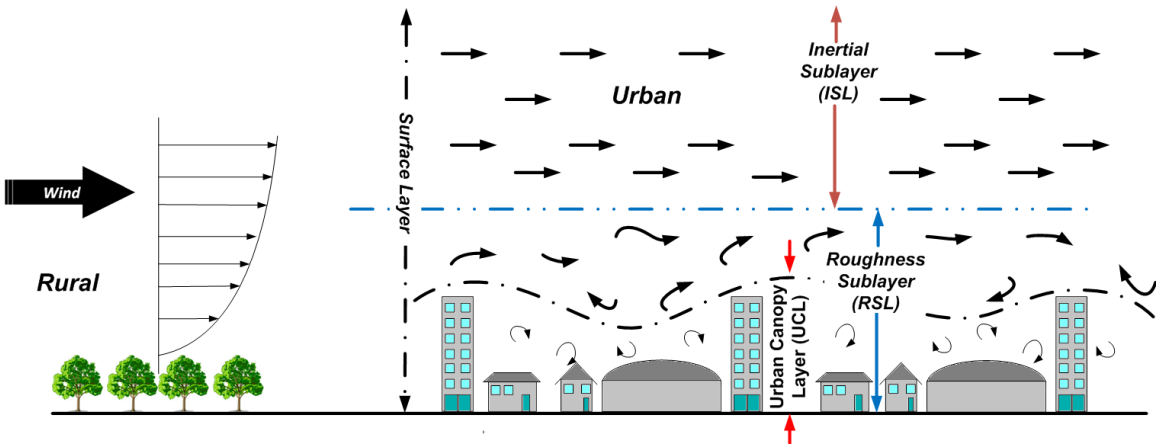

Figure 2-1: Structure of urban and rural boundary layer (adapted from Grimmond and Oke, 2002).

2.2 Surface Layer Similarity

At heights of the order of the Monin-Obukhov length, the mean and the turbulent structure of the boundary layer can be described using Monin-Obukhov similarity theory (Businger, 1973). The theory states that the mean temperature and velocity gradients can be represented by universal functions if the velocity, temperature, and height are scaled appropriately. The velocity scale is u_*, the height scale is L, and the temperature scale, θ_*, is given by;

$$\theta_* = -Q_0 / u_* . \tag{2-1}$$

Then, we can write,

$$\frac{\mathrm{du}}{\mathrm{dz}} = \frac{u_*}{kz}\phi_m\left(\frac{z}{L}\right), \tag{2-2a}$$

and

$$\frac{\mathrm{d}\theta}{\mathrm{dz}} = \frac{\theta_*}{kz}\phi_h\left(\frac{z}{L}\right). \tag{2-2b}$$

Notice that when the surface heat flux goes to zero, $L \to \infty$, and $z/L \to 0$. This means that $\phi_m(0)$ and $\phi_h(0)$ = 1 to be consistent with the gradient in the neutral boundary layer.

The forms represented by Equations (2-2a) and (2-2b) are well supported by observations (Businger et al., 1971), which indicate that

$$\phi_m = \left(1 - 15\frac{z}{L}\right)^{-1/4} \text{ for } L < 0, \tag{2-3a}$$

$$= 1 + 4.7\frac{z}{L} \text{ for } L > 0, \tag{2-3b}$$

and

$$\phi_h = 0.74\left(1 - 9\frac{z}{L}\right)^{-1/2} \text{ for } L < 0, \tag{2-4a}$$

$$= 0.74 + 4.7\frac{z}{L} \text{ for } L > 0. \tag{2-4b}$$

With these forms for ϕ_m and ϕ_h, Equations (2-2a) and (2-2b) can be integrated to yield:

For unstable conditions, ($L < 0$),

$$\frac{u}{u_*} = \frac{1}{k}\left(\ln \frac{z}{z_o} - \psi_1 \right), \tag{2-5a}$$

where $$\psi_1 = 2\ln\left[\frac{(1+x)}{2}\right] + \ln\left[\frac{(1+x^2)}{2}\right] - 2\tan^{-1} x + \frac{\pi}{2} \tag{2-5b}$$

and $$x = \left(1 - 15\frac{z}{L}\right)^{1/4}. \tag{2-5c}$$

For stable conditions, ($L > 0$),

$$\frac{u}{u_*} = \frac{1}{k}\left\{ \ln\left(\frac{z}{z_o}\right) + 4.7\frac{z - z_o}{L} \right\}. \tag{2-6}$$

The expressions for temperature are:

$$\frac{\theta - \theta_o}{\theta_*} = \frac{0.74}{k}\left[\ln\left(\frac{z}{z_o}\right) - \psi_2 \right], \tag{2-7}$$

where for **unstable conditions ($L < 0$)**

$$\psi_2 = \ln\left[\frac{(1+y)}{2}\right], \tag{2-8a}$$

where $$y = \left(1 - 9\frac{z}{L}\right)^{1/2} \tag{2-8b}$$

and for **stable conditions ($L > 0$)**

$$\frac{\theta - \theta_o}{\theta_*} = \frac{1}{k}\left[0.74\ln\left(\frac{z}{z_o}\right) + 4.7\frac{z - z_o}{L} \right] \tag{2-9}$$

In these expressions for the temperature profiles, θ_o represents the temperature obtained by extrapolating the profile to $z = 0$; this is not the surface temperature. In principle, these profiles can be used to compute surface fluxes of heat and momentum by fitting them to temperature and velocity measurements.

2.2.1 The Daytime Boundary Layer

Turbulence in the daytime boundary layer is maintained primarily by sensible heating at the surface, which results in parcels of air that are warmer than their surroundings. These parcels are subject to buoyancy forces that accelerates them upwards. The mixing induced by these parcels gives rise to the boundary layer or mixed layer, whose growth is inhibited by the stable temperature gradient of the atmosphere above the mixed layer. Often, the growth of the mixed layer is limited by a sharp subsidence inversion or temperature jump, in which case the height of this inversion determines the maximum mixed layer height.

The turbulent motion in the convective boundary layer is organized into updrafts and downdrafts that extend through the depth of the boundary layer. These structures are carried by the mean wind as illustrated in Figure 2-2.

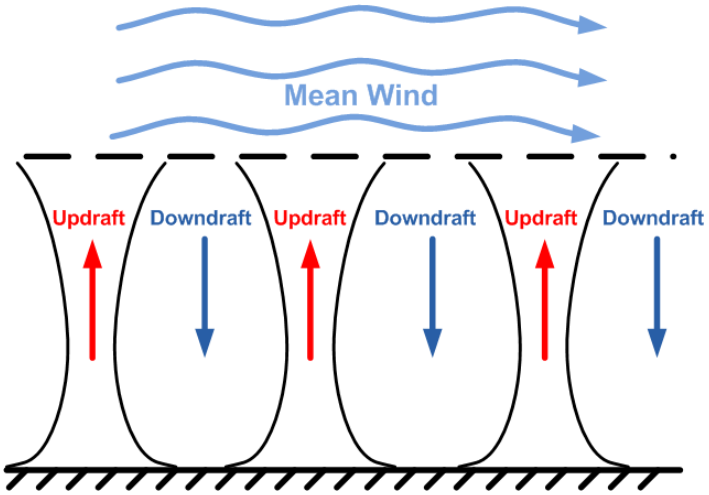

Figure 2-2: Schematic of updrafts and downdrafts caused by surface heating

The updrafts consist of accelerating parcels, while the downdrafts are caused by compensating downward motion. Thus, the velocities in updrafts are higher than those in downdrafts; mass balance requires that the horizontal area occupied by downdrafts is higher than that of updrafts. Since more plume material is released into downdrafts than updrafts, the plume centerline descends towards the ground. This feature has important effects on dispersion from elevated stacks. Venkatram (1980b) has modeled this effect on dispersion by assuming that plume impinges around a mean distance of x_i from the source.

The mean potential temperature and velocity structure in an idealized mixed layer are shown below.

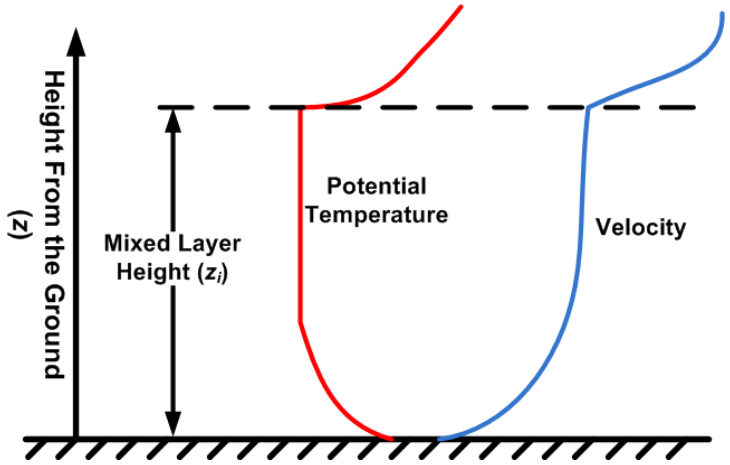

Figure 2-3: Schematic of vertical profile of potential temperature and velocity in the convective boundary layer

The potential temperature is super-adiabatic close to the surface: the potential temperature decreases with height. Above a tenth of the mixed layer height, the potential temperature is relatively uniform because of vigorous vertical mixing. The mixed layer is usually capped by a sharp inversion. This inversion limits the height of the mixed layer by resisting the vertical motion of thermals in the mixed layer. The layer above the mixed layer can be stably stratified.

The velocity profile in the daytime boundary layer is relatively flat in the mixed layer. The rapid change in velocity at the top of the boundary layer reflects the fact that the velocity distribution is affected by strong vertical mixing below the top.

2.2.2 The Night Time Boundary Layer

When the sun sets, turbulence energy production by buoyancy breaks down. Over a period of an hour, the turbulence in the mixed layer collapses, and shear becomes the primary mechanism for the production of turbulence. Because the ground is initially

warmer than the atmosphere, the thermal radiation leaving the ground exceeds that being supplied by the atmosphere. This deficit leads to the cooling of the ground.

Initially, both the sensible heat flux and the ground heat flux are directed away from the earth's surface. The surface cools rapidly, and a point is reached at which the ground becomes colder than the layers above in the atmosphere. At this stage, the heat flux from the atmosphere is directed towards the earth's surface. This process is referred to as the formation of a radiation induced surface inversion where the temperature (and the potential temperature) increases with height.

The mean temperature and velocity above the surface boundary layer increase with height as shown in Figure 2-4.

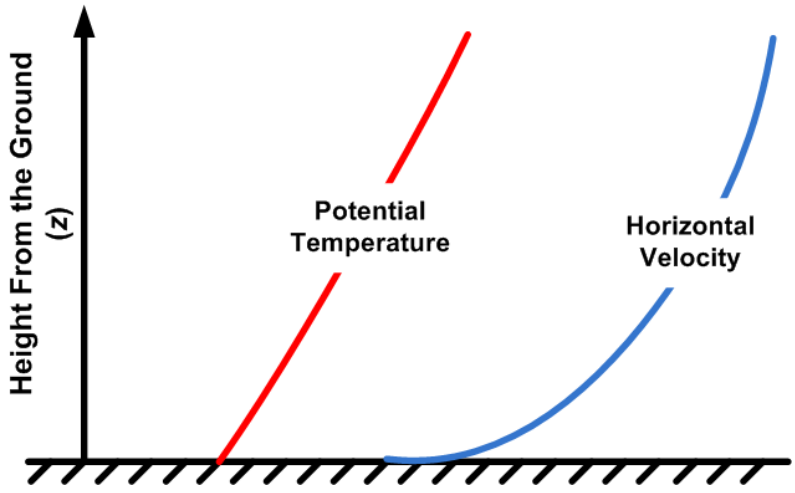

Figure 2-4: Schematic of vertical profile of potential temperature and velocity in the stable boundary layer

There is little agreement on the general form of these profiles in the stable boundary layer. On the basis of measurements made in Holland, Van Ulden and Holtslag (1985) suggest that the mean wind can be described by

$$u(z) = \frac{u_*}{k}\left[\ln\left(\frac{z}{z_o}\right) - \psi_m\left(\frac{z}{L}\right) + \psi_m\left(\frac{z_o}{L}\right)\right]$$

where . (2-10)

$$\psi_m\left(\frac{z}{L}\right) = -17\left[1 - \exp\left(-0.29\frac{z}{L}\right)\right]$$

In the absence of information through measurements, we suggest extrapolating the surface boundary layer Equation (2-10) through the boundary layer.

2.3 Gaussian Dispersion Model

The concept involved in estimating concentrations associated with the release of contaminant is best illustrated by considering the so-called Gaussian formulation for dispersion. The Gaussian dispersion model is based on a simplified analytical solution of advection-diffusion equation, assuming steady state dispersion with constant wind speed and eddy diffusivity from the ground. Since dispersion is governed by turbulence, the details of which are unpredictable, the concentration distribution of a plume has been found to be Gaussian. To express this quantitatively, consider the source illustrated in Figure 2-5.

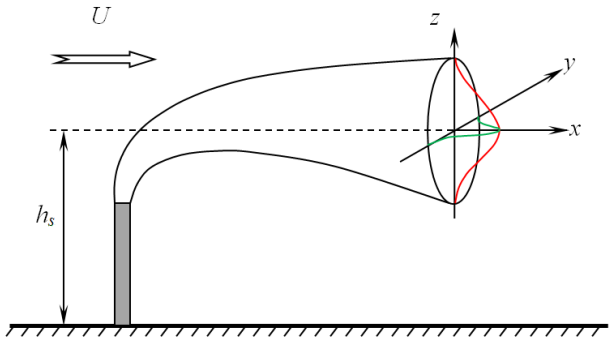

Figure 2-5: Gaussian distribution used to model a plume from a point source.

The emission occurs at a height h_s from the ground at a rate given by Q. For the time being, neglecting the effect of the ground on the concentration, the concentration within the plume $C(x,y,z)$ is given by the Gaussian distribution

$$C(x,y,z) = \mathrm{C}(\mathrm{x},0,h_s)\exp\left[-\frac{(z-h_s)^2}{2\sigma_z^2}-\frac{y^2}{2\sigma_y^2}\right], \tag{2-12}$$

where σ_y and σ_z are the standard deviations of the distribution in the horizontal and vertical directions. Notice that the maximum concentration occurs at the plume centerline $(x,0,h_s)$. By equating the emission rate Q, to the flux of material through a vertical plane

$$Q = u\iint_{\mathrm{y\,z}} C(x,y,z)\,\mathrm{dy\,dz}, \tag{2-13}$$

we find that

$$C(x,0,h_s) = \frac{Q}{2\pi\sigma_y\sigma_z u}, \tag{2-14}$$

and the expression for the concentration becomes

$$C(x,y,z) = \frac{Q}{2\pi\sigma_y\sigma_z u}\exp\left[-\frac{(z-h_s)^2}{2\sigma_z^2}-\frac{y^2}{2\sigma_y^2}\right]. \tag{2-15}$$

In cases where the plume rises due to the buoyancy, the actual height of the plume h_e at distance x from the source will be used instead of stack height h_s in this model. The Gaussian distribution can be justified theoretically for dispersion in homogeneous turbulence. The turbulence in the atmospheric boundary layer is anything but homogeneous, especially in the stable boundary layer and close to the ground. In

addition, under urban conditions, where building induce complex three dimensional flow around the stack, the assumption of a constant horizontal wind speed is not valid anymore, and the Gaussian dispersion model will likely breakdown. However, Equation (2-15) is still used because it represents a convenient framework for dispersion analysis. There are several different semi-empirical formulations for the plume dispersion parameters, σ_y and σ_z, that can account for this inhomogeneity (Venkatram, 1980; Venkatram et al., 1984;Venkatram and Paine, 1985).

2.3.1 Treatment of Boundaries

The effect of the ground on concentrations is accounted for by making sure that there is no flux of material through the plane at $z = 0$. The mathematical trick to achieve this is to place an "image" source at a distance $z = -h_s$; the upward flux from this image source essentially cancels out the downward flux from the real source. Then the concentration becomes

$$C(x,y,z) = \frac{Q}{2\pi\sigma_y\sigma_z u}\exp\left[-\frac{y^2}{2\sigma_y^2}\right]\left\{\exp\left[-\frac{(z-h_s)^2}{2\sigma_z^2}\right]+\exp\left[-\frac{(z+h_s)^2}{2\sigma_z^2}\right]\right\}. \qquad (2\text{-}16)$$

In the real atmosphere, dispersion in the upward direction is limited by the height of the atmospheric boundary layer. This limitation of vertical mixing is incorporated into the Gaussian formulation by reflecting off the top of the boundary or mixed layer. Note that when material is "reflected" from both the ground as well as the top of the mixed layer, it is necessary to account for the infinite set of "reflections" from the two surfaces.

These multiple reflections can be readily accounted for in the Gaussian formulation through additional reflection terms as follows:

$$C(x,y,z)=\frac{Q}{2\pi\sigma_y\sigma_z u}\exp\left[-\frac{y^2}{2\sigma_y^2}\right]\sum_{n=-\infty}^{n=\infty}\left\{\exp\left[-\frac{(z-h_s+2nz_i)^2}{2\sigma_z^2}\right]+\exp\left[-\frac{(z+h_s+2nz_i)^2}{2\sigma_z^2}\right]\right\} \tag{2-17}$$

where z_i is the mixed layer height.

In the following section we will discuss the theoretical foundations of the estimation of the plume dispersion parameters, σ_y and σ_z.

2.3.2 Plume Spread Formulation

There are several formulations for the plume spread (σ_y , σ_z) which can be divided in different categories such as eddy diffusivity theory (Robins, 1978; Venkatram, 1992), similarity theory (Robins, 1978; Pasquill and Smith, 1983), Pasquill-Gifford curves (Pasquill, 1961; Gifford, 1961; Briggs, 1973), and Taylor's statistical theory of turbulence (Taylor, 1921). Here we briefly discuss Taylor's statistical theory, which is mostly used in modern dispersion modeling. This method is based on the theoretical work done by Taylor (1921), in which he describes the variance of particle positions as a function of time from a fixed point of release into a homogenously steady turbulent flow field. The mathematical analysis is presented in most standard textbooks (e.g. Csanady, 1973). Here we show the results from the asymptotic plume spread behavior in which vertical spreads are given by

$$\sigma_z = \sigma_w t \quad \text{for t} << \text{T}_{\text{Lw}}$$
$$\sigma_z = \sigma_w (2tT_{Lw})^{1/2} \quad \text{for t} >> \text{T}_{\text{Lw}} \tag{2-18}$$

where $t = x/v$ is the time travel from the release point and T_{Lw} is the Lagrangian time scale representing the time over which the velocity of a particle is correlated with itself. Lateral spread (σ_y) has also a similar expression. Therefore, assuming that released pollutants are within the short time limit ($\text{t} << \text{T}_{\text{L}}$), plume spread can be expressed as

$$\sigma_z = I_z x \tag{2-19}$$

$$\sigma_y = I_y x \tag{2-20}$$

where I_z and I_y are the turbulent intensities in the vertical and crosswind directions, respectively, defined as,

$$I_z = \sigma_w / U \tag{2-21}$$

$$I_y = \sigma_v / U \,. \tag{2-22}$$

where σ_v and σ_w are the standard deviation of crosswind and vertical velocity fluctuations, respectively.

In addition to the ambient turbulence, plume spread can be also affected by the plume rise (h_p) through the buoyancy-induced dispersion (BID). BID can be formulated according to Pasquill (1976) and Weil (1988) as,

$$\sigma_b = \frac{0.4}{\sqrt{2}} h_p = \frac{0.4}{\sqrt{2}} (h_e - H_s) \,. \tag{2-23}$$

Thus, from Pasquill and Smith (1983), the final plume spread can be modeled as,

$$\sigma_{y,z}^2 = \sigma_b^2 + (I_{y,z}x)^2 . \tag{2-24}$$

2.4 Plume Rise

We derive the plume rise equations using a simple model of the plume, which assumes that the plume properties such as temperature and velocity are uniform across the cross-section of the plume; this is referred to as the top hat approximation. We will also assume that the plume bends over rapidly enough that the horizontal velocity inside the plume is equal to the horizontal wind speed, u, which is taken to be uniform with height. Figure 2-1 shows a control volume of thickness dx that encloses a plume with a radius r.

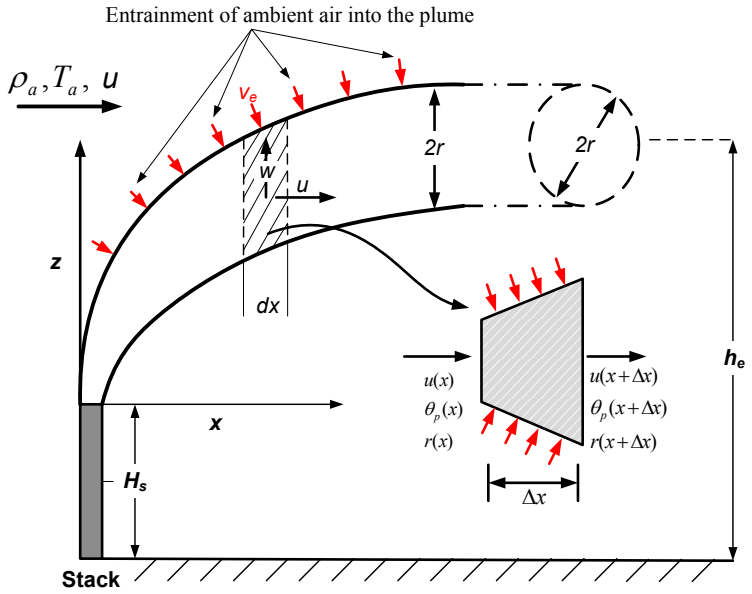

Figure 2-6: Plume control volume used to derive plume rise equations

Plume rise corresponds to the vertical position of the plume, z, as a function of distance, x, from the stack.

2.4.1 Plume Rise Equations for Neutral Stability Condition

To derive the equation of plume rise, let us first consider the mass conservation equation, which assumes that changes in the plume mass flux are due to the entrainment of ambient air into the plume as,

$$d(\rho_p u \pi r^2) = 2\pi r \rho_a v_e dx \tag{2-25}$$

where ρ_p and ρ_a are the plume and ambient densities, respectively; r is the radius of the plume; u is the ambient horizontal wind speed which is assumed to be constant; and v_e is the entrainment velocity into the plume which is formulated as,

$$v_e = \beta w \tag{2-26}$$

where w is the vertical velocity of the plume and $\beta = 0.6$ is the entrainment coefficient. Substituting equation (2-26) in equation (2-25), and assuming constant horizontal wind speed u, one can rewrite the mass conservation equation to,

$$u \frac{d}{dx}(\rho r^2) = 2 r \rho_a \beta w . \tag{2-27}$$

Following the Boussinesq approximation, assuming that the density difference of plume and ambient air ($\rho_a \approx \rho_p$) is negligible; and replacing w with dz/dt, equation (2-27) becomes,

$$\frac{dr}{dt} = \beta \frac{dz}{dt} . \tag{2-28}$$

Therefore, integrating equation (2-28) with respect to time *t*, it becomes,

$$r = \beta z \tag{2-29}$$

which relates the radius of the plume (r) to the plume rise (z).

Another conservation equation that needs to be considered in order to derive the plume rise equation is the conservation of vertical momentum, such as,

$$d(\rho_p u w \pi r^2) = F_u \rho_p \pi r^2 dx \tag{2-30}$$

where F_u is the buoyancy force on the unit mass of the plume. The buoyancy force applied on a unit mass fluid parcel with temperature (T_p) different from the ambient temperature (T_a). As shown in Figure 2-7, there are two forces applied on the air parcel; the weight (mg) and the buoyancy force ($\rho_a V_p g$). The resultant of these two forces would be,

$$F_u = V_p \rho_a g - mg = V_p g(\rho_a - \rho_p) \tag{2-31}$$

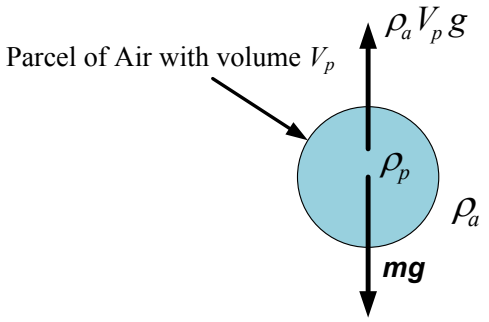

Figure 2-7: Fluid parcel used to derive resultant force on the Plume control volume

Since the parcel is assumed to have unit mass; $V_p=1/\rho_p$. Substituting this into (2-31) would yield,

$$F_u = g\frac{(\rho_a - \rho_p)}{\rho_p}. \tag{2-32}$$

Following the ideal gas law,

$$\rho = \frac{P}{RT}. \tag{2-33}$$

Substituting (2-33) into (2-32) would results into,

$$F_u = g\frac{(T_p - T_a)}{T_a} = (\frac{T_p}{T_a} - 1)g = \frac{g}{\theta_a}(\theta_p - \theta_a). \tag{2-34}$$

Replacing (2-34) into (2-30) yields,

$$d(\rho_p uw\pi r^2) = \frac{g}{\theta_a}(\theta_p - \theta_a)\rho_p \pi r^2 dx. \tag{2-35}$$

Therefore, simplifying (2-35) results in,

$$\frac{d}{dx}(uwr^2) = \frac{g}{\theta_a}(\theta_p - \theta_a)r^2 \tag{2-36}$$

The third conservation equation that needs to be considered is the conservation of energy in the plume, which simply reduces to the fact that the enthalpy flux out of the stack remains constant throughout the plume, such as,

$$\pi\rho C_p(\theta_s - \theta_0)V_s r_s^2 = \pi\rho C_p(\theta_p - \theta_0)ur^2. \tag{2-37}$$

Dividing (2-37) by θ_a / g and cancelling the $\pi\rho C_p$ from both sides, yield to,

$$\frac{g}{\theta_a}(\theta_s - \theta_0)V_s r_s^{\,2} = \frac{g}{\theta_a}(\theta_p - \theta_0)ur^2 = F_b. \tag{2-38}$$

Therefore, assuming that $\theta_a = \theta_0$ for neutrally stratified condition and substituting $F_b / u = g(\theta_p - \theta_a)r^2 / \theta_a$ into (2-36) , would results into,

$$\frac{d}{dx}(uwr^2) = \frac{F_b}{u}. \tag{2-39}$$

Replacing the $u = dx/dt$ into (2-39) will result into,

$$\frac{d}{dt}(uwr^2) = F_b. \tag{2-40}$$

Integrating (2-40) with respect to time yield to,

$$uwr^2 = F_b t + uwr^2\big|_{t=0} \tag{2-41}$$

where

$$uwr^2\big|_{t=0} = V_s^{\,2} r_s^{\,2} = F_m. \tag{2-42}$$

Therefore,

$$uwr^2 = F_b t + F_m. \tag{2-43}$$

Substituting $w = dz/dt$ and $r = \beta z$ in (2-43) results into,

$$\beta^2 z^2 u \frac{dz}{dt} = F_b t + F_m. \tag{2-44}$$

Therefore,

$$\frac{\beta^2 u}{3}\frac{dz^3}{dt} = F_b t + F_m. \tag{2-45}$$

Integrating (2-21) with respect to t will lead to,

$$z^3 = \frac{3F_b}{u\beta^2}\frac{t^2}{2} + \frac{3}{u\beta^2}F_m t + C. \tag{2-46}$$

Applying initial condition $z\big|_{t=0} = 0$, (2-46) becomes,

$$z = \left(\frac{3F_b}{u\beta^2}\frac{t^2}{2} + \frac{3}{u\beta^2}F_m t\right)^{1/3} \tag{2-47}$$

Replacing $t=x/u$, (2-47) becomes,

$$z = \left(\frac{3F_b}{u^3\beta^2}\frac{x^2}{2} + \frac{3}{u^2\beta^2}F_m x\right)^{1/3} \tag{2-48}$$

which is the equation for plume rise in neutral stability condition.

2.4.2 Plume Rise Equations for Stably Stratified Condition

In stably stratified condition, all conservation equations except for the energy remain the same as for the neutral condition. Following the schematic of a bent over plume shown in Figure 2-6, the conservation of energy under stratified atmosphere can be explained as follows,

$$\begin{aligned}&\rho C_p u(x+\Delta x)\pi r(x+\Delta x)^2\left[\theta_p(x+\Delta x)-\theta_0\right] = \rho C_p u(x)\pi r(x)^2\left[\theta_p(x)-\theta_0\right]\\&+\rho C_p u(x)\pi\left[r(x+\Delta x)^2 - r(x)^2\right]\left[\theta_a(x)-\theta_0\right]\end{aligned} \tag{2-49}$$

Therefore, dividing both side by Δx and cancelling $\pi u \rho C_p$ terms from both sides, assuming that velocity u is constant, the (2-49) becomes,

$$\frac{d}{dx}\left(r^2(\theta_p-\theta_0)\right) = (\theta_a-\theta_0)\frac{dr^2}{dx} \tag{2-50}$$

The term $(\theta_a - \theta_0)$ can be written in terms of Brunt-Vaisala frequency (N) as,

$$(\theta_a - \theta_0) = \frac{\theta_a}{g} N^2 z \tag{2-51}$$

Therefore, (2-50) becomes,

$$\frac{d}{dx}\left(r^2(\theta_p - \theta_0)\right) = \frac{\theta_a}{g} N^2 z \frac{dr^2}{dx} \tag{2-52}$$

Integrating both sides of (2-52) with respect to x, yields,

$$r^2(\theta_p - \theta_0)\Big|_0^x = \frac{\theta_a}{g} N^2 \int_0^x z \frac{dr^2}{dx} dx \tag{2-53}$$

The integration on the left hand side of (2-53) can be solved through integration by parts such as,

$$r^2(\theta_p - \theta_0)\Big|_0^x = \frac{\theta_a}{g} N^2 \left[r^2 z\Big|_0^x - \int_0^x r^2 \frac{dz}{dx} dx \right]. \tag{2-54}$$

Therefore,

$$r^2(\theta_p - \theta_0)\Big|_x = \frac{\theta_a}{g} N^2 \left[r^2 z\Big|_0^x - \int_0^x r^2 \frac{dz}{dx} dx \right] + \frac{F_b \theta_a}{gu}. \tag{2-55}$$

Conservation of momentum, (2-36) can be written as,

$$\frac{d}{dx}(uwr^2) = \frac{g}{\theta_a}\left[\left(\theta_p - \theta_0\right) - \left(\theta_a - \theta_0\right)\right] r^2 \tag{2-56}$$

Following (2-51) and (2-54), (2-55) can be written as,

$$\frac{d}{dx}(uwr^2)=\frac{g}{\theta_a}\left[\frac{\theta_a}{g}N^2\left(r^2z\Big|_0^x-\int_0^x r^2\frac{dz}{dx}dx\right)-\frac{\theta_a}{g}N^2r^2z\right]+\frac{F_b}{u} \tag{2-57}$$

Assuming $r^2z\Big|_0=0$, (2-56) can be shown as,

$$\frac{d}{dx}(uwr^2)=\frac{F_b}{u}-N^2\int_0^x r^2\frac{dz}{dx}dx \tag{2-58}$$

Following (2-29),

$$\frac{dz}{dx}=\frac{1}{\beta}\frac{dr}{dx}; \tag{2-59}$$

thus (2-57) becomes,

$$\frac{d}{dx}(uwr^2)=\frac{F_b}{u}-\frac{N^2}{3\beta}\int_0^x\frac{dr^3}{dx}dx=\frac{F_b}{u}-\frac{N^2r^3}{3\beta} \tag{2-60}$$

Substituting *w= dz/dt* results into,

$$\frac{d}{dx}\left(\frac{u^2}{3\beta}\frac{dr^3}{dx}\right)=\frac{F_b}{u}-\frac{N^2r^3}{3\beta} \tag{2-61}$$

Assuming $p=r^3$,(2-60) can be rewritten as,

$$\frac{d}{dx}\left(\frac{u^2}{3\beta}\frac{dp}{dx}\right)=\frac{F_b}{u}-\frac{1}{3\beta}N^2p \tag{2-62}$$

Note that, following (2-42),

$$\left.\frac{dp}{dx}\right|_{x=0}=\frac{3\beta F_m}{u^2} \tag{2-63}$$

Defining $l_s=\frac{u}{N}$ and $l_b=\frac{F_b}{u^3}$, (2-61) can be rewritten as,

$$\frac{d^2 p}{dx^2} + \frac{p}{l_s^2} = 3\beta l_b \tag{2-64}$$

Equation (2-63) is a second order differential equation, which the solution is,

$$p = A\sin\left(\frac{x}{l_s}\right) + B\cos\left(\frac{x}{l_s}\right) + 3\beta l_b l_s^2 \tag{2-65}$$

Applying the initial condition of $p=r_0^3$ at $x=0$;

$$B = r_0^3 - 3\beta l_b l_s^2 \tag{2-66}$$

Differentiating p with respect to distance x as,

$$\frac{dp}{dx} = \frac{A}{l_s}\cos\left(\frac{x}{l_s}\right) - \frac{B}{l_s}\sin\left(\frac{x}{l_s}\right) \tag{2-67}$$

Following (2-62) and (2-66),

$$\left.\frac{dp}{dx}\right|_{x=0} = \frac{A}{l_s} = \frac{3\beta F_m}{u^2}; \tag{2-68}$$

Thus, defining $l_m = F_m / u^2$,

$$A = 3\beta l_s l_m . \tag{2-69}$$

Therefore,

$$r = \left\{3\beta l_s l_m \sin\left(\frac{x}{l_s}\right) + 3\beta l_s^2 l_b\left(1-\cos\left(\frac{x}{l_s}\right)\right) + r_0^{\,3}\cos\left(\frac{x}{l_s}\right)\right\}^{1/3} . \tag{2-70}$$

Replacing $z=(r-r_0)/\beta$ in (2-69) results in

$$z = \left\{\frac{3}{\beta^2} l_s l_m \sin\left(\frac{x}{l_s}\right) + \frac{3}{\beta^2} l_s^2 l_b\left(1-\cos\left(\frac{x}{l_s}\right)\right) + \left(\frac{r_0}{\beta}\right)^3 \cos\left(\frac{x}{l_s}\right)\right\}^{1/3} - \frac{r_0}{\beta} . \tag{2-71}$$

For neutral stability condition where $N \to 0$ and $l_s \to \infty$; thus (2-70) becomes,

$$z = \left(\frac{3}{\beta^2} l_s^2 l_b \frac{x^2}{2 l_s^{\,2}} + \left(\frac{r_0}{\beta} \right)^3 \right)^{1/3} - \frac{r_0}{\beta} = \left(\frac{3 l_b x^2}{2\beta^2} + + \left(\frac{r_0}{\beta} \right)^3 \right)^{1/3} - \frac{r_0}{\beta}. \tag{2-72}$$

Assuming that $l_m = 0$ and neglecting the effect of r_0 in (2-47), the plume rise (z) becomes,

$$z = \left\{ \frac{3}{\beta^2} l_s^2 l_b \left(1 - \cos\left(\frac{x}{l_s} \right) \right) \right\}^{1/3}. \tag{2-73}$$

Thus, the maximum plume rise would be,

$$z_{\max} = \left\{ \frac{6}{\beta^2} l_s^2 l_b \right\}^{1/3}. \tag{2-74}$$

Substituting $l_s = \frac{u}{N}$ and $l_b = \frac{F_b}{u^3}$ into (2-74) give the final plume rise of

$$z_{\max} = \left(\frac{6}{\beta^2} \frac{F_b}{u N^2} \right)^{1/3}. \tag{2-75}$$

2.4.3 Final Plume Rise Equations

From equation (2-48), assuming that at large distances from stack plume rise is only a function of F_b and not the F_m, (2-48) can be rewritten as,

$$z = \left(\frac{3}{2\beta^2} \right)^{1/3} \frac{F_b^{\,1/3} x^{2/3}}{u} \tag{2-76}$$

Assuming that plume rise breakdown where the plume vertical velocity w, becomes comparable to the vertical component of turbulent velocity σ_w, one can write,

$$\left.\frac{dz}{dx}\right|_{z_{\max}} = \frac{2}{3}\left(\frac{3}{2\beta^2}\right)^{1/3} \frac{F_b^{1/3} x_f^{-1/3}}{u} = \sigma_w. \tag{2-77}$$

Thus,

$$x_f^{1/3} = \frac{2}{3}\left(\frac{3}{2\beta^2}\right)^{1/3} \frac{F_b^{1/3}}{u\sigma_w} \ . \tag{2-78}$$

Therefore, the final plume rise will be $z(x_f)$, following (2-48), z_{max} can be calculated as,

$$z_{\max} = \left(\frac{3}{2\beta^2}\right)^{1/3} \frac{F_b^{1/3} x_f^{2/3}}{u} = \left(\frac{2}{3\beta^2}\right)\frac{F_b}{u\sigma_w^2} \ . \tag{2-79}$$

Assuming β=0.6, the final plume rise (z_{max}) becomes,

$$z_{\max} = 1.85\frac{F_b}{u\sigma_w^2}. \tag{2-80}$$

Plume rise plays a major role in dispersion from low level buoyant sources as it can modify the ground level concentration pattern close to the source significantly. More discussion on plume rise and different methods to estimate it under complicated urban condition will be given in Chapter 7.

3 A FIELD STUDY ON DISPERSION OF EMISSIONS FROM LOW LEVEL BUOYANT SOURCES IN URBAN AREAS

3.1 Introduction

As outlined in the introduction section, the main objective of this dissertation is to develop and apply methods to estimate the air quality impact of distributed generation at source-receptor distances of hundreds of meters in urban areas. Recognizing this need, Venkatram et al. (2004a) conducted a tracer field study to simulate the dispersion from DG in urban areas. This study was conducted in a parking lot in which a tracer, SF_6, was released from the top of a trailer, surrounded by small buildings. The results of the tracer experiment indicated existing dispersion models, such as AERMOD (Cimorelli et al., 2005), do need improvement and can overestimate maximum concentrations and underestimate area-wide concentrations in urban areas. These data were instrumental in improving a micro-scale dispersion model called Air Quality Model with Meandering (AQMM), one of which is currently being used in California Energy Commission (CEC) project to model near field impacts of DGs. Although this model is the best tool available for this purpose, it has not been validated for use in real urban areas due to the lack of field data. Furthermore, this model as well as other models, such as AERMOD, do not account for the effects of multiple buildings on buoyant emissions from DGs. Therefore, there is a need for a dispersion model that can be applied to estimate the near field impact of DGs situated in a complex built-in environment. In order to develop such model, concentration measurements under urban condition are needed. Here we briefly overview some of the field studies done on urban dispersion problem in the last 50 years.

There are only few tracer field studies done in urban areas with adequate ground level concentration and meteorological measurements. Saint Louis dispersion study (McElroy, 1969) was one of the first of these studies which was carried out between 1963 and 1965. The experiment consisted of a series of 26 daytime and 16 evening experiments. Fluorescent zinc cadmium sulfide particles were released near ground level at two different locations. Up to 50 samplers were used at each arc close to the anticipated plume centerline for ground level concentration measurements. Wind, temperature, and relative humidity were measured through a meteorological network consisting of three stations on the outer area of the sampling area and an instrumented television tower. A TV tower instrumented at three levels measured profiles of wind and temperature. Winds were profiled to a height of a kilometer using a single-theodolite, free or tethered radiosonde ascents, and transponder-equipped tetroons. Using the measured ground level concentrations, the horizontal plume spreads in the St. Louis study were calculated, while the vertical plume spreads were derived indirectly by matching concentration estimates from a Gaussian dispersion model to observed surface concentrations. Measured plume spreads from this study were grouped using meteorological indices of dispersion, such as Richardson number and Pasquill stability class (McElroy and Pooler, 1968). These data were supplemented with data from other urban tracer experiments conducted in Johnstown, Pennsylvania (Smith, 1967) and Ft. Wayne, Indiana (Csanady et al., 1967) where simple power law curves fitted to these data (Briggs, 1974) formulated the urban dispersion curves which were later used in EPA models such as ISC. Copenhagen experiment (Gryning and Lyck, 1984) was done during

1978 to 1979 to investigate the dispersion of tracer released from an elevated source (≈ 115 m above the ground level) over an urban area during neutral and unstable conditions. The sampling was conducted over three different arcs ranging from 2 to 6 km from the sources. Similar to St. Luis field study, the lateral plume spreads were calculated using the ground level concentrations. The lateral plume spread was found to be correlated with the standard deviation of the horizontal velocity fluctuations (σ_v). Also using a simple Gaussian dispersion model, utilizing the mean and turbulent wind speeds as well as the stack height, the ground level concentrations were predicted reasonably well. However, due to the lack of data on vertical turbulent velocity profile, this data set could not be used to relate the dispersion to meteorological condition (Venkatram et al., 2004b). Recently there have been several urban tracer experiments in European and American cities. URBAN 2000 (Allwine et al., 2002; Hanna et al., 2003) tracer field study was conducted in Salt Lake city in October 2000 to further understand the governing processes involved in dispersion of pollutants in urban environment from the individual building to regional scale under a same meteorological condition. Hanna et al. (2003) explained the maximum concentrations observed during this field study by incorporating the initial plume spread into a simple Gaussian dispersion model. They found out that this simple modification can significantly enhance the model performance. However, the choice of initial plume spread used in this study might not be justifiable over more complex geometries and there is a high possibility that it is specific to the site. Venkatram et al. (2004b) conducted a tracer field study in Barrio Logan, California to understand dispersion in urban area with buildings of heights less than 10m. This study showed that

simple dispersion model with adequate knowledge on urban turbulent intensities can lead to an acceptable agreement between observations and model predictions. Similar conclusion was also made by Gryning and Batcherova (2005) in analyses of data from Copenhagen experiment and the Bubble experiment. The tracer experiment, BUBBLE, in an area of the city of Basel (Switzerland) named Kleinbasel was conducted in June and July 2002 where concentrations associated with a non-buoyant release from a roof-level source has been measured (Rotach et al. 2004). In this study turbulent profile has also been measured throughout the street canyon and above which gives a thorough insight into the effect of urban geometry on transport and dispersion of pollutants inside an urban area. The most important message from these tracer studies is that an adequate characterization of micrometeorology in urban area can lead to reasonable predictions of one hour averaged ground level concentrations through a simple Gaussian model. While these tracer studies provide important information on passive releases in an urban area, they do not deliver enough information on the dispersion of low level buoyant sources inside urban areas. The emissions from such sources undergo a high plume rise in an inhomogeneous boundary layer affected by complex flows induced by surrounding buildings. These complexities need to be investigated in more detail and since no such related database is available, conducting a tracer field study specific to these sources is vital. Thus, we conducted a field study to collect the data required to model dispersion from such a source. This tracer study has been conducted in Palm Springs, CA on July 2008 to investigate the dispersion of emission from such sources within source-receptor distances of tens and hundreds of meters. The results from this field study will fill a gap

in the studies conducted thus far on the air quality impact of distributed generation of energy. The details of this study will be described next.

3.2 Field Study

The tracer experiment was conducted from July 15th, 2008 to July 21st, 2008 at the Sunrise Park in Palm Springs. During the experiment, sulfur hexafluoride (SF_6) was released at the same temperature as the exhaust air at the rate of 3.3 (kg/hr) from the top of a DG stack which is situated at the top of a 7 m high building surrounded by one storey residences. The stack is 2.3 m high above roof top. The DG is driven by a 650 kW gas fired IC engine with heat recovery. 49 SF_6 samplers were arranged in arcs at distances of 60 m to 2000 m from the source during the releasing time. Fig. 3-1 shows the sampling locations relative to the release point.

The sonic anemometer in an 11 m high tripod sampled the three components of the velocity and temperature at 10 Hz. The SF_6 was released continuously over seven 6-hour periods between 15th and 21st July 2008. There were three daytime releases (15th, 16th, and 17th July 2008, from 09:00 to 15:00 PDT) and four nighttime releases (18th, 19th, 20th, and 21st July 2008, from 01:00 to 07:00 PDT). For analysis, the concentrations and meteorological measurements were averaged over 1 hour periods.

(a) (b)

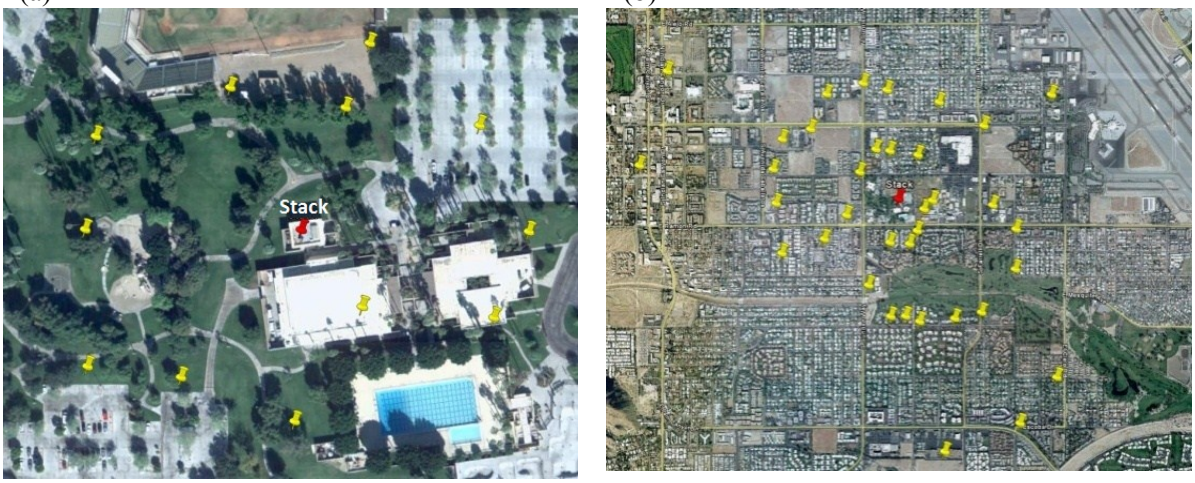

Figure 3-1: Location of sampling stations and stack (a) within 100m from the stack (b) beyond 100m from the stack

Fig. 3-2 shows the meteorological parameters as a function of time of day during the experiments. We see that the wind speeds never exceeded 3.5 ms^{-1}. They were below 2 ms^{-1} during most of the day, and below 1 ms^{-1} during most of the nighttime. The vertical turbulent velocities (σ_w) were about 20% of the mean wind speeds during most of the release periods, and the lateral turbulent velocities (σ_v) were above 0.5 ms^{-1} during most of the day; the lateral turbulent intensities are about 30% during most of the day. This indicates the need to account for horizontal meandering in modeling the concentrations. This meandering is reflected in the patterns of SF_6 concentrations observed during the experiments.

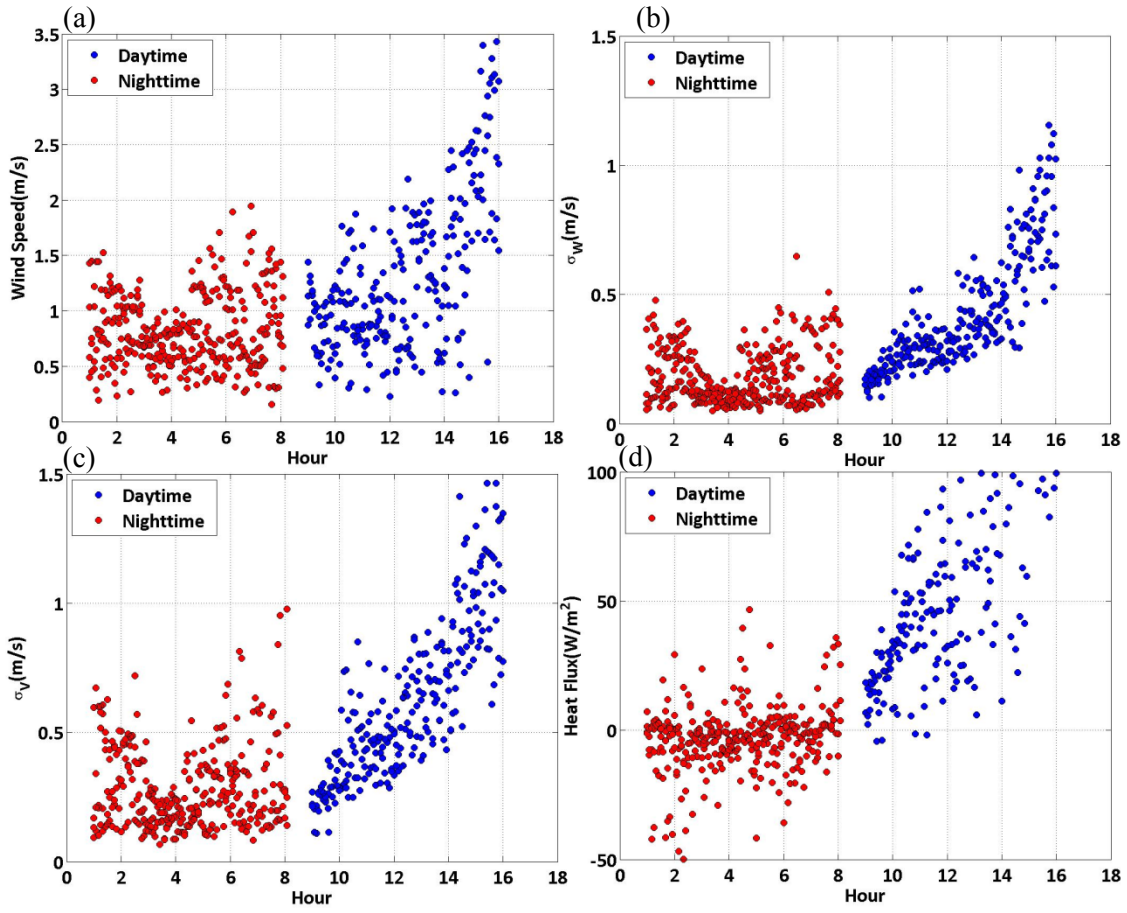

Figure 3-2: Meteorology measurements for (a) wind speed U(m/s) (b) vertical turbulent velocity σ_w (m/s) (c) lateral turbulent velocity σ_v (m/s) (d) Heat Flux $\rho C_p \overline{w'T'}$ (w/m^2)

Figure 3-3 is a typical pattern of the ground level concentrations observed during the daytime. The concentrations drop off with distance as expected, but there are small upwind concentrations up to distances of 1000 m. The pattern is very different during the night when the wind speeds are low and the turbulent intensities are high. The concentrations are generally higher than the daytime concentrations and do not fall off as rapidly as during the day, and the upwind concentrations are comparable to the downwind concentrations. This indicates that the DG plume was trapped in a relatively shallow boundary layer at night, and was spread in all directions by the meandering wind.

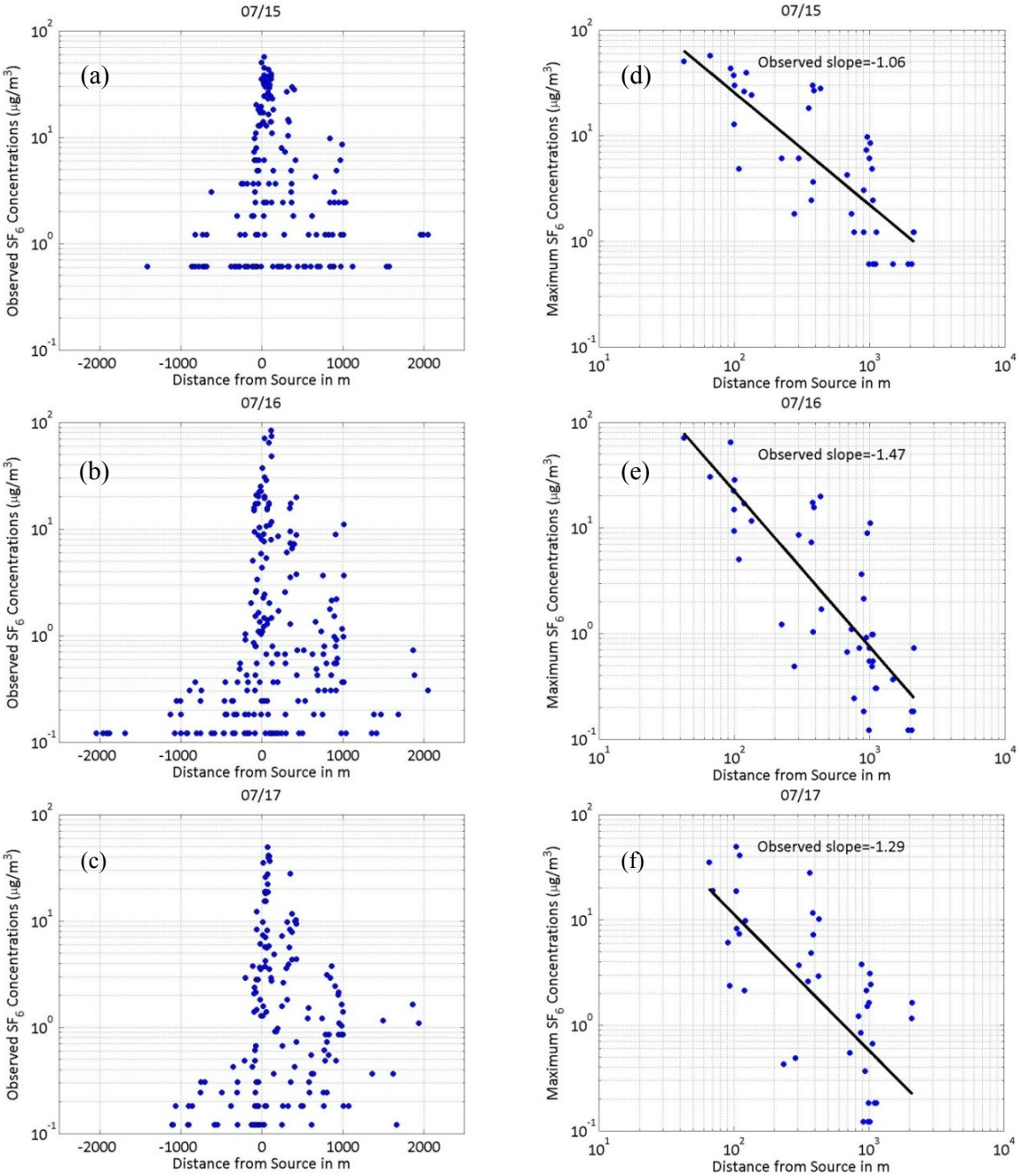

Figure 3-3: Observed daytime concentrations as a function of (a, b, c, d) downwind distance and (e, f, g, h) radial distance on 15th, 16th and 17th of July, 2008

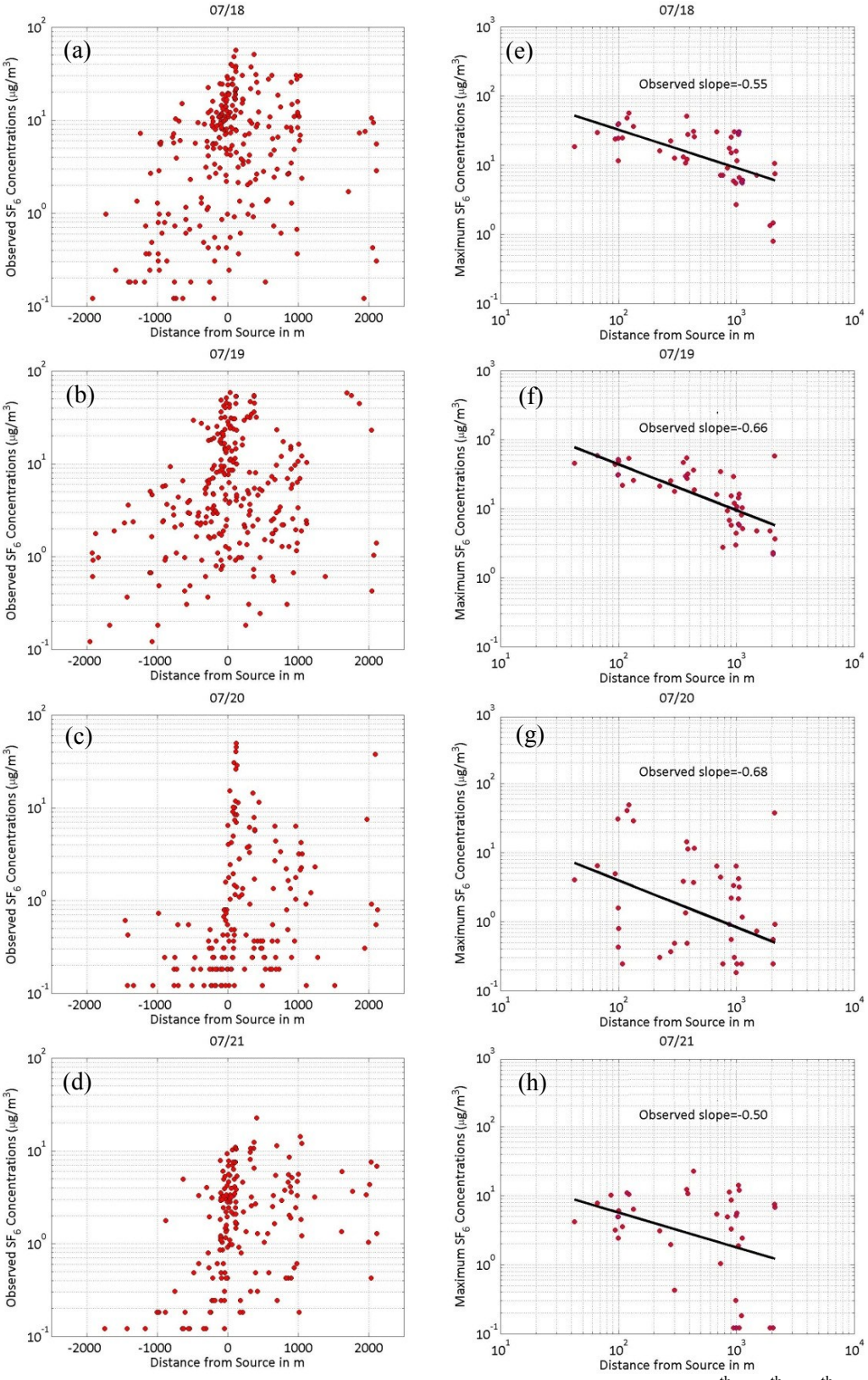

Figure 3-4: Same as Figure 3-3 but observed nighttime concentrations on 18th, 19th, 20th and 21th of July 2008

Following this field study, US EPA recommended dispersion model, AERMOD (Cimorelli et al., 2005) were used to explain the tracer concentration for both daytime and nighttime observations (Jing et al., 2009; Jing et al., 2010). AERMOD reasonably predicts daytime concentration (Fig. 3-5a); however, during nighttime, it tends to considerably underestimate ground level concentrations (Fig. 3-5b). More details on evaluation of AERMOD with the field data can be obtained from (Jing, 2011).

We suspect that this discrepancy is related to inadequate modeling of the nighttime urban boundary layer height and its interaction with the buoyant plume as well as incorrect modeling of plume lateral spread (σ_y) in urban area under neutral / stable conditions.

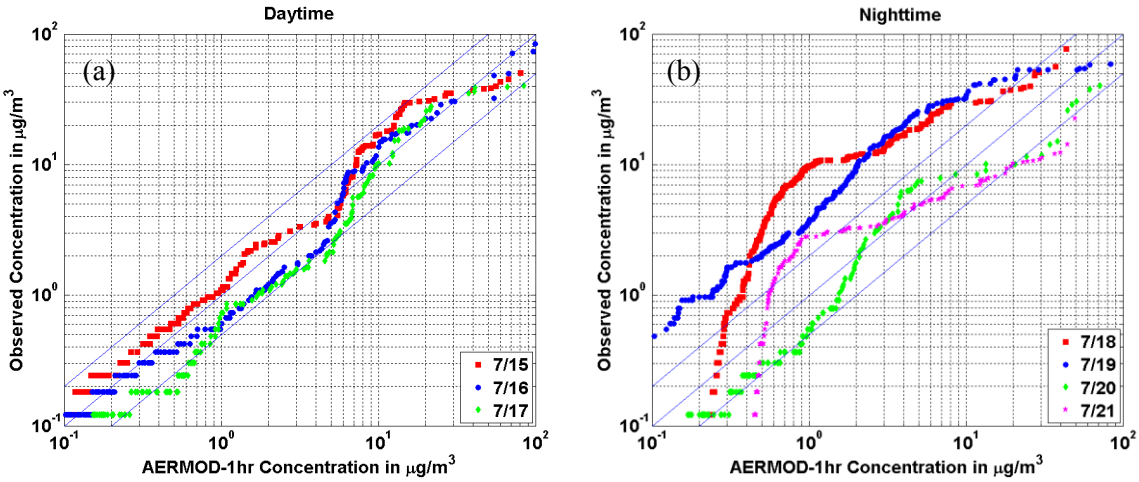

Figure 3-5: Q-Q plots of hourly observed vs. predicted concentrations during (a) Daytime and (b) Nighttime (from Jing et al., 2010)

3.3 Simple Gaussian Model Performance

A simple Gaussian model with built in meandering module (using AERMOD meandering scheme) were used to predict the concentrations. The model formulation is shown below.

3.3.1 Model Formulation

Although the Gaussian dispersion model (Sutton, 1947) might not necessarily explain the dispersion of pollutants in the urban boundary layer, due its simplicity, as mentioned in the introduction part, it is used as the main framework for the urban pollution dispersion purposes (e.g. in the US EPA regulatory model AERMOD). Therefore, we based our dispersion modeling on this model,

$$C(x,y,z) = \frac{Q}{\sqrt{2\pi}u\sigma_z}\left[\exp\left(-\frac{(z-h_e)^2}{2\sigma_z^{\,2}}\right)+\exp\left(-\frac{(z+h_e)^2}{2\sigma_z^{\,2}}\right)\right]H(x,y) \tag{3-1}$$

The horizontal concentration distribution $H(x,y)$ is a linear combination of Gaussian and uniform distribution defined as,

$$H(x,y) = f_p H_p(x,y) + (1-f_p)H_r(x,y) \tag{3-2}$$

where the plume distribution $H_p(x,y)$ is,

$$H_p(x,y) = \frac{1}{\sqrt{2\pi}\sigma_y}\exp\left(-\frac{y^2}{\sigma_y^{\,2}}\right), \tag{3-3}$$

and the uniform distribution $H_r(x, y)$ is defined as,

$$H_r(x, y) = \frac{1}{2\pi r} \tag{3-4}$$

where r is the radial distance from the source, σ_y is the is the plume spread in the crosswind direction at distance x from the source and $f_p = \frac{u^2}{u^2 + 2\sigma_v^2}$.

In this model we test our hypothesis that the relatively high ground level concentrations during last four nighttime experiments (17th - 21st of July) are associated with a shallow urban mixed layer by modeling the vertical spread as

$$\sigma_z = \min\left(\frac{\sigma_w x}{U}, \sqrt{\frac{2}{\pi}} z_i\right) \tag{3-5}$$

where σ_w / U is the observed vertical turbulent intensity and z_i is the height of the urban mixed layer.

We assume that the horizontal scale of turbulence is governed by z_i so that horizontal plume spread, σ_y, becomes

$$\sigma_y = \left(\frac{(\sigma_v / U).x}{(1 + x / x_0)^{0.5}}\right) \tag{3-6}$$

where x_0 is the length scale given by

$$x_0 = \frac{z_i}{(\sigma_v / U)} \tag{3-7}$$

where σ_v / U is the observed lateral turbulent intensity. In this model, plume effective heights were calculated through Briggs (1984) and Weil (1988) models for daytime and nighttime, respectively, as follows,

$$h_e = h_s + \left(\frac{3F_b}{u^3 \beta^2} \frac{x^2}{2} + \frac{3}{u^2 \beta^2} F_m x \right)^{1/3} \quad \text{For daytime;} \tag{3-8}$$

$$h_e = h_s + \left\{ \frac{3}{u\beta^2 N^2} \left[F_0 \left(1 - \cos \frac{Nx}{u} \right) + NF_m \sin \frac{Nx}{u} \right] \right\}^{1/3} \quad \text{For nighttime.} \tag{3-9}$$

Here $\beta = 0.6$ (Hoult and Weil, 1972) is the entrainment parameter; h_s is the stack height; and $N^2 = \left(\frac{g}{\theta_0} \frac{\partial \theta}{\partial z} \right)$ is the Brunt-Vaisala frequency where θ is the potential temperature. These plume rise equation has been explained more in detail in Chapter 2.

The plume rise calculated from Equations (3-8) is limited by the height of the boundary layer (Z_i); the input plume effective height into the model is the minimum of plume effective height, h_e, and boundary layer height Z_i.

Therefore, assuming Z_i = 1000m during daytime and Z_i = 150m during nighttime, hourly averaged concentrations were predicted. The nighttime value of boundary layer height was obtained by supposing that $\frac{\partial \theta}{\partial z}$=0.06 K m^{-1}; thus assuming that the temperature difference across the boundary layer is equivalent to the change in the surface temperature from sunset, the boundary layer height were predicted. More details about this assumption can be found in Chapter 8.

3.4 Results

Using the model explained in the previous section, Palm Springs concentration data were predicted using hourly averaged micrometeorology. Results from daytime predictions are shown in Fig. 3-6. In addition to daytime prediction, concentration observed during four consecutive nights were also predicted using the model (Fig. 3-7).

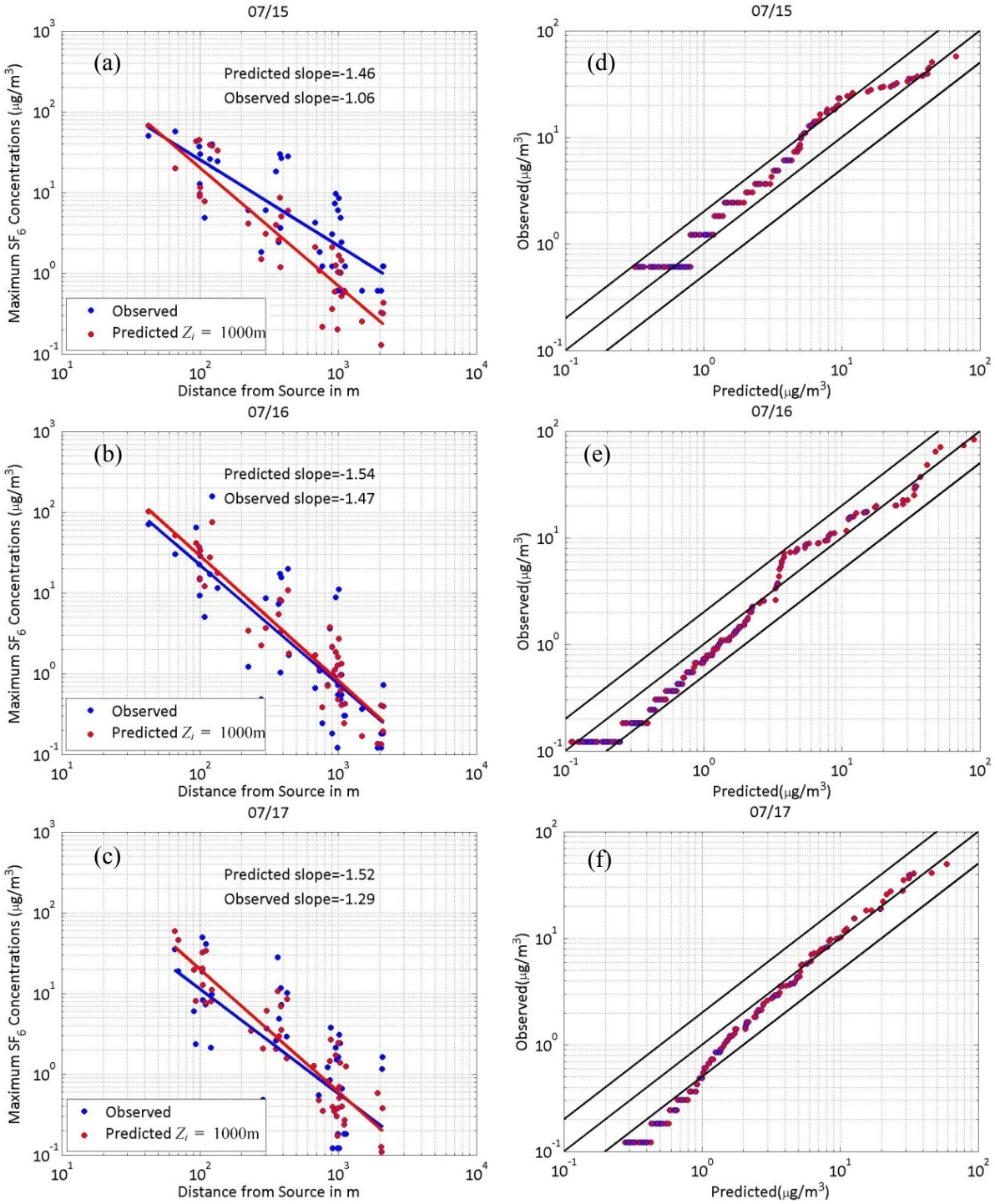

Figure 3-6: (a, b, c) Hourly maximum daytime concentrations as a function of radial distance (d, e, f) Q-Q plots of hourly daytime observed vs. predicted concentrations for 07/15, 07/16, and 07/17/2008.

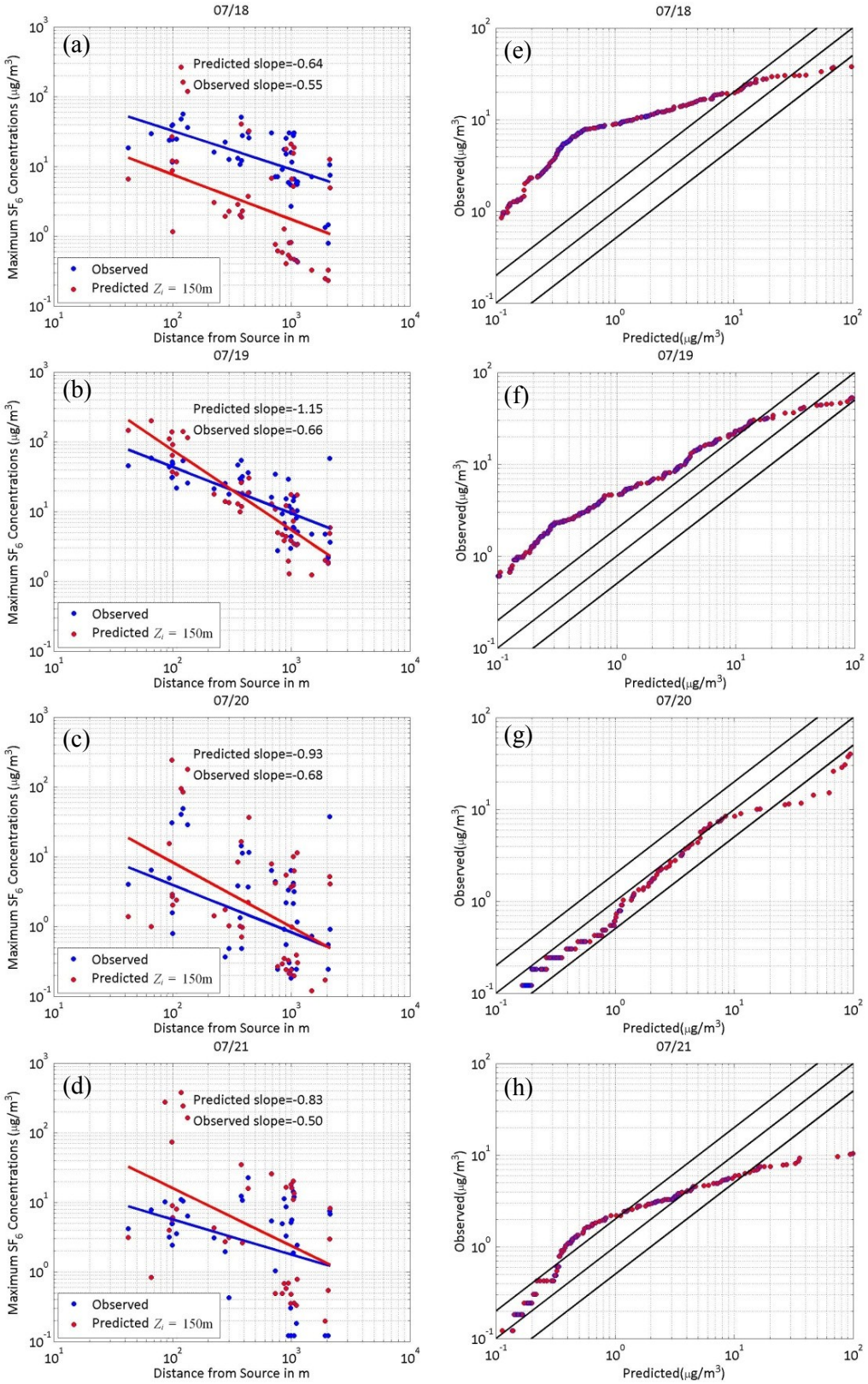

Figure 3-7: (a,b,c) Hourly maximum nighttime concentrations as a function of radial distance (d,e,f) Q-Q plots of hourly nighttime observed vs. predicted concentrations for 07/18, 07/19, 07/20, and 07/21/2008.

As it is shown in Fig. 3-6, this simple model can reasonably predict the concentration during daytime. The predicted values drops off slightly more rapidly than the observed concentration, especially for 07/15; thus underestimate the observed concentrations. However, the predicted concentrations close to the source are slightly higher than the observed values, resulting in the overestimation of concentrations during 07/16 and 07/17 days. Despite the simplicity of the model, its performance in explaining the daytime concentrations is reasonable.

However, the model does not perform well during nighttime, especially for the first two nights. The model tends to underestimate concentrations during first two nights (07/18 and 19), while the predictions are relatively better for the second two nights (07/20 and 21).

Although the model accounts for the shallow nocturnal urban mixed layer height as well as its dominance on the lateral turbulence; the rate of decrease of predicted concentration are slightly higher than those observed.

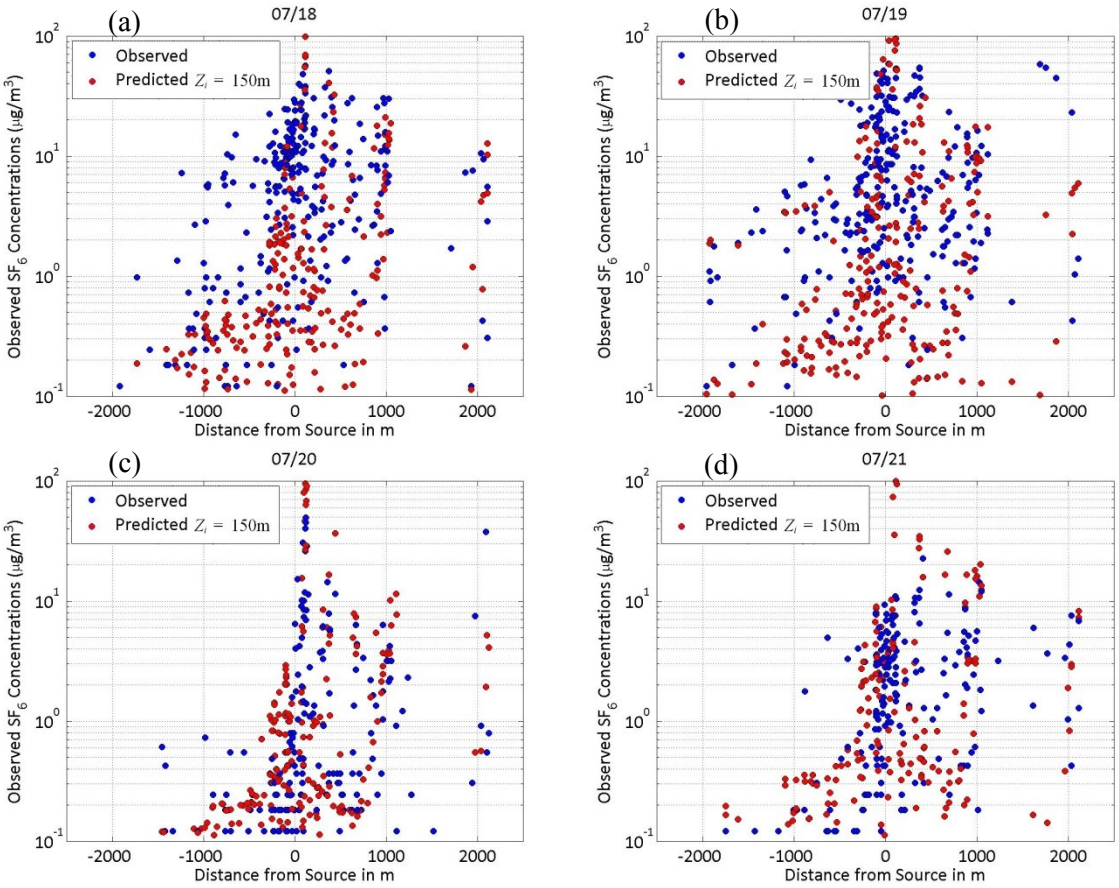

Figure 3-8: Hourly averaged concentrations as a function of downwind distance of (a) 07/18 (b) 07/19 (c) 07/20 and (d) 07/21/2008

One of the main reasons for the substantial underestimation of concentrations during first two nights can be explained through the relatively high upwind concentrations as shown in Fig. 3-8. Even though, the model accounts for the meandering behavior of the plume, it cannot predict the high upwind concentration. As it can be seen in Fig. 3-8, the magnitude of downwind predicted concentration is comparable to that of the observed values. However, this is not the case on the upwind side. Since, the upwind concentration is not high during the last two nights; the model performs reasonably well for 07/20 and 21. One of the other reasons for the different performance of the model at different nights is the presence of higher concentrations during first two nights than that of the second two nights. As it can be seen in Fig.3-4 the average concentrations, during 07/18 and 19 are almost higher by a factor of 10 than those from 07/20 and 07/21. But

the average measured micrometeorology at different nights (Table 3-1), does not show significant change from one night to another. Thus, the model cannot resolve for the substantial difference in concentrations, while the input meteorology is almost the same. The values of averaged micrometeorology parameters are shown in Table 3-1.

Table 3-1 Average nighttime micrometeorology input

	u(m/s)	σ_w (m/s)	σ_v (m/s)	$\rho C_p(\overline{w'\theta'})$ (W/m^2)	u_* (m/s)
07/18	0.67	0.13	0.22	-4.6	0.09
07/19	0.93	0.22	0.33	-4.5	0.13
07/20	0.97	0.25	0.38	2.1	0.23
07/21	0.68	0.13	0.21	1.9	0.08

3.5 Asymptotic Behavior

In the view of the uncertainty of Gaussian model explaining the nighttime observations, the asymptotic behaviors of the plume have been investigated. This asymptotes includes the uniform dispersion of plume in all direction and secondly, the simple Gaussian behavior without any meandering. These two asymptotes were obtained by fixing the value of f_p in the equation (3-2) as either 1 or 0. Selecting f_p=1 yields concentration prediction of a simple Gaussian plume where no meandering is accounted for. On the other hand, f_p=0, would corresponds to uniform distribution of the plume in all directions. Results from these two behaviors are shown in Fig. 3-9 and 10.

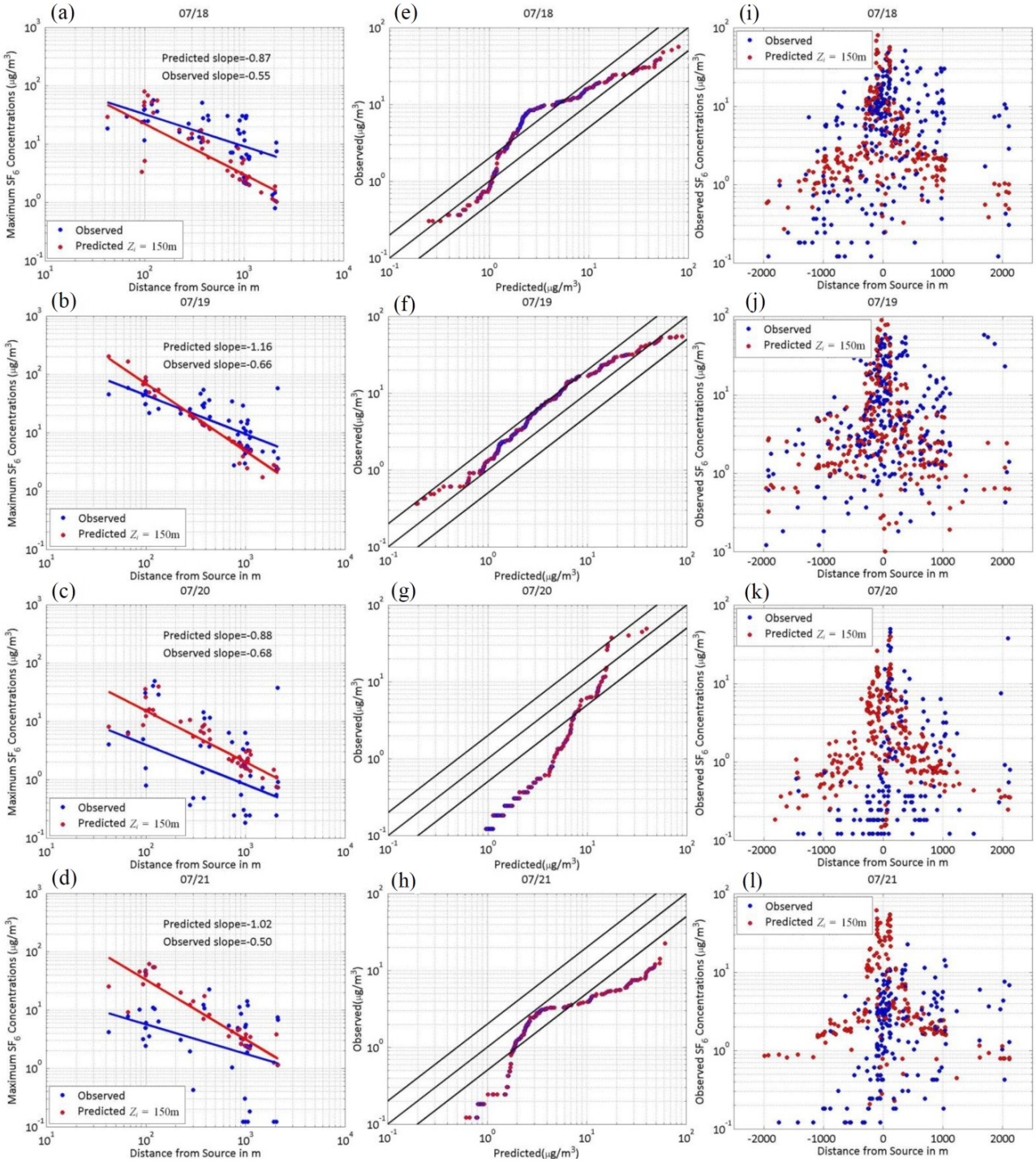

Figure 3-9: Prediction of ground level concentrations assuming that plume is uniformly distributed in all directions (f_p=0). (a, b, c, d) Hourly maximum nighttime concentrations as a function of radial distance (e, f, g, h) Q-Q plots of hourly nighttime observed vs. predicted concentrations; and (i, j, k, l) Hourly averaged concentrations as a function of downwind distance for 07/18, 07/19, 07/20, and 07/21/2008.

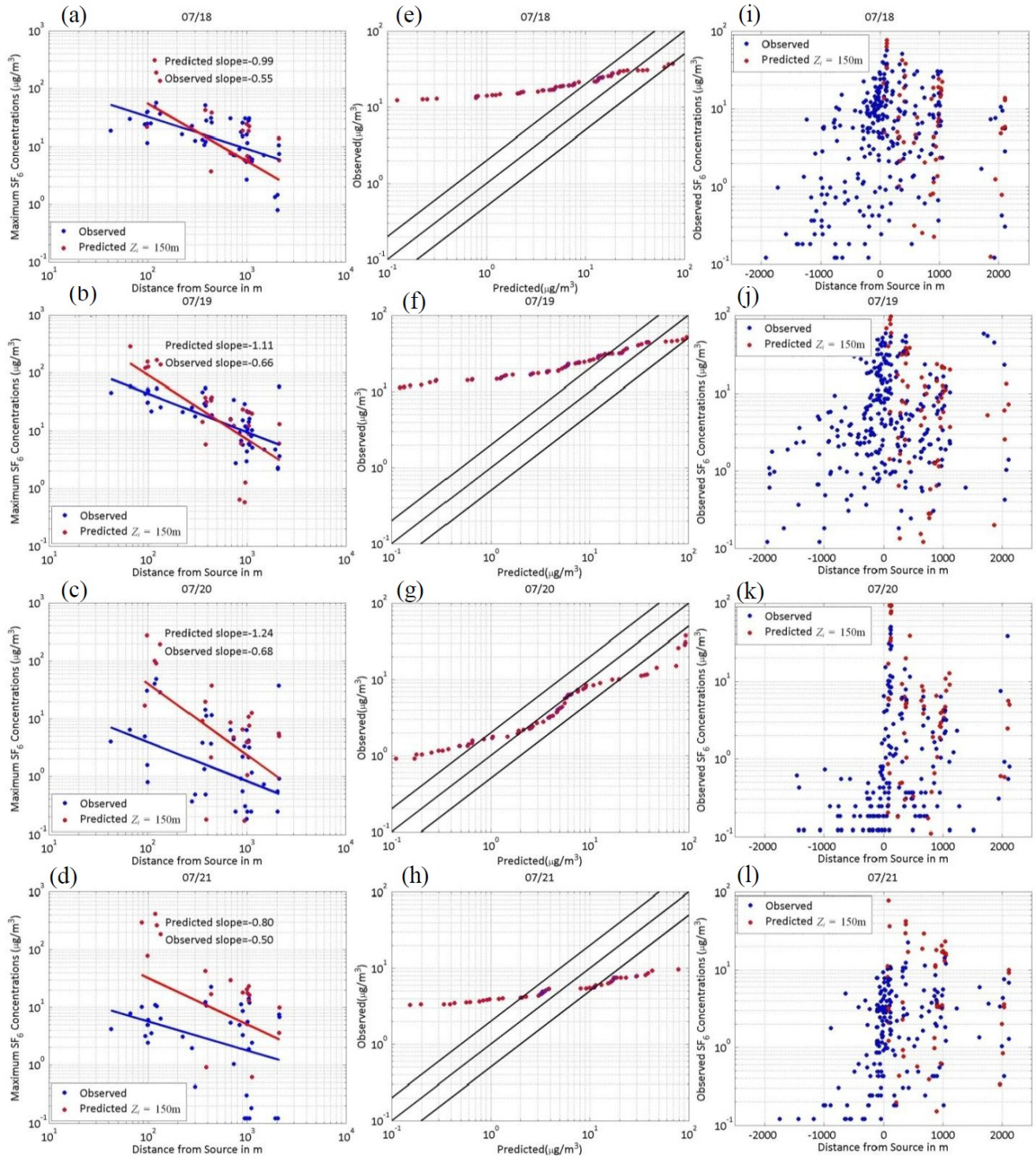

Figure 3-10: Prediction of ground level concentrations assuming that plume has a Gaussian distribution along the wind direction (f_p=1). (a, b, c, d) Hourly maximum nighttime concentrations as a function of radial distance (e, f, g, h) Q-Q plots of hourly nighttime observed vs. predicted concentrations; and (i, j, k, l) Hourly averaged concentrations as a function of downwind distance for 07/18, 07/19, 07/20, and 07/21/2008.

As it can be seen in Fig. 3-9, uniform distribution asymptotic, yields to prediction which are comparable to observed values in the first two nights. However, this behavior results in the overestimation of concentration during the last two nights, since upwind concentration in the last two nights are lower. On the other hand, the simple Gaussian plume behavior, does not provide any good description of the concentrations, since it does not have the capability to account for plume meandering, thus, no upwind concentration can be predicted. As it is shown in Figs. 3-10 d-f, downwind concentration tends to fall off much slower than the upwind concentrations, for that reason the Q-Q plot of observed vs. predicted concentration resemble a flat shape. The same case for concentration decrease rate can be observed in Fig. 3-9; the overall upwind and downwind predicted concentrations fall off much more rapidly than those of observed values.

Following the high complexities involved in the dispersion process of low level buoyant sources, neither this simple dispersion models nor the more advanced ones (such as AERMOD) were able to predict the concentrations accurately.

3.6 Conclusion

The air quality impact of buoyant emissions from low level sources such as DGs in urban areas for source receptor distances of tens and hundreds of meters is not very well understood and currently used models such as USEPA recommended dispersion model AERMOD/PRIME (Cimorelli et al., 2005; Schulman et al., 2000) are not able to reproduce ground level concentration associated with these sources accurately. Following

this need, a comprehensive laboratory and field study to understand the dispersion of pollutants released from DGs in urban areas have been conducted.

Results from a tracer field study conducted in Palm Springs in summer 2008 in the vicinity of a gas fired 650 kilowatt (kW) DG unit indicate that ground level concentrations associated with nighttime measurements do not decrease rapidly with distance in compare with daytime observations. Also, observations indicate that despite the high plume rise in Palm Springs field study, concentrations observed during the nighttime experiments are generally higher than those measured during the daytime experiments.

Simple Gaussian dispersion model with built in meandering module has also been used to predict the concentrations associated with this field study. This model showed similar performance as AERMOD. It reasonably predicts daytime concentrations while underestimated the first two nights of the experiment.

The asymptotic behavior of the plume (uniform distribution in all directions vs. Gaussian distribution along wind direction) has also been analyzed. It has been observed that the concentration behavior in the first two nights is more likely similar to the uniform distribution. This fact is also visible in the observed concentration pattern. Upwind concentrations, in the first two nights were comparable to the downwind concentrations, while for the second two nights, substantially lower upwind concentrations can be observed. The Gaussian asymptotic behavior of the plume does not provide any reasonable description of observed concentrations in any of the four nights. Following

this analysis, it has been concluded that urban dispersion models should account for the meandering although the amount of the meandering might be different at different nights and more investigation is required.

As a recommendation toward future works, more attention needs to be paid to the interaction of the low level buoyant release from a DG with the nighttime urban boundary layer. This requires measurements of mean flow and turbulence in the nighttime boundary layer. In addition, future modeling improvements will need to address concentrations at scales ranging from scales of few meters to hundreds of kilometers by combining large scale grid models with short range dispersion models, such as AERMOD. Although progress has been made in this area (Stein et al. 2007; Isakov et al. 2007), there are still unresolved issues related to combining concentrations and the associated chemistry at vastly different scales.

4 EXPERIMENTAL SETUP

Simulated flows and emissions in water channels are the most efficient ways of studying the plume motion due to the relative simplicity of generating stably stratified flows and making visualizations using fluorescent dyes (Contini and Robins 2001; Arya and Lape 1990). Examples of such applications can be found in Hunter (1992), Ohba et al. (1990), Snyder (1985), and Hoult and Weil (1972) and will not be discussed here. The laboratory study explained in this dissertation is conducted through a series of experiments in the water channel facility at University of California Riverside, Laboratory for Environmental Flow Modeling (LEFM). The main focus was to investigate the air quality impact of buoyant emissions from DGs under different building configurations and meteorological conditions.

4.1 Water Channel

A custom-designed circulating water channel with a test section that is 1.5 m long, 1 m wide and 0.5 m deep (see schematic in Fig. 4-1a and a photograph in Fig. 4-1b) was utilized for the experiments. The channel is located in the Laboratory for Environmental Flow Modeling (LEFM) at the University of California, Riverside. Water is circulated through the channel test section using a 15 kW axial pump, which produces a maximum mean velocity of 0.5 m s^{-1} in the test section. A variable frequency controller allows flow control with a resolution of 1/100 Hz (from 0 to 60 Hz). Flow conditioning is achieved with the profiled honeycombs and the custom-built perforated screens. The perforated screens are used to generate desired inflow velocity profiles as a part of the flow

conditioning. The channel flow is steady and becomes fully developed before reaching the test section. The channel has flow control capability to maintain desired velocity profile starting from the classical logarithmic to the linear profile. As needed, the channel can also maintain well defined jets at desired height. Simulating flow and dispersion in such laboratory facility requires utilizing correct scaling techniques. These scaling methods will be explained in more detail through the next chapter.

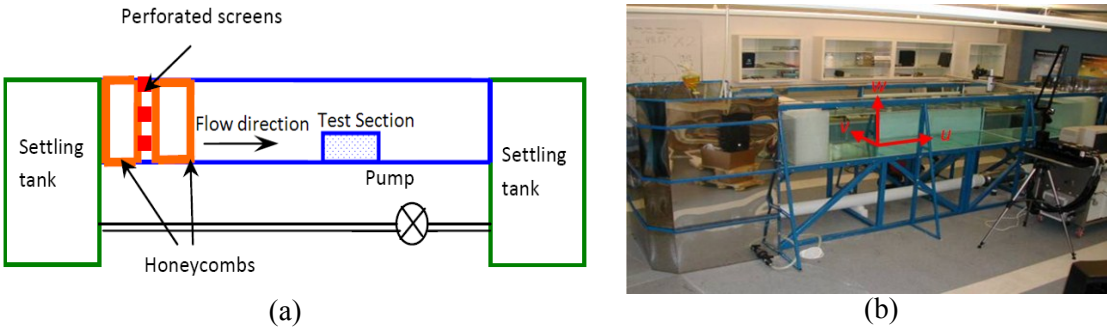

Figure 4-1: (a) Water Channel Schematic. (b) Water Channel facility at University of California Riverside (LEFM)

4.2 Concentration measurements system

The existing concentration measurements system, PLIF, is one of the most powerful techniques to measure the tracer concentrations in water channels. The principle of this technique is relatively old and well addressed in literature (e.g. Pringsheim, 1949; Kychakoff, et al., 1984; Hanson, 1986). This system is consisted of a 400 mJ Nd-YAG laser (Big Sky Laser Technologies Inc.) producing 532 nm wavelength laser beam with the frequency of up to 15 Hz as the radiation source, laser pulse synchronizer (TSI Inc.), high resolution (1600 x 1192) POWERVIEW 2M CCD camera (TSI Inc.), 575-585 nm light filter. Rhodamine 6G was used as a tracer dye. The basic equation that relates the

induced fluorescence intensity, I_f, with the fluorescent dye concentration is defined by Guilbault (1973) as

$$I_f = 2.3\ \Phi\ I_0\ \varepsilon\ b\ c \qquad (4\text{-}1)$$

where the quantum efficiency Φ is the ratio between the energy that is emitted to that of absorbed, I_0 represents the light intensity, ε is the molar absorptivity, b is the absorption path length and c is the concentration of the fluorescent dye.

We found that the PLIF results were reliable for the far field concentrations but the measurements were biased high close to the source because of four reasons. Several difficulties of PLIF measurements were identified: 1) light reflection from the water channel bottom face – this is especially pronounced when the goal is to measure near surface concentrations, 2) laser light attenuation by varying plume intensity outside of the region of interest, 3) self-illumination – this is very pronounced when extreme concentration gradients are present like in the case of near source measurements of ground level concentrations for elevated release (here ground level concentration near the stack can be four orders of magnitude less than at the nearby elevated source), and 4) averaging time – this is a problem of recirculating nature of the tank. Once dye recirculates back to the test section of the water channel, the background concentration becomes comparable to the ground level concentration. For these reasons we decided to keep PLIF for plume spread and far field concentration measurements and to conduct near source measurements using different technique.

To overcome PLIF deficiencies we tried several methods, including placing thin non-reflective enclosures in the region of interest to avoid self-illumination and laser light attenuation. These were with limited success and will not be discussed here. The satisfactorily solution was finally designed by implementing 750 μm unjacketed plastic optical fibers. Conducting laser beam through short optical fiber prevented attenuation, allowed us to direct laser beam to a point to avoid light reflection and self-illumination, and several sensors are placed in the background for real time corrections of the background concentrations to allow for longer averaging time. Each sensor consists of two optical fibers: one for delivery of a laser beam and second for delivering fluorescence light to the CCD camera. It has been experimentally shown that the best arrangement for the fibers in the sensor happens when the fibers are adjusted at an angle of 26° to each other (Kulchin et al. 2007). A sensor photo is given in Fig. 4-2a, and a schematic of the setup is given in Fig. 4-2b. Laser beam is focused on a bundle of optical fibers. Each fiber guides laser light to the location of interest. Light from the fluorescence dye at the sensor location is then conducted to the camera via second pair of fibers, referred here as return fibers. Return fibers are sparsely fixed in front of a CCD camera at predetermined location so that all fibers are recorded at the same image without interference. A filter is placed in front of the camera to prevent any laser light reaching the CCD. Each sensor has to be individually calibrated. By utilizing this system we sacrificed the whole plane PLIF measurements and replaced it with numerous point measurements. This is not a big disadvantage since sensors are inexpensive, small enough not to disturb the flow so that many of them can be placed in desired region, and light intensities from all sensors are

collected to a single image so that processing is relatively simple. Fig.4-3 shows the experiment setups for sensors, camera and laser.

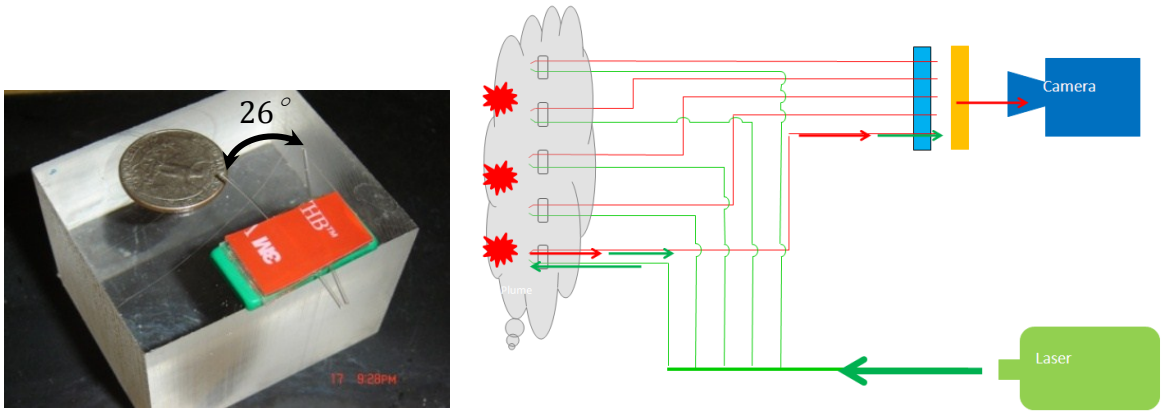

(a) (b)

Figure 4-2: (a) Optical Fiber Sensor. (b) Schematics of the concentration measurement system (green fibers are emitting fibers and red fibers are receiving fibers).

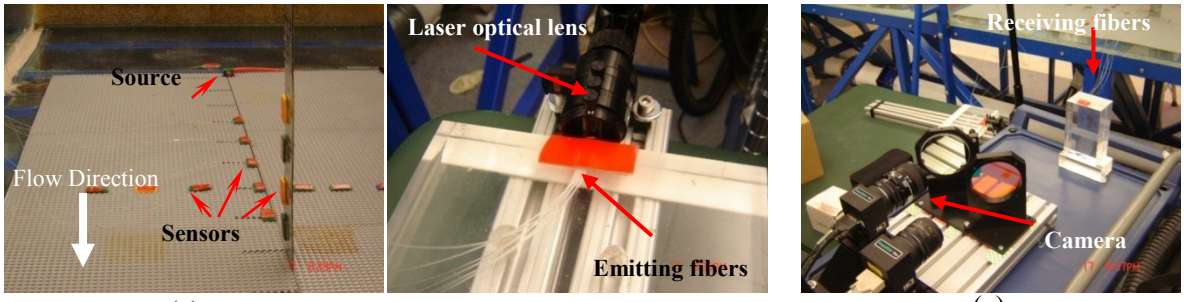

(a) (b) (c)

Figure 4-3: (a) Sensors placement in the water channel. (b) Laser setup. (c) Camera setup.

There are a variety of fluorescent substances available (Berlman 1971) however, not all are suitable for our application. The fluorescent dye suitable for this application should have the following properties: 1) solubility in water, 2) absorption and emission spectra in the range of the applicability of the devices, and 3) high resistance to photo bleaching effect. Among the commonly used tracer dyes, Rhodamine B was the most suitable tracer dye for this specific application. Rhodamine B ($C_{28}H_{31}ClN_2O_3$) is water

soluble (up to 50g/l) fluorescent dye which has the absorption spectrum of 460nm-590nm along with the emission spectrum of 550nm-680nm with the maximum occur at 590nm. There has been several different results reported for the concentration-intensity linearity limit of Rhodamine B. Guilbault (1973) stated that only when less than 5% of the exciting light is absorbed by the fluorescent dye, a linear response can be achieved from the Rhodamine B. This occurs for concentration less than 30mg/L (Walker, 1987). Arcoumanis et al. (1990) show that the concentration should be less than 0.08mg/L for linear response. However, Houcine et al. (1996) reported a concentration of less than $40\mu g/L$. Kassaro and Mungal (1997) show that the linear response is only available for concentration up to 9.57mg/L. Therefore, prior to proceeding to the measurements, this uncertainty in the linearity of light intensity and concentration made us to investigate the linear behavior of Rhodamine B. According to our results, Rhodamine B shows a linear concentration-Intensity behavior up to 10mg/L.

4.3 Velocity Measurement system (PIV)

The velocity field is measured by TSI's Particle Image Velocimetry (PIV) system. This system consists of 400 mJ Nd-YAG laser (Big Sky Laser Technologies Inc.) producing 532 nm wavelength laser beam with the frequency of 1 HZ which is expanded into a laser sheet using a sheet forming optics, Laser pulse synchronizer (TSI Inc.) and a PowerView Plus 2M and 11M camera. Pliolite Ultra 100 particles are used as seeding particles in the water channel. In order to measure the fluid's velocity, at least two separate exposures must be recorded. This typically involves producing a pair of laser

pulses which are recorded onto a pair of camera frames. The frames are then split in a large number of interrogation areas, often called tiles. Through image processing it is then possible to calculate a displacement vector for each tile. This displacement is converted to a velocity using the time step between consecutive images (in our case $\Delta t = 1.2ms$). Insight 3G (TSI Inc.) software is used for data collection and image processing. PIV measurement technique is well established and widely used for fluid flow investigations (Adrian, 1988, 1991, 1997; Prasad et al., 1992).

4.4 Plume Visualization Technique

Plume rise in the water channel have been measured through plume visualization technique. This simple technique is consisted of a commercial camera (Sony 4.1MP Cyber shot) located on a tripod and a light source illuminating the test section. Using the manual option by adjusting the lens aperture and/or shutter speed we achieve the desired exposure. Fluorescent dye, Uranine, is used as the visualizing dye as it has high light intensity in the range of visible lights. Therefore, plume visualization can be achieved by releasing the tracer dye from the source and capturing the long exposure image for 30s. This technique gives us plume averaged visualization image which can be used to measure the plume rise under different meteorological conditions and building geometries. Fig.4-4 shows some example of plume visualization images achieved using this technique.

(a) (b)

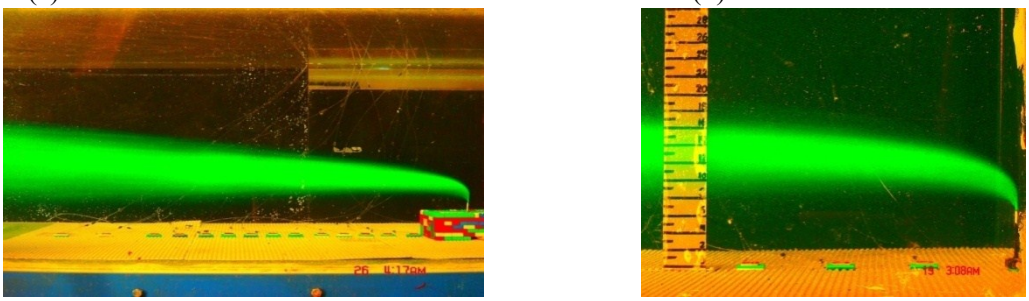

Figure 4-4: Plume Visualization (a) Palm Springs DG model (b) Single Stack Non-Buoyant Release

In the next chapter we will explain appropriate methodologies to scale real world dispersion problem in this water channel facility, and translate the results (concentration and plume rise) obtained from the laboratory measurements to those from the field for evaluation and comparison.

5 SCALING OF URBAN PLUME RISE AND DISPERSION IN WATER CHANNELS AND WIND TUNNELS*

5.1 Introduction

Site specific results of field studies and their high dependency to meteorological conditions brings up this conclusion that much of today's understanding on dispersion of urban releases results from laboratory modeling in water channels and wind tunnels (Macdonald et al., 1998; Contini and Robins, 2001; Yee et al., 2006; Klein et al., 2011). Correct modeling of atmospheric dispersion in these laboratory setups requires correct scaling of the physical properties relevant to mean flow, plume rise, and turbulent dispersion. Various scaling methods for laboratory modeling have been explained in previous studies. Kobus and Abraham (1980) defined the proper scaling laws for hydraulic modeling through dimensional analysis. Hughes (1993) addressed the similarity criteria for laboratory physical modeling of real problems in coastal engineering. He derived the similitude criteria required for scaling the hydrodynamic phenomena through the non-dimensionalized equations of motion and conservation of mass. Snyder (1981) explained atmospheric flow similarity through matching the dimensionless parameters involved in the physics of the flow. Similarity criteria for the atmospheric boundary layer have been investigated by Snyder (1972) and Plate (1999) for neutrally stable atmosphere, by Meroney et al. (1975) and Avissar et al. (1990) for stably stratified atmospheric conditions, and by Rau et al. (1991), Poreh et al. (1991), and

* Reprinted from Journal of Wind Engineering and Industrial Aerodynamics, Vol 103, Pournazeri S, Princevac M, Venkatram A, "Scaling of building affected plume rise and dispersion in water channels and wind tunnels—Revisit of an old problem", Pages. 16-30, Copyright (2012), with permission from Elsevier.

Meroney and Melbourne (1992) for convective boundary layers (Meroney, 1998). Snyder (1981) summarized a variety of techniques used to simulate the plume rise associated with buoyant emissions at various fluid modeling facilities where different scaling parameters such as Froude number, initial velocity ratio, and initial density ratio were matched in order to achieve the minimum possible scaling effect. Robins (1980), Obasaju and Robins (1998), and Robins (2003) also investigated the applicability of various plume rise scaling techniques for laboratory modeling of atmospheric dispersion. They compared the performance of these techniques in simulating the plume rise from isolated stacks. Their analysis showed that results from different combinations of plume rise similarity criteria derived from Briggs (1984) formulation are in agreement with results from a plume rise field study (Hamilton, 1967) that took place downwind of the *Tilbury and Northfleet* power station resembling an isolated stack with undisturbed flow. Obasaju and Robins (1998) have also investigated the effectiveness of scaling techniques applied to building affected plume dispersion problems. They studied the effect of different scaling methods on the ground level concentrations rather than the plume rise itself. Accordingly, Robins (2003) validated these scaling techniques with data from a buoyant tracer field study conducted in the vicinity of *Hinkley Point A* nuclear power station building. In addition, Robins (1980) and Snyder (1981) explained the scaling of dispersion through non-dimensionalization of concentration (C) with respect to wind speed (v), stack height (H_s), and source emission rate (Q). Meroney (1982, 1986a, 1986b, 1987) has also explained the similarity criteria, limitations, and constraints involved with the fluid modeling of dense gas cloud dispersion. Following these results, a complete set

of scaling laws associated with similarity of flow, plume rise and dispersion may be attained. Since some of these similarity criteria need to be relaxed and distorted in order to obtain feasible laboratory parameters, their applicability must be investigated. These relaxed criteria have been evaluated for the dispersion and plume rise from tall isolated stacks where the effect of surrounding buildings can be neglected (Robins, 1980; Meroney, 1986a, 1986b; Obasaju and Robins, 1998). However, their performance is unknown for laboratory modeling of dispersion from low-level buoyant sources in urban areas where surrounding buildings can significantly influence the plume behavior. Although, as mentioned earlier, there are studies (Obasaju and Robins, 1998; Robins, 2003) on evaluating the plume scaling techniques for plumes affected by buildings. However, these studies focused on the ground level concentrations, which depend on both plume spreads, and plume trajectory and they did not explicitly illustrate the impact of scaling distortion on different parameters (e.g. plume rise) involved in dispersion process of a buoyant plume. Therefore, in order to have a detailed understanding on the laboratory scaling of the dispersion from such sources, there is a need to investigate the impact of different scaling methods on dispersion parameters individually.

Motivated by this need, a systematic laboratory study has been performed and appropriate scaling methods for urban dispersion are presented. The correct scaling of the atmospheric dispersion problems in wind tunnels and water channels requires similarity of 1) mean flow; 2) plume rise; and 3) turbulence governed plume spreads with appropriate boundary conditions. The following sections discuss the scaling laws relevant to each of these three similarities. Section 5.2 gives details of scaling the flow in

water channel and wind tunnels. Details of plume rise similarity are explained in Section 5.3. Laboratory setup and experiments used to investigate plume rise are explained in Section 5.3.1. Section 5.3.2 briefly explains the widely used Briggs (1984) plume rise model and introduces a new model that accounts for building influence on the plume rise. Plume rise model evaluation with experiments is shown in Section 5.3.3 followed by a plume rise scaling method in Section 5.3.4. Sensitivity study of the proposed technique under urban conditions is given in Section 5.3.5. Concentration scaling methods are explained in Section 5.4. Finally, a summary and conclusions are given in Section 5.5.

5.2 Flow Similarity

A good foundation for this analysis is the work done by Snyder (1981), where the similarity criteria for flow modeling are described. Starting with the full conservation equations of mass, momentum, and energy, non-dimensionalizing them by characteristic length L, velocity v, angular velocity Ω_R, reference density ρ_R, and reference temperature T_R, four dimensionless parameters, Reynolds (*Re*), Rossby (*Ro*), Peclet (*Pe*), and densimetric Froude (Fr_d) number were created (Snyder, 1981).

1. $\mathrm{Re} = UL/\nu$ is the Reynolds's number representing the ratio between inertial and viscous forces where ν is the fluid kinematic viscosity
2. $Ro = U / L\Omega_R$ is the Rossby number representing the ratio between inertial and Coriolis effects

3. $Pe = UL/K$ is the Peclet number defined to be the rate of advection of heat by the flow to the rate of diffusion of heat, *K*, and it can be written as the product of *Re* and Prandtl number, $\Pr = \nu/\alpha$, where α is the thermal diffusivity, i.e. $Pe = \mathrm{Re}.\Pr$

4. $Fr = U/\left(g\,L\,\Delta T/T_0\right)^{1/2}$ is the Froude number showing the ratio of inertial and buoyancy forces. Here ΔT is temperature difference, T_0 reference temperature and *g* is gravitational acceleration.

Satisfying these four dimensionless numbers with appropriate boundary conditions will result in similar flow characteristics for the model and the field. However, duplicating all these dimensionless numbers is impossible; thus, some of them must be relaxed at the expense of satisfying the others. In practicality, for scales less than 5 km (Mery, 1969), *Ro* similarity can be neglected as the Coriolis effect is relatively small and results in significantly large *Ro*. Townsend (1956) has also shown that in the absence of Coriolis and thermal effects, turbulent structure of flow is similar for all sufficiently high *Re* except for very small-scale turbulent structures with sizes comparable to Kolmogorov length scale. In terms of scaling the dispersion of elevated releases, Reynolds independency has to be satisfied for both the ambient flow and the efflux from the stack. Sustaining the *Re* independency at the stack exit will be further explained in Section 5.3.4.

Since *Pe* is expressed as the product of *Re* and Prandtl (*Pr*) number, for sufficiently high *Re* numbers, the flow is also independent of *Pe* number. This independency is easier to achieve in water channel rather than wind tunnels since the *Pr* of water (≈ 7) at

room temperature is nearly one order of magnitude larger than *Pr* of air (≈ 0.7). This leaves us with Fr_d as the only parameter left to be matched to achieve dynamic flow similarity, which is not very difficult.

In addition to the above-mentioned similarity criteria, specifying the correct boundary conditions is necessary for correct flow scaling. Due to the no-slip condition at the solid boundaries, flow velocity and all of its moments are zero at the boundaries. Hence, satisfying the geometrical similarity by reproduction of associated obstacles, buildings, etc. (undistorted replicas), would be necessary to satisfy the velocity boundary condition (Snyder, 1972, 1981). Jensen (1958) has suggested that geometrical details with sizes smaller than the roughness length (z_0) have very little effect on the overall flow. Therefore, geometric similarity is only required for geometries larger than the height of the roughness length and is not necessary for the details below this scale.

Flow adjacent to smooth boundaries is not *Re* independent and is dominated by viscous stresses. The presence of surface irregularities larger than the thickness of viscous sub-layer induces a flow resistance, which is caused by the pressure gradient across the obstacle and not the viscous stresses (Snyder, 1981). This feature allows the flow to be *Re* independent. Since atmospheric flows are always turbulent, over-roughening of the laboratory surface might be necessary to satisfy the *Re* independence criterion and produce turbulent flows near all surfaces.

In addition to geometrical similarity, atmospheric boundary conditions, such as 1) surface temperature distribution; 2) upstream distribution of mean and turbulent (*rms*)

velocities; 3) upstream distribution of mean and turbulent (*rms*) temperatures; 4) mixing layer height; and 5) near zero pressure gradient aloft the boundary layer, should also be satisfied in order to achieve full similarity of atmospheric flow in the laboratory scales (Meroney, 1998). Details of atmospheric boundary layer simulations can be found in Snyder (1972), Meroney et al. (1975), and Meroney (1998). The following section describes the criteria involved in the similarity of plume rise.

5.3 Plume Rise Similarity

Plume rise plays an important role in determining the ground level concentrations associated with low-level buoyant sources. Realistic modeling of plume rise is critical for DG sources because one way of increasing the efficiency of a DG is by capturing the waste heat from its exhaust, which results in reduced plume rise and increased ground-level concentrations. Formulation of plume rise in current dispersion models such as AERMOD (Cimorelli et al., 2005) is designed primarily for elevated emissions from large power plants (Briggs, 1984; Weil, 1988), and does not account for the effects of multiple surrounding buildings on buoyant emissions from low-level sources, where updrafts and downdrafts induced by buildings have significant effects. Some of the modern dispersion models such as AERMOD-PRIME (Schulman et al., 2000) and ADMS (Carruthers et al., 1994) include effects of vertical wind shear and streamline ascent and descent on plume rise and dispersion near buildings. These models have been extensively evaluated using different wind tunnel and field datasets (Robins et al., 1997a; Carruthers et al., 1999; Schulmann et al., 2000). Although the building effect modules in these models (Robins et al., 1997b; Schulman et al., 2000; Robins and McHugh, 2001)

are designed to be generic, they compute the dispersion and plume rise from sources near isolated large buildings or an effective building representing a group of closely spaced blocks, which is not always the case in urban areas. Hence, they do not describe the plume rise within complex urban morphology, which requires information on the flow field affected by surrounding buildings near the stack. In order to clarify these effects, a systematic laboratory study was conducted in the water channel facility described in Chapter 4.

5.3.1 Laboratory Experiment

Using the PIV system flow velocities in the water channel for the pump frequency of 17.5 Hz were measured. Profiles of the mean horizontal (v) and vertical (w) velocities together with their standard deviations (σ_v and σ_w) and the shear stress (τ) are shown in Fig. 5.1.

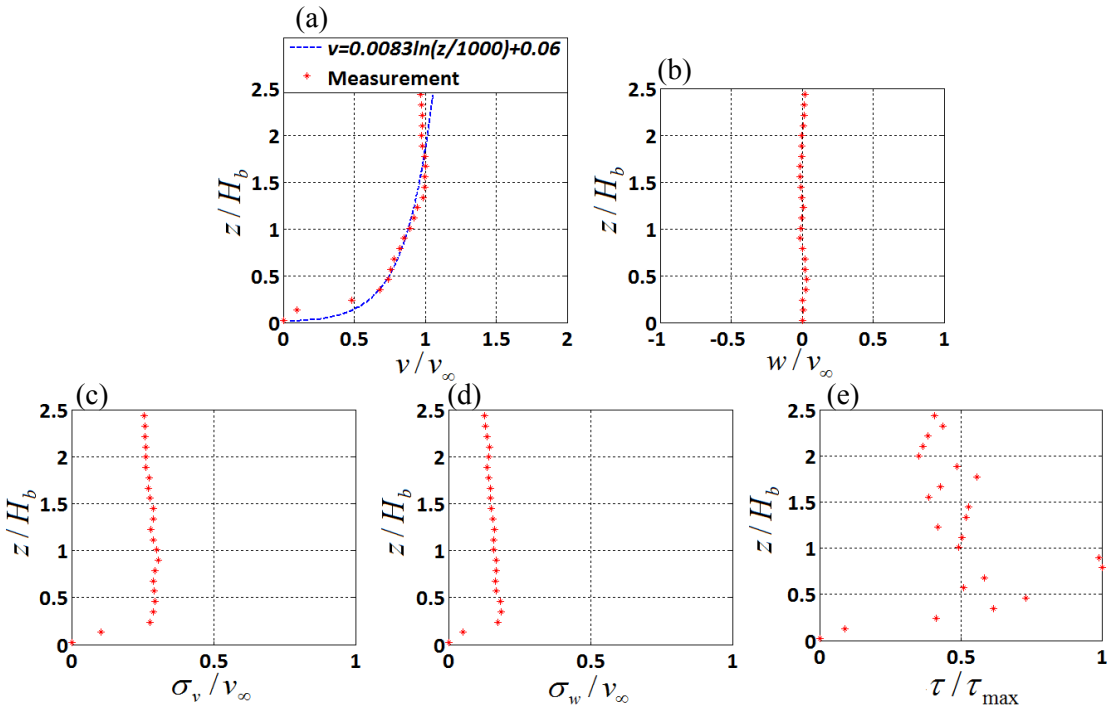

Figure 5-1: Profiles of ambient mean (a) horizontal v (m/s) and (b) vertical w (m/s) velocities; standard deviations of (c) horizontal σ_v (m/s) and (d) vertical σ_w (m s^{-1}) velocities; and (d) mean shear stress τ (N m^{-2}). Dashed blue line represents the logarithmic wind profile. Vertical distance z and velocities are normalized with respect to building height H_b = 0.07 m and free stream horizontal velocity (v_∞= 0.045 ms^{-1}). Shear stress (τ) is normalized with respect to maximum shear stress of $\tau_{max} = 0.03\ Nm^{-2}$.

Distances, velocities, and shear stresses are normalized with respect to building height, H_b = 0.07 m, horizontal free stream velocity, v_∞ = 0.045 m s^{-1}, and maximum shear stress of $\tau_{max} = 0.03\ N\ m^{-2}$, respectively. It can be seen that the vertical profile of horizontal wind speed matches well with the logarithmic wind profile especially for heights up to 2.5 H_b. Vertical profiles of standard deviation of horizontal and vertical velocities (σ_v and σ_w) and the shear stress (τ) are maintained almost constant with a slight peak at 0.5H_b from the ground.

In order to investigate plume rise associated with low-level buoyant sources, a DG building from Palm Springs, California ($L \times W \times H$=$15\,m \times 15\,m \times 7\,m$) with stack height ($H_s$) of 9.3 m above ground level (2.3 m above roof level) has been modeled in the water channel at scale of 1:100. It should be mentioned that the laboratory study shown in this chapter does not represent the scaled problem from the Palm Springs field study (Jing et al., 2010), except for the DG geometry. In this set of laboratory experiments, the field wind speeds of ≈ 3 m s^{-1} and stack exit velocity of ≈ 12.5 m s^{-1} were simulated in the water channel. The reference Reynolds number, based on the free stream velocity (v_∞) and characteristics building frontal length scale, H_b^* (length scale based on the obstacle frontal area; $H_b^* = (WH)^{1/2}$) was *Re*=4600, which is sufficient to satisfy Reynolds number independency criteria of *Re* ≈ 4000 (Halitsky, 1968; Fackrell and Pearce, 1981; Snyder, 1981; Yee et al., 2006). However, a study by Robert Meroney and David Neff at Colorado State university (private communication) showed that this criteria (*Re* ≈ 4000) is limited only to flow around cubical buildings oriented perpendicular to the wind direction and sources located in the near wake of the building. Given the complexities involved with flow around different building shapes and orientations, they suggested *Re* ≥ 15000 for model simulations. Since in this study we are utilizing cubical building oriented normal to the flow direction, we consider that the *Re* ≥ 4000 is sufficient to satisfy Reynolds number independency criteria. In addition, the Lego blocks with sufficiently rough surfaces help the flow to become Reynolds number independent.

A fluorescent dye, Uranine, is used as the tracer dye for plume visualizations because of its high light sensitivity in the range of visible light. Uranine has a very low molecular diffusivity; hence, the corresponding Schmidt number is relatively large ($Sc \approx$ 2000). Due to high Re, turbulence will be the leading mechanism in dispersing the tracer dye, and the molecular diffusivity will serve as a smoothing mechanism for small-scale concentration discontinuities (Snyder, 1972). Therefore, due to the turbulent nature of the flow, the matching of Sc number to the field is not required. Desired plume buoyancies are achieved by mixing the tracer dye with water and alcohol (specific gravity SG = 0.8). Another way to simulate buoyant emissions would be to use an inverted experimental setup and release a salt-water solution at the top of the channel (e.g. Contini and Robins, 2001, 2004). Images of the dyed plume were captured using long exposure imaging. This technique gives us averaged plume behavior, which is used to measure the plume rise under different buoyancies, flow conditions, and building geometries. Experiments were repeated for at least three times and in several instances up to four and five times. The root mean squared error (Contini et al., 2011; RMSE = $\sqrt{\sum\left(h_p - \overline{h_p}\right)^2 / N}$, where h_p and $\overline{h_p}$ are the observed and mean values of plume rise, respectively, and N is the number of data points) was less than 5% of the mean plume rise for all of the experiments.

Plume rise has been measured under two different buoyancies (SG = 0.98 and 0.96). These plume buoyancies were selected in order to observe how a major increase in buoyancy can alter the effect of buildings on plume rise (buoyancy associated with tracer

of $SG = 0.96$ is equivalent to two times that of a tracer with $SG = 0.98$ since the buoyancy is proportional to 1-SG). Details of experimental conditions are given in Table 5.1.

Next, these plume rise measurements were compared with Briggs' (1984) plume rise equation and a numerical plume rise model, which are explained next.

Table 5-1: Experimental parameters for plume rise measurements

Parameters	Value
Free stream horizontal velocity (v_∞)	0.045 m s^{-1}
Re (based on H_b^*)	4600
Internal Diameter of the stack (D)	3×10^{-3} m
Stack exit velocity (V_s)	0.19 m s^{-1}
Stack exit Reynolds number (Re_s)	570
Average vertical turbulent velocity (σ_w)	0.0056 m s^{-1}
Vertical turbulent intensity of flow ($I_z=\sigma_w/v$)	~0.12-0.14
Surface friction velocity (u_*)	0.0034 m s^{-1}
Roughness length of Lego blocks (z_0)	~6×10^{-4} m
Plume specific gravity (SG)	0.96 and 0.98

5.3.2 Plume Rise Model

As shown in Chapter 2, the Briggs (1984) plume rise model,

$$h_p = \left(\frac{3}{2\beta^2} \frac{F_b x^2}{v^3} + \frac{3}{\beta^2} \frac{F_m x}{v^2} \right)^{1/3}, \tag{5-1}$$

was derived by solving the mass, momentum and energy conservation equations analytically (eqs. 4-7), assuming a bent-over plume released in a neutrally stratified

atmosphere with a constant horizontal wind speed, *v*, where no updrafts and downdrafts exist. Due to the vigorous mixing that occurs in daytime urban boundary layer, the potential temperature gradient just above the roof level is close to zero (Cermak et al. 1995). Thus, the neutral stability assumption for simulating the daytime plume rise using Briggs (1984) is mostly valid. Here $\beta = 0.6$ (Hoult and Weil, 1972) is the entrainment parameter; F_b and F_m are the buoyancy and momentum flux parameters, respectively, expressed as,

$$F_b = g b_0^{\,2} V_s \left(\frac{T_p - T_0}{T_p} \right) \tag{5-2}$$

$$F_m = b_0^{\,2} V_s^{\,2} \left(\frac{T_p}{T_0} \right) \tag{5-3}$$

where b_0 is the radius of the stack, V_s is the stack exit velocity, T_p is the temperature of the exhaust plume, and T_0 is the ambient temperature. Although widely used, this simple model has no capability to incorporate building influence.

As explained earlier, plume rise and dispersion modules in AERMOD-PRIME (Schulman et al., 2000; Cimorelli et al., 2005) and ADMS (Carruthers et al., 1994; Robins et al., 2005) can only account for the effects of isolated buildings and do not describe the plume rise within complex urban morphology (Pournazeri et al., 2011). In order to account for the effects of complex flows induced by surrounding buildings on the plume rise, a numerical plume rise model has been developed. The starting point of this model is the plume rise governing equations by Hoult et al. (1969), where the plume is

assumed to be slender and continuous with a circular cross section and uniform properties within the plume (Contini et al., 2011). These equations are the modified version of the plume rise model by Morton et al. (1956), where the classical theory of the Boussinesq plume was established. These governing equations were derived for the case of horizontal wind speed only. Therefore, modifying these equations and re-deriving them, by assuming that wind speed has both vertical and horizontal components, allows us to account for the effect of updrafts/downdrafts induced by buildings. Similar concepts to account for building effects are used in ADMS (Robins et al., 1997a) and AERMOD-PRIME (Schulman et al., 2000) building modules. Schematics of the plume rise and parameters involved are shown in Fig. 5.2.

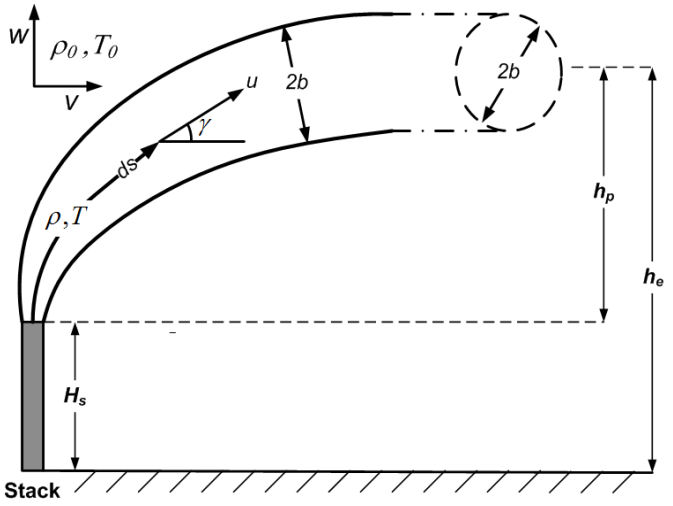

Figure 5-2: Schematic for plume in a 2-dimensional flow. Here, u is the velocity of plume along its centerline, v and w are the horizontal and vertical ambient velocities, s is along the centerline coordinate, γ is the plume centerline inclination, b is the averaged plume radius, ρ is the plume density, T is the plume absolute temperature, H_s is the height of the stack, h_p is the plume rise and h_e is the actual plume height.

The modified governing equations are:

Conservation of mass flux

$$\frac{d}{ds}(\pi b^2 u\rho) = 2\pi b\rho_0\left[\alpha|u - v\cos(\gamma) - w\sin(\gamma)| + \beta|v\sin(\gamma) - w\cos(\gamma)|\right] \quad (5\text{-}4)$$

Conservation of momentum flux –along the plume centerline

$$\frac{d}{ds}(\pi b^2 u^2\rho) = \left(v\cos(\gamma) + w\sin(\gamma)\right)\frac{d}{ds}(\pi b^2 u\rho) + (\rho_0 - \rho)\pi b^2 g\sin(\gamma) \quad (5\text{-}5)$$

Conservation of momentum flux –normal to the plume centerline

$$\pi b^2 u^2\rho\frac{d\gamma}{ds} = -\left(v\sin(\gamma) - w\cos(\gamma)\right)\frac{d}{ds}(\pi b^2 u\rho) + (\rho_0 - \rho)\pi b^2 g\cos(\gamma) \quad (5\text{-}6)$$

Conservation of buoyancy flux

$$\frac{d}{ds}(\pi b^2 u(\rho - \rho_0)g) = -\pi b^2 u\rho_0\left(\frac{g}{\theta_a}\frac{d\theta_a}{dz}\right)\sin(\gamma) \quad (5\text{-}7)$$

where ρ is the plume density, ρ_0 is the density of the ambient air, u is the velocity of the plume centerline, v and w are the horizontal and vertical ambient velocities, γ is the plume centerline inclination and θ_a is the ambient potential temperature. As reported by Hoult and Weil (1972), the entrainment coefficients $\beta = 0.6$ and $\alpha = 0.11$ are independent of plume parameters for a fully turbulent plume. Contini et al. (2011) showed that the entrainment coefficient α, corresponding to the horizontal velocity difference between the plume and ambient flow, does not have significant impact on the performance of this model. One needs to keep in mind that these governing equations are

derived based on assumptions (such as Boussinesq plume) which might not be necessarily valid for all different plume conditions (e.g. dense gas plumes).

After solving equations (5-4)–(5-7) numerically for b, u, ρ, and γ as function of s (distance on the plume centerline), the plume rise h_p and distance x associated with it can be calculated as

$$h_p = \int_0^s \sin(\gamma) ds \tag{5-8}$$

$$x = \int_0^s \cos(\gamma) ds \tag{5-9}$$

In this model, the influence of updrafts and downdrafts induced by buildings on the plume rise is taken into account through the measured velocity (*v* and *w*) field (Fig. 5.3b). Velocity field was measured at the centerline of the building without the plume in place (see schematic in Fig. 5.3a).

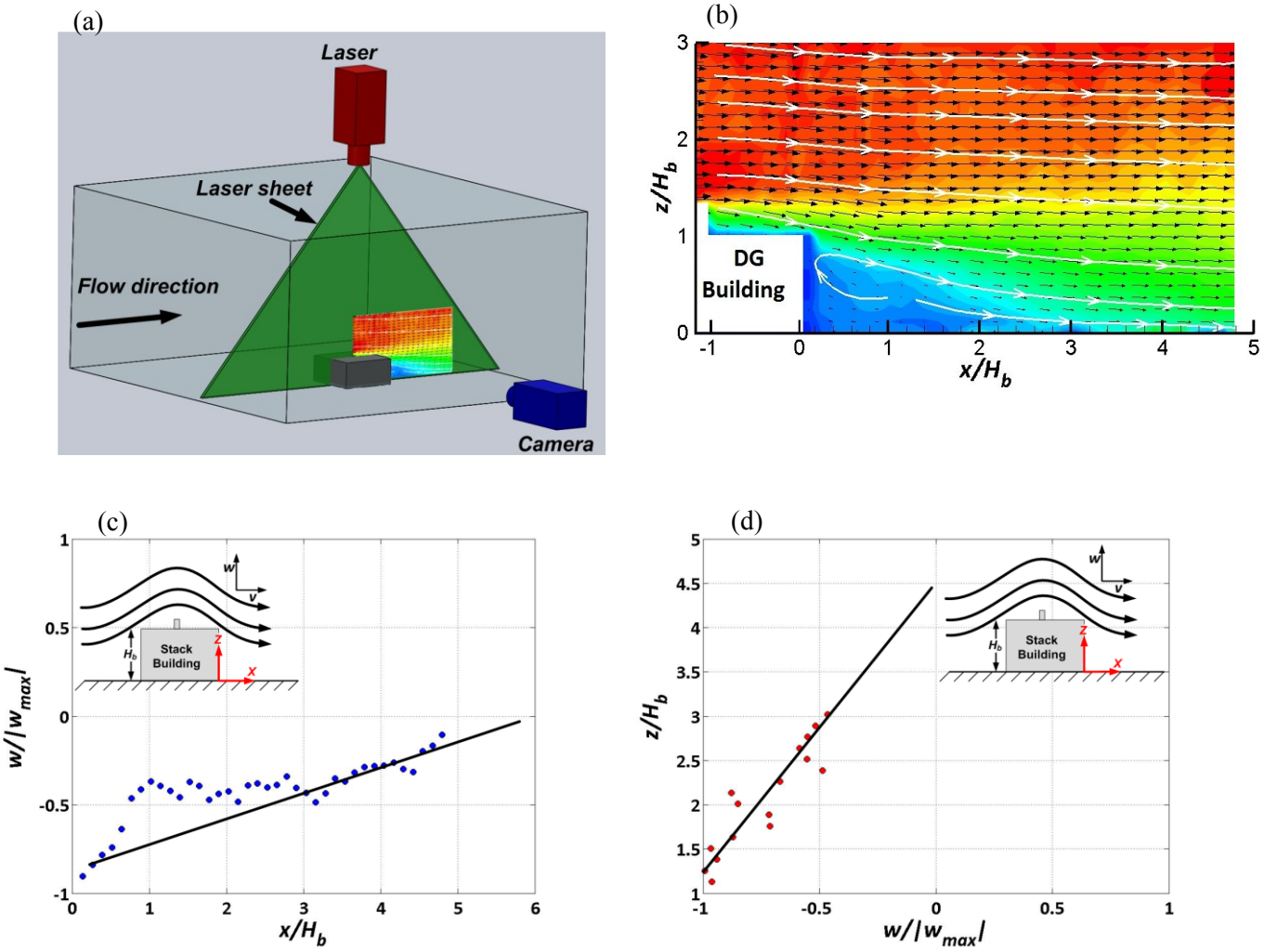

Figure 5-3: (a) Schematic of PIV measurement setup. (b) Averaged velocity field over 180 images measured using PIV system (the dark blue vector lines show the velocity of less than 1 cm/s and the dark red vector lines show the velocity equal/above 5 cm/s). Streamlines are calculated using a commercial plotting software package (TECPLOT 10). This software plots the streamlines by interpolating the velocity between the grid points. Normalized measured downdraft velocity, $w/|w_{max}|$ (w_{max} = 4.5 × 10^{-3} ms^{-1} is the maximum downdraft velocity, measured at the lee wall of the building at $z=H_b$, where H_b is the building height) is presented (c) vs. normalized downwind distance from the DG building at $z=H_b$ and (d) vs. normalized vertical distance above the ground level next to the lee wall of the building. The reference wind speed is v_∞= 0.045 ms^{-1}.

For these experiments, due to relatively high ambient velocity, the flow perturbation by the plume was not significant. In addition, since we modeled the DG using Lego blocks with relatively large roughness length of ≈ 0.6 mm, the flow at the rooftop is highly perturbed and once separated at the leading edge, it quickly re-attaches.

Furthermore, the presence of 3 mm diameter stack on the rooftop further contributes to the flow perturbation and causes the separated flow to re-attach rapidly. In another study (Princevac et al., 2010), our PIV measurements of flow around modeled buildings made of highly polished acrylic cubes do show separation starting from the leading edge of the building rooftop. Fig. 5.3c-d shows the downdraft velocities measured downstream and above the DG model in the water channel. From Fig. 5.3c-d, it can be assumed that downdraft velocity decays almost linearly to zero within approximately 6 building heights (H_b) downwind of the building and 3.5 H_b above the rooftop of the building. In addition, due to the solid surface boundary condition, downdraft velocity becomes zero at the ground level (z=0). This is modeled as,

$$w(x,z) = w_{\max}\left[1-\left|\frac{z-H_b}{\lambda_1 H_b}\right|\right]\cdot\left[1-\frac{x}{\lambda_2 H_b}\right] \text{ for } x \le \lambda_2 H_b \text{ and } z \le (\lambda_1+1)H_b \qquad (5\text{-}10)$$

where $\lambda_1 = 3.5$, $\lambda_2 = 6$ and $w_{\max} = -4.5\times10^{-3}$ (m s^{-1}) is the maximum downdraft velocity which occurs on the lee wall of the building (x = 0) near the rooftop ($z = H_b$). It needs to be noted that equation (5-10) describes the downdraft velocity for the particular case considered in this study and might not be generic to all building configurations and wind directions. However, similar interpolation for the downdraft velocity can be made for other building and flow conditions.

In addition to the above-mentioned properties, this model also accounts for the effect of ambient turbulence. It is assumed that, at large distances where the entrainment due to the horizontal and vertical velocity difference between plume and ambient

becomes relatively small, the entrainment process is dominated by the plume growth due to ambient turbulence (Schulman et al., 2000). As per Schulman et al. (2000), this effect can be modeled as,

$$\frac{d}{ds}(\pi b^2 u\rho) = \max\left[\frac{d}{ds}(\pi b^2 u\rho)_{entrainment}, 2\pi b\rho_0 v\left(\frac{db}{ds}\right)_{amb.\ \text{turb.}}\right] \tag{5-11}$$

where

$$\left(\frac{db}{ds}\right)_{amb.\ \text{turb.}} = \sqrt{\frac{\pi}{2}}\frac{\sigma_w}{v}. \tag{5-12}$$

This effect is negligible for distances close to the stack with relatively small turbulent intensities (σ_w/v). However, in cases with relatively high turbulent intensities, ambient turbulence can reduce the plume rise at large distances.

5.3.3 Comparison of Models and experiments

Fig. 5.4 shows the comparison between Briggs' (1984) plume rise formulation (eq. 5-1) and the numerical solution of equations (5-4) through (5-7) (with vertical velocity given by eq. 5-10), together with the results from the plume rise measurements in the water channel Fig. 5.4a and 4c show the recorded averaged plume. Plume rise has been measured by determining the location of the plume centerline in these images. As can be seen in Fig. 5.4b and 4d, Briggs' (1984) formulation tends to overestimate the plume rise, as it cannot account for the downdraft velocities induced in the near-wake region of the building. This causes the plume to rise more slowly even though the maximum downdraft velocity is relatively small ($|w_{max}/v| \sim 0.1$, where v is the horizontal wind speed

measured at $z = H_b$ at the lee wall of the building). As shown in Fig. 5.3, downdraft velocity decays with height from the rooftop of the building. Therefore, the higher the plume rises, the less effect downdrafts have on plume rise. This effect can be observed in Fig. 5.4; as the buoyancy is increased from $SG = 0.98$ to $SG = 0.96$, the discrepancy between plume rise predicted by Briggs (1984) and measured plume rise becomes smaller.

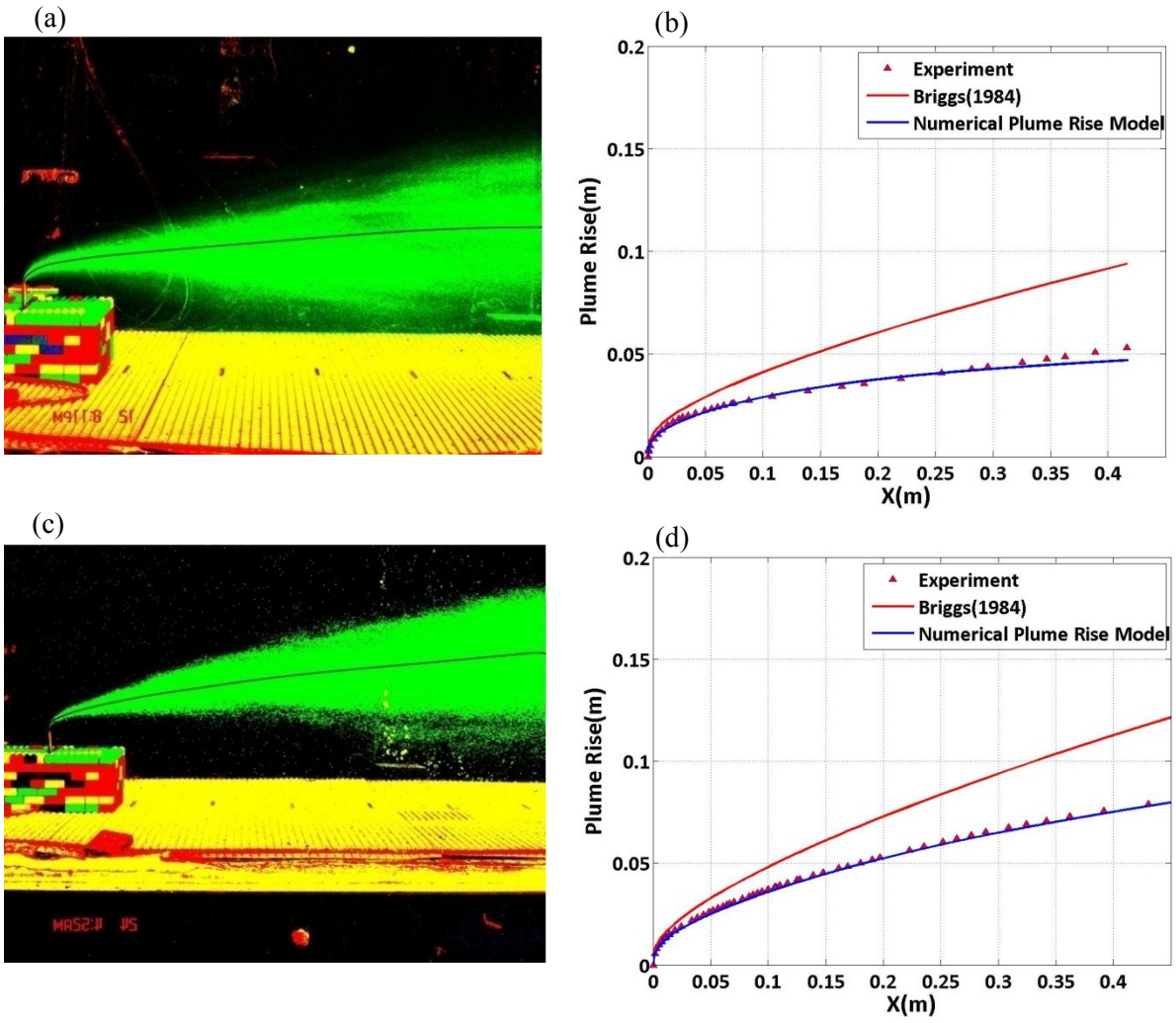

Figure 5-4: Plume visualization for modeled DG source (geometric scaling ratio of 1:100) with buoyant emission of different specific gravity (SG): (a) SG=0.98, (c) SG=0.96. Comparison between the plume rise observations (▲); Briggs (1984) plume rise formulation (red–); and numerical plume rise model (blue–) for (b) SG=0.98, (d) SG=0.96.

However, by accounting for flow modifications induced by the building in vertical direction, the numerical plume rise model produces an accurate prediction of the plume rise in the water channel. Although the flow downstream of the building is three-dimensional, flow features in lateral direction do not influence the plume rise significantly. Thus, accounting only for the flow in horizontal (along the stream) and vertical direction is sufficient to predict the plume rise. These results show the performance of the model at distances close to the stack, but does not provide a description of model performance at large distances from the stack where the variation of wind speed and plume parameters become significant along the plume width and depth.

Different plume rise scaling methods are described in the next section.

5.3.4 Plume Rise Scaling

There are several scaling methods of plume rise explained in the literature (Isyumov and Tanaka 1979; Robins, 1980; Snyder, 1981; Obasaju and Robins, 1998; Robins, 2003) that are derived from the mass, momentum and energy conservation laws. Robins (1980) and Obasaju and Robins (1998) evaluated different plume rise scaling methods for isolated stacks and concluded that by relaxing the initial density ratio and matching the non-dimensional buoyancy and momentum flux parameters, plume rise can be accurately scaled from the field to the laboratory. However, all these methods were only evaluated for plume rise from isolated stacks where the effect of surrounding buildings can be neglected, but we have already shown that plume rise is significantly affected by updrafts and downdrafts caused by the surrounding buildings. Therefore, using the plume rise

governing equations that account for the building effects, we reconstructed the complete scaling method. These equations (eqs. 4–7) are now used to develop appropriate scaling.

Non-dimensionalizing equations (5-4) through (5-7) with respect to ambient density ρ_0, ambient velocity v, and stack radius b_0 results in

$$\frac{d}{ds^*}(\pi b^{*2} u^* \rho^*) = 2\pi b^* \left[\alpha \left| u^* - \cos(\gamma) - \left(\frac{w}{v}\right)\sin(\gamma) \right| + \beta \left| \sin(\gamma) - \left(\frac{w}{v}\right)\cos(\gamma) \right| \right] \tag{5-13}$$

$$\frac{d}{ds^*}(\pi b^{*2} u^{*2} \rho^*) = \left(\cos(\gamma) + \left(\frac{w}{v}\right)\sin(\gamma) \right) \frac{d}{ds^*}(\pi b^{*2} u^* \rho^*) + \frac{g b_0}{v^2}(1-\rho^*)\pi b^{*2} \sin(\gamma) \tag{5-14}$$

$$\pi b^{*2} u^{*2} \rho^* \frac{d\gamma}{ds^*} = -\left(\sin(\gamma) - \left(\frac{w}{v}\right)\cos(\gamma) \right) \frac{d}{ds^*}(\pi b^{*2} u^* \rho^*) + \frac{g b_0}{v^2}(1-\rho^*)\pi b^{*2} \cos(\gamma) \tag{5-15}$$

$$\frac{d}{ds^*}(\pi b^{*2} u^* (\rho^* - 1)) = -\pi b^{*2} u^* \left(\frac{1}{\theta_a} \frac{d\theta_a}{dz^*} \right) \sin(\gamma) \tag{5-16}$$

where $b^* = b/b_0$, $u^* = u/v$, $\rho^* = \rho/\rho_0$, $s^* = s/b_0$, $z^* = z/b_0$.

Three dimensionless numbers appeared in the non-dimensionalized governing equations (eqs. 5-13 through 5-16). Except for the ratio between the vertical and horizontal velocities (w/v), all of the other parameters can also be found by non-dimensionalizing the plume rise governing equations in Hoult et al. (1969). Although detailed description of these dimensionless parameters can be found in the literature, we briefly discuss them here. The first dimensionless parameter is $1/\theta_a \cdot \left(d\theta_a / dz^*\right)$, which is a measure of the background atmospheric stability and needs to be matched in both model and field. Following the similarity of flow and atmospheric boundary layer described in section 5.2, this parameter is matched automatically for stable and

convective boundary layers. For the neutral atmospheric stability condition, this parameter is equal to zero in both the model and field. The second dimensionless parameter is the ratio between the vertical and horizontal velocities (w/v). Per the flow similarity explained in the previous section, by satisfying the Reynolds independence criterion and applying correct boundary conditions, the ratio of the vertical velocity to the horizontal velocity at all locations will be automatically matched in the model and field. The third dimensionless parameter is gb_0/v^2, which is ½ inversed squared of the Froude number ($v/\sqrt{gD}$ where $D = 2b_0$). In order to match this single parameter in the model and field, the velocity scale ratio should be equal to the square root of the geometrical scaling ratio. As also discussed by Meroney (1986b), and Robins (2003), even for cases where wind speeds (v) in the field are relatively high (≈ 5 ms^{-1}), a typical geometrical scaling ratio, such as 1:400, would yield exceptionally low flow velocities in the model (in this case ≈ 0.25 ms^{-1}) which are not easy to manage in wind tunnels. These low flow velocities introduce difficulties concerning the *Re* independency criteria (Meroney, 1986b). In the water channel due to the higher flow control capabilities matching the Froude number is not difficult in most cases. Since kinematic viscosity (ν) of water at room temperature (≈10^{-6} m^2 s^{-1}) is approximately 10 times smaller than that of air (≈10^{-5} m^2 s^{-1}), it is easier to satisfy the *Re* independency criteria in water channel even under low flow velocities.

In addition to the Froude number, the similarity of initial conditions at the stack exit should also be satisfied by matching the initial magnitudes of b^*, u^* and ρ^* in the model

and field. As the magnitude of b at the stack exit is equal to b_0, b^* will be unity at the stack exit in both the field and model, which means that the initial value of b^* is automatically matched. This leaves us with matching the initial values of u^* and ρ^* at the stack exit (eqs. 18-19).

At the stack exit, u^* is equal to the ratio of the stack exit velocity V_s to the ambient velocity v (V_s/v), characterizing the jet (momentum) behavior of the plume. This behavior has been the subject of numerous theoretical and laboratory studies. Hoult and Weil (1972) have defined $R = V_s / v$ as the speed ratio in order to define the region of the plume governed by the initial momentum. Davidson and Slawson (1967) have shown that for distances x where $R << g(\Delta\rho/\rho_0)(x/v^2)$ ($\Delta\rho = \rho_0 - \rho_p$ where ρ_p is the exhaust plume density), the effect of initial momentum can be neglected and plume rise becomes buoyancy dominated. Barilla (1968) has shown that for $R \leq 2$ in non-buoyant plumes and $R \leq 1$ in buoyant plumes, the entrapment of plume in the cavity produced by the stack or buildings (known as downwash) may occur. The downwash effect has also been investigated by Fay et al. (1970) and it has been observed that in industrial chimneys this effect happens for $R \leq 1.25$ (Hoult and Weil, 1972). Wind tunnel simulation by Snyder and Lawson (1991) has also shown that downwash occurs for $R \leq 1.5$ when Re is smaller than critical Reynolds number of $Re_c = 2\times10^5$ and happens for $R \leq 1.1$ when $Re \geq Re_c$. Therefore, different values of speed ratio would yield different near source plume behavior.

The initial value of ρ^* is equal to the ratio of the exhaust plume density ρ_p to ambient density ρ_0, presenting a measure of the non-Boussinesq effect. Non-Boussinesq effects arise when the difference between the plume density and ambient density at the source is significantly large compared to the reference (ambient) density ρ_0 (Carlotti and Hunt, 2005). This effect may have a significant impact on the shape of the plume over a distance z_s above the source, as the entrainment velocity is a function of the plume to ambient density ratio (Ricou and Spalding, 1961). This distance (z_s) may be as large as 0.3 m for smoke plumes produced by small fires in buildings ($T \sim 400^{\circ}C$) and extends to several kilometers in large volcanic eruptions ($T \sim 2200^{\circ}C$) (Woods, 1997). Since temperatures are usually within $150 - 500^{\circ}C$ in our case, the non-Boussinesq effects would not play a major role except very close to the source, and the motion will quickly converge to that of the Boussinesq plume.

As a result, three scaling factors associated with plume rise can be expressed as,

$$\left(gb_0 / v^2\right)_m = \left(gb_0 / v^2\right)_f \tag{5-17}$$

$$\left(V_s / v\right)_m = \left(V_s / v\right)_f \tag{5-18}$$

$$\left(\rho_p / \rho_0\right)_m = \left(\rho_p / \rho_0\right)_f \tag{5-19}$$

where the subscripts m and f denote model and field, respectively.

Satisfying the above-mentioned parameters will result in correct similarity of plume rise. These parameters were also reported by Isyumov and Tanaka (1979); Robins

(1980); Snyder (1981) and several other studies, as required criteria for accurate scaling of near/far field plumes.

Following eqs. (17-19) and satisfying the geometric similarity (required for similarity of the flow) as,

$$\left(\frac{H_s}{b_0}\right)_m = \left(\frac{H_s}{b_0}\right)_f, \tag{5-20}$$

laboratory plume rise can be scaled back to the field through equation (5-21), which is obtained by non-dimensionalizing equations (5-8) and (5-9) with respect to stack height (H_s) as

$$\left(\frac{h_p(x^*)}{H_s}\right)_m = \left(\frac{h_p(x^*)}{H_s}\right)_f \tag{5-21}$$

where h_p is the plume rise and x^* is the dimensionless distance from the source ($x^* = x/H_s$).

As explained in section 5.3.1, in the water channel, plume buoyancies are achieved by mixing the tracer dye with water (SG = 1) and alcohol (SG = 0.8); thus, the maximum achievable buoyancy is associated with the mixture of dye with pure alcohol (SG = 0.8). Therefore, in addition to difficulties associated with satisfying the Froude number criteria, for very hot plumes with temperatures (T_p) higher than 460K (i.e. $\rho_P / \rho_0 \leq 0.65$), it becomes difficult to satisfy the density condition (eq. 5-19) in the water channel. Further increases in buoyancy, up to SG = 0.76, can be achieved by using heated alcohol (at boiling temperature of T = 65°C). It is also possible to use salty water in the water

channel and by injecting heated alcohol achieve SG = 0.74 (for salty water of ρ_0 = 1.025 kg m^{-3}), which is a 30% increase in buoyancy (1-SG) compared to that of pure alcohol at room temperature (SG = 0.8). However, since a buoyancy increase of 75% (for T_p = 460 K) to 250% (for T_p = 1000 K) is required, this is not large enough. Additionally, this would introduce additional uncertainty (heat loss from the hot alcohol during its pumping from the beaker to the source inside the water channel) and risk causing corrosion due to the water salt mixture in the channel. Similar to Robins (1980), in order to achieve similarity for the case of high buoyancy and low ambient velocity, we relax the Froude number and define a similarity criteria where we match the initial values of $gb_0/\nu^2\,(1-\rho^*)$ (this parameter appears in eqs. 14-15) in the model and the field. This parameter is ½ inversed squared of the densimetric Froude number ($\nu/\sqrt{g'D}$ where $g'=g\Delta\rho/\rho_0$). Therefore, this similarity can be expressed as,

$$\left(\frac{gb_0}{\nu^2}\frac{\Delta\rho}{\rho_0}\right)_m=\left(\frac{gb_0}{\nu^2}\frac{\Delta\rho}{\rho_0}\right)_f \tag{5-22}$$

where $\Delta\rho=\rho_0-\rho_p$.

Although not necessarily needed, keeping a constant velocity scaling ratio (due to the constraints imposed by the *Re* independency criteria and water channel flow control capabilities) and matching the densimetric Froude number with a higher density ratio (ρ_p/ρ_a) in the model than that in the field, yield to a larger stack diameter (D = 2b_0) for the model. Consequently, the Reynolds number associated with stack becomes larger

compared to the case when the density ratio (ρ_p / ρ_a) in the model and field is the same. This feature allows us to choose the density ratio in the model such that the stack Reynolds number meets the Reynolds independence criterion, which states that as long as the plume is in turbulent regime at the stack exit, plume behavior is independent of the Reynolds number (Snyder, 1981). Snyder (1981) reported that for buoyant plumes, the critical Reynolds number *Re* = 200, based on stack diameter, is sufficient for formation of a fully turbulent plume at the stack exit. In addition, using higher density ratio (ρ_p / ρ_a) yields larger ratio of Peclet (based on mass diffusion) to Richardson number ($v^3 / g' K_m$ where K_m is the molecular diffusivity of the tracer), which reduces the microscopic diffusion effects (Meroney, 1986b). As reported by Meroney (1986b), this ratio should be larger than 1500 for accurate simulations.

As mentioned earlier, many studies such as Robins (1980); Arya and Lape (1990); and Obasaju and Robins (1998) have used similar criteria to the densimetric Froude number as a proper scaling method in the characterization of the buoyant plume rise.

Matching this similarity criterion (eq. 5-22) in the model and field would lead to satisfying the initial condition on the right hand side of conservation of momentum flux equations (eqs. 5-14 and 5-15) where the buoyancy force term appears. However, it would change the initial value of ρ^* on the left hand side of equations (5-13) through (5-16). Several studies by Meroney (1982, 1986a, 1986b) on wind tunnel simulation of dense gas dispersion suggested that distorting the initial value of ρ^* in order to allow for more convenient flow velocities in the model can delay the time of arrival and departure

of the model plume. Neff and Meroney (1981) have also observed that under distorted density conditions, the cloud of dense gas moves slower comparing to undistorted model. However, it needs to be mentioned that these limitations are specific to emissions heavier than air and might not necessarily hold for buoyant emissions described in this study, since the source effects persists over much longer times in dense gas plume than in buoyant plumes. The effect of this distortion have also been investigated for plume rise from isolated tall stacks by comparing plume rise results from wind tunnel simulations (with distorted density condition) with field results (Robins, 1980) and Briggs (1984) plume rise predictions (Obasaju and Robins, 1998). Thus, there is a need to examine the performance of this scaling method under buoyant emissions affected by buildings. Robins (2003) illustrated the performance of similar scaling methods on building affected plumes by investigating the ground level concentrations. Since the plume rise is one of the major parameters that affect the ground level concentration, here we focus on plume rise rather than directly on concentrations. The sensitivity of plume rise to the scaling distortion is investigated next.

5.3.5 Plume Rise Similarity Sensitivity Study

In order to investigate the sensitivity of the plume rise scaling method shown in previous section, plume rise from the 650 kW distributed power generator in Palm Springs has been simulated using the numerical plume rise model described in Section 5.3.2. As it was mentioned previously, DGs are highly efficient because they have heat recovery from their coolant and exhaust, providing both electricity and heating/cooling to the neighborhood. Thus, for the Palm Springs DG, depending on how much heat is

recovered from the exhaust, the temperature of the exhaust may differ between 460 K (~75% heat recovery) and 800 K (~20% heat recovery). Therefore, in this study we have chosen four different stack temperatures ranging from 460 K – 800 K. According to Jing et al. (2010), typical average wind speed in Palm Springs urban area (from a sonic anemometer located at Sunrise Park in Palm Springs, California, on the rooftop of the DG at 11 m from the ground) is $v_f \approx 1$ m s^{-1}. Note that the sensitivity analysis presented in this section is separate from the laboratory study shown in section 5.3.1 - 5.3.3.

By selecting $v_m = 0.045$ m s^{-1}, (velocity scaling ratio of 1:22.5) the plume rise from the Palm Springs DG has been scaled through:

1) *Scaling method 1* by matching the Froude number (eq. 5-17), initial velocity ratio (eq. 5-18) and initial density ratio (eq. 5-19);

2) *Scaling method 2* by matching the densimetric Froude number (eq. 5-22), initial velocity ratio (eq. 5-18) and choosing $\left(\rho_P / \rho_0\right)_m = 0.96$.

Table 5-2: Model Parameters with *Scaling Method 1*

Model Parameters Scaling with $\left(\rho_p/\rho_0\right)_m = \left(\rho_p/\rho_0\right)_f$	Case 1	Case2	Case 3	Case 4
Inside diameter of stack (D)	0.6mm	0.6mm	0.6mm	0.6mm
Stack height (H_s)	18.6mm	18.6mm	18.6mm	18.6mm
Geometrical scaling ratio	1:500	1:500	1:500	1:500
Reference flow velocity (v_∞)	0.045 m s^{-1}	0.045 m s^{-1}	0.045 m s^{-1}	0.045 m s^{-1}
ρ_p/ρ_0	0.6522	0.5	0.4286	0.3750
gb_0/v_∞^2	1.47	1.47	1.47	1.47
V_s/v_∞	11	11	11	11
$\frac{gb_0}{v_\infty^2}\frac{\Delta\rho}{\rho_0}$	0.5118	0.7358	0.8408	0.9197

Table 5-3: Model Parameters with *Scaling Method 2*

Model Parameters Scaling with $\left(\rho_p / \rho_0\right)_m = 0.96$	Case 1	Case2	Case 3	Case 4
Inside diameter of stack (D)	5.2 mm	7.6 mm	8.6 mm	9.4 mm
Stack height (H_s)	16.1 cm	23.5cm	26.6 cm	29.1 cm
Geometrical scaling ratio	1:58	1:40	1:35	1:32
Reference flow velocity (v_∞)	0.045 m s^{-1}	0.045 m s^{-1}	0.045 m s^{-1}	0.045 m s^{-1}
ρ_p / ρ_0	0.96	0.96	0.96	0.96
gb_0 / v_∞^2	12.8	18.4	21	23
V_s / v_∞	11	11	11	11
$\frac{gb_0}{v_\infty^2}\frac{\Delta\rho}{\rho_0}$	0.5118	0.7358	0.8408	0.9197

Table 5-4: *Field* Parameters

Field Parameters	Case 1	Case2	Case 3	Case 4
Stack exit plume temperature	460K	600K	700K	800K
Inside diameter of stack (D)	0.3m	0.3m	0.3m	0.3m
Stack height (H_s)	9.3 m	9.3 m	9.3 m	9.3 m
Reference wind speed (v_∞)	1 m s^{-1}	1 m s^{-1}	1 m s^{-1}	1 m s^{-1}
ρ_p / ρ_0	0.6522	0.5	0.4286	0.3750
gb_0 / v_∞^2	1.4715	1.4715	1.4715	1.4715
V_s / v_∞	11	11	11	11
$\frac{gb_0}{v_\infty^2}\frac{\Delta\rho}{\rho_0}$	0.5118	0.7358	0.8408	0.9197

Each of these scaling methods results in a set of model parameters that include internal stack diameter (D), stack exit velocity (V_s), and plume initial density (ρ_P). These parameters (Tables 5-2 and 5-3) are then used as the inputs to the numerical plume rise model, and the plume rise associated with each set of model parameters is calculated and then scaled to the field through equation (5-20). In addition to the results from the scaling methods, plume rise associated with the Palm Springs DG is also calculated directly from the field (non-scaled) parameters (Table 5.4). The results of these simulations are shown and compared (Fig. 5.5), and stack parameters corresponding to the field and each of the scaling methods are given in Tables 5-2 through 5-4.

As the actual plume height (h_e) is the key factor for determining the ground level concentrations rather than plume rise itself, in these simulations, plume rise is shown in terms of actual plume height h_e where

$$h_e = H_s + h_p . \tag{5-23}$$

Following equations (5-20), (5-21), and (5-23), plume actual height associated with the model can be scaled to the field through the equation (5-24) as,

$$\left(\frac{h_e}{H_s}\right)_m = \left(\frac{h_e}{H_s}\right)_f . \tag{5-24}$$

Fig. 5.5 shows the results from the simulations of plume rise at four different stack exit temperatures using parameters associated with 1) *Field* (Table 5.4); 2) *Scaling method 1* (Table 5.2); and 3) *Scaling method 2* (Table 5.3).

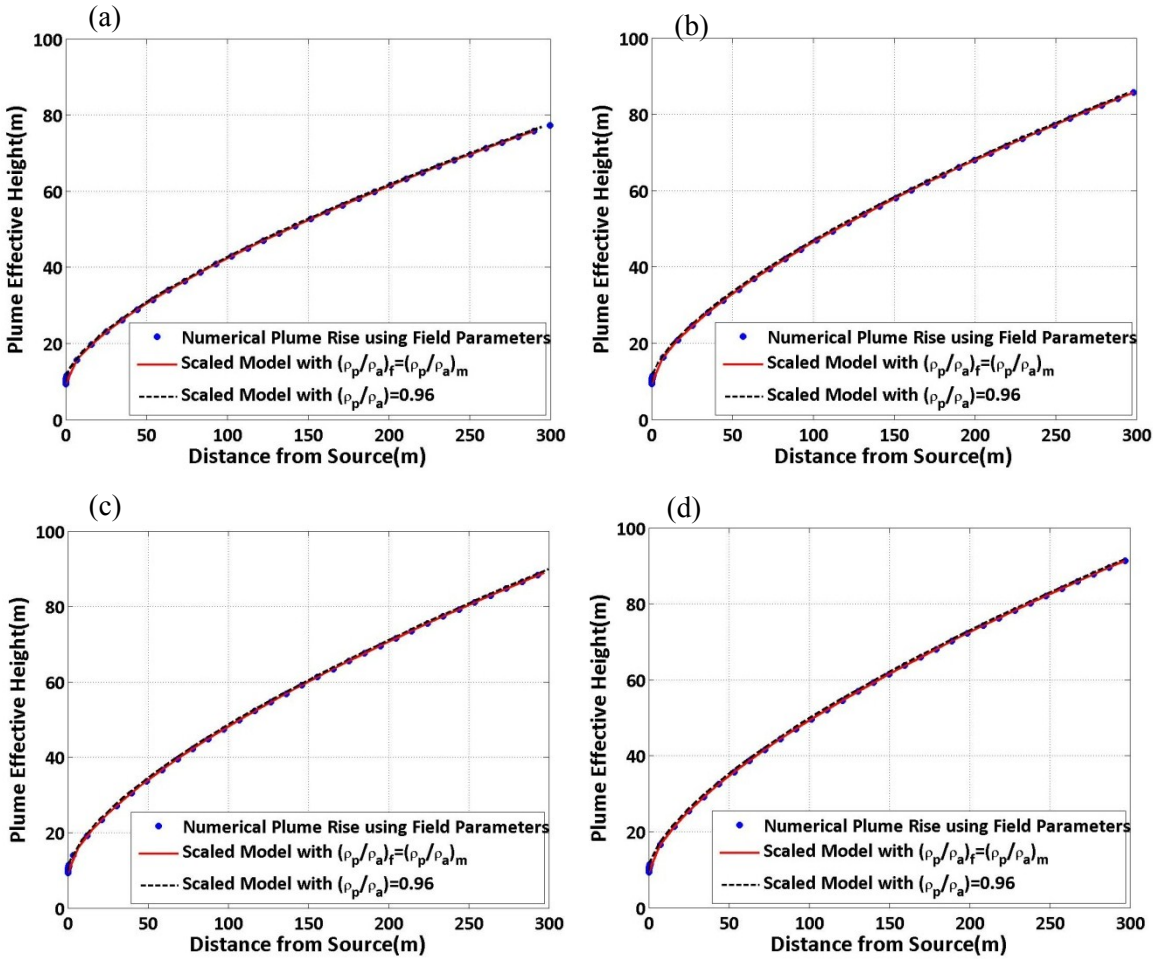

Figure 5-5: Simulation of Palm Springs DG Plume Rise using parameters associated with *Field* •, *Scaling method 1* ▬ (matching the *Fr* and initial density condition) and *Scaling method 2* - - - (matching the densimetric *Fr* and relaxing the initial density condition) with stack exit temperature of (a) T_p=460K (b) T_p =600K (c) T_p =700K (d) T_p = 800K. Velocity scaling ratio of v_f/v_m=22.5 was used for simulations. The geometric scaling ratio is 1:500 for *Scaling method 1* and it varies for *Scaling method 2* as shown in Table 5.3. Results shown in this figure are calculated using the numerical plume rise model.

As can be seen in Fig. 5.5, plume actual height associated with *Scaling method 2* (scaling using the densimetric Froude number) yields almost identical results compared with the field simulation. In order to clarify the accuracy of this scaling method (method 2) under urban conditions, the errors associated with this method have been calculated as,

$$\%\, error = \left| \frac{h_e(Field) - h_e(Scaling\ method\ 2)}{h_e(Field)} \right| \times 100\% \tag{5-25}$$

where $h_e(Field)$ is the plume actual height calculated using the field parameters (Table 5.3) and h_e *(Scaling method 2)* is the scaled plume actual height calculated using parameters associated with the *Scaling method 2* (Table 5.3). These errors are shown in Fig. 5.6.

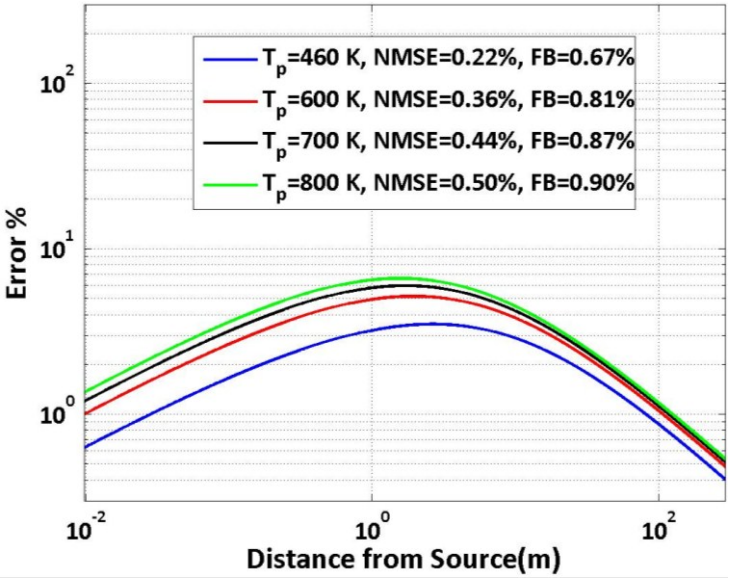

Figure 5-6: Actual calculated plume height errors associated with distorting the initial density condition in plume rise scaling method using the densimetric Froude number vs. distance from the stack at four different stack exit temperatures ranging from 460K-800K.

In addition to these errors, the performance of this scaling method (method 2) is also investigated through the normalized mean square error (*NSME*) and fractional bias (*FB*) which are the standard method for comparing field, model, and numerical predictions. These methods are explicitly discussed in the Model Validation Kit (MVK) package (Olesen, 2005) and Contini et al. (2011).

It can be seen from Fig. 5.6 that the maximum error occurs at distance of 2 m from the stack and ranges from 3.5% (at T_p = 460 K) up to 7% (at T_p = 800 K). The error reduces to less than 1% at distance of 120 m from the stack. In addition, the maximum *NSME* and *FB* is associated with T_p = 800 K, and are equal to 0.5% and 0.9%, respectively. This shows that, similar to isolated stacks, scaling using densimetric Froude number (*Scaling method 2*) is also accurate (over the range of parameters considered) under urban conditions even though it is not satisfying the initial value of ρ^*. Also, results from *Scaling method 2* show larger values (≥ 5.2 mm) of the model stack diameter (Table 5.3) than those obtained from *Scaling method 1* (Table 5.2) since the velocity scaling ratio remained constant (1:22.5) for both scaling methods. A small stack diameter yields a lower stack Reynolds number, which might lead to a laminar plume. This will not satisfy the Reynolds independency, resulting in non-similar plume motion close to the stack. Therefore, larger stack diameters (such as those given by *Scaling method 2*) are more desirable in laboratory modeling. In addition, small stack diameters ($\leq 1\,\text{mm}$) are more difficult to fabricate due to manufacturing limitations, and are more prone to clogging.

5.4 Similarity of Dispersion

Although the Gaussian dispersion model (Sutton, 1947) might not necessarily explain the dispersion of pollutants in the urban boundary layer, due to its simplicity, it is used as the main framework for the urban pollution dispersion purposes (e.g. in the US

EPA regulatory model AERMOD). Therefore, we based our dispersion similarity on this model:

$$\frac{C(x,y,z)}{Q} = \frac{1}{2\pi\sigma_y\sigma_z v}\exp\left(-\frac{y^2}{2\sigma_y{}^2}\right)\left[\exp\left(-\frac{(z-h_e(x))^2}{2\sigma_z{}^2}\right)+\exp\left(-\frac{(z+h_e(x))^2}{2\sigma_z{}^2}\right)\right] \quad (5\text{-}26)$$

where as explained chapter 2, C is the concentration; σ_y and σ_z are the plume spreads in the horizontal and vertical directions, respectively, at distance x from the source; v is the ambient velocity at the plume height; h_e is the actual height of the plume defined in the previous section; and Q is the pollutant mass emission rate. This model will perform well for cases where the plume can rise above the wake of the stack building and it is not trapped in the recirculation region downwind. Due to the typically low wind speeds in urban areas and relatively high buoyancy and momentum of the exhaust plumes, urban plumes rise rapidly near the stack and in most cases escape the wake of the stack buildings.

The Gaussian dispersion model can be re-written in terms of dimensionless parameters as,

$$C = \frac{Q}{2\pi H_s{}^2 v\sqrt{(I_y{}^2 x^{*2}+\sigma_b^{*2})(I_z{}^2 x^{*2}+\sigma_b^{*2})}}\exp\left(-\frac{y^{*2}}{2(I_y{}^2 x^{*2}+\sigma_b^{*2})}\right)$$
$$\left[\exp\left(-\frac{(z^*-h_e{}^*(x))^2}{2(I_z{}^2 x^{*2}+\sigma_b^{*2})}\right)+\exp\left(-\frac{(z^*+h_e{}^*(x))^2}{2(I_z{}^2 x^{*2}+\sigma_b^{*2})}\right)\right] \quad (5\text{-}27)$$

where x^*, y^*, and z^* are dimensionless spatial coordinates; and $h_e{}^*$ is the dimensionless actual height of the plume, which is defined as,

$$h_e^* = \frac{h_p + H_s}{H_s}. \tag{5-28}$$

The dimensionless buoyancy induced dispersion (σ_b^*) can also be defined as,

$$\sigma_b^* = \frac{0.4}{\sqrt{2}}\left(h_e^* - 1\right). \tag{5-29}$$

As most of the studies involved with the dispersion of pollutants are focused on the ground level concentrations, we simplify the Gaussian dispersion model to calculate only the downstream ground level concentration as,

$$C(x^*,0,0) = \frac{Q}{\pi v {H_s}^2 \sqrt{({I_y}^2 x^{*2} + \sigma_b^{*2})({I_z}^2 x^{*2} + \sigma_b^{*2})}} \exp\left(-\frac{{h_e}^*(x)^2}{2({I_z}^2 x^{*2} + \sigma_b^{*2})}\right). \tag{5-30}$$

The dimensionless ground level concentration becomes

$$C^*(x^*) = C(x^*)\frac{{H_s}^2 v\sqrt{({I_y}^2 x^{*2} + \sigma_b^{*2})({I_z}^2 x^{*2} + \sigma_b^{*2})}}{Q} \exp\left(\frac{h_e^*(x^*)^2}{2({I_z}^2 x^{*2} + \sigma_b^{*2})}\right), \tag{5-31}$$

and can be used to convert concentration levels from laboratory to field scale.

If the turbulent intensities, I_y and I_z, are the same for both the field and model, then the above expression (eq. 5-31) reduces to the non-dimensional concentration proposed by Robins (1980) and Snyder (1981) as,

$$C^*(x^*) = C(x^*)\frac{{H_s}^2 v}{Q}, \tag{5-32}$$

since I_y, I_z and the exponential term cancel out. In cases where the full flow similarity is achieved such that the turbulent intensities are the same in both field and

model, equation (5-32) can be used to scale the concentration levels from laboratory to the field and vice-versa. However, this condition is not likely to occur in water channels as the turbulent intensities are not easy to control and are often different from those in the field. Turbulent intensities are difficult to control since their magnitudes are very sensitive to the adjustment of flow conditioners as well as to the roughness elements used in the water channels. Turbulent intensities in the water channels are typically within 10 - 30% while in urban areas they range from 20% on windy days to more than 100% during low wind (< 1 m s^{-1}) conditions. Therefore, a correction (eq. 5-31) to account for the discrepancy in the turbulent intensities is often required. In order to clarify the effect of this correction method, ground level concentrations associated with the Palm Springs DG are predicted using the Gaussian dispersion model and compared with those predicted using the scaled model with and without correction for discrepancy in turbulent intensities. Average turbulent intensities associated with the field (Jing et al., 2010) and laboratory model are listed in Table 5.5.

Using the field stack parameters in Table 5.4 and scaled stack parameters corresponding to *Scaling method 2* (scaling using densimetric Froude number) in Table 5.3, assuming T_p = 460 K, ground level concentrations in the field and model are predicted through the Gaussian dispersion model (eq. 5-26).

Table 5-5: Turbulent intensities associated with the field and laboratory model

	I_y	I_z
Field*	0.5	0.3
Laboratory model	0.2	0.12

*Field data are provided by Jing et al., (2010) obtained from a sonic anemometer located on the rooftop of the DG, at 11m from the ground, in Sunrise Park at Palm Springs, California averaged over the period of July 15, 2008 to July 21, 2008.

The predicted ground level concentrations in the laboratory model are then scaled back to the field with and without correction for discrepancy in turbulent intensities through equations (5-31) and (5-32), respectively. These concentrations are shown in terms of normalized concentration, d, defined as,

$$d = C/Q. \tag{5-33}$$

Results from these simulations and the ratio of concentrations associated with the field to the scaled concentrations (d_{Scaled}/d_{Field}) with and without correction are shown in Fig. 5.7.

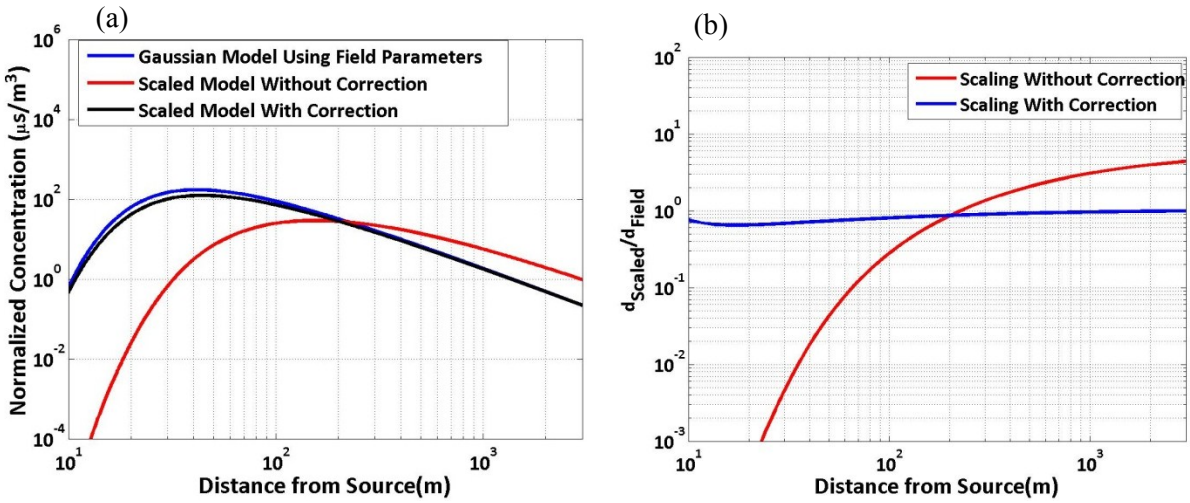

Figure 5-7: (a) Normalized ground level concentrations (μs/m^3) associated with the Palm Springs DG (blue) vs. Scaled ground level concentrations with (black) and without (red) correction for turbulent intensity discrepancy (b) ratio of scaled to field normalized simulated concentrations with (blue) and without (red) correction.

It can be seen in Fig. 5.7a that scaled ground level concentration (d_{Scaled}), corrected for the difference in turbulent intensities of the model and field, is almost identical to the ground level concentration predicted using field parameters (d_{Field}), since plume spread is mostly dominated by the ambient turbulence. The minimum scaled to field normalized concentration ratio (d_{Scaled}/d_{Field}) associated with this scaling is about 0.6 close to the source (~15 m) and becomes almost unity for distances larger than 100m (Fig. 5.7b). This discrepancy between scaled and field concentration (at distances of $x \le 100\,m$) results from the errors (~3.5%) due to the plume rise scaling (scaling using the densimetric Froude number and relaxing the initial density ratio), explained in the previous section, which significantly affects ground level concentrations very close to the source and becomes negligible at larger distances ($x \ge 100\,m$). However, for the case when no correction has been made, there is a large discrepancy between field predictions and scaled model predictions (Fig. 5.7a); also, scaled to field normalized concentration

ratio (d_{Scaled}/d_{Field}) is less than 10^{-3} at 20 m from the source and increase to 5 at 3 km from the source (Fig. 5.7b). Therefore, it may be concluded that neglecting the above-mentioned correction in laboratory dispersion studies, where turbulent intensities differ from that in the field, might lead to significant errors. However, this simple correction can be of great help in modeling real world dispersion problems in the laboratory without a need to match the turbulent intensities.

Following these procedures gives a proper scaling of the flow, plume rise, and dispersion for problems involving buoyant releases from low-level sources in urban areas.

5.5 Summary and Conclusion

The rapid growth of urbanization in recent decades has forced the air quality modelers to focus on air quality impact of pollutants released within the urban canopy. Although numerous field studies have been performed, results of these field measurements are always specific to the site geometry, and thus are difficult to extrapolate meaningfully to other settings. For these reasons, laboratory modeling inside water channels or wind tunnels is expected to provide major contributions. In order for these measurements to be applicable to real cases, correct methods for scaling of flow, plume rise and turbulence governed plume spread are needed.

The first part of this study explains the scaling of the flow. Flow similarity has been explained by Snyder (1981) through non-dimensionalizing the equations of motion. This yields four dimensionless parameters. As the urban flow length scales are less than 5 km, the Coriolis effect can be neglected; thus, there is no need to match the Rossby

number. As long as the Reynolds number is sufficiently high, the large-scale flow features are similar and independent from the Reynolds number (Townsend, 1956). This approach for high Reynolds number automatically satisfies the Peclet number in both the model and field. Therefore, the only dimensionless parameter that must be matched is the densimetric Froude number, which accounts for buoyancy effects in the flow. The geometric similarity is also required to satisfy the velocity boundary conditions.

The second part of the study describes the scaling of plume rise and dispersion in urban areas. Based on the observation from plume rise measurements in the water channel, it has been shown that plume rise of pollutants released inside urban areas is highly sensitive to the updrafts and downdrafts induced by the surrounding buildings. Consequently, the plume rise formulation of Briggs (1984) is unable to reproduce results accurately since it does not account for the streamline ascents and descents. A plume rise model based on the conservation equations of mass, momentum and buoyancy flux has been developed which accounts for the flow velocity in both vertical and horizontal (along the stream) directions. Providing the measured flow field in the vicinity of the source, stack exit velocity (V_s), and plume buoyancy (ρ_p) as input variables, this model has been evaluated with data from the water channel experiments and the results show that this numerical model is able to accurately predict the plume rise affected by flow modifications caused by buildings. The downside of this model is that it requires measured flow velocities as inputs, which are not usually available. However, even when the full flow field data is not available, linear interpolation of limited available flow data points can be sufficient to construct the required inputs for this model. For practical

applications, this plume rise model can be easily implemented in an urban computational fluid dynamic (CFD) model for accurate calculations of the plume height.

Next, non-dimensionalization of the plume rise governing equations and satisfying the boundary conditions at the source yields dimensionless parameters such as Froude number (gb_0 / v^2), velocity ratio (V_s / v) and density ratio (ρ_p / ρ_0) that must be matched between model and field to ensure the correct scaling. These parameters are the same as those discussed in the literature for scaling plume rise from tall isolated stacks. It has been shown that among the dimensionless parameters involved in the scaling process, it would be difficult to match the Froude number in wind tunnels (over a considerable range of atmospheric wind speeds) since it implies significantly low flow velocities. These velocities create difficulties satisfying the *Re* independency criteria and are not easy to control. In addition to Froude number, matching initial (stack exit) dimensionless density (ρ_p / ρ_0) in the laboratory model and the field is challenging in the water channels, due to the limitations on the density of the tracer that can be used. By relaxing these dimensionless parameters and matching the densimetric Froude number for the plume in the laboratory model and field, plume rise can be scaled from the field to the laboratory. The performance of this method and similar scaling methods has been evaluated in previous studies (e.g. Robins, 1980) for tall isolated stacks. In this study, results from this scaling technique and the original scaling have been compared for an urban case. It has been shown that scaling using the densimetric Froude number is relatively accurate, and the model stack dimensions derived from this scaling method (under constant

velocity scaling ratio) result in higher stack *Re* which makes it easier to achieve *Re* independent plume motion at the stack exit. In addition, larger model stack diameter may be sometimes easier to manufacture and they will be less prone to clogging by particles used for PIV measurements. In this study, the errors associated with scaling of a low wind speed urban condition under four different stack exit temperatures were investigated; thus the analysis does not necessarily hold for all urban condition (higher wind speeds and stack exit temperatures). Furthermore, the validation of this scaling technique was accomplished using the numerical plume rise model explained in section 5.3.2. As explained earlier, this model is developed based on different assumptions, which might not be valid under certain source conditions. For example, the entrainment relationship in this model does not account for the density difference between the plume and ambient and thus, it does not necessarily hold for conditions where large density differences are used. Therefore, results from this analysis are not necessarily generic to all source conditions. In addition, according to Meroney (1982, 1986a, 1986b), scaling using densimetric Froude number might have significant impact on time scale ratios specifically for dense gas plume dispersion problem. Therefore, further investigation is needed to address the generality of this scaling method for all urban conditions and its impacts on averaging time.

Following the correct scaling of flow and plume rise, concentration is scaled through the Gaussian dispersion model for the case when turbulent intensities in the laboratory and field are not the same. If the turbulent intensities are matched, then there is no need for the Gaussian formulation and concentration is directly scaled through non-

dimensional concentration proposed by Robins (1980) and Snyder (1981). Although Gaussian model does not account for all of the urban dispersion effects, it can be considered as an appropriate framework for correcting the scaling distortions (different turbulent intensities in the laboratory and the field). This scaling method will allow experimental investigators to correctly model real-world problems associated with air quality in urban areas inside water channels and wind tunnels, where conditions are more controllable and geometry can be easily adjusted.

6 DISPERSION OF BUOYANT EMISSIONS FROM LOW LEVEL SOURCES IN URBAN AREAS: WATER CHANNEL MODELING

6.1 Introduction

As already been mentioned in previous chapters, it is very difficult (mostly impossible) to extrapolate results from a field study to other meteorological situation and urban morphologies different than the original study. In this matter, wind tunnel and water channels plays a major role in providing supplementary data to support the datasets from tracer field studies during the model development. There have been many water channels and wind tunnel studies done in the past years which here we briefly explain some of them. Meroney (2004) has provided a detailed literature review on the "*Chronology of Applications of Fluid Modeling*" in dispersion studies. One of the earliest laboratory studies done on the plume dispersion affected by buildings was that by Sherlock and Stalker (1940) where the dispersion of emission from the Crawford Power Station, Chicago II were simulated in the wind tunnel in order to investigate the downwash effect under different wind and stack exit velocities. McElroy et al. (1944) initiated one of the first quantitative wind tunnel studies to investigate the impact of a chimney jet on the ground level concentrations in a built-in environment. Following 1970's US EPA constructed the wind tunnel facility in Raleigh, NC where many different tracer and flow studies such as those by Snyder (1981) on flow over complex terrains were conducted. This facility was a turning point on the laboratory dispersion studies done up to that date. One of the most relevant studies is the wind tunnel simulation done by Thompson (1993) which has been conducted in this facility. During this laboratory

study, ground level concentrations, associated with passive emissions released from a rooftop source were measured downwind of the building. Rectangular buildings with different aspect ratios were tested and a detailed wind and turbulent wind speed measurements were documented. The measured concentrations were used to calculate the building amplification factor which is a measure of the impact of the building on the maximum ground level concentration downwind. Davidson et al. (1997) has conducted a wind tunnel simulation on the surface release of a passive tracer upwind a large group of obstacles. Their concentration measurements and flow visualizations has shown that there are several different mechanism involved as the plume passes through the array of buildings. It has been shown that despite the higher turbulence level inside the built-environment, the lateral spread does not change significantly compared to the locations outside the obstacle array. Further in this chapter we will show this conclusion more clearly through a set of plume visualization experiments. We will describe this phenomenon through the dependency of turbulent length scale on the building geometries. However, the divergence of streamlines upwind of the array significantly contributes to the vertical plume spreads. Macdonald et al. (1998) has investigated the plume dispersion in an urban model using a wind tunnel. Unlike Davidson et al. (1997), it has been shown that both the lateral and vertical plume spreads in the presence of buildings are almost 2 – 4 times higher than cases where no buildings were present. Also, concentration profiles can be very well described by a simple Gaussian dispersion model at downwind distances beyond the two rows from the building array. However, at short distances from the stack, substantial variations in concentrations profile were observed,

which could not be explained through a Gaussian model. In addition Gailis and Hill (2006) simulated the large scale field experiment of MUST inside a wind tunnel. One of the most important observations in this study which has not been mentioned in previous obstacle array studies was that the narrow street induces less mixing and channeling along the wind direction. Several water channel studies have also been conducted by Contini and Robins (2004, 2011) where the impact of two different buoyant plumes released from adjacent sources were analyzed. These measurements were conducted under different wind directions in order to observe its impact on the mixed plume shape. They have reported that one of the main consequences of this mixing is the reduced plume rise which is due to the interaction of two counter-rotating vorticities at the plume cores. A near field laboratory dispersion study in a large array of buildings was conducted by Yee et al. (2006). In this study, results from a field study were compared with those from a water channel and wind tunnel simulations. Evolution of mean concentrations, fluctuation intensity and integral time scale of concentrations fluctuations were compared to those obtained from the field. Yee et al. (2006) have shown that water channel simulation provided more close quantitative results to those from the field rather than the wind tunnel. Princevac et al. (2010) also conducted a series of flow measurements through an array of building. They have shown that the intensity of the channeling flow inside building arrays is highly sensitive to the building heights. This can significantly modify the dispersion pattern in urban areas in which simple Gaussian – based model would not be able to predict.

Although all these studies, provide valuable information on the impact of building on the ground level concentration from sources close to the ground, however, none of them addresses this question that how effectively buildings can modify the dispersion pattern when highly buoyant plumes are released in a built-in environment, since unlike the passive releases, these emissions can escape the urban canopy in a very short distance from the source. Although the Palm Springs field study has provided valuable information on dispersion from a distributed generator in a real urban setting, it is limited by the fact that its results are specific to the site geometry and the meteorological conditions of the field study. Furthermore, the concentration measurements were made at distances at which the plume from the generator had spread above the average height of the buildings. So the field concentration measurements do not directly reflect building effects that might result in relatively high concentrations close to the source. Therefore, in order to explain the dispersion behaviors observed in the field study, it is useful to conduct simulations in a water channel where the site geometry and selected meteorological parameters such as wind speed can be varied. The water channel simulations can also focus on dispersion close to the source where the flow and hence the plume is affected by the details of the building geometry. In this laboratory study, the effects of surrounding buildings geometry on ground level concentrations associated with a modeled DG is investigated.

Section 6.2 will show the water channel simulation of urban dispersion and section 6.3 will describe the dispersion model used to explain data associated with laboratory measurements.

6.2 Results from Urban Dispersion Measurements

As it was mentioned earlier, the main objective of this study is to investigate the impact of DGs on air quality in urban areas within short source-receptor distances. In order to do so, similar to study shown in chapter 5, $15m \times 15m \times 7m (L \times W \times H)$ Palm Springs DG building with stack height of 9.3 m has been modeled in the water channel at scale of 1:100 and downstream concentrations has been measured at 15 locations downstream of the stack. In this set of experiments the effect of presence of upstream buildings on the ground level concentration of buoyant emissions released from DG has been investigated. Therefore, an array of 3×2 of buildings in 2 different heights have been created and situated upstream of the DG buildings. The schematic of the setup and water channel models of DG and buildings are shown in Fig. 6-1.

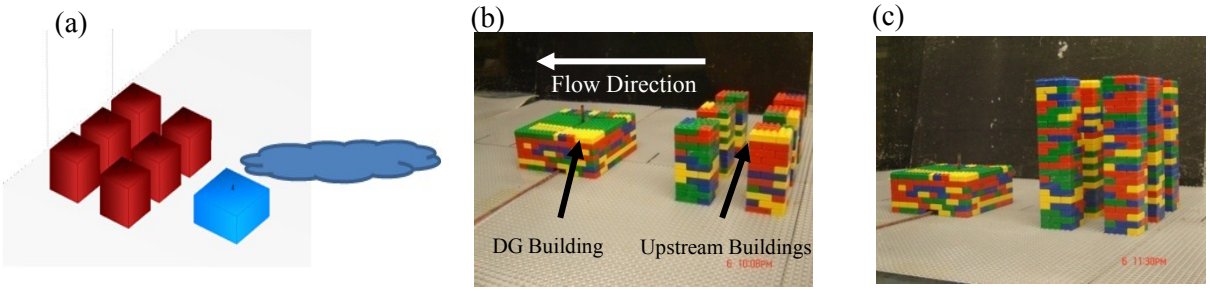

Figure 6-1: (a) Schematic of urban dispersion measurements (b) DG and single storey upstream buildings modeled in water channel using Lego. (c) DG and double storey upstream buildings modeled in water channel using Lego

6.2.1 Ground Level Concentration Measurements

Experiments regarding the air quality impact of DG have been done in three different cases: 1) DG with no upstream building 2) DG with upstream buildings the same height as of the stack (single storey) 3) DG with upstream buildings of double the height of the stack (double storey).

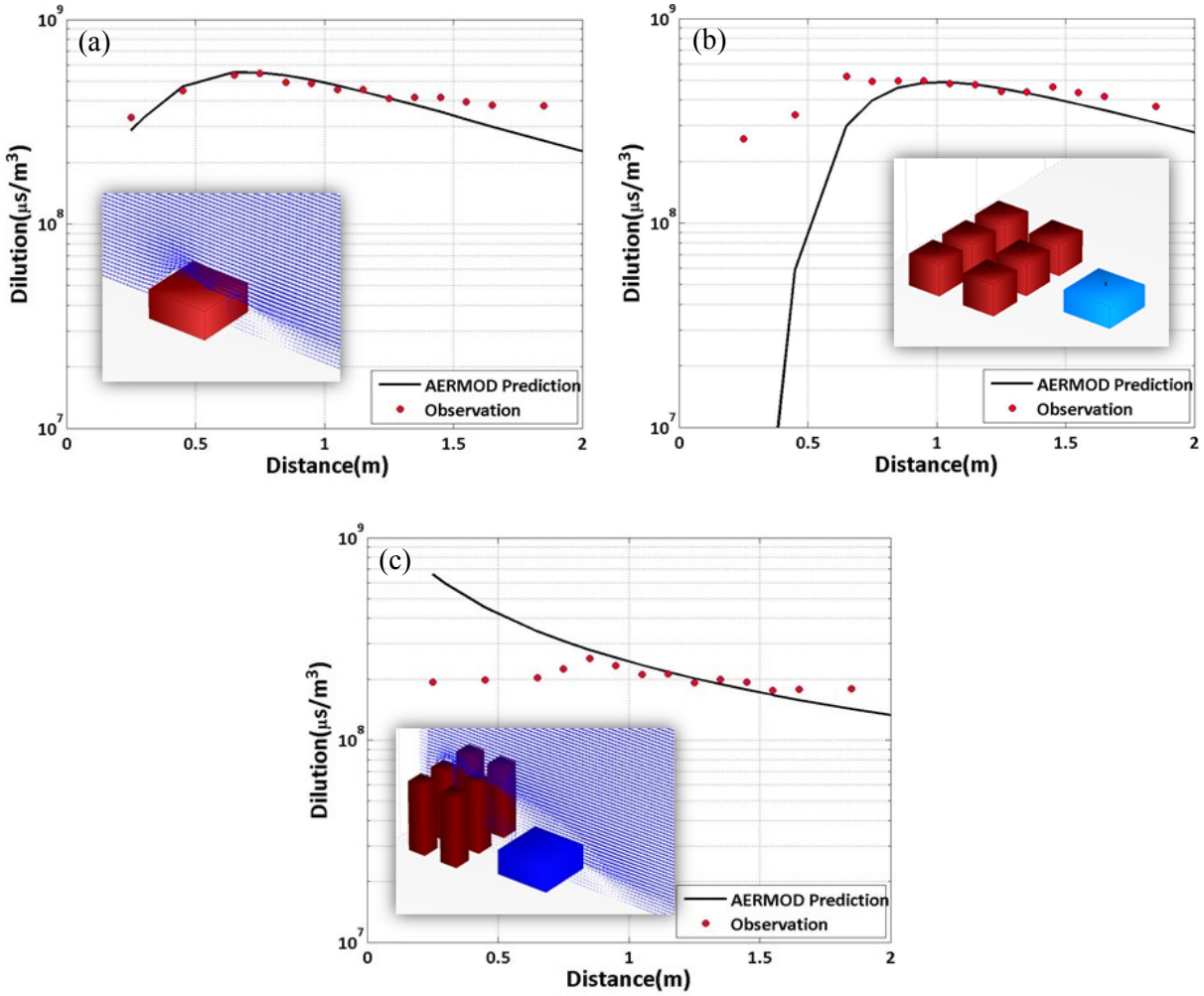

Figure 6-2: Effect of the presence of the upstream building on the ground level dilution and prediction by AERMOD (a) No upstream buildings (b) Single storey upstream buildings (c) Double storey upstream buildings (red dots(●) represents the observed ground level concentrations and solid black line(▬) represents AERMOD predictions on ground level concentrations)

Results from concentration measurements have been compared with AERMOD predictions (Fig. 6-2). Comparison shows that AERMOD predicts the concentration associated with single DG well while underestimate/overestimate concentrations associated with single/double storey upstream buildings, respectively. Fig. 6-2 also shows that the presence of upstream buildings reduce concentrations close to stack, however, as

the height of the upstream buildings is increased (double storey) concentrations decreases much slower.

In order to understand the reason to this strange behavior turbulence and velocity measurements as well as plume visualization experiments have been done where the effect of upstream buildings were investigated.

6.2.2 Turbulence and Velocity Measurements

Results from velocity measurements show that presence of upstream buildings induces a low velocity as well as highly turbulent region near the stack and this effect become more significant when heights of the upstream buildings are increased (Fig. 6-3).

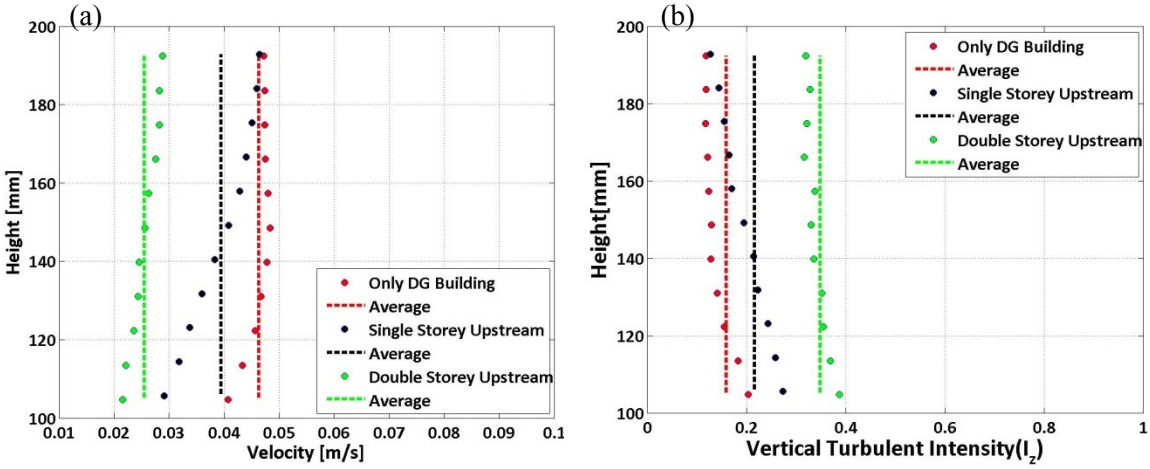

Figure 6-3: Laboratory velocity measurements in vicinity of the DG building under 3 different building geometry of 1) Only DG building (●); 2) Single storey upstream buildings (●); and 3) Double storey upstream buildings (●) for a) mean velocity b) vertical turbulent intensity (iz).

6.2.3 Vertical Mixing

Vertical mixing induced by buildings has also been investigated by long exposure imaging of the plume released from DG under different building geometries. Results

from plume visualization (Fig. 6-4) indicate that as upstream buildings decrease the wind speed near the stack, this fact yields to higher plume rise. However, at the same time, upstream buildings increase turbulent intensities near the stack resulting in rapid vertical mixing. Thus, the presence of buildings results in effects that counteract each other in changing the ground-level concentrations relative to the no upstream building case. A higher plume rise lowers the concentrations while increased vertical mixing increases ground level concentrations.

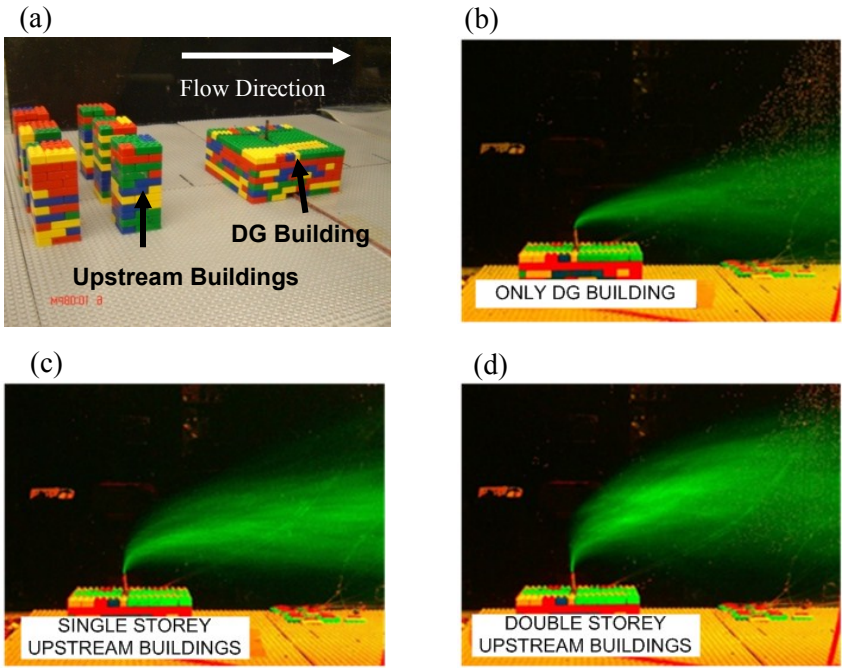

Figure 6-4: (a) DG and upstream buildings modeled in water channel using Lego and Plume visualizations for (a) No upstream buildings (b) Single storey upstream buildings (c) Double storey upstream buildings

6.2.4 Plume Lateral Spread

In order to investigate lateral spread of plume released from low level sources (below the canopy layer height) inside the urban area, the modeled stack was placed in a 5x5 array of buildings with heights slightly higher than the stack height in order to make

sure that plume is released within the urban canopy. Plume visualization was used to observe the averaged lateral spread of the plume. Figure 6-5 shows the laboratory setup for this experiment.

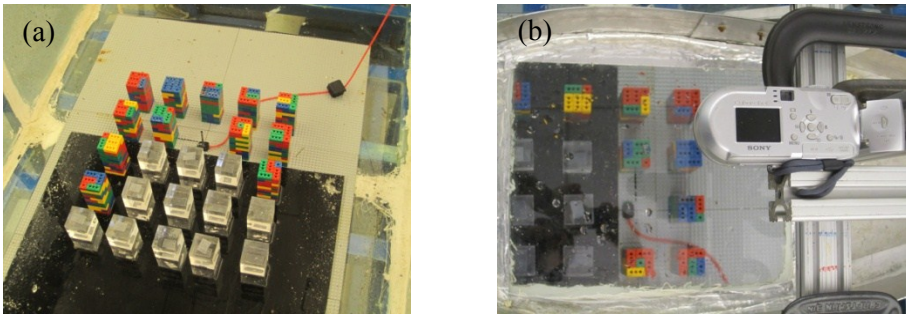

Figure 6-5: Laboratory setup for plume lateral spread visualization (a) 5x5 array of building (b) Camera configuration to buildings and stack

We also examined the roles of wind meandering and building induced turbulence on the lateral spread of the plume. The meandering in the water channel was controlled by adding or removing the flow conditioners (honeycombs). Figure 6-6 shows the visualization of plume lateral spreads with and without buildings and with and without meandering. As can be seen in Figure 6-6, in the presence of meandering, the lateral spread in the absence of buildings increases linearly and is higher than that in the presence of buildings. The plume lateral spread in the presence of buildings does not increase linearly and is closer to $\sim x^{1/2}$ behavior. These results indicate that buildings reduce the effects of meandering on plume spread, and at the same time impose a length scale on the horizontal turbulence. This length scale gives rise to the observed $x^{1/2}$ behavior.

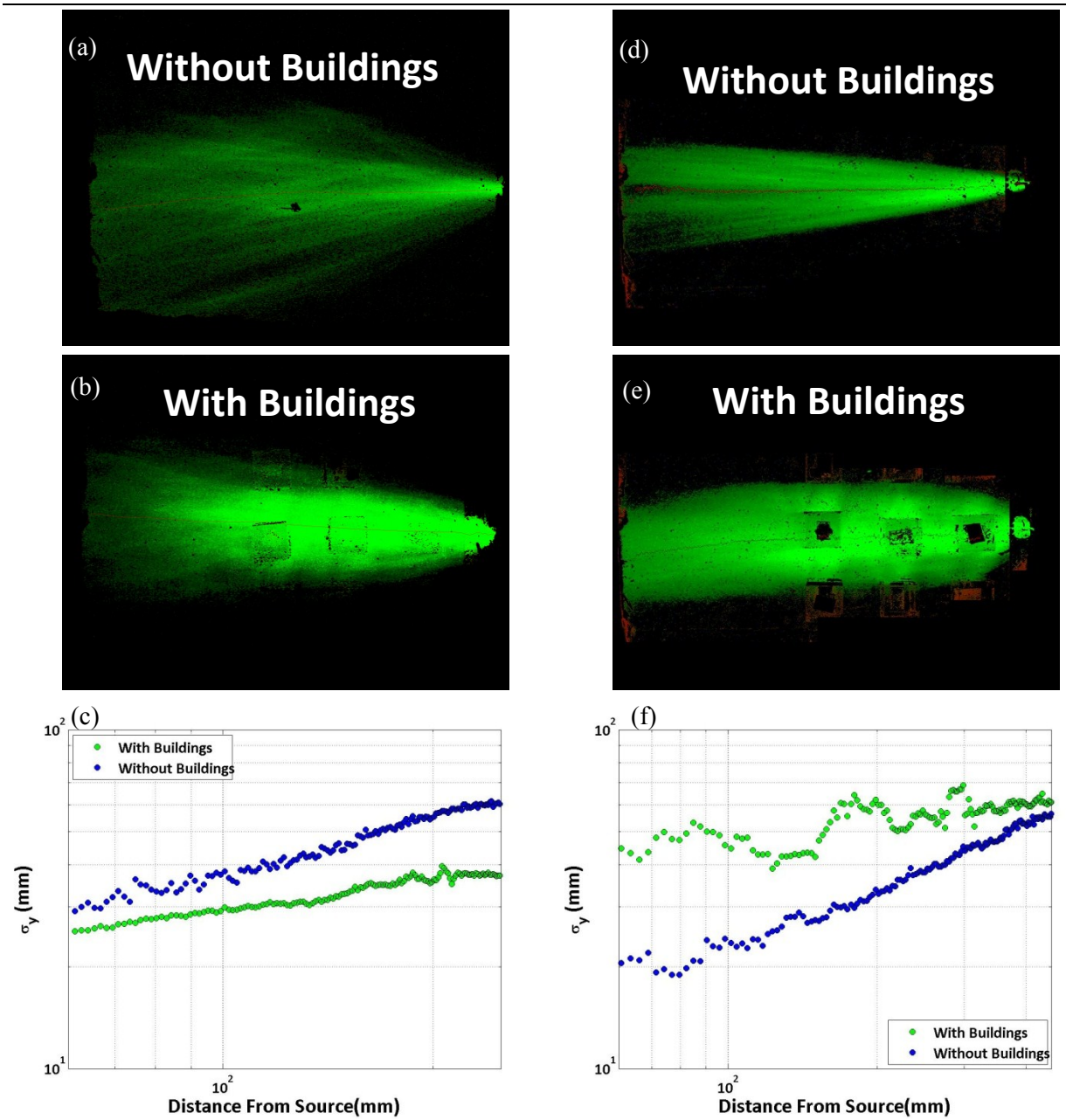

Figure 6-6: Plume lateral spread visualization in presence of meandering for (a) with buildings (b) without buildings (c) comparison (log-log plot) of lateral spread (σ_y) for with/without buildings and in absence of meandering for (d) with buildings (e) without buildings (f) comparison of lateral spread (σ_y) for with/without buildings

To examine the interaction between wind meandering and building induced turbulence, we decreased the effect of meandering by adding an additional flow conditioner to the water channel setup. In the absence of meandering, the presence of buildings results in rapid initial mixing followed by relatively slow spread that indicates the imposition of a lateral length scale by the building geometry (Fig. 6-6); the lateral spread of plume behaves as $\sim x^{1/2}$. In the absence of buildings, the lateral plume spread shows more linear behavior. The effect of buildings on lateral plume spread can be modeled through the following expression

$$\sigma_y^2 = \left(\frac{(\sigma_v / U)x}{(1 + x/L_b)^{1/2}} \right) + \sigma_{y0}^2 \tag{6-1}$$

where L_b is the length scale associated with urban geometry. We tentatively chose $L_b = W_b$ (W_b is the width of the buildings) and σ_{y0} is the initial spread of the plume which is taken to be $W_b / \sqrt{2\pi}$. L_b becomes infinity in the absence of buildings.

When $x >> L_b$ Equation (6-1) yields square root growth of lateral spread

$$\sigma_y^2 = \left(\sigma_v (x L_b)^{1/2} / U \right)^2 + \sigma_{y0}^2 \tag{6-2}$$

Figure 6-7a shows a schematic of the plume lateral spread in presence of buildings and Figure 6-7b express the comparison between the proposed model (Eq. 6-1) and observation from the water channel simulation. It is seen that model predicts the lateral spread well using the measured turbulent intensity.

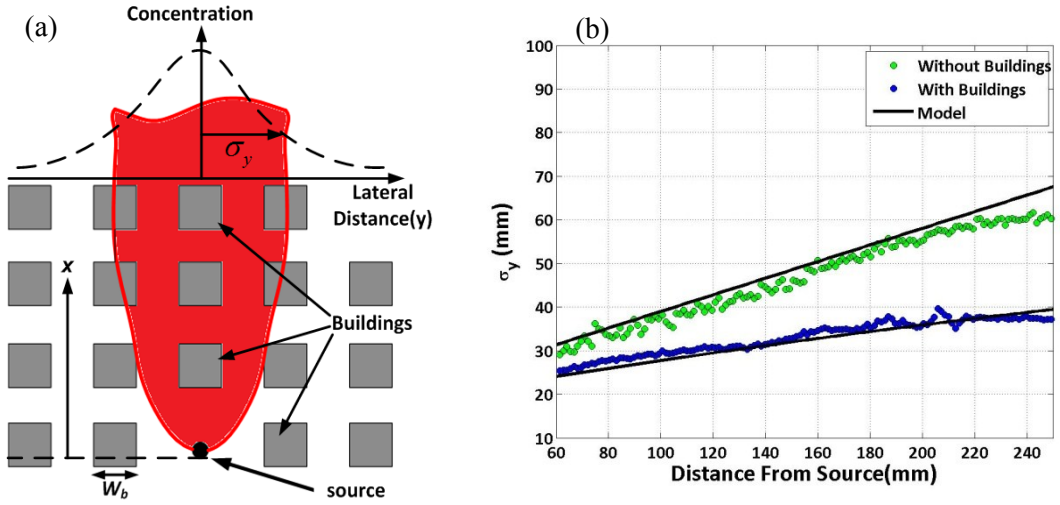

Figure 6-7: (a) Schematic of plume lateral spread(σ_y) in the presence of buildings, W_b represents the averaged width of the buildings (b)Measured plume lateral spread in case of 1) presence of buildings(blue dots ●), 2) Absence of buildings(green dots ●) and the comparison with the suggested model (black solid line▬)

6.3 Model Modification

Results from the water tank laboratory experiments at UCR indicate the need to include the following physical features in modeling the dispersion from low level buoyant sources:

1. Rapid vertical mixing of material within the urban canopy;
2. Length scale for horizontal mixing within urban canopy layer is set by building morphology for near field dispersion (Eq.6-1).

The effects of including these two features can be illustrated by modifying a Gaussian dispersion model (see Fig. 6-8 for schematic). Effect of rapid vertical mixing within the urban canopy can be modeled by assuming that ground level concentrations can be calculated by averaging the concentrations associated with the Gaussian

dispersion model (including the reflection term) over the height of the urban canopy layer as follows:

$$C(x,y,0)=\frac{1}{2\pi\sigma_y\sigma_z U}\exp\left(-\frac{y^2}{2\sigma_y^2}\right)\frac{1}{h_c}\int_0^{h_c}\left[\exp\left(-\frac{(z-h_e)^2}{2\sigma_z{}^2}\right)+\exp\left(-\frac{(z+h_e)^2}{2\sigma_z{}^2}\right)\right]dz \qquad (6\text{-}3)$$

where U is the wind speed, h_e is the effective plume height, h_c is the height of the urban canopy layer and σ_y,σ_z are the lateral and vertical spreads of the plume.

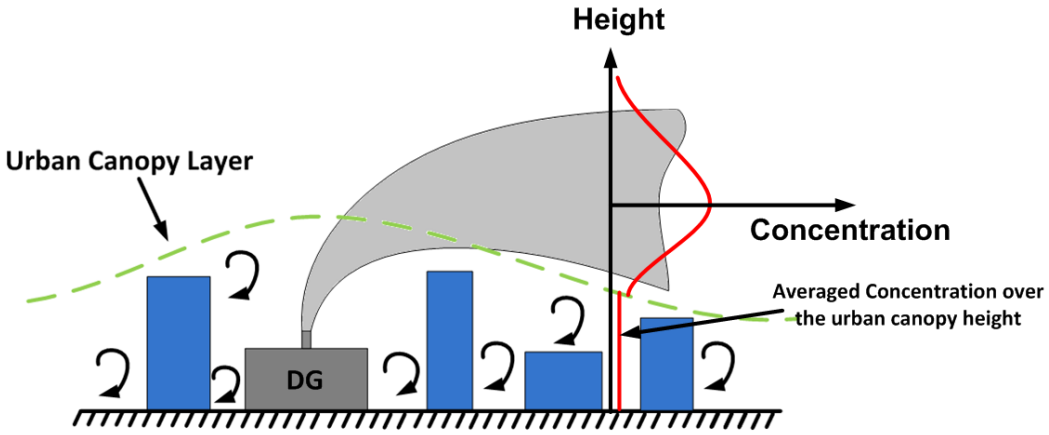

Figure 6-8: Schematic of the modified Gaussian model (well mixed model)

Equation (6-3) yields the analytical expression

$$C(x,y,0)=\frac{1}{2\sqrt{2\pi}\sigma_y U\,h_c}\exp\left(-\frac{y^2}{2\sigma_y^2}\right)\left[erf\left(\frac{h_e+h_c}{\sqrt{2}\sigma_z}\right)-erf\left(\frac{h_e-h_c}{\sqrt{2}\sigma_z}\right)\right]. \qquad (6\text{-}4)$$

In the modified model, the decrease of concentrations depends on the lateral spread, σ_y, which is a function of building dimensions in the urban canopy and is modeled through Equation (6-1). Plume rise is also calculated through the numerical plume rise

model explained in Chapter 5, where the effect of surrounding buildings as well as the effect of ambient turbulence is taken into account.

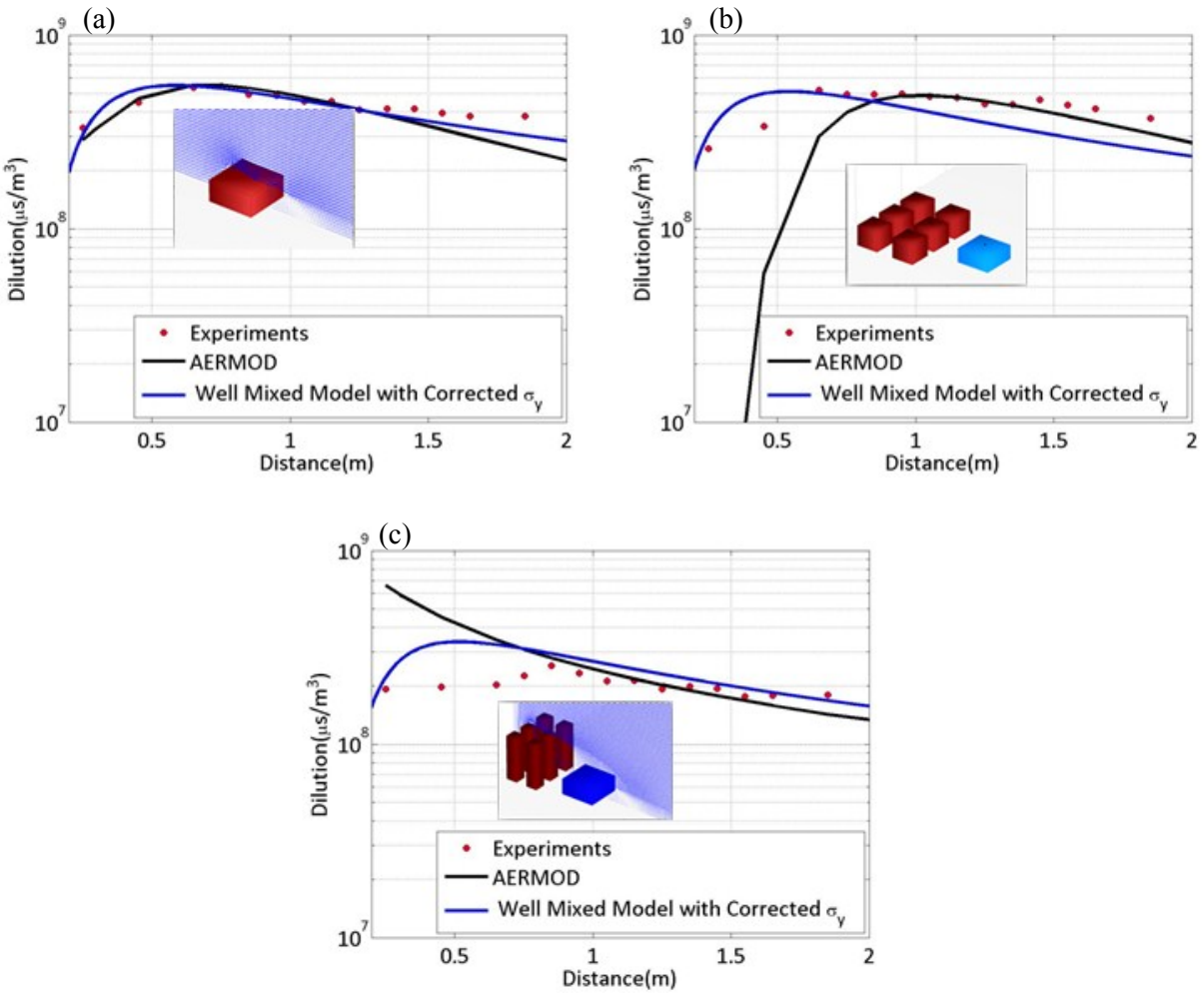

Figure 6-9: Performance of AERMOD (black solid line ▬) and well mixed model (blue solid line ▬) explaining the ground level concentrations associated with buoyant emission in water channel (red dots ●) in the presence of (a) Only DG Building (b) single storey upstream buildings (c) Double storey upstream buildings

Figure 6-9 shows the effect of using Equation (6-4) to explain concentrations observed in the water tank which resembles the near field dispersion behavior. AERMOD underestimates/overestimate the concentrations close to the source (Fig.6-9b and c),

while the modified Gaussian model, Equation (6-4), provides a better description of the near field concentrations.

6.4 Summary and Conclusion

Many of the previous laboratory studies on urban dispersion were focused on a passive plume released within a regular urban array, and almost there has been no study done on the release of buoyant emission from low-level sources in urban areas. In the previous chapters the importance of investigating such sources has been explained through the concerns regarding the rapid increase in the use of distributed power generators in urban areas with the highly possible adverse impact on the air quality. Following the field tracer study done in Palm Springs, CA in 2008, in order to have better understanding on the dispersion process of DG emissions and provide a more generic dataset (in terms of urban geometry and meteorological conditions) for future modeling, laboratory simulations were conducted in a custom designed water channel. Palm Springs DG has been modeled in the water channel and tested under different surrounding building geometries. Ground level concentration associated with a buoyant emission has been measured at different downstream distances. These data were used to evaluate the performance of AERMOD dispersion model in predicting ground level concentrations associated with these sources. It has been observed that AERMOD performs well in the absence of surrounding buildings. However, AERMOD tend to underestimate/overestimate ground level concentrations in the presence of single/double storey upstream buildings, respectively.

Data from ground level concentration measurements have been supplemented with data from velocity and turbulence measurements. Plume visualization has also been used to examine the behavior of the plume in the presence of upstream buildings.

Results have shown that upstream buildings can produce low velocity regions as well as high turbulence levels near the stack. Low velocity region allows the plume from the DG stack to rise higher and decrease the ground level concentration while high turbulence levels results in larger plume spread and increase in the ground level concentration near the stack.

Lateral plume spread in an array (5x5) of buildings with heights relatively higher than the stack were also measured in the water channel. Results have shown that an urban building canopy imposes a horizontal length scale on lateral turbulence. This scale depends on the dimensions of buildings within the canopy. Material released within the canopy first undergoes rapid horizontal spread that is dependent on building width, and then spreads at a rate dependent on the lateral turbulent velocity within the canopy and the horizontal length scale set by the buildings. The horizontal spread within the canopy can differ substantially from that above the urban canopy.

These effects have been accounted for in a simple model which assumes that buildings in urban areas produce a highly turbulent boundary layer called urban canopy layer. Therefore pollutants released from low level buoyant sources, entrain into this boundary layer and immediately get well mixed. The height of this canopy layer is highly dependent on the average height of the buildings in urban areas. Lateral plume spread has

also been modeled using data from laboratory. This model allows the plume to spread with square root of distance from the source. Comparisons between the model and laboratory observations show that the model has a relatively acceptable estimate of the concentrations. The encouraging results from this model suggest modifications to AERMOD to allow its application to buoyant low level releases in urban areas.

7 RISE OF BUOYANT EMISSIONS FROM LOW LEVEL SOURCES IN URBAN AREAS[†]

7.1 Introduction

The ground level concentration of pollutants emitted from a stack is extremely sensitive to plume rise. Since the 1950s, many studies have been made in an attempt to provide accurate numerical and analytical models to predict plume rise from large centralized power plants (Halliday, 1968), or sources located far away from urban environments with stack heights of 200 to 300 m (Fay, 1973). In 1963 the Tennessee Valley Authority (TVA) initiated a comprehensive plume rise study with relatively tall stacks (about 150 m) during stable, neutral, and slightly unstable conditions (Carpenter et al. 1968). The analysis of the data obtained from this field study revealed that wind speed and stack heat emission rate are the most significant parameters determining the plume rise from large power generating stations. Halliday (1968) carried out field measurements of plume rise from a 76.3 m stack in order to verify plume rise equations developed by Priestly (1956), Bosanquet (1957), and Lucas et al. (1963). They measured the plume rise by taking photographs of the plume. The disadvantage of Halliday's (1968) plume rise measuring technique was that plume rise could only be correctly measured when the wind direction was perpendicular to the camera lens orientation. Hence, for cases when the wind direction was not perpendicular to the camera orientation, this technique did not

[†] Springer / Boundary Layer Meteorology, 2012, "Rise of Buoyant Emissions from Low-Level Sources in the Presence of Upstream and Downstream Obstacles", Pournazeri S, Princevac M, Venkatram A, original copyright is given to the publication in which the material was originally published; with kind permission from Springer Science and Business Media

give accurate results. In other studies, Hamilton (1967) and Bacci et al. (1974) also measured plume rise using the *LI*ght *D*etection *A*nd *R*anging (*LIDAR*) technique. They related their data to the meteorological variables and power station operating conditions and showed that the plume rise measurements were in agreement with the models developed by Lucas et al. (1963) and Briggs (1969).

As explained in previous chapters, the ability to explain the concentrations associated with a low level buoyant source through a model, such as AERMOD (Cimorelli et al. 2005), was limited (Jing et al. 2010). One of the reasons for this limitation can be the formulation of plume rise. In AERMOD, the plume rise formulation (Weil, 1988; Briggs, 1984) is designed primarily for elevated emissions from large power plants where it neglects building effects, as well as the effects of the variation of meteorological parameters with height that govern the plume rise for near surface DG sources. DGs commonly deploy heat recovery to increase the efficiency during power generation. This heat recovery lowers the exhaust gas temperature which results in lower plume rise. The lower plume will be much more affected by surrounding buildings. This further increase the uncertainty of simple models (e.g. Weil, 1988; Briggs, 1984) in predicting the plume rise associated with DGs, since they have no capability to incorporate building effects.

None of the past and current studies have focused on plume rise from low-level buoyant sources. Furthermore, none of them have studied the effects of buildings on plume rise. Hence, this study was motivated by the need for a better understanding of the plume rise from low level buoyant sources in urban areas and reliable models to predict

it. As the first step toward satisfying this need, a field study was conducted in Palm Springs, California, USA. Plume rise from a DG located in Sunrise Park was measured using a new plume rise photography method where, unlike the previous photography methods applied by Halliday (1968) and Bringfelt (1968), plume rise was correctly measured even if the wind direction was not perpendicular to the camera lens orientation.

Results from the field study are highly dependent to the site meteorological conditions and it would be difficult to extrapolate the plume rise results from Palm Springs' study to other urban settings. Also, conducting field studies for various wind conditions at different sites would be prohibitively expensive. For these reasons, in addition to the field study, a systematic laboratory investigation was done, and plume rise under several different upstream and downstream building geometries was measured in the water channel facility at UC Riverside. Using the measurements from the laboratory study, the performance of numerical plume rise model explained in chapter 5, which accounts for the effect of surrounding buildings on plume rise, was examined.

Field measurements are explained in Section 7.2, followed by the laboratory and numerical study in Section 7.3, and summary and conclusion are presented in Section 7.4.

7.2 Field Study

In November of 2010, a field study was conducted in Palm Springs, California, USA. In this study, the plume rise from a DG, located in Sunrise Park, with a stack height of 9.3 m and stack diameter of 0.3m was measured under different source conditions. Sunrise Park is located in the central area of Palm Springs close to the downtown,

between Ramon Road and E. Baristo Road. This park consists of 38 acres of grassy area and is surrounded by residential area with mostly single storey (≈ 5 – 7m height) buildings and 10 - 15m tall palm trees. The site has an approximate roughness length of z_0 = 0.5 m; zero plane displacement height of d_h = 2.5 m ($d_h = 5z_0$ based on Britter and Hanna, 2003); Bowen ratio of Bo = 1.5; and surface albedo of al = 0.22. These surface parameters corresponds to those recommended by the South Coast Air Quality Management District, which are obtained by applying AERSURFACE (EPA, 2008), a program developed by US EPA, to the Palm Springs urban area (SCAQMD, 2009). DG was surrounded by Palm Spring swim center (a single storey $L \times W \times H$ = 50m×30m×7m building) to the south, a baseball stadium to the north-east, and a playground to the west. The plume rise measurements were accompanied with basic meteorological measurements, which are described next.

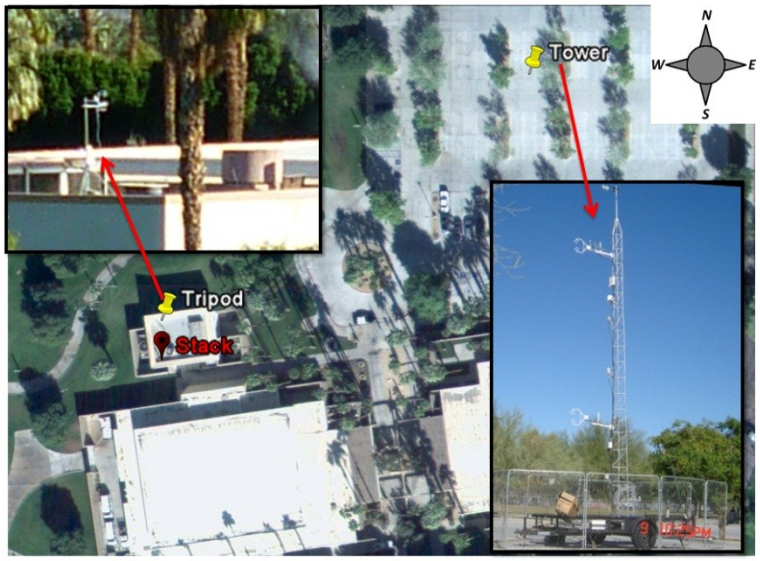

Figure 7-1: Location of the meteorology stations (yellow pins) in Sunrise Park, Palm Springs, CA (aerial picture is produced using Google Earth)

7.2.1 Meteorology

Two meteorological stations, a tower (with two sonic anemometers at 3m and 8m above ground level) and a tripod (with a sonic anemometer at approximately 4m above the rooftop of the DG, i.e. 11m from the ground) were set up. The locations of these two stations are shown in Fig. 7-1. The tower was set up on the parking lot of Sunrise Park within 100m of the DG facility, and the tripod was set up on the roof of the DG building. Three components of wind speed and the ambient virtual temperature were measured by sonic anemometers at the rate of 10 samples per second. Using these measurements, mean and turbulent wind speeds, and surface heat flux were calculated and averaged over periods of 15 minutes (9000 samples).

Fig. 7-2 shows the meteorology measured from November 7 to November 10 from the sonic located on the roof of the DG at 11m from the ground. The data show that wind speeds are less than 1 m s^{-1} for most of the days. This makes Palm Springs a low wind speed case compared to other urban areas, where wind speeds mostly exceed 3 m s^{-1} during the day (Allwine et al., 2006; Venkatram et al., 2004b; Rotach et al., 2004). It can be observed that the wind direction is variable, vertical turbulent velocities (Fig. 7-2d) are approximately 0.25 m s^{-1}, and lateral turbulent velocities (Fig. 7-2c) are generally higher around 0.5 m s^{-1}. The site in Sunrise Park has relatively high turbulent intensities of about 25% in the vertical direction and about 50% in the horizontal direction. In addition, as the wind direction changes substantially (Fig. 7-2b), plume meandering can play a major role in the dispersion of pollutants released from the DG.

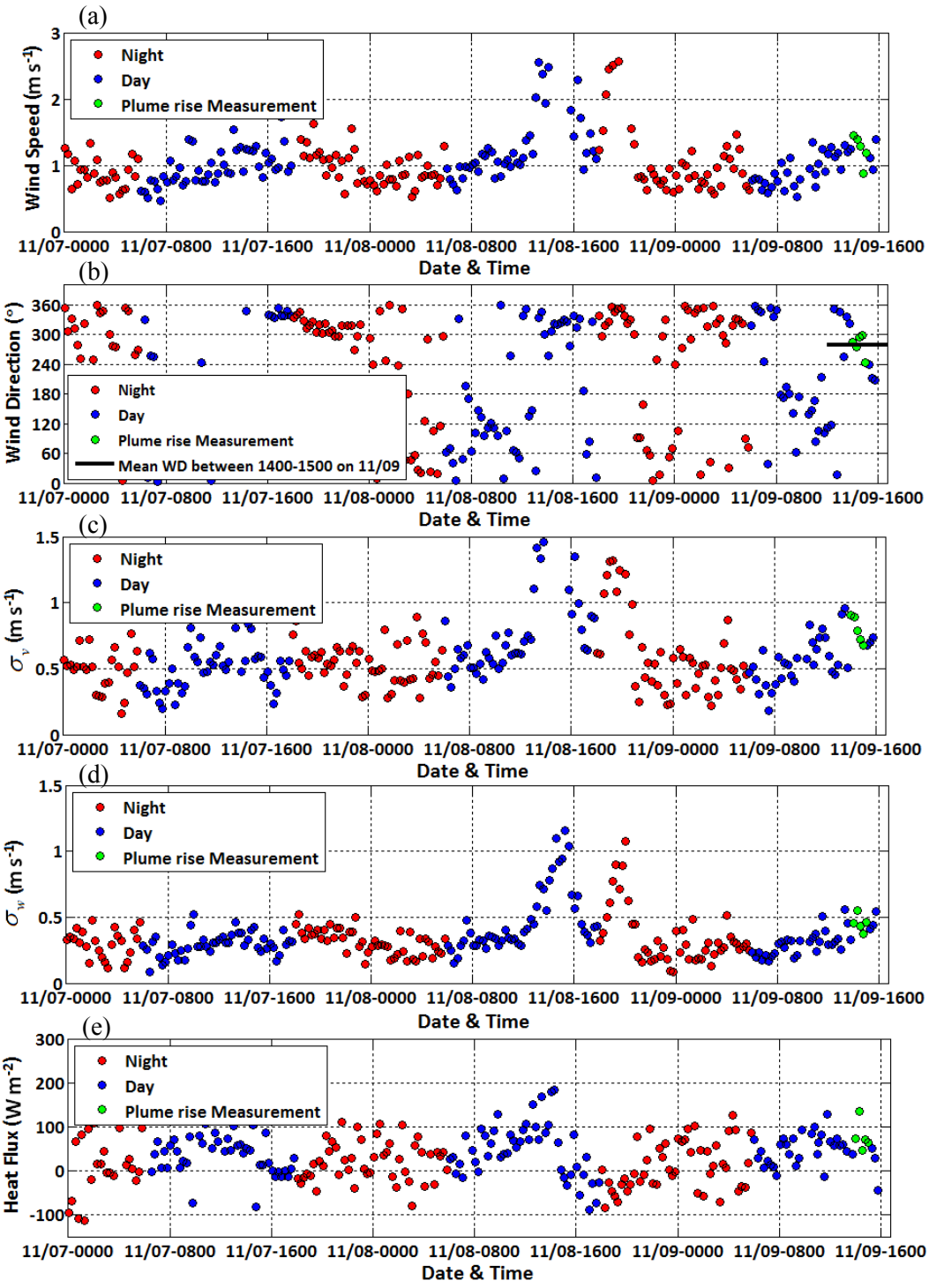

Figure 7-2: Meteorology measurements for (a) wind speed U (m s^{-1}), (b) wind direction, (c) lateral turbulent velocity σ_v (m s^{-1}), (e) vertical turbulent velocity σ_w (m s^{-1}), and (e) sensible heat flux $\rho C_p \overline{w'T'}$ (W m^{-2}) (green dots show the meteorology at the time of the plume rise measurements on Nov-09 from 1400 to 1500 PST).

A comparison between data from different sonics showed that there is no significant spatial variation of micrometeorology between the roof of the DG and the tower site. In addition, it has been observed that wind direction does not change substantially with height up to 11m from the ground.

7.2.2 Plume rise

In order to visualize the plume released from the DG, smoke oil (Super*Dri® Aviation Smoke Oil) was injected into the stack four meters below the stack exit to allow for oil evaporation and mixing. This produced a thick white smoke visible to the naked eye. Consecutive images of the plume were taken from different locations close to the stack using commercial digital cameras (Fig. 7-3a). The plume images were averaged over 5 min periods and the background image (an image that was taken from the same location when there was no visible plume exiting the stack) was subtracted from the averaged images (Fig. 7-3b). After the contrast enhancement, only the region of the highest smoke concentration (i.e. the plume centerlines) remained on the image. The height from the stack of the line passing through the center of this region (green line in Fig. 7-3b) represents the average plume rise, i.e. averaged location of the plume centerlines. The horizontal and vertical distances (L) of the plume centerline can be calculated as,

$$L = L_{image}\left(H_{s-field} \Big/ H_{s-image} \right) \tag{7-1}$$

where L_{image} is the distance (horizontal or vertical) of the plume centerline measured on the averaged image; $H_{s-field}$ and $H_{s-image}$ are the height of the stack in the field and the image, respectively. However, it needs to be noted that the calculation of the plume centerline height from such an image is only accurate when the plume direction (i.e. wind direction) is perpendicular to the camera lens orientation. Therefore, for the cases where the wind direction was not perpendicular to the camera orientation, corrections were made to calculate the correct plume rise. The following section describes the correction method for the discrepancy in wind direction and camera orientation.

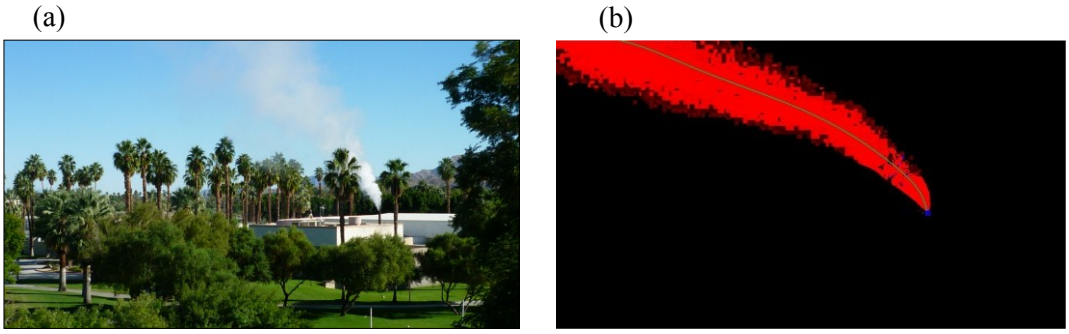

Figure 7-3: Measurement of plume rise associated with the Palm Springs DG (a) Example of an instantaneous photograph of the plume released from the DG and (b) The averaged image of the plume with the background subtracted and contrast enhanced. This is considered as the region of the plume centerlines. The mean plume centerline is shown as a green line.

7.2.3 Correction Method

Fig. 7-3 gives the schematic used for the correction method. The plume centerline plane (brown line in Fig. 7-4) in general does not overlap with a plane that is normal to the camera orientation and passes through the stack (*Normal plane* in Fig. 7-4). The plume centerline plane deviates from the *Normal plane* by an angle θ_1; the camera is located at a distance D_{stack} from the stack; X_m is the downwind distance of the plume

centerline calculated from the averaged plume images through equation (7-1) assuming that plume direction is perpendicular to the camera lens orientation; L_{cam} is the distance of the camera to the *Normal plane*; λ is the angle between the *Normal plane* and the line connecting the stack to the camera. The corrected plume centerline downwind distance X_{real} can be calculated as follows:

$$X_{real} = X_m\left(\cos(\theta_1) + \sin(\theta_1)\tan(\theta_3)\right) \tag{7-2}$$

where $\theta_3 = \theta_1 + \theta_2$, and

$$\theta_2 = \tan^{-1}\left(\frac{X_m - X_{centre}}{L_{cam}}\right) \tag{7-3}$$

where X_{center} is the distance in the field from the stack to the center of the image and

$$L_{cam} = D_{stack}\sin(\lambda). \tag{7-4}$$

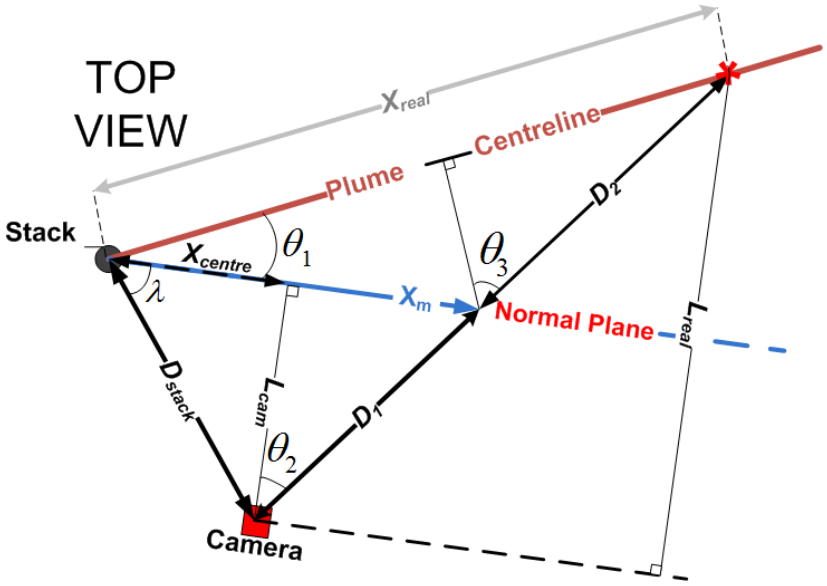

Figure 7-4: Schematic used for the correction technique for the case when the plume centerline (brown line ▬) is deviated from the normal plane of the camera lens (blue line ▬).

Assuming that plume rise measured from the averaged image is Z_m, the corrected plume rise Z_{real} is calculated as follows,

$$Z_{real} = Z_m \left(L_{real} / L_{cam} \right) \tag{7-5}$$

where $L_{real} = L_{cam} + X_{real} \sin(\theta_1)$.

By utilizing this method, the numerical value for plume rise was corrected for all wind directions measured by sonic anemometers located at the roof of the DG. This method cannot incorporate the change in the wind direction with height. Since our measurement of the plume rise are limited to 35m from the ground and the wind direction measurements at three different heights (up to 11m) do not differ significantly, we assumed that there is no significant variation in wind direction over the observed plume.

7.2.4 Field Measurements

Plume rise measurements were conducted on November 9, 2010. Fig. 7-5 shows the wind speed and direction measured 1 hour before the experiment (13:00) until 1 hour after the experiment (16:00). It can be seen that the wind direction is mostly towards the east; however, its deviation from the mean is relatively large. Therefore, most of the cases needed correction.

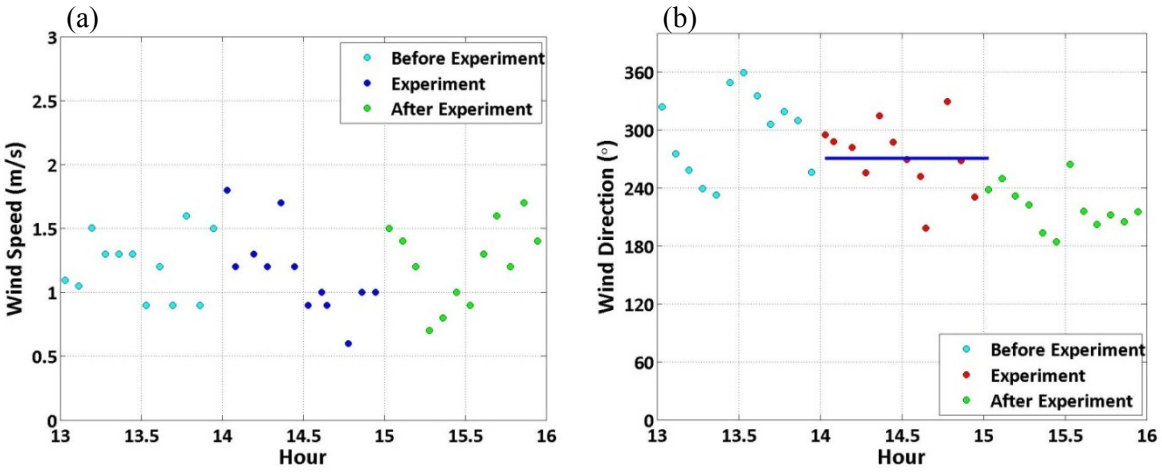

Figure 7-5: (a) Wind speed and (b) wind direction, measured from 13:00 to 16:00 on November 9th, 2010, during plume rise measurements.

Plume rise data were gathered by five cameras at different locations relative to the stack (Fig. 7-6) in order to have full coverage of the plume under different wind angles. The orientation of each camera and their distance from the stack are shown in Table 7-1.

Table 7-1: The distance of each camera from the stack and their orientation relative to the North

Camera	Distance From Stack (m)	Camera Orientation from North
CAM 1	119	125°
CAM 2	67	100°
CAM 3	67	35°
CAM 4	67	65°
CAM 5	34	275°

Images were captured at the rate of approximately 1 image per second. Experiments were conducted for two power outputs of the DG. By changing the power output of the DG, the stack exit velocity changed. Since the heat recovery was not modified, due to the need of the community center, the exhaust temperature also changed for each power setting. The stack exit velocity and exhaust temperature were measured using a pitot tube

and a k-type thermocouple, respectively. Details of the parameters involved in each DG power setting are shown in Table 7-2. For each DG power setting, the average plume rise was measured in intervals of 5 min and was compared with the Briggs (1984) plume rise formulation described in previous chapters.

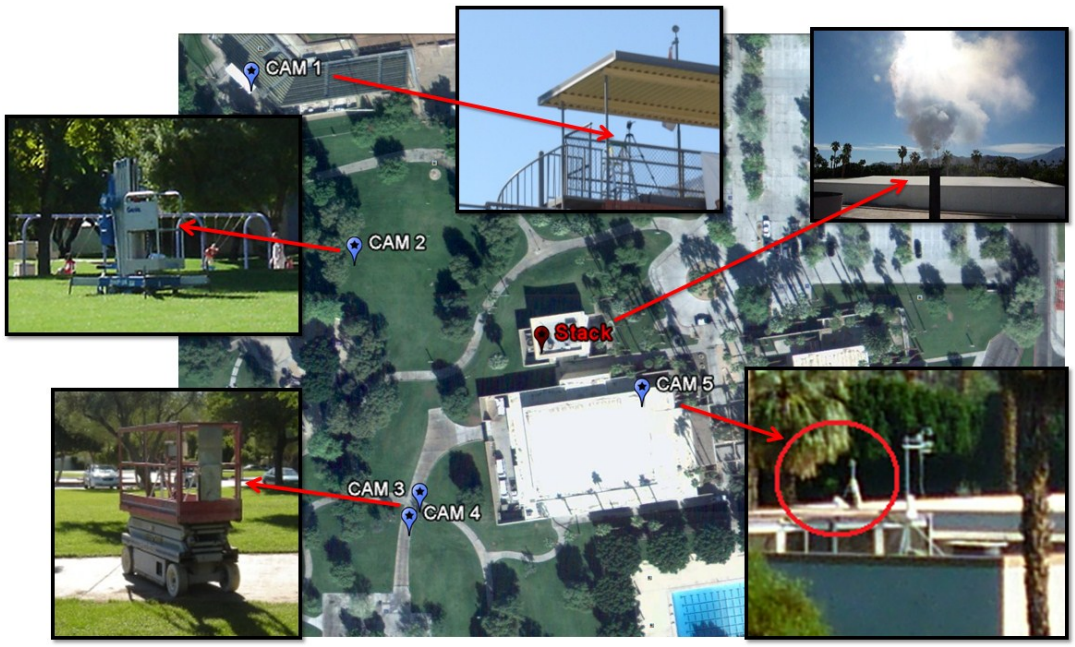

Figure 7-6: The location of the five cameras (blue pins) with respect to the location of the stack (red pin) (aerial picture is produced using Google Earth)

Table 7-2: Stack properties for each DG power setting

Stage #	Time Interval	Stack Exit Temperature	Stack Exit Velocity ($m\ s^{-1}$)	DG Output (kW)
1	*1400 - 1420*	248.5 °C	15.4	600
2	*1425 - 1440*	210.7 °C	9.5	300

7.2.5 Results

The results of plume rise measurement and uncertainties associated with them were compared with the Briggs (1984) formulation, as shown in Fig. 7-7. Here, the uncertainties σ were obtained by calculating the standard deviation of the height of plume centerlines from the averaged and contrasted plume images (e.g. Fig. 7-3b). We employed the measured wind speed at the roof of the DG building (11m from the ground) in predicting the plume rise. It can be seen that for most of the cases the predictions made by utilizing the Briggs plume rise model are in good agreement with the observations from the field experiment. Although the experimental uncertainties are relatively higher than the differences between the observations and predictions, in most cases it can be seen that plume rise is slightly over-predicted close to the stack, and is under predicted by Briggs formulation further downwind. The primarily reasons for these differences are likely the lower wind speed at the stack exit (z = 9.3 m) and the effect of the ambient turbulence on the plume rise at larger downwind distances. Lower wind speed allows the plume to rise higher near the stack, and ambient turbulence suppresses the plume rise at larger distances. Although these effects can slightly modify the plume rise behavior, Briggs' formulation appears to perform reasonably well in predicting the plume rise.

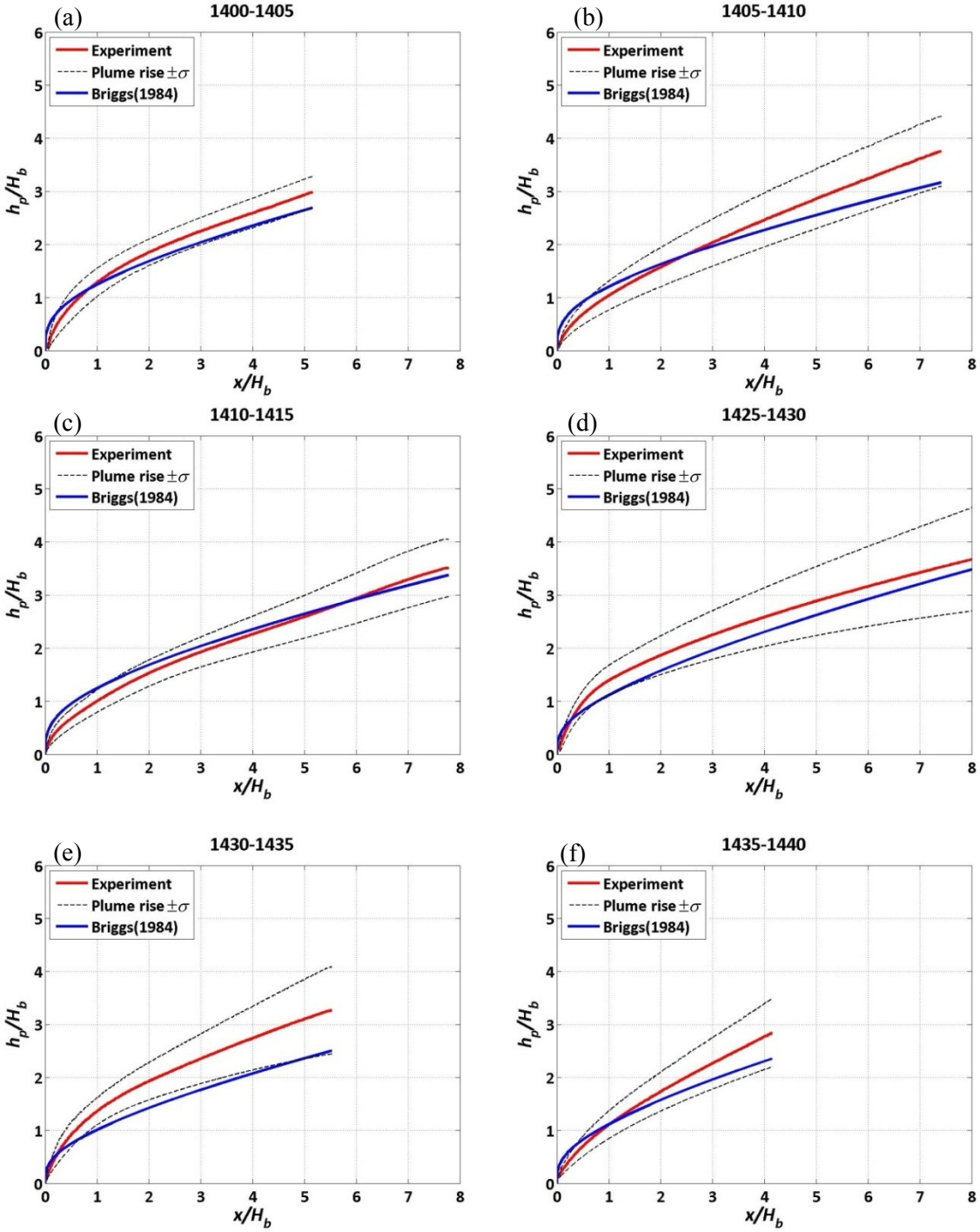

Figure 7-7: Normalized measured plume rise (red ▬) vs. Briggs (1984) plume rise model (blue ▬) for time intervals of (a) 1400-1405 (b) 1405-1410 (c) 1410-1415 (d) 1425-1430 (e) 1430-1435 (f) 1435-1440 (Plume rise, h_p, and distance x, are normalized with respect to building height H_b = 7m). The error bars for measured centerline ($h_p \pm \sigma$) are also shown as black dashed (----) line. Both the error lines and the plume centerline are smoothed.

As it was shown in Fig. 7-2a, Palm Springs was dominated by low wind speeds with a mean value of approximately 1 m s^{-1} and a maximum of 1.5 m s^{-1} for most of the days. This allowed the plume to rise relatively high making the effect of nearby buildings on the plume rise non-existent. Also, because Palm Springs' urban morphology consists of mostly low rise (single storey) buildings, approximately the same height as that of the DG, it is not expected for the plume to be affected by complex flows caused by buildings (e.g. updrafts and downdrafts) in the region where it tends to rise.

Conducting different field tests in order to examine the effect of various urban geometry and meteorology, is prohibitively time consuming and expensive. Also, preparation for field measurements includes proper permit seeking and there are not many DG owners willing to allow plume visualization from their DG stacks. Therefore, in order to have a better understanding of plume rise in the presence of upstream and downstream obstacles near the source under more controlled stack and wind conditions, a laboratory study was done. Unlike the Palm Springs field study where low wind condition was considered; in the laboratory study, we examine the plume rise under relatively high wind speeds.

7.3 Laboratory Study

The laboratory study to understand the effect of nearby buildings (upstream and downstream) on the plume rise was conducted in a custom-designed water channel, which is described next.

In order to investigate plume rise associated with DGs, a DG building similar to Palm Springs DG ($L \times W \times H$ = 15 m × 15 m × 7 m) with stack height of 9.3 m and stack diameter of 0.3 m (stack is located in the middle of the building) was modeled in the water channel at a scale of 1:100. It must be mentioned that the laboratory study shown in this study does not represent the scaled problem from the Palm Springs field study, except for the geometry. In order to observe the effect of surrounding buildings on plume rise, arrays of buildings (2 rows and 3 columns) of two different heights (single and double storey, with the heights of H_{single} = 100 mm and H_{double} = 200 mm, respectively) were created using Lego blocks, and were situated as follows: 1) upstream of the DG building; 2) downstream of the DG building; and 3) upstream and downstream of the DG building (Fig. 7-8). The upstream and downstream building arrays were located at a distance of 150 mm from the upwind and downwind side of the DG building, respectively. We are aware of the fact that the building configurations used in the laboratory study do not necessarily resemble a typical urban environment. However, since hot plume rises above the urban canopy in relatively short distance from the stack, its rise would be mainly affected by the nearby buildings rather than the overall urban geometry. We should note that the background micrometeorology that governs the plume rise near the stack is surely dependent to the urban morphology. The influence of urban morphology on the upwind micrometeorology in urban areas has been widely explained in the literature (e.g. Venkatram and Princevac 2008; Princevac and Venkatram 2007; Luhar et al. 2006) and will not be discussed here.

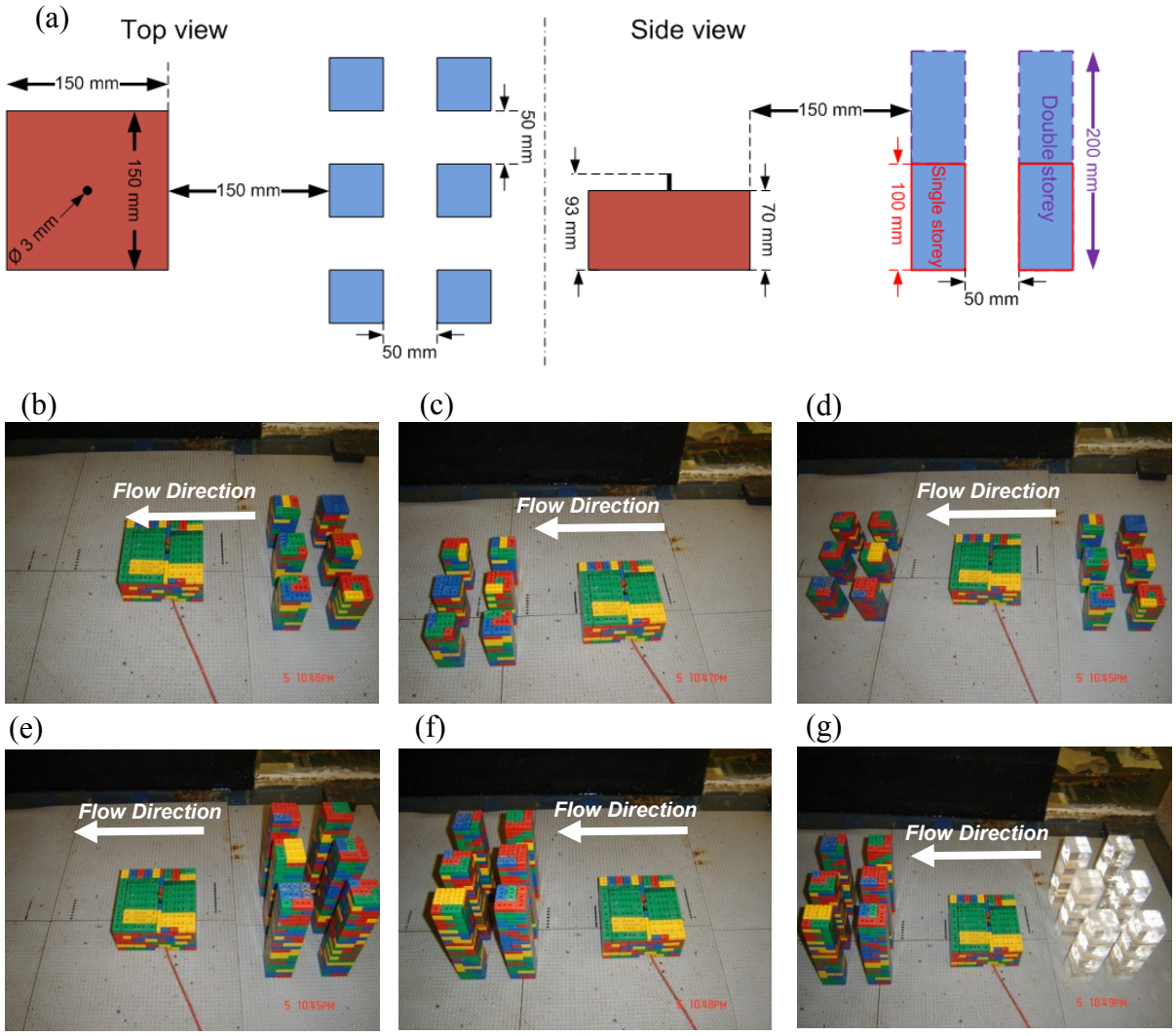

Figure 7-8: (a) Schematic of the buildings configuration. Model of the DG and surrounding buildings situated upstream (b, e), downstream (c, f), both upstream and downstream (d, g). Single storey (b, c, d) and double storey (e, f, g) buildings are investigated.

Different tracer buoyancies were achieved by using different mixtures of alcohol and water and expressed as specific gravity (*SG*). Plume rise was measured under two different buoyancies (*SG* = 0.98 and 0.96). These plume buoyancies were selected in order to observe how plume rise affected by buildings changes with an increase in buoyancy (buoyancy associated with a tracer of *SG* = 0.96 is equivalent to two times that of a tracer with *SG* = 0.98, since the buoyancy is proportional to 1-*SG*).

As explained in chapter 5, in scaling the free stream velocity, the most important is to satisfy Reynolds number independence criteria. Following Yee et al. (2006) and Snyder (1981), in order to satisfy this criteria, the reference Reynolds number (*Re*), based on the free stream velocity (v_∞) and characteristics building frontal length scale, H_b^* (length scale based on the obstacle frontal area; $H_b^* = (WH)^{1/2}$) should be larger than 4000. In the water channel, this is obtained for velocities larger than 3.9 cm s^{-1}. Therefore, in order to scale the field velocity of 3 - 4 m s^{-1}, velocity scale of 3:200 was used. This velocity scale was selected to have sufficiently fast flow to satisfy *Re* independence criteria and at the same time to be slow enough to allow for accurate measurements of plume rise. Using this velocity scale, average stack exit velocity of 12.5 m s^{-1} in the field were scaled and modeled in the lab. Details of experimental conditions are given in Table 7-3.

Table 7-3: Experimental parameters for plume rise measurements

Parameters	Value
Free stream horizontal velocity (v_∞)	4.5 cm s^{-1}
Diameter of the stack (D)	3mm
Stack exit velocity (V_s)	19 cm s^{-1}
Roughness length of Lego blocks (z_0)	≈ 0.6mm
Plume specific gravity (SG)	0.96 and 0.98

7.3.1 Upstream Buildings

Fig. 7-9 shows the results of the flow and plume rise measurements when buildings (of two different heights) are situated upstream of the DG building. It can be seen from Fig. 7-9 a-b that upstream buildings increase the plume rise, compared to the case when no buildings are present. Fig. 7-9 a-b also shows that an increase in the height of the upstream buildings further increases the plume rise. This effect can be explained through the flow measurements (Fig. 7-9 c-e) associated with these three cases (only DG building, single storey upstream buildings and double storey upstream buildings). From Fig. 7-9 c-e, it can be inferred that the presence of upstream buildings increases the flow resistance and induces a low wind speed condition near the DG building, which allows the plume to rise higher. The increase in the height of the upstream buildings decreases the wind speed in a larger region above the DG which enables the plume to rise much higher.

However, as can be seen from Fig. 7-9 b, the rate of plume rise in the presence of upstream buildings (especially for the case of double storey upstream buildings) is slower compared to the case of an isolated DG without any surrounding buildings. This suppression of the plume rise is due to the higher levels of turbulence caused by the upstream buildings. This higher turbulence leads to enhanced entrainment of ambient fluid and causes the plume to levels off. In addition to the above mentioned observations, Fig. 7-9 also shows that an increase in the buoyancy from $SG = 0.98$ to $SG = 0.96$ reduces the discrepancy between the plume rise measurements under the three different conditions; since the effect due to buildings becomes smaller as the plume rises higher.

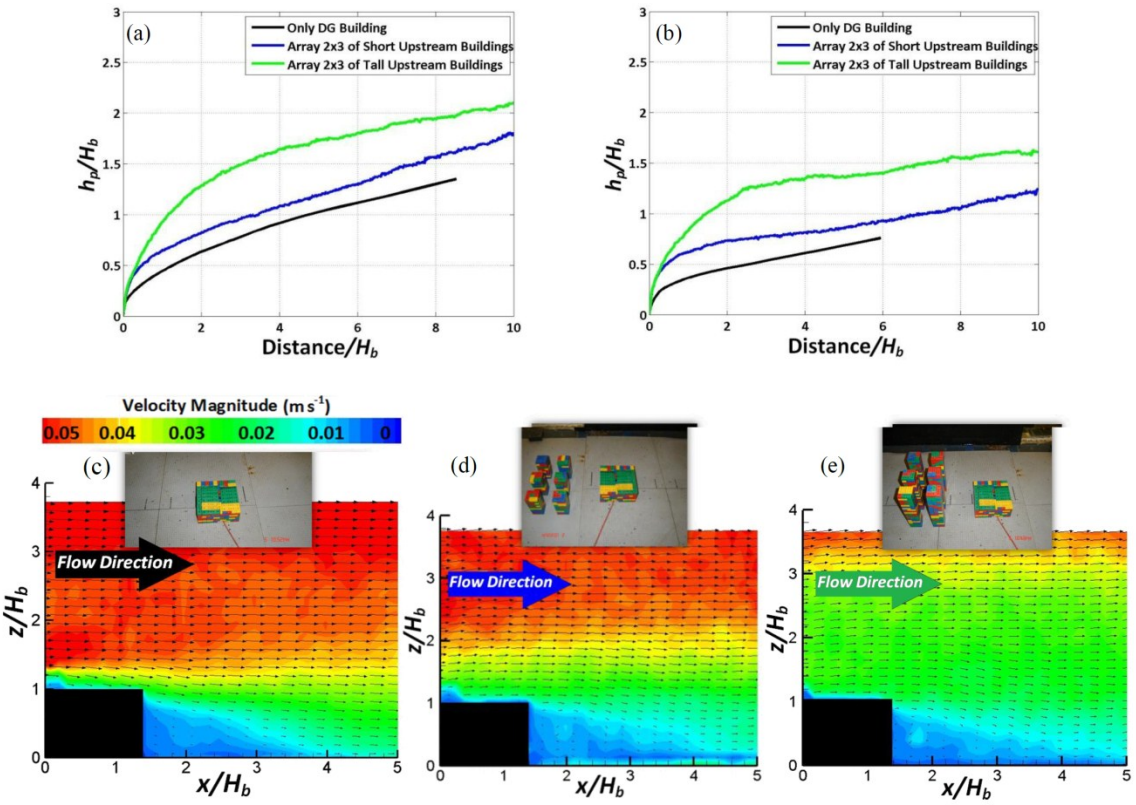

Figure 7-9: Results from measurements of plume rise (h_p) associated with a DG with and without upstream buildings for (a) SG = 0.96 and (b) SG = 0.98 (distances in horizontal and vertical directions are normalized with respect to the height of the DG model building H_b = 0.07 m). Flow measurements associated with (c) only the DG building, (d) the DG building with single storey upstream buildings, and (e) the DG building with double storey upstream buildings (the blue vector lines show the velocity of less than 0.01 m s^{-1} and the dark red vector lines show the velocity equal/above 0.05 m s^{-1} corresponding to approximate velocity of 3.5 m s^{-1} in the field).

7.3.2 Downstream Buildings

The results from the measurement of flow and plume rise when the buildings are situated downstream of DG building are shown in Fig. 7-10.

From Fig. 7-10 a-b it can be seen that single storey (short) downstream buildings with the height approximately the same as that of the stack height, increase the plume rise, compared to the case when there are no surrounding buildings. However, by

increasing the height of the downstream buildings, the plume rise is reduced. As in the previous case, flow measurements are used to explain the observations (Fig. 7-10 c-e).

Fig. 7-10 c-e shows that the presence of single storey downstream buildings lowers the wind speed. In addition, these buildings reduce the downdrafts induced by the DG building and instead, create slight updrafts in vicinity of the DG. Due to these two effects, the plume rises higher when single storey downstream buildings are present. However, the effect of buildings on plume rise is significantly different when the height of the downstream buildings is doubled. As the flow approaches the double storey downstream buildings, flow above the stagnation point passes over the buildings and produces an updraft; but most of the flow is deflected towards the ground and produces a strong downdraft (Fig. 7-10 e). This effect has also been studied by Oke (1987) where he mentioned that the stagnation point occurs at approximately 2/3 height of the building while a result from our flow measurements in Fig. 7-10e shows this stagnation height as the 3/4 of the building height. For the presented analysis the exact stagnation height is not crucial. Depending whether the plume approaches the updraft above the stagnation height of the downstream building or the downdraft below this height, it can rise higher or lower. In the case of our laboratory study, due to the low buoyancy and high wind speeds, the plume could not reach above the stagnation height and pass over the downstream buildings. Therefore, the plume approached the region where it was dominated by downdrafts, which resulted in lower plume rise. This effect became more apparent when the buoyancy was decreased from $SG = 0.96$ to $SG = 0.98$. The plume rise associated with the double storey downstream buildings became even slightly lower than for the

case when no surrounding buildings were present. Since the plume passes through the array of downstream buildings, no accurate plume rise measurements were possible in the vicinity of these buildings (discontinuity in the green line in Fig. 7-10 a-b).

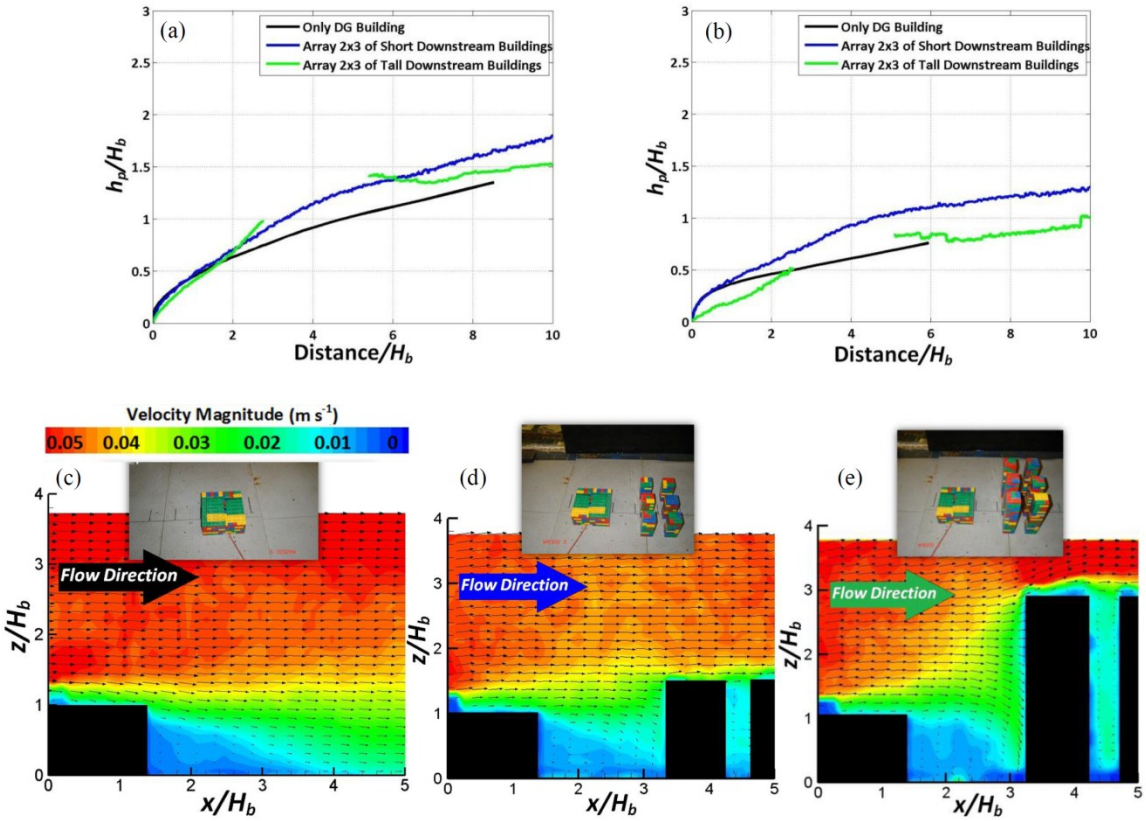

Figure 7-10: Results from measurements of plume rise (h_p) associated with a DG with and without downstream buildings for (a) SG = 0.96 (b) SG = 0.98 (Since for the case of tall, double storey, downstream buildings, plume passes through the buildings, no measurements of plume rise were available in this region. This explains the discontinuity of the green line). Flow measurements associated with (c) only the DG building, (d) the DG building with single storey downstream buildings and (e) the DG building with double storey downstream buildings.

7.3.3 Upstream and Downstream Buildings

Fig. 7-11 shows the results from the flow and plume rise measurements when both upstream and downstream buildings were present. From Fig. 7-11 a-b, it can be observed that a combination of both upstream and downstream buildings cause the plume to rise

higher; this increase in plume rise becomes larger when the height of the buildings is doubled. As in the previous cases, flow measurements were used to explain the observed effects.

As it can be seen in Fig. 7-11 d, in the case of the single storey buildings, the upstream buildings slightly reduce the wind speed. In addition, the downstream buildings reduce the downdrafts caused by the DG building. The reduced wind speeds and weaker downdrafts cause the plume to rise higher. In the case of the double storey buildings (Fig. 7-11 e), the upstream buildings significantly reduce the wind speed close to stack. This allows the plume to rise relatively high within a short distance from the stack.

Unlike for the case where only downstream buildings were present, the plume reaches above the stagnation height of the downstream buildings, where updrafts help the plume to rise higher. Because of these two complementary effects (lower wind speed and updrafts), plume rises the most when both double storey upstream and downstream buildings are present. It is interesting to note that in the case of the double storey upstream and downstream buildings, plume rise does not change significantly when buoyancy is increased from $SG = 0.98$ to $SG = 0.96$ as the plume rise is dominated by the stack momentum and updrafts induced by the downstream buildings in close vicinity of the DG building. In addition, these buildings increase the ambient turbulence, which dominates the entrainment of ambient air into the plume and causes the plume to rise slower at larger distances from the stack.

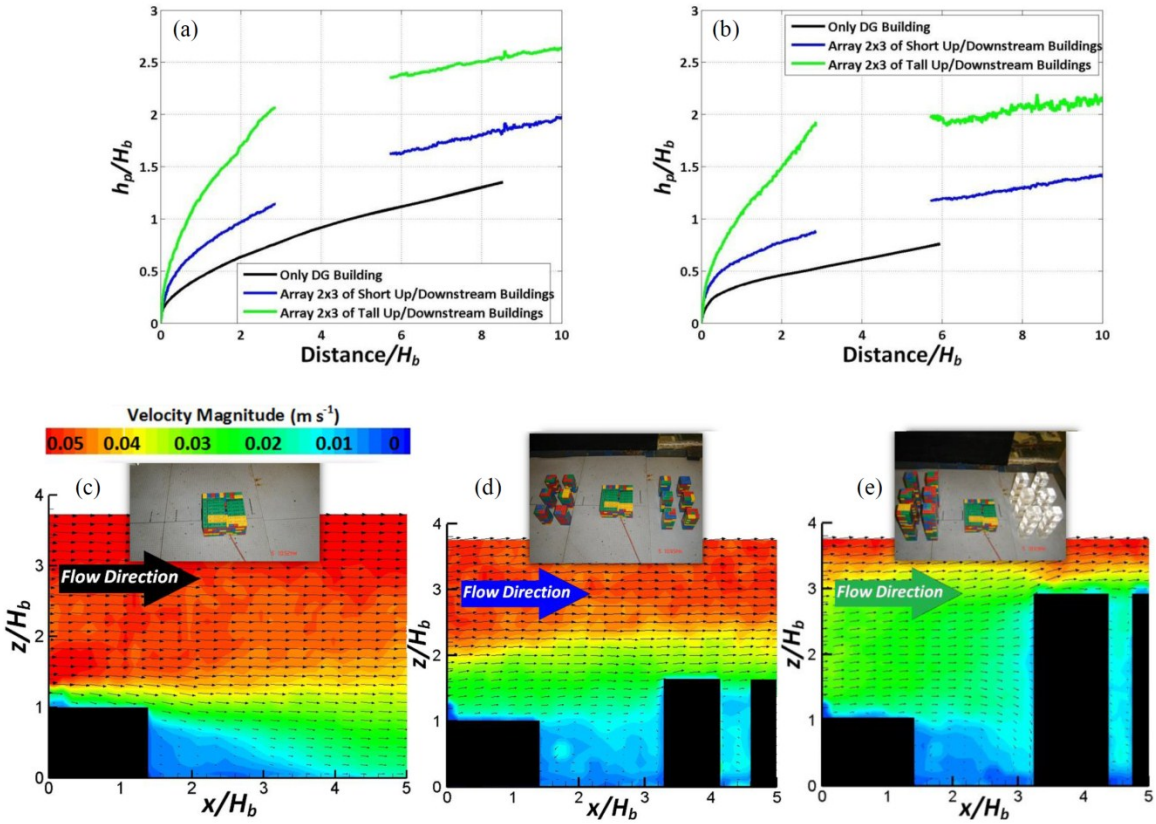

Figure 7-11: Results from measurements of plume rise (h_p) associated with a DG with and without upstream/ downstream buildings for (a) SG = 0.96 and (b) SG = 0.98. Flow measurements associated with (c) only the DG building, (d) the DG building with single storey upstream and downstream buildings, and (e) the DG building with double storey upstream and downstream buildings.

7.4 Comparison with Numerical Plume Rise Model

The results from the plume rise measurements discussed in the previous section have also been compared with the numerical plume rise model which has been explained in Chapter 5.

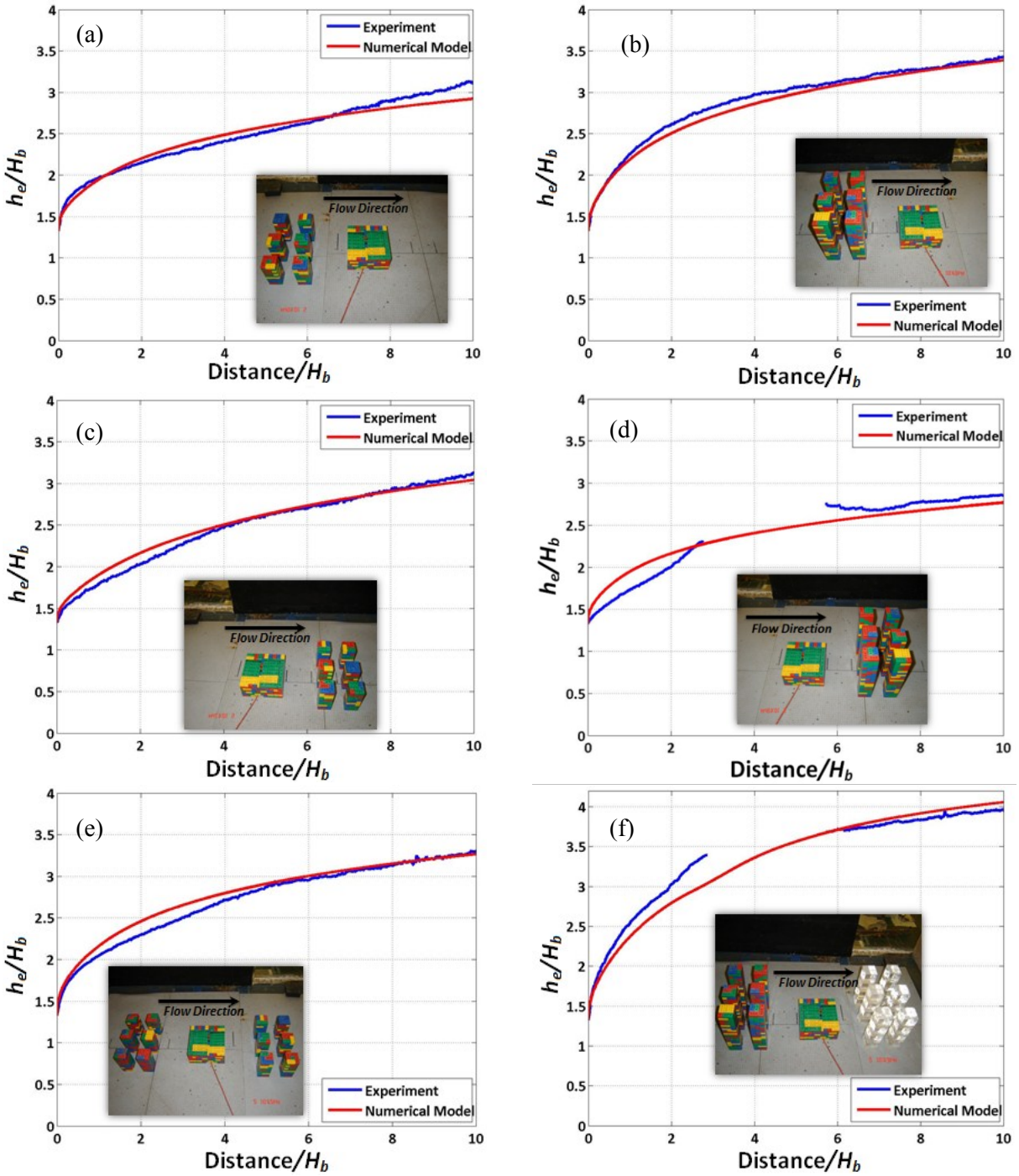

Figure 7-12: Comparison of the plume effective height (h_e) observations (blue ▬) with the numerical plume rise model (red ▬) for plume buoyancy of $SG = 0.96$. Comparisons were done for cases (a) with an upstream single storey buildings array; (b) with an upstream double storey building array; (c) with a downstream single storey building array; (d) with a downstream double storey building array; (e) with upstream and downstream single storey building arrays; and (f) with upstream and downstream double storey building arrays. Distances in horizontal and vertical directions are normalized with respect to the height of the DG model building $H_b = 0.07$m.

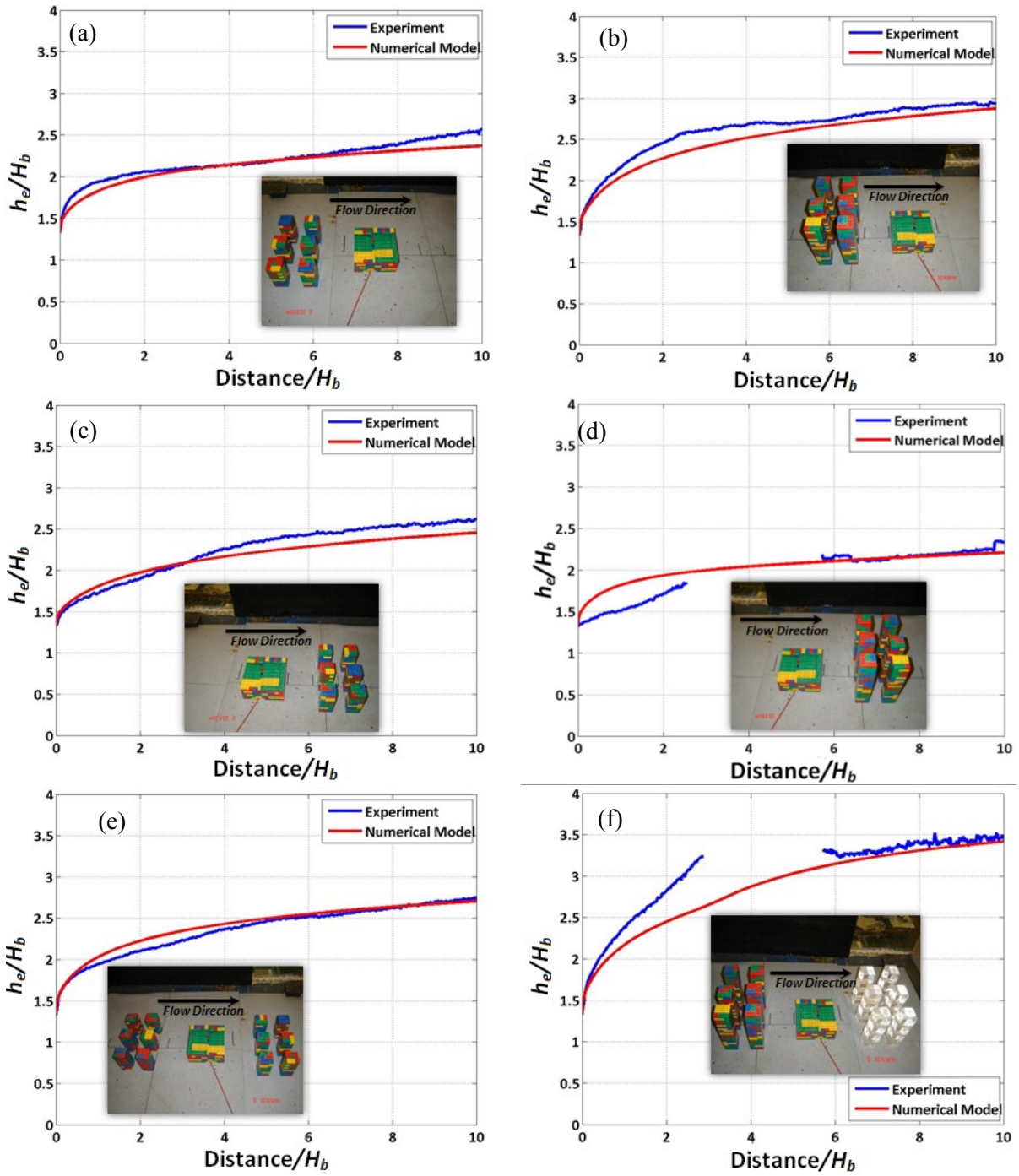

Figure 7-13: Comparison of the plume effective height (h_e) observations (blue ▬) with the numerical plume rise model (red ▬) for plume buoyancy of $SG = 0.98$. Comparisons were done for cases (a) with an upstream single storey buildings array; (b) with an upstream double storey building array; (c) with a downstream single storey building array; (d) with a downstream double storey building array; (e) with upstream and downstream single storey building arrays; and (f) with upstream and downstream double storey building arrays. Distances in horizontal and vertical directions are normalized with respect to the height of the DG model building $H_b = 0.07$m.

In chapter 5 this model is evaluated with the case when only the DG building is present. In this chapter, using the flow measurements shown in the previous section, the plume effective height ($h_e = h_p + H_s$) associated with the DG model under different surrounding building geometries has been predicted and compared with the plume effective height measured in the laboratory (Fig. 7-12 and 7-13).

Fig. 7-12 shows the results where the plume specific gravity is *SG* = 0.96. The results from model comparison under the buoyancy of *SG* = 0.98 are given in Fig. 7-13. It can be seen from Fig. 7-12 that the numerical plume rise model performs reasonably well in predicting the plume rise as it accounts for the flow modifications induced by the surrounding buildings. Same results have also been obtained for plume buoyancy of *SG* = 0.98 (Fig. 7-13). The downside of this model is that it requires measured flow velocities as inputs, which are not usually available. However, even when the full flow field data is not available, linear interpolation of limited available flow data points can be sufficient to construct the required inputs for this model, although the results might not be as accurate as if the detailed flow velocities were available. For the complex flow conditions that include updrafts, downdrafts, regions of increased and decreased flow velocities, one cannot expect a simple plume rise formulation to perform satisfactorily. This plume rise model can be easily implemented in an urban Computational Fluid Dynamical model for accurate calculations of the plume height.

7.5 Summary and Conclusion

DGs are highly efficient as they customarily deploy heat recovery, thus providing both electricity and heating/cooling to nearby facilities. This heat recovery decreases the exhaust temperature which leads to a lower plume rise that can result in higher ground level concentrations. Therefore, realistic modeling of plume rise from DGs plays a major role in determining the ground level concentrations associated with these sources. In this study, laboratory and field measurements have been conducted to investigate the plume rise associated with these low-level buoyant sources under different meteorological conditions and surrounding building geometries.

The first part of this chapter describes the field study conducted in November of 2010, where the plume rise associated with a DG located at Palm Springs, California, USA was measured. Meteorological parameters, such as the mean and turbulent wind speeds, and the sensible heat flux, were measured using sonic anemometers. On November 9, plume rise was measured for a 40 minute period (1400-1440). The measured plume rise was compared with the Briggs (1984) plume rise model. The Briggs plume rise prediction was in good agreement with the observations from the field study, which shows that the relatively sparse and small buildings surrounding the DG do not have significant impact on plume rise. The low wind speeds in Palm Springs allow the plume to rise high relative to the stack avoiding possible trapping by the updrafts/downdrafts caused by DG and surrounding buildings. The higher the plume rise, the smaller effects of the buildings on plume rise can be observed.

Results from the Palm Springs field study are specific to the site and cannot be extrapolated to other settings. In addition, Palm Spring represented a low wind case which might not be necessarily a general case in urban environments. In order to have more generalized understanding of the plume rise affected by buildings, experiments under relatively high wind conditions are required. Since conducting multiple field studies are prohibitively expensive and time consuming, laboratory simulation would be the most efficient way of studying such problem. Accordingly, the second part of this chapter describes the water channel simulations that were conducted to observe the effects of nearby buildings (upstream and downstream) on plume rise under relatively high wind speeds (≈ 3 to 4 m s^{-1}). Plume rise from a DG model was measured under different surrounding geometries and source conditions. Arrays of buildings (2×3) of two different heights (single and double storey) were created and situated upwind and downwind of the DG building (Fig. 7-8). Due to the lack of complexity of these building geometries, they do not necessarily represent a typical urban environment, and the plume rise measurements demonstrate a first order sensitivity of the plume to surrounding buildings rather than urban effect. However, it needs to be noted that due to the relatively high momentums and buoyancies, such plumes tends to rise rapidly close to the source. As a result, they are only affected by the updrafts/downdrafts of the buildings within relatively short distances from the stack and not further. Conversely, we should mention that the upwind meteorology that governs the plume rise near the stack is surely dependent to the urban morphology and is not limited to nearby buildings.

The results from laboratory measurements show that, in most cases, the presence of surrounding buildings increases the plume rise as buildings reduce the wind speed close to the stack and induce updrafts in the region where the plume tends to rise. As mentioned earlier, these results do not declare the urban influence on plume rise; however, they provide very useful data for analyzing the plume rise in urban areas where geometries are significantly complex.

In the third part of this chapter, the results from the plume rise measurements in the laboratory were compared with the results from the numerical plume rise model explained in Chapter 5. Using the flow measurements explained in section 7.3, plume rise associated with each laboratory case study was predicted and compared with the measured plume rise experiments conducted in the water channel. It was observed that this model is able to accurately predict the plume rise as it can account for the effect of surrounding buildings. To apply this plume rise model to the field case, measurements of building caused flows are needed. However, with the significant improvement in CFD models throughout the past decade, the future work will be to combine this plume rise model with a CFD model and evaluate it with field measurements.

8 ESTIMATING THE HEIGHT OF THE NOCTURNAL URBAN BOUNDARY LAYER FOR DISPERSION APPLICATIONS[‡]

8.1 Introduction

Following the Palm Springs field study conducted in July 2008, it has been shown that the highest concentrations occur during the night even though the emissions were highly buoyant (Jing et al., 2011). The ability to explain these concentrations through a model, such as AERMOD (Cimorelli et al., 2005), was limited by the uncertainty in describing the structure of the stable boundary layer (SBL) over an urban area. Thus we initiated the following study in order to address the need for a model to estimate ground-level concentrations associated with emissions from low-level buoyant sources, such as distributed power generators.

The height of the atmospheric boundary layer (ABL) is highly variable with time and ranges from tens of meters at nights to thousands during daytime (Stull 1988). One of the main characteristics of the ABL is the presence of relatively high turbulence near the ground. Pollutants emitted in this layer are dispersed in both horizontal and vertical direction as a result of turbulence and eventually become well mixed throughout this layer. As a result of this mixing, the height of this layer can strongly influence the ground level concentrations especially during nighttime where boundary layer is relatively shallow.

[‡] Reprinted from Atmospheric Environment, Vol 54, Pournazeri S, Venkatram A, Princevac M, Tan S, Schulte N, "Estimating the height of the nocturnal urban boundary layer for dispersion applications", Pages. 611-623, Copyright (2012), with permission from Elsevier.

Characteristics of atmospheric boundary layer are well described in the literature and there are several textbooks (Arya 1988; Stull 1988; Sorbjan 1989; Garratt 1992; Kaimal and Finnigan 1994) which provide detailed description on the mean and turbulent structure of ABL. Here we mention some basic characteristic of ABL related to the scope of this study.

It has been found that ABL becomes stably stratified during nighttime due to the surface cooling (Stull 1988). As a result of this, turbulence is suppressed due to stability damping. In Urban areas, presence of roughness elements can generate high levels of mechanical turbulence which can overcome the damping effect by stability. Due to this turbulence, two different regions can be distinguished within the boundary layer (Seibert et al. 2000). The first region is a layer with periodic and relatively strong turbulence which extends from the ground, and the second region is an outer layer with sporadic and relatively weak turbulence. Since in air pollution dispersion, regions with relatively high turbulence are of interest, the height of the first layer is taken as the boundary layer height (Seibert et al. 1998).

Many studies are also focused on the parameterizing of the nighttime boundary layer height using surface based meteorology (Hanna 1969; Zilitinkevich 1972; Etling and Wippermann 1975; Venkatram 1980; Arya 1981; Mahrt 1981b; Nieuwstadt 1984; Koracin and Berkowicz 1988). Hanna (1969) examined several methods for predicting the boundary layer thickness. It has been shown that models by Lettau (1962) and Blackadar (1962) which uses the surface observations, works only for very near neutral conditions and have extremely poor performance under highly stable conditions. It has

also been shown that the formulation of boundary layer height by Laikhtman (1961) can approximate the observations very well. However, in order to perform this model, meteorological information along the boundary layer is needed. Zilitinkevich (1972) has proposed a diagnostic formulation for predicting the boundary layer height using similarity consideration and scaling arguments. Venkatram (1980) has empirically shown that in the absence of any information regarding surface heat flux, boundary layer height can be predicted as $h = 2300 u_*^{3/2}$. Following the Taylor (1931) classical theory, assuming that the turbulence production vanishes if the bulk/gradient Richardson number (*Ri*) exceed a critical value of Ri_{cr}, Mahrt (1981b), Holstag et al. (1990) and Nieuwstadt and Tennekes (1981) proposed several diagnostic equation for predicting the equilibrium nocturnal boundary layer height.

Due to the unsteady behavior of the nocturnal boundary layer (Zilitinkevich and Baklanov 2002), high accuracy cannot be expected from the above mentioned diagnostic equations. Therefore, assuming that actual boundary layer height tends to adjust to the equilibrium boundary layer height (The equilibrium height h_e is often parameterized using one of the diagnostic equations given above) with a time response of τ_{SBL}, several prognostic equations were proposed (Deardorff 1972; Zilitinkevich et al., 2002). A review paper by Seibert et al. (2000) indicates that although these models show some skills in explaining selected data sets, they lack general applicability. This situation is more severe for the nocturnal boundary layer over an urban area, where heat fluxes can be positive while the upwind rural areas are stable. A report by Baklanov et al. (2006) concludes that one-dimensional models developed for horizontally homogeneous

conditions have limited applicability to urban conditions. In principle, two or three dimensional boundary layer models should be able to provide better estimates of boundary layer heights. However, evaluation against observations has not yet confirmed this expectation.

There is a need for a method to estimate the height of the SBL for dispersion applications in urban areas. All of the studies to date indicate that diagnostic equations that ignore the history of the boundary layer provide poor estimates of the boundary layer height. In this study, we focus on one-dimensional prognostic models for the height of the SBL. As pointed out by Siebert et al. (2000), there is a paucity of the time-resolved data required to test these models. Thus, it was necessary to conduct a field study to provide the required information. Because this field study covers only two nights, we supplement our data with the relatively small data sets that are currently available.

Section 8.2 describes the field study, section 8.3 presents analyses of the observations, section 8.4 describes the supplementary field data from VTMX, Milan and Wangara experiments, section 8.5 discusses evaluation of diagnostic and prognostic models that are employed to describe data, and section 8.6 describes the resulting conclusions.

8.2 Field Study

The field study was conducted in Riverside, California, in March 2011 in the grassy area next to the parking lot of the College of Engineering's Center for Environmental Research and Technology (CE-CERT). This site is located in a low-density urban area

surrounded by sparse trees, bushes, and one-storey buildings that do not vary much in height. The degree of urbanization of this area can be characterized in terms of the plan area fraction, λ_p, which is the ratio of the plan area of the roughness elements to the total lot area, and the frontal area fraction, λ_f, which is the ratio of the frontal area of roughness elements to the total lot area. Table 8-1 compares approximate values of the average building height (h_b), plan area fraction, λ_p, and frontal area fraction, λ_f associated with the Riverside urban area with those from a high-rise settlement urban area such as Los Angeles downtown (near 6th St./Grand Ave. intersection), and a low-density settlement such as Anaheim (near Harbor Blvd./Lampson Ave. intersection) obtained from Boarnet et al. (2009).

Table 8-1: Morphological parameters (λ_p, λ_f) and average building heights (h_b) associated with three different urban areas.

City	*Type*	h_b (m)	λ_p	λ_f
Riverside	low-rise settlement	4	0.3	0.1
Los Angeles	high-rise settlement	42	0.36	0.47
Anaheim	low-density settlement	4	0.26	0.12

Meteorological measurements were made over the period starting at noon on March 9, 2011 and extending to noon, March 11, 2011 under clear skies and low winds. Surface micrometeorological variables were measured using a sonic anemometer placed at a height of 3.4 m above the ground. The sonic was located at a distance of about 25m towards the north of a building ($L \times W \times H$= 62m×20m×5m). A tethersonde was used to measure vertical profiles of temperature, wind speed, and humidity up to height of 500 m. The locations of the instrumentation are shown in Fig. 8-1.

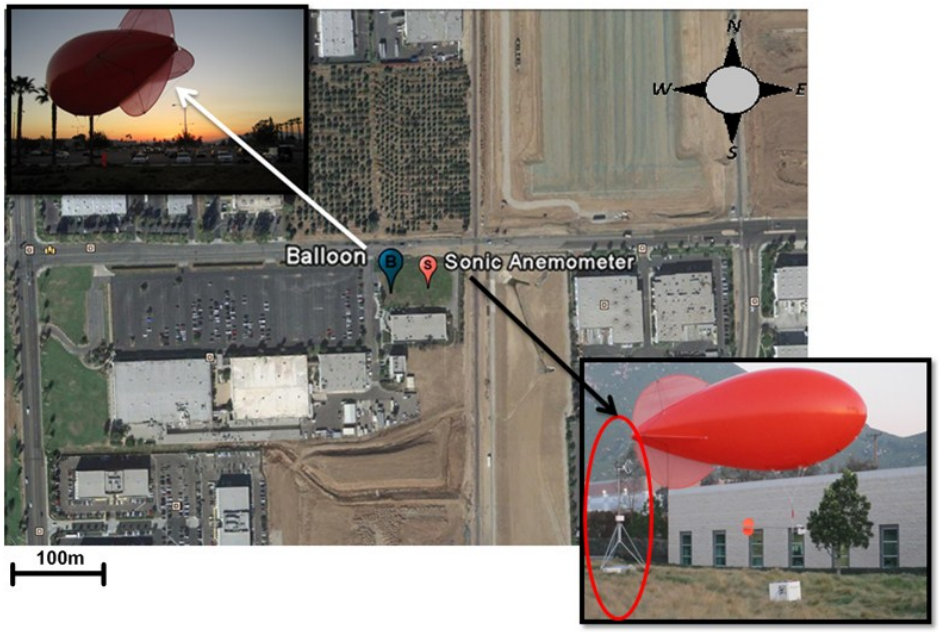

Figure 8-1: Location of the meteorological station (red pin) and tethered balloon (blue pin) at College of Engineering - Center for Environmental Research and Technology (CE-CERT), Riverside, CA (aerial picture is produced using Google Earth).

8.2.1 Surface Micrometeorology

Three components of wind speed and virtual temperature were measured using a Campbell Scientific CSAT3 sonic anemometer located at 3.4 m above the ground, at the sampling rate of 10 Hz. These measurements were processed to obtain mean and turbulent wind speeds and surface heat fluxes averaged over periods of 15 minutes. Fig. 8-2 shows the results from these measurements.

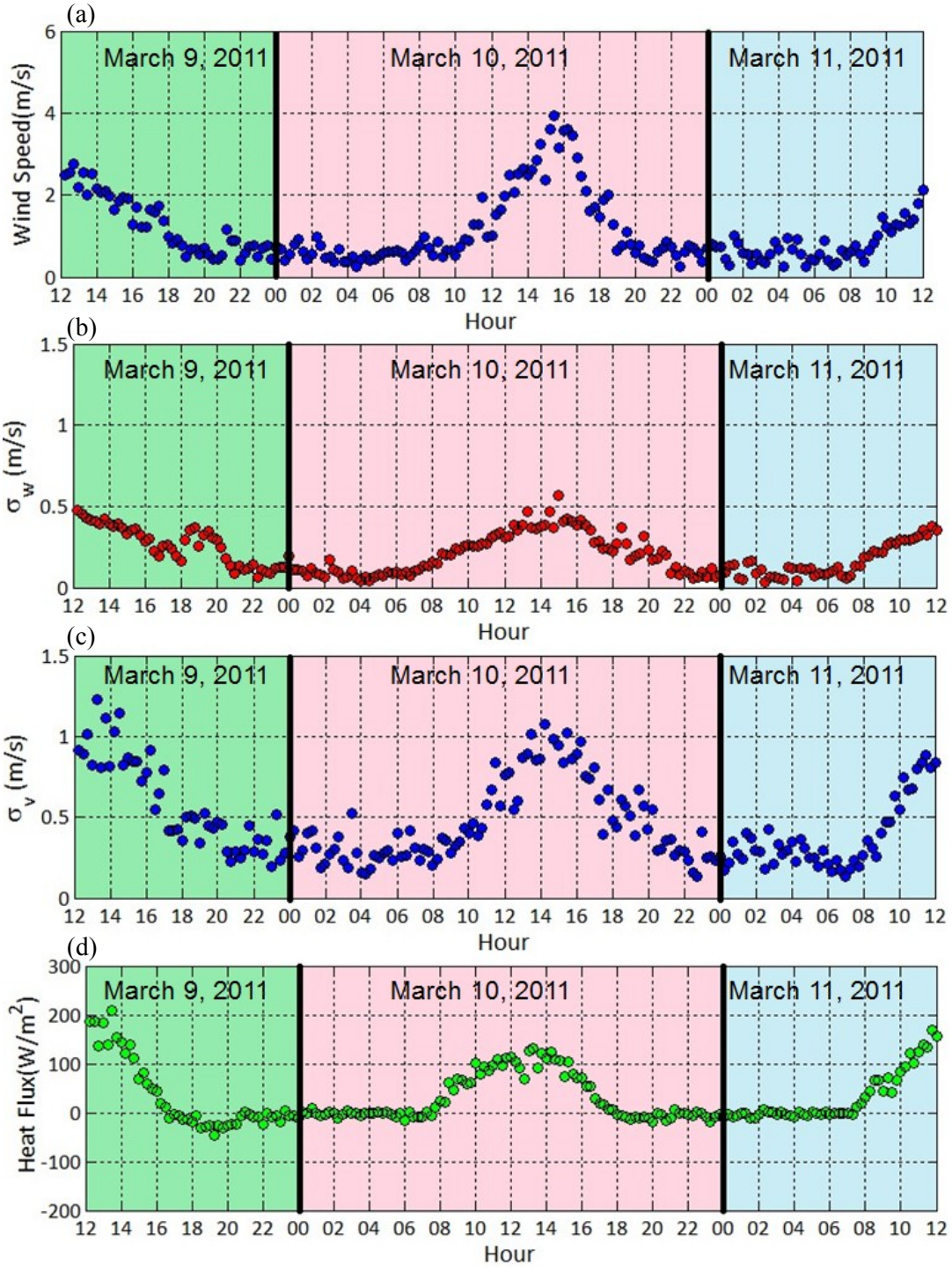

Figure 8-2: Measurements of 15min averaged (a) wind speed U (ms^{-1}); (b) vertical turbulent velocity σ_w (ms^{-1}); (c) lateral turbulent velocity σ_v (ms^{-1}); and (d) surface sensible heat flux $\rho C_p \overline{w'T'}$ (Wm^{-2}).

The near surface wind speeds are less than 1 ms^{-1} during most of the nighttime. Vertical turbulent velocities are approximately 0.15 ms^{-1} during nighttime and increase to a maximum of 0.5 ms^{-1} during daytime. Lateral turbulent velocities are less than 0.3 ms^{-1} during nighttime with the maximum of about 1 ms^{-1} during the daytime. This translates into turbulent intensities of about 20% in the vertical direction and about 50% in the horizontal direction. The near surface sensible heat flux ($\rho C_p \overline{w' T_v'}$ where ρ is the air density, C_p is the specific heat of air, and $\overline{w' T_v'}$ is the correlation of fluctuations of vertical velocity w and virtual temperature T_v) reaches a maximum of about 200 Wm^{-2} at noon and approaches to zero during nighttime.

8.2.2 Boundary Layer Profiling

Vertical profiles of temperature, relative humidity, and wind speed along the Riverside urban boundary layer were obtained up to 500 m above ground level using a Vaisala tethersonde system. The measurements were made during three nights. Data from the first night were used to check out the instrumentation. The main field experiments were conducted on two consecutive nights (March 9 – 11) starting at 18:00 PST to 6:00 PST of the following morning. Data from these nights were used in the modeling described in sections 8.5.3 and 8.5.4. The tethered balloon was raised periodically up to a height of 500 m and lowered to the ground within 20 min. This resulted in two profiles of boundary layer parameters per hour.

Selected results from these measurements (Fig. 8-3) show that the urban boundary layer over Riverside, California, was stably stratified throughout the three nights of the

field study. The absolute temperature (Fig. 8-3a, b) gradient was positive near the surface and become negative far from the ground. The potential temperature gradient (Fig. 8-3c, d) was about 8° C/100 m near the ground and approached zero in the upper part of the boundary layer. The potential temperature of the upper part of the boundary layer remained almost constant (~25°C) while the surface temperature decreased with time. Therefore, assuming a well-mixed temperature profile at the time of sunset, the temperature difference over the depth of the boundary layer can be estimated from the variation of the near surface temperature after sunset. This approach can be used to estimate the temperature gradient across the boundary layer, which is a critical input to dispersion models, such as AERMOD.

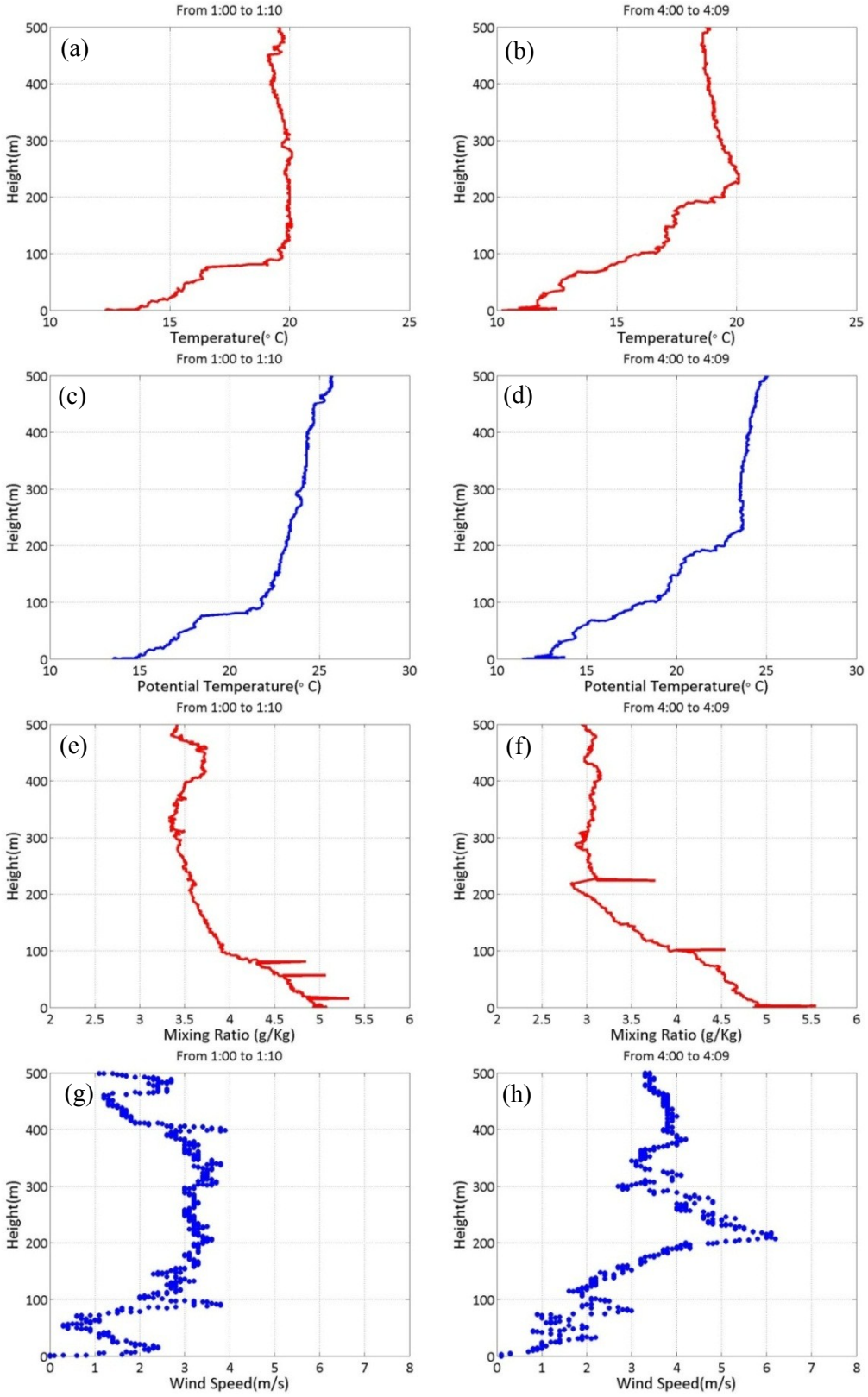

Figure 8-3: Vertical profiles for (a, b) temperature (˚C); (c, d) potential temperature (˚C); (e, f) mixing ratio (g/kg); and (g, h) wind speed (ms^{-1}) at 1:00 and 4:00 PST on March 10, 2011.

In describing the vertical profiles, we tentatively identify the top of the stable boundary layer as the height at which the absolute temperature gradient becomes negative. We will provide a more precise definition later.

Figs. 3e, f show that the mixing ratio decreases with height from the ground and the gradient approaches zero at the top of the boundary layer. The vertical profile of wind speed (Fig. 8-3g, h) shows the presence of wind shear across the boundary layer, in which the wind speed reaches a maximum of 6 ms^{-1} at the boundary layer height (Fig. 8-3h).There is a suggestion of a low level jet at the top of the boundary layer.

In the absence of turbulence measurements as a function of height, the height of the nocturnal boundary layer has to be inferred from profiles of mean temperature and wind speed. There is little consensus on the method for this indirect estimation as evidenced in many different definitions of the boundary layer height found in literature. Seibert et al. (1998) summarized the most popular algorithms used to determinate the nocturnal boundary layer height from vertical sounding data.

We examined the usefulness of some of the methods. Cuxart et al. (2006), Garratt (1982, 1992), and Mahrt et al. (1982) suggest using the value of the gradient Richardson number to estimate the height of the stable boundary layer in mesoscale numerical models. When applied to our field data, this approach left too much room for interpretation to be useful.

In this study, we found it convenient to use the definition proposed by Yu (1978), which assumes that the height of the nocturnal boundary layer (h) is the height at which

$\partial T / \partial z = 0$. Fig. 8-4 illustrates this method, which, in most cases, allowed an unambiguous identification of the boundary layer height. Our assumption that this height represents the vertical extent of mixing is supported by the observation that this height often coincided with the height at which the water vapor mixing ratio gradient approached zero and the velocity gradient changed sign.

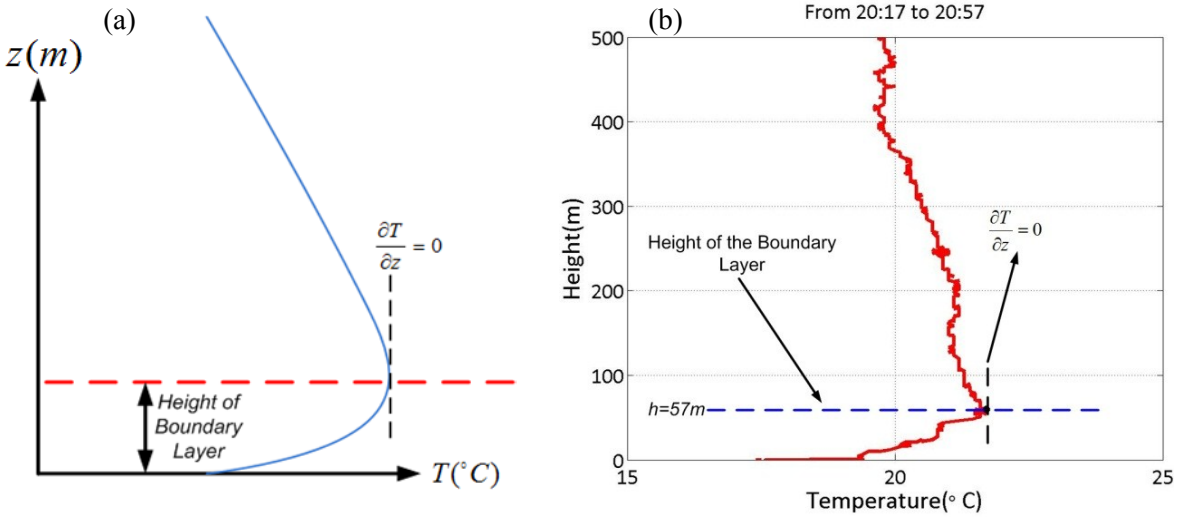

Figure 8-4: (a) Schematic of the method used for determination of nocturnal boundary layer height, and (b) boundary layer height determination on temperature profile measured during 20:17- 20:57 PST on March 9.

Boundary layer heights for the 56 profiles from the vertical sounding data were obtained based on this definition. We also estimated the boundary layer height using an approach suggested by Melgarejo and Deardorff (1974). They defined *h* as the height to which significant cooling can be recognized, which is determined by superimposing vertical profiles of potential temperature at successive time intervals. Selected results from this comparison are shown in Fig. 8-5. As can be seen, for most of the cases, significant cooling (the area between the two profiles) occurs just below the height at

which $\partial T / \partial z$ of the second profile approaches zero. Because the two different definitions yield similar results, we used the more convenient method based on the criterion, $\partial T / \partial z = 0$, to estimate the boundary layer heights for the 56 profiles from the vertical sounding data. Table 8-2 presents the relevant boundary layer parameters associated with these profiles: boundary layer height (h), wind velocity and potential temperature difference across the boundary layer (ΔU, $\Delta \theta$).

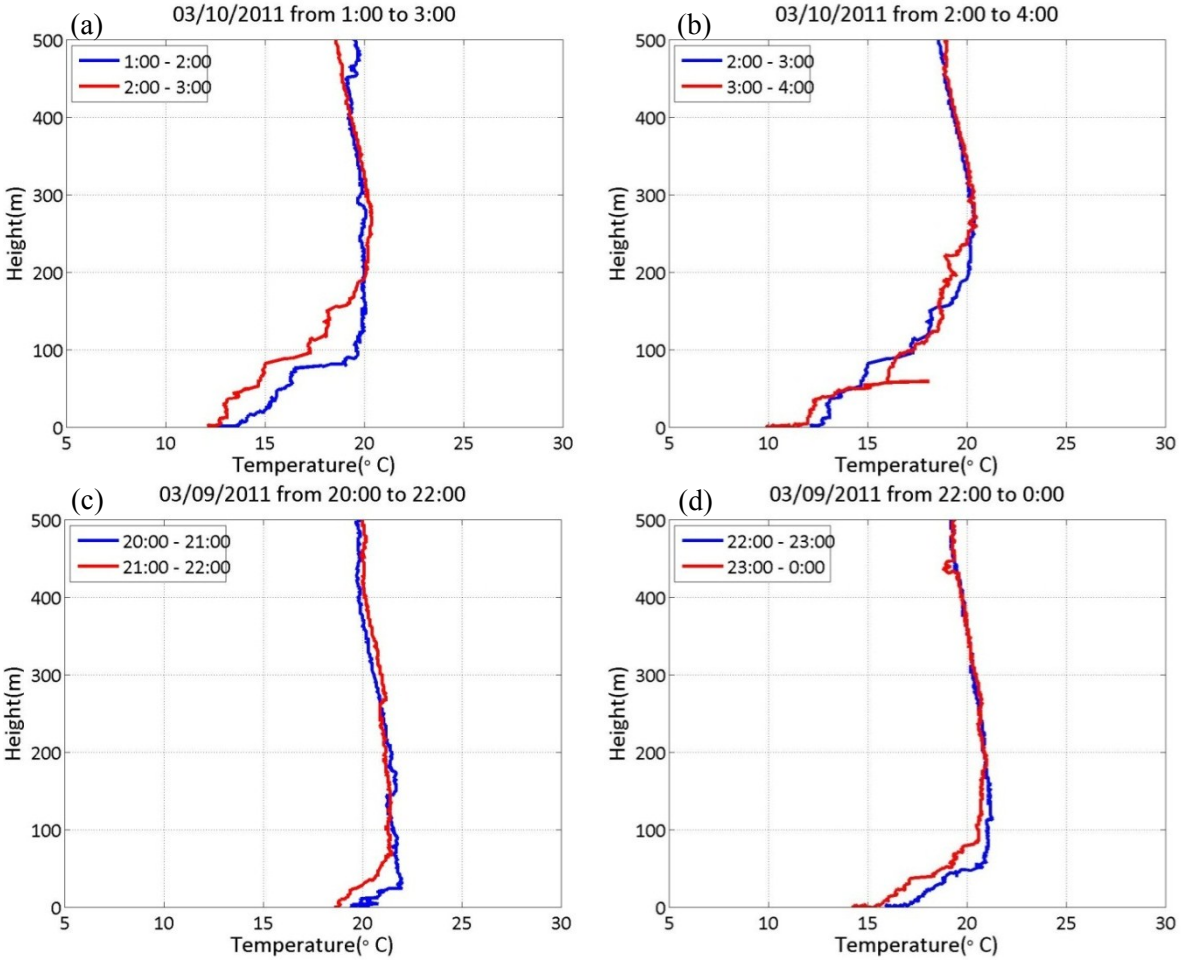

Figure 8-5: Successive vertical profiles of temperature (˚C) (a) from 20:00 to 22:00; (b) from 22:00 to 00:00; (c) from 1:00 to 3:00; and (d) from 2:00 to 4:00.

Table 8-2: Meteorological and boundary layer parameters from 56 vertical sounding data (Different color shading corresponds to measurements at different nights)

Profile Number	Day of Year	Boundary Layer Height h(m)	u_* (ms^{-1})	U (ms^{-1})	Heat Flux (Wm^{-2})	L_{M-O} (m)	$\Delta\theta$ (˚C)	ΔU (ms^{-1})	T_0 (K)
1*	60.793	33	0.14	0.54	-11.25	16.22	1.60	1.10	287.7
2*	60.803	26	0.09	0.56	-9.10	6.38	1.80	1.50	287.2
3*	60.814	15	0.12	0.59	0.47	-269.69	1.90	1.40	287.2
4*	60.823	36	0.10	0.74	3.76	-22.05	1.90	2.80	286.8
5*	60.875	25	0.26	0.75	-26.17	50.59	2.00	1.10	285.8
6*	60.887	39	0.23	0.84	-20.00	44.79	2.90	3.20	284.5
7*	60.917	24	0.46	1.01	-91.14	75.37	0.80	3.90	285.1
8*	60.926	24	0.47	1.19	-90.82	85.39	1.40	2.70	284.2
9	68.761	26	0.22	0.81	-6.49	125.94	0.70	2.20	297.6
10	68.772	22	0.27	0.93	-32.38	47.30	1.77	2.80	295.5
11	68.785	30	0.16	0.50	-25.09	13.24	1.43	2.70	296.0
12	68.799	27	0.25	0.67	-45.08	26.88	1.60	2.10	295.1
13	68.833	37	0.21	0.70	-25.20	26.76	2.90	4.40	293.6
14	68.845	57	0.15	0.56	-23.60	10.82	4.60	1.10	291.6
15	68.876	73	0.09	0.53	1.04	-56.34	3.60	1.80	292.7
16	68.882	74	0.11	1.16	-3.19	33.68	4.43	2.30	291.9
17	68.917	66	0.13	0.41	-22.89	6.90	5.67	2.40	290.1
18	68.926	60	0.01	0.60	-1.59	0.11	7.63	1.60	288.2
19	68.960	84	0.12	0.50	-19.18	6.07	7.07	1.90	288.4
20	68.976	88	0.04	0.70	4.37	-1.12	5.93	3.30	288.2
21	69.001	109	0.06	0.73	-10.85	1.31	6.00	3.20	288.5
22	69.007	113	0.10	0.69	2.02	-34.10	6.67	3.00	286.9
23	69.042	76	0.11	0.79	-2.30	46.07	5.87	2.40	286.5
24	69.046	96	0.08	0.93	-6.99	4.61	6.77	2.30	286.9

Profile Number	Day of Year	Boundary Layer Height h(m)	u_* (ms^{-1})	U (ms^{-1})	Heat Flux (Wm^{-2})	L_{M-O} (m)	$\Delta\theta$ (˚C)	ΔU (ms^{-1})	T_0 (K)
25	69.083	200	0.03	0.55	-0.34	4.29	10.03	4.10	286.3
26	69.091	218	0.09	0.99	-10.70	4.78	10.30	2.30	285.2
27	69.128	231	0.05	0.49	-1.60	7.37	12.10	4.60	284.1
28	69.135	258	0.07	0.38	-1.07	20.07	12.00	5.10	285.2
29	69.167	234	0.02	0.39	-0.30	1.38	12.27	6.10	284.4
30	69.173	204	0.07	0.51	-0.66	34.91	11.27	4.80	285.0
31	69.208	212	0.02	0.54	1.35	-0.24	11.30	4.30	284.7
32	69.214	215	0.06	0.42	-4.21	4.24	11.30	3.80	284.8
33	69.750	11	0.13	1.46	-2.85	62.46	0.60	0.70	296.0
34	69.758	5	0.17	1.89	-5.33	67.29	0.10	0.60	295.6
35	69.792	12	0.10	0.64	-8.65	8.73	0.40	0.90	295.1
36	69.799	24	0.18	0.77	-12.37	34.02	1.00	2.70	293.1
37	69.833	38	0.18	0.59	-18.71	23.35	1.73	2.40	292.4
38	69.839	45	0.14	0.76	-0.41	482.91	2.93	3.70	291.0
39	69.875	39	0.16	0.38	-11.06	27.86	2.93	2.80	290.8
40	69.881	31	0.10	0.61	5.45	-14.77	3.60	0.80	290.0
41	69.917	43	0.12	0.73	-2.53	53.02	4.40	1.50	289.2
42	69.923	81	0.07	0.52	-6.35	3.74	3.97	1.10	289.3
43	69.958	50	0.11	0.77	-9.25	10.74	5.57	1.00	286.9
44	69.965	93	0.10	0.71	-18.25	4.46	5.60	1.60	286.9
45	70.006	98	0.10	0.70	-7.87	10.71	3.90	3.10	287.9
46	70.013	81	0.07	0.79	-3.90	7.62	5.17	2.30	286.9
47	70.043	88	0.06	0.44	-1.32	10.61	5.30	2.30	286.8
48	70.050	119	0.03	0.30	-1.12	1.04	5.53	1.90	286.4
49	70.084	110	0.05	0.60	-3.10	2.94	5.20	2.10	286.4
50	70.091	100	0.10	0.54	5.37	-12.74	5.23	2.50	285.4

Profile Number	Day of Year	Boundary Layer Height h(m)	u_* (ms^{-1})	U (ms^{-1})	Heat Flux (Wm^{-2})	L_{M-O} (m)	$\Delta\theta$ (˚C)	ΔU (ms^{-1})	T_0 (K)
51	70.126	93	0.05	0.42	-2.92	2.57	5.17	3.10	285.0
52	70.132	99	0.02	0.35	1.82	-0.50	5.60	1.60	284.8
53	70.167	171	0.11	0.68	-7.75	13.31	6.87	2.80	284.7
54	70.173	113	0.04	0.27	1.35	-2.85	3.63	0.90	284.8
55	70.208	261	0.11	0.92	1.42	-62.95	8.77	3.50	285.1
56	70.213	233	0.06	0.54	-2.00	8.30	8.67	1.80	284.4

** Data from a test field study conducted in March 1, 2011, at the same location from 19:00-22:00 PST.*

Table 8-2 also presents surface based (*z=3.4m*) meteorological parameters such as mean wind speed (U), friction velocity (u_*), ground sensible heat flux, surface temperature (T_0), and Monin-Obukhov length (L_{M-O}) averaged over 15 min prior to each profiling time. The time corresponding to each profile is shown in terms of Day of Year (DOY), where DOY of 68 represents March 9 and DOY of 70 represents March 11.

The data show that the nocturnal boundary layer height (top of the surface inversion) ranges from ~10 m after sunset (18:00 PST) to ~260 m before sunrise (6:00 PST). Note that the surface wind speed is less than 1 ms^{-1} during most of the soundings. The surface heat flux is negative most of the time and its magnitude varies from approximately -30 Wm^{-2} after sunset (18:00 PST) up to approximately -1 Wm^{-2} before sunrise (6:00 PST).

8.3 Analysis of Observations

Fig. 8-6 shows the variation with time from sunset of some broad features of the nocturnal boundary layer. Fig. 8-6a indicates that boundary layer height (*h*) varies almost linearly with time ($h \propto t^{0.9}$) from sunset. Fig. 8-6b shows that the temperature difference across the boundary layer increases with time ($\Delta\theta \propto t^{0.8}$); the near surface temperature decreases, while the temperature at the top of the boundary layer remains almost constant.

Because both temperature difference across the boundary layer ($\Delta\theta$) and height of the boundary layer (*h*) increase with time, the mean potential temperature gradient ($\Delta\theta / h$) shows little variation and has a mean value of about 0.062 Km^{-1} (Fig. 8-6c). Fig.

8-6d reveals that the velocity difference across the boundary layer (ΔU) does not have any trend with time from sunset and it ranges from 1 to 5 m s^{-1}.

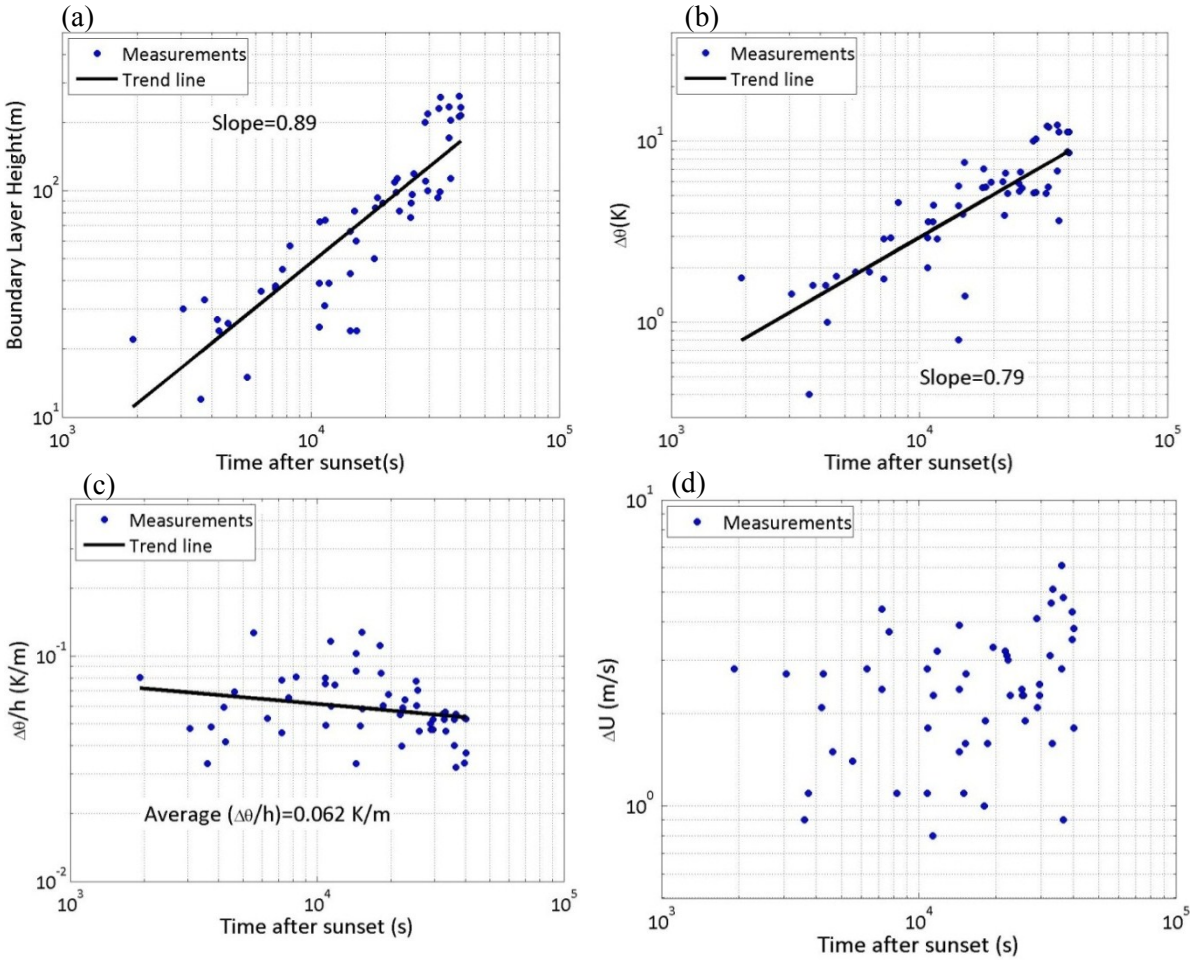

Figure 8-6: Nighttime boundary layer parameters vs. time for (a) boundary layer height (h); (b) temperature difference across boundary layer ($\Delta\theta$); (c) mean potential temperature gradient across boundary layer ($\Delta\theta/h$); and (d) velocity difference across boundary layer (ΔU) (data from all nights are included).

Yamada (1979) and Stull (1983) have developed prognostic models for the height of the nighttime boundary layer by equating the energy loss in the boundary layer to the integrated downward surface heat flux. We test the usefulness of this approach by comparing the cooling of the boundary layer,

$$Boundary\ Layer\ Heat\ Loss = \rho C_p \int_0^{h(t)} [\theta(z,t) - \theta(z,t_0)] dz, \quad (8\text{-}1)$$

where t_0 is the time of sunset, to the integrated downward surface heat flux at the surface,

$$Integrated\ \ downward\ surface\ heat\ flux = \rho C_p \int_{t_0}^{t} \overline{w'T'} dt\,. \quad (8\text{-}2)$$

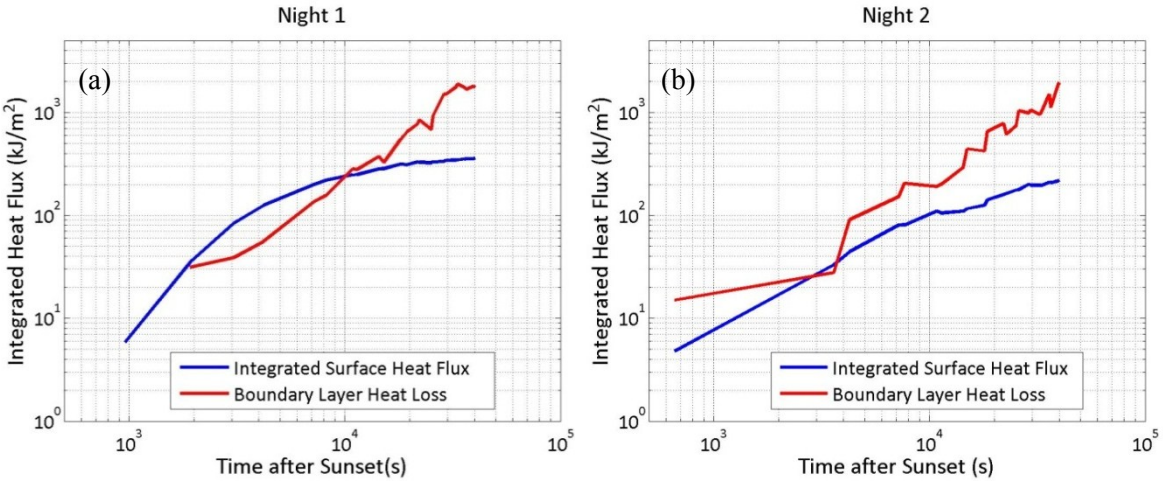

Figure 8-7: Comparison of cooling of the boundary layer with integrated surface heat flux for (a) Night 1 on March 09, 2011 and (b) Night 2 on March 10, 2011.

Fig. 8-7 indicates that there are substantial differences between the boundary layer cooling and the integrated surface heat flux, which cannot be explained in terms of radiative cooling or heating. Therefore, an estimate of the boundary layer height based on equality between these two energy terms cannot be justified in this case. For this reason, we focus on methods that assume that the boundary layer height corresponds to the upward diffusion of shear-generated turbulence at the surface. The most well-known methods are based on that proposed by Zilitinkevich (1972). We will evaluate some of them in section 8.5.

8.4 Supplementary Field Data

We supplemented the Riverside data with data sets from three field studies. The Milan data corresponds to urban conditions, the VTMX data set was obtained in a suburban area, while the Wangara data set corresponds to rural conditions. The rationale for choosing the Wangara data set is to ensure that if model works in an urban setting, it should also do so in the simpler rural setting of Wangara. These field studies are briefly described next.

8.4.1 VTMX Study

The Vertical Transport and Mixing (VTMX) field study was conducted during October 2000 in the Salt Lake Valley, Utah. The main goal of this field study was to investigate the transport and mixing processes under (nocturnal) stable conditions. The site was equipped with a variety of meteorological instruments such as sonic anemometers and tethersondes in order to measure three dimensional wind speed as well as vertical temperature profile. More details of the field campaign can be found in Doran et al. (2002). Data used in this study were collected by environmental fluid dynamic group in Arizona State University. These data covered six different nights; however, data from first three nights were insufficient to be used in our analysis and only data from last three nights (October 14, 16 and 17) were used.

8.4.2 Milan Experiment

The Milan experiment (Lena and Desiato, 1999) took place in the area of Milan, Italy in the northwest part of Po valley from May to August 1996. Profiles of wind speed

and temperature were measured using Doppler SODAR and Radio Acoustic Sounding System (RASS). The measurement site was located at a distance of about 8 km from the center of Milan, which according to Lena and Desiato (1999) is a typical urban environment. In this study, boundary layer heights were determined through the 1) height of the low-level jets (h_u); 2) height of the surface inversion ($h_{\theta g}$); 3) height of the elevated inversion ($h_{\theta e}$); and 4) depth of the adiabatic layer ($h_{\theta a}$). Lena and Desiato (1999) compare the values of mixing heights derived from the wind (h_u) and temperature profiles (h_θ) with predictions from 10 different mixing height algorithms. Results showed that the h_u values provide the best correlation with model estimates. Assuming that the models are based on data that reflect the vertical extent of mixing, they conclude that the h_u values are good indicators of boundary layer height. They also find that the heights of the surface based inversion layer ($h_{\theta g}$) are close to that of h_u values. This supports our use of the height of the surface based inversion as a measure of boundary height in our analysis of the Riverside data.

8.4.3 Wangara Data

The Wangara boundary layer experiment was conducted in July and August 1967 at Hay, New South Wales, Australia (Clarke et al., 1971) to describe characteristics of the atmospheric boundary layer (Hess et al., 1981). During this experiment, 5000 balloon ascents were used to obtain temperature profiles up to 2000m from the surface every 3 hours (nighttime data are available for 18:00, 21:00, 00:00, 3:00, 6:00) with the resolution of 50m in the first 1000m and 100m after that. Horizontal wind speed was

also measured at three different heights of 2, 4 and 8m from the ground. Surface meteorological data from this experiment were analyzed by Melgarejo and Deardorff (1974) in order to obtain the surface friction velocities (u_*) and Monin-Obukhov lengths ($L_{M\text{-}O}$). The data analysis by Melgarejo and Deardorff was limited to cases where no frontal systems existed within 500 km from the town of Hay. These data are available in Yu (1978).

8.5 Model Evaluation

We focus on prognostic models that are based on surface variables, and thus can provide inputs to the current generation of dispersion models, such as AERMOD. The boundary layer height in most of these models is controlled by the surface friction velocity, u_*. We apply these models assuming that the appropriate friction velocity corresponds to the inertial sublayer (ISL) which lies above the roughness sublayer (RSL). The ISL refers to the layer that is about 1 to 3 times the average building height where the flow can be considered to be in equilibrium with the underlying rough surface. The RSL lies below the ISL, and corresponds to the lowest layer that is governed by the spatially averaged properties of the urban surface. Fluxes of momentum, energy, and moisture vary with height in the RSL. The shear stress (and local friction velocity) reach a maximum at the bottom of the ISL. Rotach (1993) proposes an empirical formula for the variation of the friction velocity with height in the RSL. In principle, this formula can be used to relate a friction velocity measured within the RSL to its maximum in the ISL. Because such measurements are not made routinely, it is useful to examine the possibility

of estimating the friction velocity in the RSL from routine surface meteorological measurements.

8.5.1 Estimating the Friction Velocity (u_*)

We compare the observed values of friction velocity with estimates obtained by fitting the MOST wind speed profile (Businger, 1973) to the measured mean wind speed (U) and Monin-Obukhov length (L_{M-O}),

$$u_* = \kappa U_{ref}\left[\ln\left(\frac{z_{ref}-d_h}{z_0}\right)-\psi\left(\frac{z_{ref}-d_h}{L_{M-O}}\right)\right]^{-1} \tag{8-3}$$

where z_0 is aerodynamic roughness length, κ is von Karman constant, U_{ref} is the mean wind speed measured at reference height (z_{ref}), d_h is the zero plane displacement which is taken as $d_h = 5z_0$ (Britter and Hanna, 2003) and

$$\psi\left(\frac{z}{L_{M-O}}\right) = -4.7\frac{z}{L_{M-O}}. \tag{8-4}$$

Because the surface heat flux is not measured routinely, it is useful to estimate the surface friction velocity using an approach (Venkatram, 1980; Qian and Venkatram, 2011) that assumes that the temperature scale, $\theta_* = -\overline{w'T_v'}/u_*$, varies little with time and has a value of about 0.08 K, which might be site specific. The variation of θ_* and u_* shown in Fig. 8-8 indicates that θ_* varies about a mean value of about 0.053 K while u_* shows a decreasing trend with time throughout the night. We used $\theta_* = 0.053K$ in our

analysis to be consistent with the measurements, although a value of 0.08 K yields very similar results.

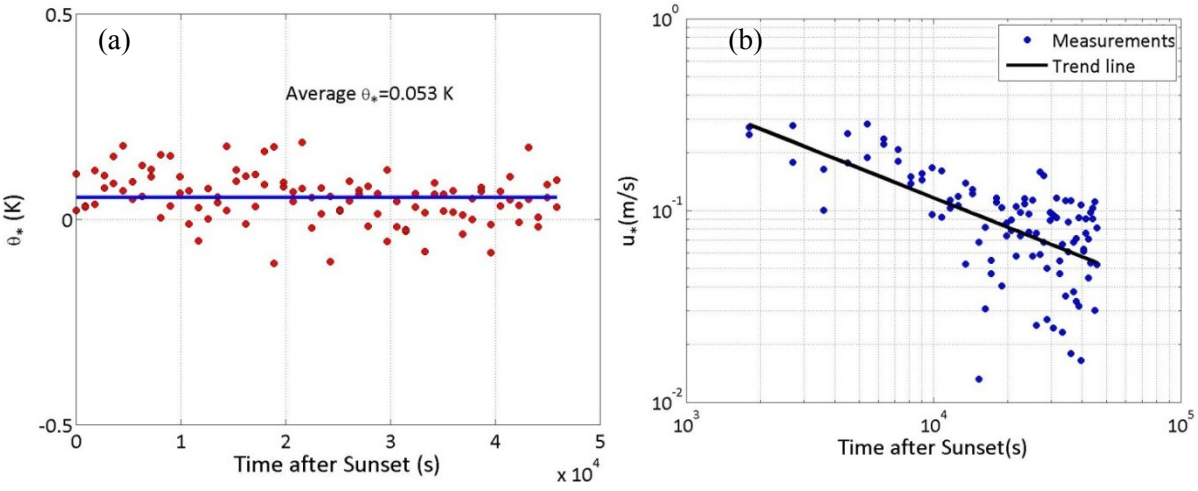

Figure 8-8: Variation of (a) surface layer temperature scale ($\theta_* = -\overline{w'T_v'}/u_*$) and (b) friction velocity (u_*) with time (15min averaged data from all nights are used).

The performance of the SBL models evaluated in this study are measured through the statistics, m_g and s_g, which are the geometric mean and standard deviation of the ratios of the observed to estimated u_*, respectively (Venkatram, 2008). Deviation of m_g from unity indicates whether the model is overpredicting or underpredicting and expresses the bias of the model estimates. The standard deviation, s_g, measures the spread of the observations about the model estimate, and s_g^2 is approximately the 95% confidence interval for the ratio of observed to predicted values.

Performance statistics m_g and s_g are defined as,

$$m_g = \exp\left(\left\langle \varepsilon_m \right\rangle\right) \tag{8-5}$$

$$s_g = \exp\left(std\left[\varepsilon_m\right]\right) \tag{8-6}$$

where $\langle\ \rangle$ represents the mean, std is the standard deviation and ε_m can be expressed as

$$\varepsilon_m = \ln\left(u_{*o}\right) - \ln\left(u_{*p}\right) \tag{8-7}$$

where subscripts p and o represents the predicted and observed values, respectively.

We derive our estimate of roughness length by treating z_0 as a parameter that provides the best fit between the observed u_* and that estimated from the mean wind speed with MOST. We find that z_0 = 0.3 m yields the results shown in Fig. 8-9a, which indicates that the values of u_* based on MOST and measured heat fluxes are within a factor of two of the observed values. The values of m_g and s_g, indicate that the bias is about 13% and the 95% confidence interval for the ratio of predicted to observed u_* is about 2.75.

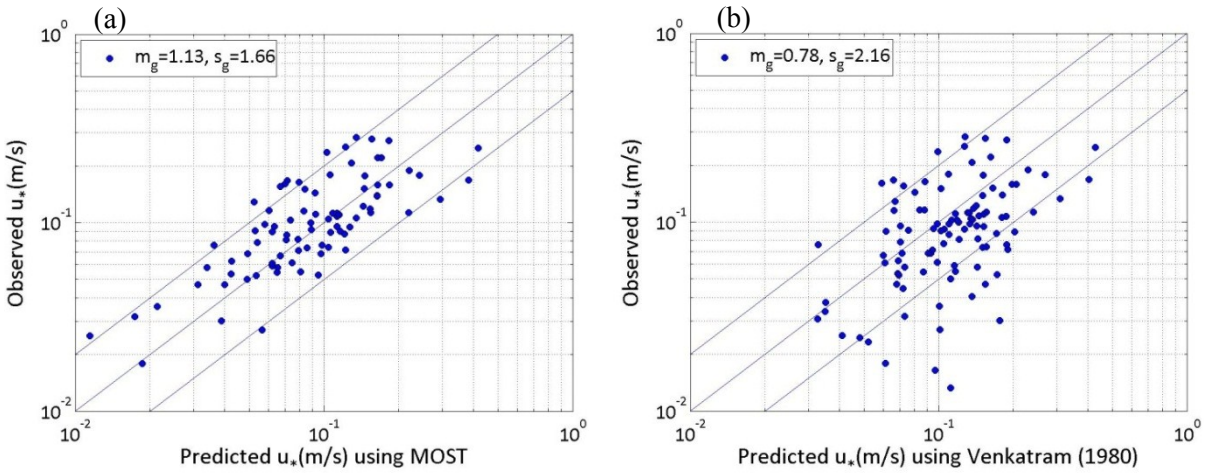

Figure 8-9: Comparison of nighttime observed vs. predicted u_* from (a) MOST using measured wind speed and sensible surface heat flux and (b) Venkatram (1980) using only measured wind speed (data from all nights are included).

Fig. 8-9b shows that the estimates of u_* based on a constant $\theta_* = 0.053K$, compare well with observations (bias of 22% and 95% confidence interval of 4.66) although the scatter is larger than those based on the measured heat fluxes.

As mentioned earlier, observations made by Rotach (1993) suggests that the Reynold's stress, $\overline{u'w'}$, increases with height within the RSL before reaching its maximum value in the ISL. We can estimate the value of u_* in the ISL using Rotach's (2001) profile for the variation of the surface friction with height in the RSL,

$$u_{*ISL} = \frac{u_*(z_{ref})}{\left[\sin\left(\frac{\pi}{2}Z\right)\right]^{a/b}} \tag{8-8}$$

where a=1.28 and b=3.0 are empirical constants and

$$Z = \frac{z_{ref} - d_h}{h_{RSL} - d_h} \tag{8-9}$$

where h_{RSL} is the height of the RSL. We take h_{RSL} to be the average building height in the urban area, $h_b = 4m$. The models described in sections 8.5.3 and 8.5.4 use u_{*ISL} to predict the SBL height.

8.5.2 Analysis of Field Data

Before describing the performance of prognostic models, we examine the relationship between the measured boundary layer heights and the variables used in diagnostic models, which are based on data from relatively homogeneous rural terrain. Some of these models assume that the SBL height is proportional to the neutral length scale, u_* / f (Arya, 1981; Mahrt et al., 1982) where f is the coriolis parameter. Another popular length scale is $\left(u_* L_{M-O} / f\right)^{1/2}$ (Zilitinkevich, 1972; Arya, 1981; Mahrt et al., 1982). Other models assume that the boundary layer height is proportional to the near surface wind speed (Nieuwstadt, 1984; Benkley and Schulmann, 1979). Steeneveld et al. (2007) finds that the SBL height is proportional to u_* / N, where N is the Brunt-Vaisala frequency of the temperature profile above the stable boundary layer.

Fig. 8-10a shows that, except for the Milan data, the SBL heights show little correlation with u_*. Fig. 8-10b and 8-10c indicates similar results for the correlation between the urban SBL height and $\left(u_* L_{M-O}\right)^{1/2}$ and surface wind speed (U), respectively. We did not evaluate the usefulness of u_* / N because the potential temperature gradient above the boundary layer was essentially zero in the Riverside and VTMX experiments, and was not available for Milan studies.

As a prelude to the examination of prognostic models, we examined the relationship between the boundary layer height and the time integral of friction velocity, $\int u_* dt$, which is a measure of the height over which the surface shear stress exerts its influence after sunset. Fig. 8-11 indicates that SBL height correlates well with the time integral of friction velocity for the Riverside and VTMX data sets; the correlation is lower for the Wangara data, and is poor for the Milan data. Table 8-3 indicates that this integral provides a better description of the SBL height than the variables used in diagnostic models.

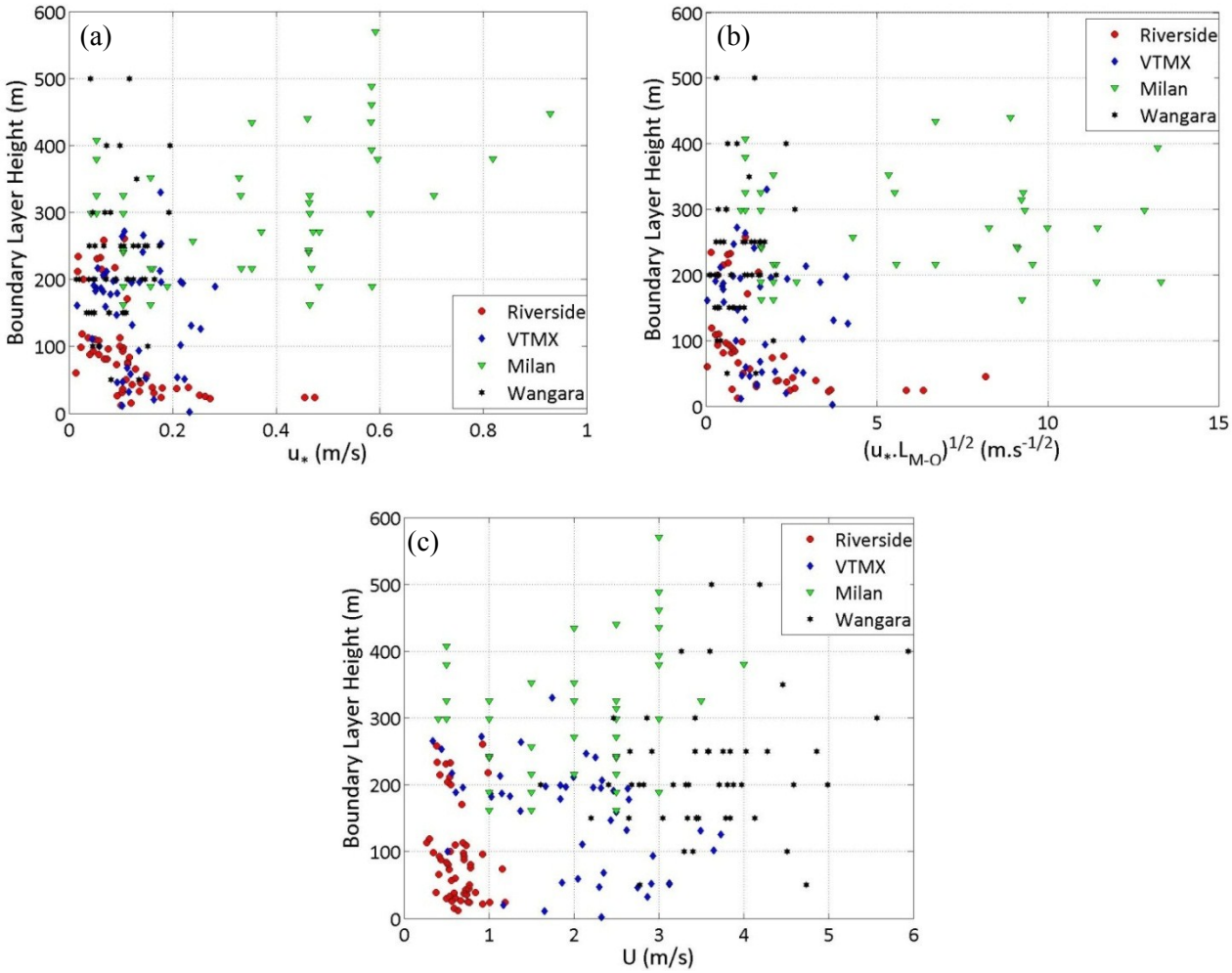

Figure 8-10: Measured boundary layer height in Riverside, VTMX, Milan, and Wangara field studies vs. (a) friction velocity (u_*), (b) $\left(u_* L_{M-O}\right)^{1/2}$, and (c) wind speed ($U$).

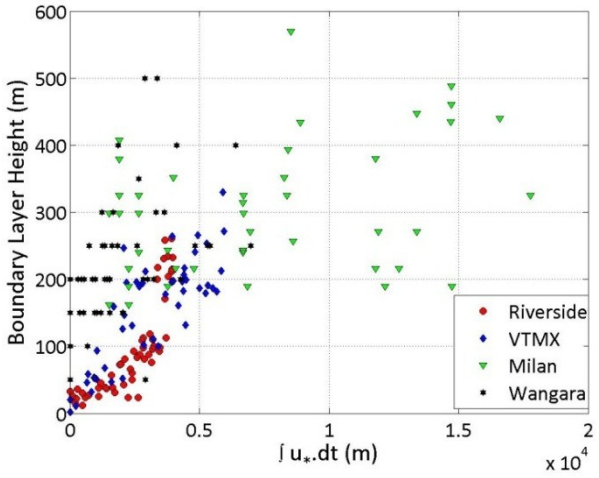

Figure 8-11: Measured boundary layer height in Riverside, VTMX, Milan and Wangara field studies vs. $\int u_* dt$.

A summary of the correlation coefficients (r) of different parameters explained above with the field data are shown in Table 8-3.

Table 8-3: Correlation coefficient (r) between the boundary layer height data and different modeling parameters

Field Data	$\int u_* dt$	u_*	$(u_* L_{M-O})^{1/2}$	U
Riverside	0.82	-0.51	-0.45	-0.25
VTMX	0.82	-0.14	-0.21	-0.44
Milan	0.26	0.38	0.42	0.34
Wangara	0.5	0.18	0.18	0.21

8.5.3 Performance of Prognostic Models

We now examine the performance of a class of prognostic models that simulate the time variation of the SBL height by relaxing the height towards an equilibrium height using the equation,

$$\frac{dh}{dt} = -\frac{(h - h_E)}{\tau} \tag{8-10}$$

where h_E is the equilibrium height corresponding to a diagnostic model, and τ is a relaxation time scale. We investigate two versions of this formulation. AERMOD (Cimorelli et al., 2005), a dispersion model that is recommended for regulatory applications in the US, uses an equilibrium boundary layer height (Venkatram, 1980) that is based on the Zilitinkevich's (1972) formulation, $\left(u_* L_{M-O} / f\right)^{1/2}$:

$$h_E = 2300\ u_*^{3/2}. \tag{8-11}$$

The relaxation time scale τ is formulated as,

$$\tau = \frac{h}{2u_*} \tag{8-12}$$

which roughly corresponds to the time taken for changes at the surface to be transmitted to the top of the boundary layer.

The model proposed by Zilitinkevich et al. (2002) predicts that the boundary layer height in the absence of the large-scale vertical velocity approaches an equilibrium height given by:

$$h_E = \frac{C_R u_*}{|f|}\left\{1 + \frac{C_R{}^2 u_*\left(1 + C_{uN}.Fi\right)}{C_s{}^2 |f| L_{M-O}}\right\}^{-1/2} \tag{8-13}$$

where $C_R = 0.4, C_{uN} = 0.25$ and $C_s = 0.74$ are empirical constants and *Fi* is inverse Froude number given by,

$$Fi = \frac{L_{M-O} N}{u_*} \tag{8-14}$$

where $N = \left[g\left(\partial\theta/\partial z\right)/T_0 \right]^{1/2}$ is the free flow Brunt-Vaisala frequency above the SBL.

The relaxation time scale, τ , is given by,

$$\tau = \frac{1}{C_E |f|} \tag{8-15}$$

where $C_E = 1$ is an empirical dimensionless constant.

We integrate the equation (8-10) through the numerical approximation,

$$h(t + \Delta t) = h(t) e^{(-\Delta t/\tau)} + h_E (t + \Delta t)\left[1 - e^{(-\Delta t/\tau)}\right] \tag{8-16}$$

where *t* is the time from sunset.

Fig. 8-12 indicates that AERMOD predictions show variations, governed by the surface friction velocity, that are not reflected in the observations. The model overestimates the boundary layer height during the first 4 hours of the night (due to large u_*) and tends to underestimate it after that. Evaluation of this model using predicted and observed u_* yield similar results.

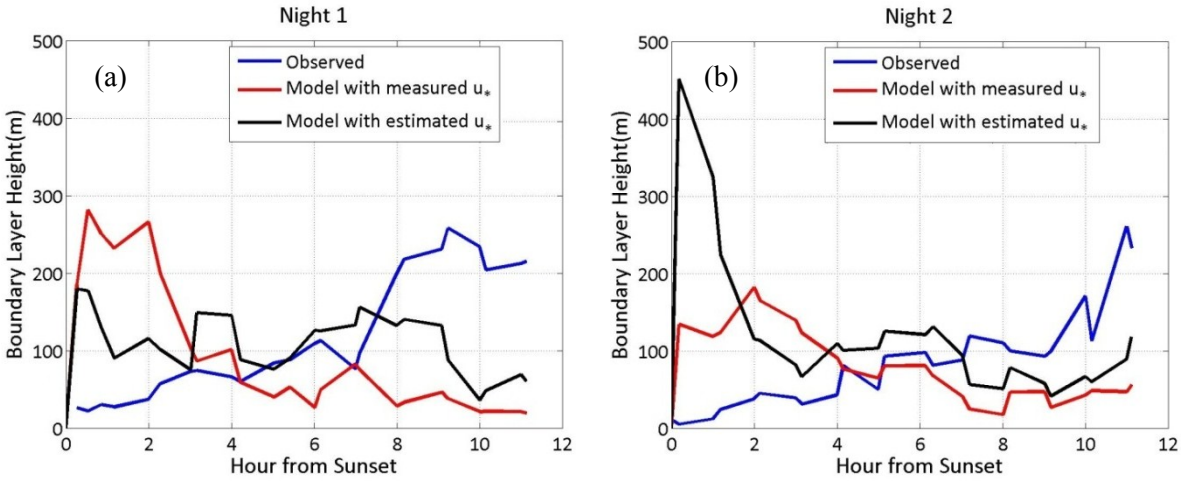

Figure 8-12: Comparison of AERMOD stable boundary layer height model predictions with observations from Riverside field study for (a) Night 1 and (b) Night 2.

Fig. 8-13 indicates that the Zilitinkevich et al. (2002) model predictions are of the right order of magnitude but they do not vary significantly with time; they range from 30 m up to 160 m throughout the night, while the observed values show larger variation. Predicted values of boundary layer height using estimated u_* and L_{M-O} (Venkatram, 1980) are relatively higher than those based on the measured u_* and L_{M-O}.

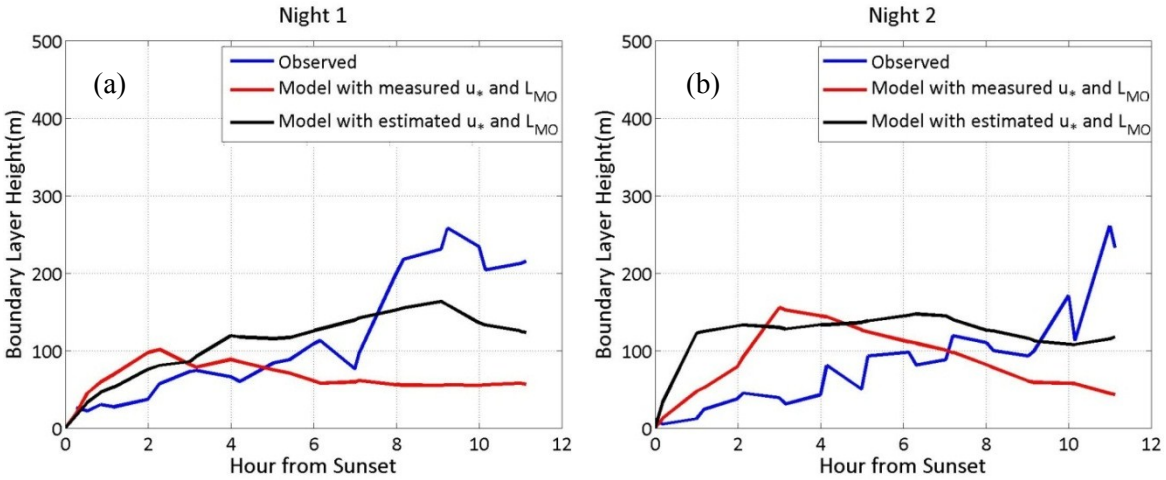

Figure 8-13: Comparison of predictions by Zilitinkevich et al. (2002) model with observations from Riverside field study for (a) Night 1 and (b) Night 2.

8.5.4 Time Integrated Friction Velocity Model

The analysis performed in section 8.5.2 suggests the simple model,

$$\frac{dh}{dt} = \alpha u_*, \tag{8-17}$$

which is based on that proposed by Deardorff (1972) (see Yu, 1978), which unlike equation (8-17), ensures that the boundary layer height starts to decrease with time once it exceeds an equilibrium height of $0.35u_*/f$. The empirical constant α in Deardorff (1972) is 0.025. We find that $\alpha = 0.04$ provides the best fit between the observed boundary layer heights and model estimates. Fig. 8-14 shows that this model performs adequately in predicting the boundary layer height for both nights in Riverside except that there is slight overestimation in the second night. In addition, Fig. 8-14 reveals that using the u_* predicted from the measurements of surface mean wind speed at one level, the model performs reasonably well in predicting the boundary layer height.

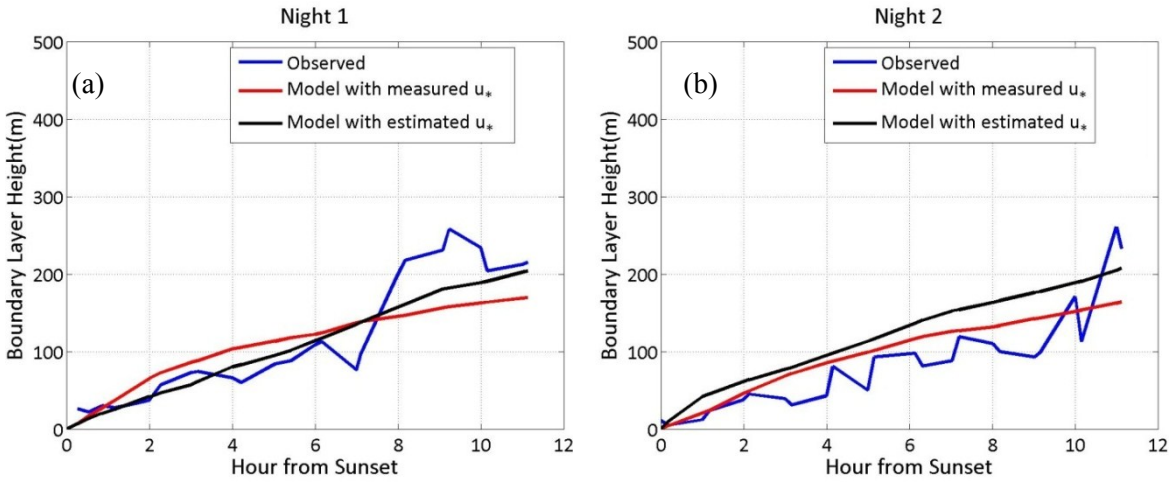

Figure 8-14: Comparison of the *time integrated friction velocity* (eq. 17) model predictions with observation from Riverside field study for (a) Night 1 and (b) Night 2.

This model has also been evaluated with data from VTMX and Wangara field experiments as shown in Fig. 8-15. Boundary layer heights are predicted from 18:00 local time for both VTMX and Wangara field data. Mahrt (1981a) argues that turbulence does not breakdown completely at sunset during the Wangara experiment, and that the minimum boundary layer height is about 125 m. This is the initial value used in our simulations.

As seen in Fig.15 a-c, the model performs adequately for the first two nights of the VTMX experiment and slightly underestimates the boundary layer height on the third night. The evaluation of the model with Wangara data is shown in a scatter plot (Fig. 8-15d), since the data are associated with 16 different nights. Evaluation of model with Wangara data shows that over 90% of data lies within a factor of two of the observed values. There is a bias of 4% with the 95% confidence interval for the ratio of observed to predicted values of 2.3. This shows that although the vertical (~50 m) and temporal (~3 hrs) resolution of data is low; this model performs well in predicting the boundary layer height in the Wangara field experiment using the estimated friction velocities from Melgarejo and Deardorff (1974).

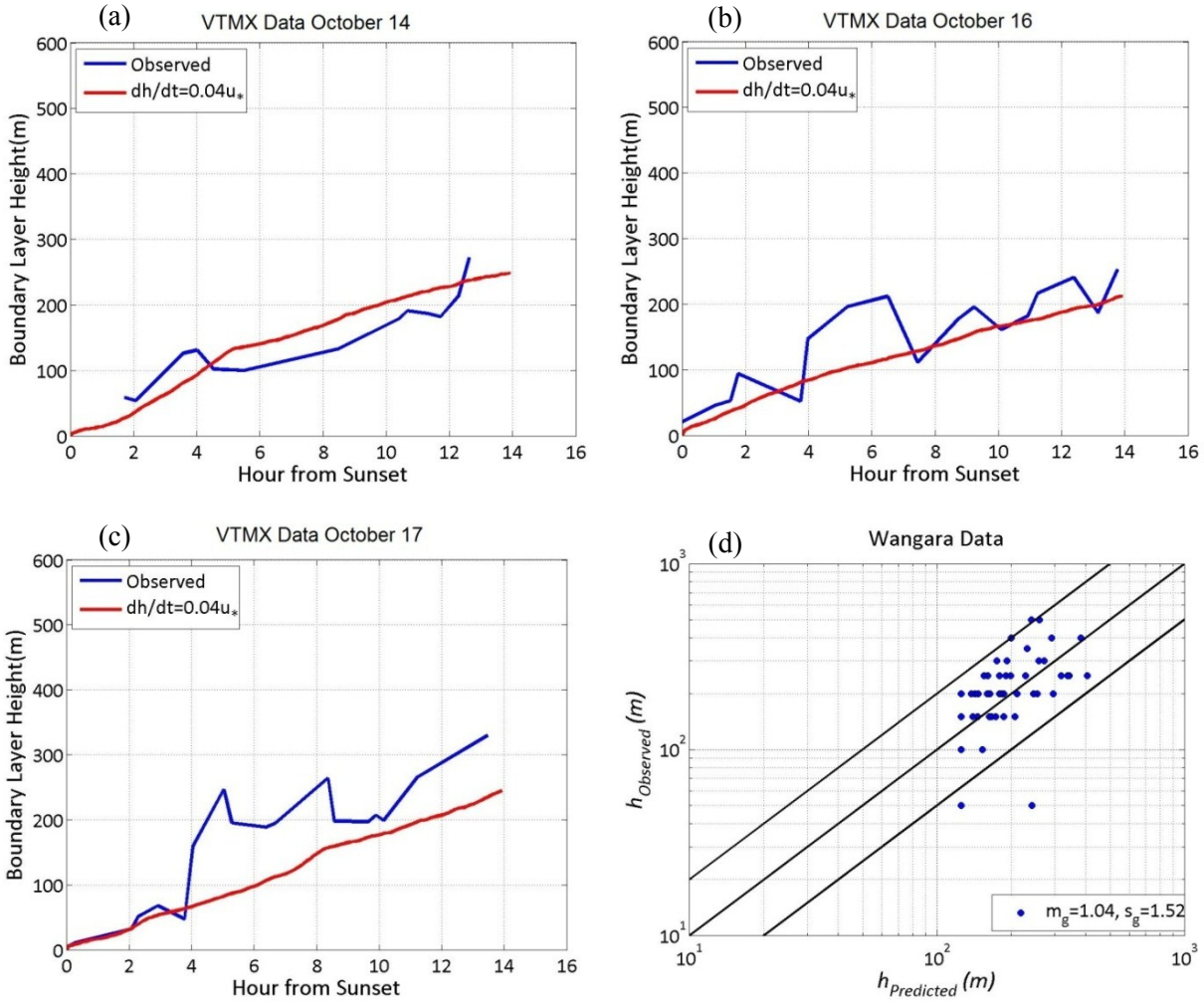

Figure 8-15: Comparison of the *time integrated friction velocity* (eq. 17) model predictions with observation from VTMX field study for (a) October 14; (b) October 16; (c) October 17 and with (d) Wangara field experiment data.

As seen Figs. 8-14 and 8-15, the time integrated friction velocity model, follows the boundary layer height for the first 4 - 8 hrs after sunset, but underestimates the boundary layer height at the end of the night due to the rapid increase of the SBL height starting from midnight. Mahrt (1998) suggests that this rapid increase in boundary layer height is related to the presence of a nocturnal jet (this is clearly illustrated in Fig. 8-3h at $z \approx 200$ m), which represents an elevated source of turbulence. This source of turbulence can

dominate surface shear generation in governing the growth of the SBL. The simple model based on the surface friction velocity cannot account for this elevated source of turbulence.

8.6 Conclusions

Our analysis of data from three field studies conducted in urban areas confirms earlier results that diagnostic models of the SBL provide poor estimates of the height of the SBL. One-dimensional prognostic models also fare poorly in estimating the SBL height. These results are not unexpected in view of the spatial inhomogeneity of the urban surface. Under these circumstances, it is still necessary to estimate the stable boundary layer height for diffusion applications. Our analysis indicates that observed boundary layer height correlates best with the $\int u_* dt$ where time is counted from sunset; the constant multiplying the integral might be site specific. Note that this relationship also implies that the boundary layer height is correlated with the integrated surface heat flux (Yamada ,1979; Stull, 1983) only because the heat flux is correlated with the surface friction velocity. An estimate of the boundary layer height based on the integrated surface friction velocity has practical value because the surface friction velocity can be estimated from a measured surface wind speed, and an estimate of the surface roughness length.

9 SUMMARY AND CONCLUSION

Human health is negatively impacted by many types of pollutants. Air pollution mainly from vehicles, industries, and power plants, raises the chances of variety of health problems in people exposed to it long, and even short term. One of the main sources of air pollution is the vehicular emission especially in metropolitan cities. However, the type of surrounding built environment has a significant effect on how resulting pollution can be dispersed. During the past century there has been many studies done to investigate the impact of buildings and obstacles on the dispersion and consequently ground level concentrations in urban areas. These studies mostly started with ground level line sources which resembled the emission released from vehicles in a traffic line. Both comprehensive field and laboratory studies were done on flow and dispersion inside arrays of buildings. However, most of these studies were focused on passive (non-buoyant) releases, which assume that the plume height remained the same as the stack height. Thus, the plume stays within the urban canopy layer. After the western U.S energy crisis in 2000 and 2001, schools, businesses and hospitals moved toward the independency from centralized power generating stations by installing on site small scale power generators, known as distributed power generators. These small power plants are highly efficient as they have heat recovery from their waste exhaust and coolant, providing both electricity and heating/cooling to the neighborhood. Although DGs were beneficial for providing power independency, they might have significant effect on air quality in urban areas. Unlike CG plants, exhausts from DG sources are released from

relatively low stacks with heights of approximately 10 meters and can be captured in the wake produced by surrounding buildings.

Since January 2001 through May 2002, the power capacity from DGs has been increased by 400 MW (Heath et al. 2005). This rapid increase in the distributed power generation raised the concerns on the air quality impacts of DGs in urban areas. On the other hand, modeling the dispersion from such sources was also impossible due to the lack of available data on their dispersion pattern. Thus, in 2008, a tracer field study was conducted in Palm Springs, CA. where ground level concentrations associated with the release of SF_6 tracer from a 650 kW DG in the Sunrise Park (surrounded by residential buildings) were measured. The stack height was 9.3 m with exhaust temperature of about 460 K. Concentrations were measured over 5 different arcs from 60 m up to 2 km from the stack at the rate of 1 sample per second. Detailed meteorology such as mean and turbulent wind speeds were measured using 3D sonic anemometers located on the roof of the DG and a tower located at distance of approximately 100 m from the stack. Using these measurements the micrometeorological parameters such as heat flux and surface friction velocity were calculated. The measurements were done over 7 days period, 3 daytimes and 4 nighttimes. It has been observed that Palm Springs is mostly dominated by low wind speeds with relatively high turbulent intensities. The observations from concentration measurements show that the concentrations decrease rapidly during daytime, while the decrease rate is much slower during the nighttime. Moreover, relatively high concentrations were seen upwind of the source, which indicated the importance of plume meandering in the dispersion process of such emissions. Following

this field study, Jing et al. (2011) evaluated the performance of US EPA recommended dispersion model AERMOD, in predicting the ground level concentrations associated with DGs. AERMOD predicted the daytime concentrations reasonably well while it substantially underestimated the nighttime concentrations. Similarly we utilized a simple Gaussian dispersion model, to predict the concentration observed during the Palm Springs field study. However, despite the simplicity of this model similar results to those from AERMOD were obtained; daytime predictions were within a factor of two of those observed, while nighttime predictions were substantially lower than the observed values. One of the main reasons for the discrepancy between the results from nighttime observations and model predictions, were assumed to be the dispersion formulation, which was initially designed for emissions released from large power plant where no buildings are in the vicinity. Therefore, this discrepancy suggested further investigation in 1) turbulent enhanced plume spread in urban canopy layer; 2) plume rise affected by surrounding buildings; and 3) nighttime urban boundary layer structure.

In order to have a better understanding on the dispersion process of such sources, experiments under different conditions are needed. However, conducting multiple field studies, are highly time consuming and significantly expensive. In addition results from field studies are specific to the site geometry and meteorological conditions and cannot be extrapolated to other settings. Therefore, the most efficient way to investigate such problems is to conduct laboratory experiments. Laboratory experiments described in this dissertation were done inside the water channel facility at UC Riverside which is explained in more details in Chapter 4. Laboratory simulation of dispersion in water

channels and wind tunnels requires corrects scaling of flow, plume rise and plume spreads. Thus, in chapter 5, we focused on developing an appropriate scaling method for the purpose of this study. Although numerous literatures has studies such problem since 1980s, however, none of this study were focused on scaling of urban dispersion where buildings induced flows, can significantly impact the plume rise and plume spreads. Therefore, in this chapter we started with flow scaling through the EPA report by Snyder (1981) and then explained the scaling of plume rise using the non-dimensional plume rise governing equations. Non-dimensionalizing the plume rise governing equations yield to dimensionless parameters that need to be matched in the model and field to assure the correct scaling. It has been shown that among the dimensionless parameters involved in the scaling process, it would be very difficult to match the initial (stack exit) dimensionless density (ρ_p / ρ_0) in the laboratory and the field due to the limitations on the density of tracer that can be used. By relaxing this dimensionless parameter, a new scaling method has been proposed where the densimetric Froude number has been matched for the plume in the model and field. Following the scaling of plume rise, concentration in the laboratory can be translated into the field scale through the Gaussian dispersion model when the turbulent intensities are not matched. In cases where the experiment facility has the ability to match the turbulent intensities, there is no need for the Gaussian model, and the scaling of concentrations can be done through the old fashioned way of $C^* = CUL^2/Q$. Following these scaling methods, we started our very first study on the dispersion from low-level buoyant sources. In order to conduct this laboratory study, we modeled the Palm Springs DG inside the water channel at scale of

1:100 and measured the ground level concentration downwind under three different cases: 1) no surrounding buildings; 2) DG with upwind arrays of buildings with the height almost the same as the stack height; and 3) DG with upwind arrays of buildings with the height almost double the stack height. The results obtained from this study, revealed relative high concentration in close distances to stack which were observed as a result of building caused downwash. The presence of single and double story upstream buildings did not modify the concentration patterns significantly, and they tend to flatten the concentration pattern, similar to those observed during the Palm Springs nighttime experiments. Results obtained in this study, were compared with the prediction from AERMOD. It has been seen that AERMOD performs reasonably well in the case where no surrounding buildings were present, while it significantly under/over-estimated the concentration close to the stack in the presence of single and double story upstream buildings. In order to investigate the details of plume spread under these different building configurations, plume visualizations were conducted in the vertical and horizontal plane. It has been seen that the upstream buildings, increases the plume rise while at the same time they enhance the turbulent mixing which results in a larger vertical plume spreads. These two counter reacting phenomena can increase/ decrease the ground level concentrations.

On the other hand, our visualizations of lateral plume spread have shown that, when plume is inside the urban canopy layer, it spread in a $\sim x^{0.5}$ pattern rather than a linear one and the length scale dominating this spread pattern is to proportional to the average building widths. Additionally, it has been observed that the plume meandering can play a

major role in the initial spread of the plume. All these parameters were accounted into a simple Gaussian dispersion model which was then used to reproduce the results obtained in the laboratory measurements.

As explained earlier, in addition to turbulent plume spreads, one of the important parameters controlling the ground level concentration associated with low level buoyant sources is the plume rise. Plume rise has been widely investigated through the work done by Gary Briggs in late 1970's and 1980's. The results from Briggs study lead to the well-known Briggs plume rise formulation which is also known as 2/3 law. The derivation of this formulation is discussed in Chapter 2. However, Briggs formulation is designed primarily for plume rise from large stacks where buildings impacts can be neglected. Thus, it does not have the capability to predict the plume rise affected by buildings. We suspected one of the reasons for the discrepancy in AERMOD prediction during nighttime, might be the wrong formulation of plume rise in AERMOD for urban dispersion applications. In order to understand the plume rise under urban conditions, we conducted a field study on the same DG as the one used for the 2008 tracer field study, and measured the plume rise associated with this DG. Results from this field study shows that, unlike our assumptions that Briggs formulation should break down under urban conditions, it can predict the plume rise reasonably well. The rationale for this behavior was explained through the observed meteorology. It has been seen that similar to the 2008 field study, wind speeds in Palm Springs are mostly less than 1 ms^{-1}. In addition the building morphology in Palm Springs is mostly consisted of single storey buildings with height of approximately around 5 m. Thus, due to these two effects, as soon as the plume

exits the stack, it rises substantially high and escapes the urban canopy layer within short distance from the stack. Hence the plume is not affected by flows induced by surrounding buildings and it would not be surprising that the plume rise in Palm Springs can be well predicted by the Briggs plume rise model. However, the low wind speeds and short buildings morphology is not always the case in urban areas. As a result, there is still a need to investigate the plume rise under strong wind speeds, with tall surrounding buildings. In order to address this need, we conducted a series of laboratory experiments where plume rise under relatively high wind speeds were measured. Different building geometries were used. It has been seen that surrounding buildings, mostly increase the plume rise by reducing the wind speeds and inducing updraft in the region where the plume tends to rise. Using these observations, the newly developed numerical plume rise model explained in Chapter 5 was evaluated. This model is the numerical solution of the plume rise governing equations developed by Hoult et al (1969). However, these equation were modified to account for the vertical flows (updrafts and downdrafts) induced by surrounding buildings. A comparison between the results from this model and those obtained from the water channel simulations revealed that this model can accurately predict the plume rise affected by surrounding buildings. The main downside of this model is that it requires the velocity field in the vicinity of the stack in order to predict the plume rise which is not usually available. However, following the recent improvements in CFD models, this plume rise model can be implemented into a CFD model to predict the plume rise under complex urban conditions.

As mentioned in the beginning of this section, one of the main reasons that we suspected to cause the high ground level concentrations observed during Palm Springs nighttime field study was the presence of a shallow nocturnal boundary layer. This boundary layer act as a cap to the dispersion of pollutants and can substantially reduce the decrease rate of ground level concentrations, as the pollutants becomes vertically well mixed in a short distance from the stack. Due to the lack of boundary layer heights measurements during the Palm Springs field study, we were not able to surely relate the nighttime concentration patterns to the structure of the nocturnal boundary layer. Thus, in order to fill this gap, we conducted a field study in Riverside, CA and measured the height of the urban nocturnal boundary layer formed over the Riverside area for two consecutive nights. These data show that the nocturnal boundary layer grows almost linearly from the time of the sunset and growth rate is highly correlated with the surface friction velocity. Based on these observations, we developed a simple model to predict the nocturnal boundary layer height, by estimating the friction velocity from mean wind speed measured close to the ground. This model has also been evaluated with data from VTMX and Wangara field studies, and results shows that although very simple, it can reproduce the observations reasonably well.

In summary, following this dissertation several important features associated with the urban dispersion problem were characterized, and accurate techniques for estimating them were proposed. A list of main contributions associated with this dissertation is given below:

1. New scaling method for simulation of plume rise and dispersion in urban areas were proposed, which can significantly help experimentalists to further investigate the urban dispersion problem in water channels and wind tunnels.

2. The main mechanism for relatively high ground level concentrations close to the source was explained by the vigorous mixing of the plume material below the urban canopy layer and a simple well mixed model was proposed to account for this effect.

3. It was clearly shown that the lateral spread under influence of surrounding buildings does not anymore follow the short-time limit of Taylor's statistical theory, and it shows a $\sim x^{0.5}$ behavior rather than a linear one.

4. Plume rise was thoroughly investigated under different urban geometrical and meteorological conditions. Simple numerical model for urban plume rises was developed which can account for the building effects and provide realistic values of plume rise for urban dispersion applications.

5. The urban nocturnal boundary layer height was characterized through a systematic field study. It has been shown that nocturnal boundary layer height increases almost linearly with time and its growth rate is proportional to the friction velocity (u_*). This important observations yields to a simple model that can be used to predict the nocturnal boundary layer height as an important parameter for night time dispersion applications.

Following these understandings, we have seen that the assumptions made earlier in chapter 3 for the height of the boundary layer (≈ 150 m) as a significant parameter into the simple Gaussian dispersion model were not significantly different from what it can be predicted using the model explained in Chapter 8. Also, the use of Briggs plume rise model has been proved to be an appropriate choice in the Palm Springs due to the low wind speeds and relatively short surrounding buildings. Although the Gaussian dispersion model utilized with meandering module showed some success in describing the ground level concentrations during the last two nights, however, it tends to under predicts concentrations during the first two nights. Therefore, the main message delivered from this study is that in the view of spatial inhomogeneity of urban surface and boundary layer, simple dispersion models have limited performance in predicting the concentrations associated with low-level buoyant sources. Although the ease of access and applicability of these models still is of a significant value. On the other hand, the unsteadiness of urban micrometeorology (such as rapid changes in wind direction) makes it significantly difficult (almost impossible with the current available computational power) for numerical models (i.e. CFD) to predict the concentrations. Thus, we have to accept this fact that unlike the rural dispersion problems where predictions lies within factor of two of the observations, the uncertainty in urban dispersion problems is significantly higher.

Thus, with this clear insight into the problem of dispersion from low-level buoyant sources, we suggest the future works to more focus on the regional impact of distributed power generators on ground level NO_x, O_3, and NO_2 since the cumulative impact might

be significantly higher than the short range impact. More details on this matter can be found in Appendix A.

REFERENCES

Adrian, R.J., 1988. Review of particle image velocimetry research. In: The symposium on optical methods in flow and particle diagnostics, 6th International Congress on Applications of Lasers and Electro-Optics. Vol. 9, 317-319, San Diego, CA: Optics and Lasers in Engineering.

Adrian, R.J.,1991. Particle-imaging techniques for experimental fluid-mechanics, *Ann. Rev. Fluid Mech.* 23, 261-304.

Adrian, R.J.,1997. Dynamic ranges of velocity and spatial resolution of Particle Image Velocimetry, *Meas. Sci. & Tech.* 8(12), 1393-1398.

Allison, K.E., Lents, J., 2002. Encouraging distributed generation of power that improves air quality: can we have our cake and eat it too? J. *Energy Policy*, 30, 737-752.

Allwine, K.J., Flaherty, J.E., 2006. Joint Urban 2003: Study overview and instrument locations. PNNL-15967, Prepared for the U.S. Department of Homeland Security under a Related Services Agreement with the U.S. Department of Energy under contract DE-AC05-76RL01830. Pacific Northwest National Laboratory, Richland, WA.

Allwine, K.J., Shinn, J.H., Streit, G.E., Clawson, K.L., Brown, M. 2002. Overview of URBAN 2000: a multiscale field study of dispersion through an urban environment. *Bulletin of the Am. Met. Soc.*, 83, 521–536.

Arcoumanis, C., McGuirk, J.J, Palma J., 1990. On the use of Fluorescent dyes for concentration measurements, *Exp. Fluids*, 10. 171-180. doi: 10.1007/BF00215028

Arya, S.P.S., 1981. Parameterizing the height of the stable atmospheric boundary layer. *J. App.Meteorol.,* 20, 1192-1202.

Arya, S.P.S., 1988. Introduction to Micrometeorology. San Diego, Academic Press., 307

Arya, S.P.S., Lape, J.F., 1990. A comparative study of the different criteria for the physical modeling of buoyant plume rise in a neutral atmosphere. *Atmos. Environ.*, 24A, 289–295.

Avissar, R., Moran, M.D., Wu, G., Meroney, R.N., Pielke, R.A., 1990. Operating ranges of mesoscale numerical models and meteorological wind tunnels for the simulation of sea and land breezes. *Boundary-Layer Meteorol*. 50, 227–275.

Bacci, P., Elisei, G., Longhetto, A. 1974. Lidar measurement of plume rise and dispersion at Ostiglia power station. *Atmos. Environ.* 8 (11), 1177-1186.

Baklanov, A., Joffre, S.M., Piringer, M., Deserti, M., Middleton, D.R., Tombrou, M., Karppinen, A., Emeis, S., Prior, V., Rotach, M.W., Bonafè, G., Baumann-Stanzer, K., Kuchin, A., 2006. Towards estimating the mixing height in urban Areas. Recent experimental and modelling results from the COST-715 Action and FUMAPEX project. Scientific Report 06-06. Digital ISBN: 87-7478-540-0 ISSN: 1399–1949

Barad, M. L., 1958. Project Prairie Grass, A Field Program in Diffusion, Vol. 1, Geophysics Research Paper No. 59. Air Force Cambridge Research Center, Bedford, MA.

Barilla, P.A., 1968. Dependence of entrainment coefficients upon orifice conditions in model studies of a smoke plume in a laminar cross wind. M. S. Thesis, Massachusetts Institute of Technology, Cambridge, MA.

Benkley, C.W., Schulman, L.L., 1979. Estimation hourly mixing depth from historical meteorological data, *J. App.Meteorol.,* 18, 772-780.

Berkowicz, R, Ketzel, M, Vachon, G, Louka, P, Rosant, JM., Mestayer, P. G., et al. 2002. Examination of traffic pollution distribution in a street canyon using the Nantes 99 experimental data and comparison with model results. *Water, Air & Soil Pollution. Focus*, 2(5), 311 324.

Berkowicz, R., 2000. A Simple Model for Urban Background Pollution. *Environmental Monitoring and Assessment,* 65, 259-267.

Berlman, I. B., 1971. Handbook of fluorescence spectra of aromatic molecules, 2nd edition. New York: Academic Press

Blackadar, K., 1962. The vertical distribution of wind and turbulent exchange in a neutral atmosphere. *J. geophys. Res*., 67,3095-3101.

Boarnet, M.G., Edwards, R., Princevac, M., Wu, J., Pan, H., Bartolome, C., et al., 2009. Near-Source Modeling of Transportation Emissions in Built Environments Surrounding Major Arterials. UC Berkeley: University of California Transportation Center. Research paper No. 886. Retrieved from: http://escholarship.org/uc/item/5w357946

Bornstein, R., 1987. Mean diurnal circulation and thermodynamic evolution of urban boundary layers, from Modeling the Urban Boundary Layer, *Am. Met. Soc.*, Boston, MA, 52-94.

Bosanquet, C.H., 1957. The rise of a hot waste gas plume. *J. Inst. Fuel* 30, 322-329. *Boundary Layer Meteorology*. 20, 135–174.

Briggs, G.A., 1969. Plume rise. U.S Army Environmental Center Critical Review Series. Report Number TID-25075, USAEC Technical Information Center, Oak Ridge, TN, USA.

Briggs, G.A., 1973. Diffusion estimation for small emissions. *USAEC Report ATDL-106*, Air Resources Atmospheric Turbulence and Diffusion Lab, NOAA.

Briggs, G.A., 1974. Diffusion estimation for small emissions. ERL, ARL USAEC Report ATDL-106, US Atomic Energy Commission, Oak Ridge, Tennessee.

Briggs, G.A., 1984. Plume rise and buoyancy effects. In: Atmospheric Science and Power Production (D.Randerson, Ed.), Chapter 8, 327-366. DOE/TIC-27601, DE84005177. U.S. Dept. of Energy Office of Sci. and Tech. Information, Springfield, VA.

Bringfelt, B., 1968. Plume rise measurements at industrial chimneys. *Atmos. Environ.* 2 (6), 575-598.

Britter, R.E. and Hanna, S.R., 2003. Flow and dispersion in urban areas, *Annual Review of Fluid Mechanics*, 469-496

Brode, R. W., 2002. Implementation and Evaluation of PRIME in AERMOD. The 12th Joint Conference on Applications of Air Pollution Meteorology with A&WMA, Norfolk, VA.

Businger, J.A., 1973. Turbulent transfer in the atmospheric surface layer. In: Haugen DH (ed) Workshop on Micrometeorology. *Am. Met. Soc.*, Boston, MA pp 67–100

Calle E.E., Thun M.J., 2005. Spatial analysis of air pollution and mortality in Los Angeles. *Epidemiology*, 16. 727-736.

Carlotti, P., Hunt, G.R., 2005. Analytical solutions for turbulent non-Boussinesq plumes. *J. Fluid Mech.* 538, 343–359.

Carpenter, S.B., Frizzola, J.A., Smith, M.E., Leavitt, J.M., Thomas, F.W. 1968. Full-Scale Study of Plume Rise at Large Electric Generating Stations, *J. Air Pollut. Control Assoc.*, 18 (7), 458-465

Carruthers, D.J., Holroyd, R., Hunt, J., Weng, W.S., Robins, A.G., Apsley, D., Thomson, D., Smith, F., 1994. UK-ADMS: a new approach to modelling dispersion in the earth's atmospheric boundary layer. *J. Wind Eng. Ind. Aerodyn*., 52, 139–153

Carruthers, D.J., Mckeown, A.M., Hall, D.J., Porter, S., 1999. Validation of ADMS against wind tunnel data of dispersion from chemical warehouse fires. *Atmos. Environ*., 33, 1937-1953.

Cermak, J.E., Davenport, A.G., Plate, E.J., Viegas, D.X., 1995. Wind Climate in Cities, Proceedings of a NATO Advanced Study Institute, NATO ASI Series E, 277, Kluwer Academic Publishers, Dordrecht, The Netherlands, 772 pp. ISBN 0-7923-3202-4.

Cimorelli, A. J., Perry, S. G., Venkatram, A., Weil, J. C., Paine, R. J., Wilson, R. B., Lee, R. F., Peters, W. D., Brode, R. W. and Paumier, J. O., 2004. Aermod: Description of Model Formulation. U.S. Environmental Protection Agency Office of Air Quality

Planning and Standards Emissions Monitoring and Analysis Division Research Triangle Park, North Carolina.

Cimorelli, A.J., S.G. Perry, A. Venkatram, J.C. Weil, R.J. Paine, R.B. Wilson, R.F. Lee, W.D. Peters, and R.W. Brode, 2005. AERMOD: A dispersion model for industrial source applications. Part I: General model formulation and boundary layer characterization*, J. App. Meteorology*., 44(5), 682-693

Clarke, R.H., Dyer, A.J., Brook, R.R., Reid, D.G., Troup, A.J., 1971. The Wangara Experiment: Boundary layer data, Tech. Paper No. 19, Div. Meteorol. Phys., CSIRO, Australia.

Contini, D., Donateo, A., Cesari, D., Robins, A.G., 2011. Comparison of plume rise models against water tank experimental data for neutral and stable crossflows, *J. Wind Eng. Ind. Aerodyn.*, 99, 5, 539-553

Contini, D., Robins, A.G., 2001. Water tank measurements of buoyant plume rise and structure in neutral crossflows. *Atmos. Environ.* 35, 6105–6115.

Contini, D., Robins, A.G., 2004. Experiments on the rise and mixing in neutral crossflow of plumes from two identical sources for different wind directions. *Atmos. Environ.* 38, 3573–3583.

Csanady, G.T., 1973. Turbulent Diffusion in the Environment, Reidel, Dordrecht, pp. 248.

Csanady, G.T., Hilst, G.R., Bowne, N.E., 1967. The diffusion from a cross-wind line source at Fort Wayne, Indiana. Unpublished Report, Travelers Research Center, Hartford, CT.

Cuxart, J. and coauthors, 2006. Single-column model intercomparison for a stably stratified atmospheric boundary layer. *Boundary-Layer Meteorol.*, 118, 273–303.

Davidson, G.A., Slawson, P.R., 1967. Effective source flux parameters for use in analytical plume rise models*, Atmos. Environ.*, 16, 2, 223-227

Davidson, M.J., Snyder, W.H., Lawson, R.E. Jr., Hunt, J.C.R., 1996. Wind tunnel simulations of plume dispersion through groups of obstacles, *Atmos. Environ.* 30,3715–3731

Deardorff, J.W., 1972. Rate of growth of the nocturnal boundary layer. In H. W. Church and R.E. Luna (eds.) *Proceeding of American Meteorological Society Conference on Air Pollution, Turbulence & Diffusion*, Las Cruces, U.S.A., 183-190

Doran, J. C., Fast, J. D., Horel, J., 2002. The VTMX 2000 campaign. *Bulletin of the Am. Met. Soc.*, 83:537–551.

Eckman, R.M., 1994. Re-examination of empirically derived formulas for horizontal diffusion from surface sources. *Atmos. Environ*. 28. 265–272.

EPA, 2008. AERSURFACE User's Guide, EPA-454/B-083-001. U.S. Environmental Protection Agency, Research Triangle Park, NC.

Etling, D., Wippermann, F., 1975. The height of the planetary boundary layer and of the surface layer. *Beitraege zur Physik der Atmosphaere,* 48, 250-254.

Fackrell, J. E., Pearce, J. E., 1981. Parameters affecting dispersion in the near wake of buildings, Central Electricity Generating Board, Report RD/M/1179N81, Marchwood Engineering Laboratories, UK (1981), pp. 41.

Fay, J.A., 1973. Buoyant plumes and wakes. *Ann. Rev. Fluid Mech*. 5, 151–160. DOI: 10.1146/annurev.fl.05. 010173.001055

Fay, J.A., Escudier, M.P., Hoult, D., 1970. A correlation of field observations of plume rise. *J. Air Pollut. Control Ass.* 20, 291-397.

Gailis, R.M., Hill, A., 2006. A wind tunnel simulation of plume dispersion within a large array of obstacles. *Boundary-Layer Meteorol.*, doi: 10.1007/s10546-005-9029-1.

Garratt, J.R., 1982. Observations in the nocturnal boundary layer. *Boundary-Layer Meteorol*., 22, 21-48.

Garratt, J.R., 1992. The Atmospheric Boundary Layer. *University Press*, Cambridge, 316

Gifford, F.A., 1961. Use of routine meteorological observations for estimating atmospheric dispersion. *Nucl. Saf.* 2, 47-51.

Greene, N., Hammerschlag, R.,2000. Small and Clean Is Beautiful: Exploring the Emissions of Distributed Generation and Pollution Prevention Policies. *The Electr. J.*, 13 (5), 50-60, DOI: 10.1016/S1040-6190(00)00118-4.

Grimmond, C. S. B., Oke, T. R., 2002. Turbulent heat fluxes in urban areas: observations and a local-scale urban meteorological parameterization scheme (LUMPS). *J. App.Meteorol.*. 41(7):792-810.

Gryning, S., Lyck, E., 1984. Atmospheric dispersion from elevated sources in an urban area: comparison between tracer experiments and model calculations. *J. Clim. App. Meteorol.*, 23, 651–660

Gryning, S.E., Batchvarova, E., 2005. Advances in urban dispersion modelling. In: Advances in air pollution modeling for environmental security. NATO advanced research workshop: Advances in air pollution modeling for environmental security, Borovetz (BG), 8-12 May 2004. Faragó, I.; Georgiev, K.; Havasi, A. (eds.), (Springer, Berlin, 2005) (Nato Science Series. IV: Earth and Environmental Sciences, 54) p. 243-252

Guilbault, G.G., 1973. Practical Fluorescence : Theory , Methods and Techniques, Dekker, New York

Hadley, S.W., Van Dyke, J.W., 2003. Emissions benefits of distributed generation in the Texas market. Prepared for the United States, Dept. of Energy under contract No. DE-AC05-00OR2272, Report Number ORNL/ TM-2003/100, Oak Ridge National Laboratory, Oak Ridge, TN.

Halitsky, J., 1968. Gas diffusion near buildings, D.H. Slade, Editor, TID-24190, Meteorology and Atomic Energy, chapter 5-5, 221–231.

Halliday, E.C., 1968. Measurements of the rise of hot plumes. *Atmos. Environ.* 2 (5), 509-516.

Hamilton, P.M., 1967. Paper III: plume height measurements at Northfleet and Tilbury power stations. *Atmos. Environ.*, 1, 4, 379-387.

Hanna, S.R., 1969. The thickness of the planetary boundary layer. *Atmos. Environ.*, 3 519-536.

Hanna, S.R., Britter, R.E., Franzese, P., 2003. A baseline dispersion model evaluated with Salt Lake City and Los Angeles tracer data. *Atmos. Environ.*, 37, 5069–5082.

Hanson, R.K., 1988. Combustion diagnostics: Planar imaging techniques, 21st International Symposuim on Combustion 21.1677-1680.doi: 10.1016/S0082-0784(88)80401-6

Harrison, R.M., Leung, P.L., Somerville, L. 1999. Analysis of incidence of childhood cancer in the West Midlands of the United Kingdom in relation to the proximity of main roads and petrol stations. *Journal of Occupational and Environmental Medicine* 56, 774-780.

Heath, G.A., Granvold, P.W., Hoats, A.S., Nazaroff, W.W., 2005. Quantifying the air pollution exposure consequences of distributed electricity generation. Final Report to the University of California Energy Institute.

Heath, G.A., Granvold, P.W., Hoats, A.S., Nazaroff, W.W., 2006. Intake fraction assessment of the air pollutant exposure implications of a shift toward distributed electricity generation. *Atmos. Environ.*, 40, 7164-7177.

Hess, G. D., Hicks, B. B., Yamada, T., 1981. The Impact of the Wangara Experiment, *Boundary-Layer Meteorol.*

Holtslag, A.A.M., De Bruin, E.I.F., Pan, H.L., 1990. A high resolution air mass transformation model for short range weather forecasting, *Mon. Weather Rev*. 118, 1561-1575.

Houcine, I., Vivier, H., Plasari, E., David, R., Villermaux, J., 1996. Planar laser induced Fluorescence technique for measurements of concentration fields in continuous stirred reactors. *Exp. Fluids,* 22: 95-102

Hoult, D.P., Fay, J., Forney, L., 1969. A theory of plume rise compared with field observations. *J. Air Pollut. Control Assoc*. 19, 585–590.

Hoult, D.P., Weil, J.C., 1972. Turbulent plume in a laminar cross flow. *Atmos. Environ.* , 6 (8), 513-530, DOI: 10.1016/0004-6981(72)90069-8.

Hughes, S.A., 1993. Physical models and laboratory techniques in coastal engineering. Advanced series on ocean engineering, v. 7. Singapore, World Scientific., pp. 568.

Hunter, G.C., 1992. The behavior of plumes from point sources in stratified flows. Ph.D. Dissertation, National Power Research and Technology Department. 275 pp. Available from British Library Document Supply Center DSC: DX172355

Iannucci, J., Horgan, S., Eyer, J., Cibulka, L. 2000. Air pollution emission impacts associated with economic market potential of distributed generation in California. Final Report to the California Air Resources Board, Sacramento, CA.

Isakov, V., Venkatram, A., Touma, J. S., Koracin, D. and Otte, T. L., 2007. Evaluating the use of outputs from comprehensive meteorological models in air quality modeling applications. *Atmos. Environ.*. 41(8):1689-1705..

Isyumov, N., Tanaka, H. 1979, Wind tunnel modelling of stack gas dispersion: difficulties and approximations. In *Wind Engineering* (edited by Cermak J. E.), 2, 987-1001. Pergamon Press, Oxford.

Jensen, M., 1958. The Model Law for Phenomena in Natural Wind, *Ingenioren*, 2, 121–128 .

Jerrett, M., Burnett, R., Pope, 3rd C.A., Krewski, D., Newbold, K.B., Thurston, G., Shi, Y., Finkelstein, N., Calle, E.E, Thun, M.J., 2005. Spatial analysis of air pollution and mortality in Los Angeles. *Epidemiology,* 16, 727-736.

Jing Q., Venkatram A., 2011. The relative impacts of distributed and centralized generation of electricity on local air quality in the South Coast Air Basin of California, *Energy Policy*, 39, 9, 4999-5007, doi: 10.1016/j.enpol.2011.05.056.

Jing, Q., 2011. Air Quality Impact of Distributed Generation of Electricity, Dissertation (PhD), University of California, Riverside.

Jing, Q., Pankratz, D., Princevac, M., Venkatram, A., 2009. Modeling Dispersion of Buoyant Releases in an Urban Area,89th AMS Annual Meeting, 11th Conference on Atmospheric Chemistry Special Symposium on Aerosol–Cloud–Climate Interactions, 89th Annual Meeting, Phoenix, AZ, January 2009.

Jing, Q., Venkatram, A., Princevac, M., Pankratz, D., Qian, W., 2010. Modeling Dispersion of Buoyant Emissions from Low Level Sources in an Urban Area, 90th AMS Annual Meeting, 16th Conference on Air Pollution Meteorology, 90th Annual Meeting, Atlanta, GA, January 2010.

Kaimal, J.C., Finnigan, J.J., 1994. Atmospheric Boundary Layer Flows: Their Structure and Measurement, New York- Oxford: University Press Inc.

Karasso, P.S., Mungal, M.G., 1997. PLIF measurements in aqueous flows using the Nd: YAG laser, *Exp. Fluids*, 23.382-387

Klein, P., Leitl, B., Schatzmann, M., 2011. Concentration fluctuations in a downtown urban area—part II: analysis of joint urban 2003 wind-tunnel measurements. *Environ. Fluid Mech.*, 11, 1, 43-60, doi:10.1007/s10652-010-9195-7.

Kobus, H., Abraham, G., 1980. Hydraulic modelling. Hamburg [West Germany], Parey, pp.323

Koracin, D., Berkowicz, R. 1988. Nocturnal boundary layer height: observations by acoustic sounders and prediction in terms of surface layer parameters. *Boundary-Layer Meteorol.*, 43, 65-83

Kulchin Y.N, Voznesenskiy S.S., Gamayunov E.L., Gurin A.S., Korotenko A.A., Maior A.Y., 2007. An Immersible Fiber-Optic Fluorometer , *Instruments and Experimental Techniques*, 6. 117–122

Kumar, P., Garmory, A., Ketzel, M., Berkowicz, R., Britter, R., 2009. Comparative study of measured and modelled number concentrations of nanoparticles in an urban street canyon. *Atmos. Environ.,* 43, 949 - 958.

Kychakoff, G., Howe, R.D., Hanson, R.K., 1984. Quantitative Flow visualization technique for measurements in combustion gases, *Applied Optics,* 23.704-712

Laikhtman, L., 1961. Physics of the Boundary Layer of the Atmosphere. Translated by the Israel Program for Scientific Translations, Jerusalem, 1964. Available from the office of Technical Services, U.S. Dept. of Commerce, Wash., D.C., 200

Lena, F., Desiato, F., 1999. Intercomparison of nocturnal mixing height estimate methods for urban air pollution modeling. *Atmos. Environ.,* 33(15):2385–2393

Lettau, H.H., 1962. Theoretical wind spirals in the boundary layer of a barotropic atmosphere. *Beit. Phys. Atmos.*, 35,195-212.

Lucas, D.H., Moore, D.J., Spurr, G., 1963. The rise of hot plumes from chimneys. *Int. J. Air Wat. Pollut.,* 7, 473-500.

Luhar, A.K., Venkatram, A., Lee, S.M., 2006. On relationships between urban and rural near-surface meteorology for diffusion applications. *Atmos. Environ.*, 40 (34), 6541-6553.

Macdonald, R.W., Griffiths, R.F. and Hall, D.J., 1998. A comparison of results from scaled field and wind tunnel modelling of dispersion in arrays of obstacles. *Atmos. Environ.*, 32, 22, 3845–3862.

Mahrt, L., 1981a. The early evening boundary layer transition. *Quarterly. J. Roy. Met. Soc.*, 107, 329–343.

Mahrt, L., 1981b. Modeling the depth of the stable boundary layer. *Bound-Layer Meteorol.*, 21, 3-19

Mahrt, L., 1998. Stratified atmospheric boundary layer. *Boundary-Layer Meteorology*, 90, 375–396.

Mahrt, L., Andre, J.C., Heald, R.C., 1982. On the depth of the nocturnal boundary layer, *J. App.Meteorol.*, 21, 90-92

McConnell, R., Berhane, K., Yao, L., Jerrett, M., Lurmann, F., Gilliland, F., Kuenzli, N., Gauderman, J., Avol, E., Thomas, D., Peters, J., 2006. Traffic, susceptibility, and childhood asthma, *Environmental Health Perspectives*, 114 (5).766–772.

McElroy, G.E., Brown, C.E., Berger, L.B., and Schrenk, H.H., 1944. Dilution of Stack Effluents. US Bureau of Mines Tech. Paper 657 US Gov. Print. Ofc.

McElroy, J.L., 1969. A comparative study of urban and rural dispersion. *J. App.Meteorol.*, 8, pp. 19-31.

McElroy, J.L., Pooler, F., 1968. The St. Louis dispersion study-volume II-analysis. National Air Pollution Control Administration, Pub. No. AP-53, US DHEW Arlington, 50pp.

Melgarejo, J.W., Deardorff, J.W., 1974. Stability functions for the boundary layer resistance laws based upon observed boundary layer heights, *J. Atmos. Sci.*, 31, 1324-1333

Mensink, C., Lefebre, F., Janssen, L., Cornelis, J., 2006. Comparison of three street canyon models with measurements at an urban station in Antwerp, Belgium. *Environmental Modelling & Software*, 21, 514-519.

Meroney, R.N., 1982. Wind tunnel experiments on dense gas dispersion, *Special Issue J. of Hazardous Materials*, 6, 85-106

Meroney, R.N., 1986a. Guideline for fluid modeling of liquefied natural gas cloud dispersion - Vol. I: Instruction Guide, Final Report for Gas Research Institute, Contract No. 5083-252-0962, Report GRI86/0102.1, May 1986, pp. 57

Meroney, R.N., 1986b. Guideline for fluid modeling of liquefied natural gas cloud dispersion - Vol. II: Technical Support Document, Final Report for Gas Research Institute, Contract No. 5083-252-0962, Report GRI86/0102.2, May 1986, pp. 262

Meroney, R.N., 1987. Validation of fluid modeling techniques for assessing hazards of dense gas cloud dispersion, Journal of Hazardous Materials, 15, 377-417.

Meroney, R.N., 1988. Guidelines for fluid modeling of dense gas cloud dispersion, *J. of Hazardous Materials*, 17, 23-46.

Meroney, R.N., 1998. Wind tunnel simulation of convective boundary layer phenomena: simulation criteria and operating ranges of laboratory facilities. Buoyant Convection in Geophysical Flows, E. J. Plate et al., Eds., Kluwer, 313-326.

Meroney, R.N., 2004. Wind tunnel and numerical simulation of pollution dispersion: a hybrid approach. Working paper, Croucher Advanced Study Institute on Wind Tunnel Modeling, Hong Kong University of Science and Technology, 6–10 December 2004, 60pp.

Meroney, R.N., Cermak, J.E., Yang, B.T., 1975. Modeling of atmospheric transport and fumigation at shoreline site. *Boundary-Layer Meteorol.*, 9, 69–90.

Meroney, R.N., Melbourne, W.H., 1992. Operating Ranges of Meteorological Wind Tunnels for the Simulation of Convective Boundary Layer (CBL) Phenomena, *Boundary-Layer Meteorol.* ,61, 145-174.

Mery, P., 1969. Reproduction en Similitude de la Diffusion dans la Couche Limite Atmospherique, la Houille Blanche, 4, 327-343.

Morton, B.R., Taylor, G.I., Turner, J.S., 1956. Turbulent gravitational convection from maintained and instantaneous sources. *Proc. R. Soc. Lond.*, A 234, 1–23.

Neff, D.E., Meroney, R.N., 1981. The behavior of LNG vapor clouds: wind-tunnel simulation of 40 m3 LNG spill tests at China lake Naval Weapons Center, California, Final Report for Gas Research Institute, Report GRI 80/0094, pp. 155

Nieuwstadt, F.T.M., 1984. Some aspects of the turbulent stable boundary layer. *Boundary-Layer Meteorol.*, 30, 31-55.

Nieuwstadt, F.T.M., Tennekes, H., 1981. A rate equation for the nocturnal boundary layer height. *J. Atmos. Sci*., 38, 1418-1428

Obasaju, E.D., Robins, A.G., 1998. Simulation of pollution dispersion using small scale physical models - an assessment of scaling options. *Environ. Monitoring Assessment*, 52 1–2, 239-254

Ohba, R., Kakishima, S., Ito, S., 1990. Water tank study of plume rise and diffusion in a stably stratified layer under calm conditions. *Il Nuovo Cimento C*, 13(6), 1017–1028.

Oke, T.R. 1987. Boundary Layer Climates, 2nd ed. Routledge, London, 435 pp. ISBN 0-415-04319-0.

Oke, T.R., 1982. The energetic basis of the urban heat island. *Q. J. Roy. Meteorol. Soc.,* 108 (455), 1-24.

Olesen, H.R., 2005. User's guide to the Model Validation Kit. Initiative on harmonisation within atmospheric dispersion modeling for regulatory purposes. Available at http://www.harmo. org/kit.

Olesen, H.R., Løfstrøm, P., Berkowicz, R. and Jensen, A.B. (1992) An improved dispersion model for regulatory use: the OML model. In: van Dop, H. and Kallos, G. Editors, 1992. Air Pollution Modeling and its Application IX Plenum Press, New York

Pan, H., 2011, Investigation of Flow, Turbulence, and Dispersion within Built Environments, Dissertation (PhD), University of California, Riverside.

Pasquill, F.A., 1961. The estimation of the dispersion of windborne material. *Meteorol. Mag.*, 90, 33-49.

Pasquill, F.A., 1976. Atmospheric dispersion parameters in Gaussian plume modeling - Part III: possible requirements for change in the Turner's Workbook values. EPA-600/4-76-030B, U. S. Environmental Protection Agency, Research Triangle Park, NC.

Pasquill, F.A., Smith, F.R., 1983. Atmospheric Diffusion. John Wiley and Sons Inc., New York, pp. 440

Peters, A., von Klot, S., Heier, M., Trentinaglia, I., Hormann, A., Wichmann, E., Lowel, H., 2004. Exposure to traffic and the onset of myocardial infarction. *New England Journal of Medicine*, 351.1721-1730.

Plate, E.J., 1999. Methods of Investigating Urban Wind Fields – Physical Models, *Atmos. Environ*, 33, 3981–3989.

Poreh, M., Rau, M., Plate, E.J., 1991. Design considerations for wind tunnel simulations of diffusion within the convective boundary layer. *Atmos. Environ.,* 25A, 1250–1257.

Prasad, A.K., Adrian, R.J., Landreth, C.C., Offutt, P.W., 1992. Effect of resolution on the speed and accuracy of Particle Image Velocimetry interrogation. *Exp. Fluids*, 13(2-3), 105-116.

Priestly CHB (1956) A working theory of the bent-over plume of hot gas, *Q. J. Roy. Meteorol. Soc.*, 82 (352), 165-176. DOI: 10.1002/qj.49708235203

Princevac, M., Baik, J., Li, X., Pan, H., Park, S., 2010. Lateral channeling within rectangular arrays of cubical obstacles. *J. Wind Eng. Ind. Aerodyn.* 98, 377-385, DOI: 10.1016/j.jweia.2009.11.001.

Princevac, M., Venkatram, A., 2007. Estimating micrometeorological inputs for modeling dispersion in urban areas during stable conditions, *Atmos. Environ.*, 41 (26), 5345-5356.

Pringsheim, P., 1949. Flourescence and Phosphorescence. Interscience, New York

Qian, W., Venkatram, A., 2011. Performance of Steady-State Dispersion Models Under Low Wind-Speed Conditions, Boundary-Layer Meteorol., 138, 475-491

Rau, M., Bachlin, W., Plate, E.J., 1991. Detailed design features of a new wind tunnel for studying the effects of thermal stratification, *Atmos. Environ.*,25, 7, 1257-1262, DOI: 10.1016/0960-1686(91)90236-Z.

Ricou, F.P., Spalding, D.B., 1961. Measurements of entrainment by axisymmetrical turbulent jets. *J. Fluid Mech.* 8, 21–32.

Robins, A. G., Apsley, D. D., Carruthers, D. J., McHugh, C. A., Dyster, S. J., 2005. Plume rise model specification. ADMS 3 documentation (P11/02N/05), Cambridge Environmental Research Consultants Ltd.

Robins, A.G. and McHugh, C, 2001. Development and Evaluation of the ADMS Building Effects Module. *Int. J. Environ. and Poll.*, 16, 1-6, 161-174

Robins, A.G., 1978. Plume dispersion from ground level sources in simulated atmospheric boundary layers. *Atmos. Environ.*, 12, 1039–1044.

Robins, A.G., 1980. Wind Tunnel Modelling of Buoyant Emissions, In: Michel M. Benarie, Editor(s), *Studies in Environmental Science*, 8, 117-124, ISSN 0166-1116, ISBN 9780444418890.

Robins, A.G., 2003. Wind-tunnel modelling some recent and not so recent achievements. *J. Wind Eng. Ind. Aerodyn.*, 91, 1777–1790.

Robins, A.G., Carruthers, D.J., McHugh, C.A., 1997a.The ADMS building effects module. *Int. J. Environ. and Poll.*, 8, 708–717.

Robins, A.G., McHugh, C.A., Carruthers, D.J., 1997b. Testing and evaluating the ADMS building effects module *Int. J. Environ. and Poll.*, 8, 3-6, 708-717

Rodriquez, M.A., Carreras-Sospedra, M., Medrano, M., Brouwer, J., Samuelsen, G.S., Dabdub, D., 2006. Air quality impacts of distributed power generation in the South Coast Air Basin of California 1: Scenario development and modeling analysis. *Atmos. Environ.*, 40 (28), 5508-5521.

Rotach, M.W., 1993. Turbulence Close to a Rough Urban Surface Part I: Reynolds Stress. *Boundary-Layer Meteorol.,* 65, 1–28.

Rotach, M.W., 2001. Simulation of urban-scale dispersion using a lagrangian stochastic dispersion model, *Boundary-Layer Meteorol*, 99, 379-410

Rotach, M.W., Gryning, S.E., Batchvarova, E., Christen, A., Vogt, R., 2004. Pollutant dispersion close to an urban surface—the BUBBLE tracer experiment. *Meteorol. Atmos. Phys.*, 87 (1-3), 39–56.

SCAQMD, 2009. 26 Sites with AERMOD-Ready Meteorological Data, South Coast Air Quality Management District, Diamond Bar, CA (http://www.aqmd.gov/smog/metdata/AERMOD_Table2.html).

Schulman, L.L., Strimaitis, D.G., Scire, J.S., 2000. Development and evaluation of the PRIME plume rise and building downwash model, *J. Air Waste Manag. Assoc*. 50 , 378–390.

Seibert, P., Beyrich, F., Gryning, S.E., Joffre, S., Rasmussen, A., Tercier, P., 1998. Mixing layer depth determination for dispersion modelling. European Commission. In: Fisher BEA, Erbrink JJ, Finardi S, Jeannet P, Joffre S, Morselli MG, Pechinger U, Seibert P, Thomson DJ (Eds.) (1998) COST Action 710-Final Report. Harmonisation of the pre-processing of meteorological data for atmospheric dispersion models. L-2985 Luxembourg: European Commission, EUR 18195 EN (ISBN 92- 828-3302-X).

Seibert, P., Beyrich, F., Gryning, S.E., Joffre, S., Rasmussen, A., Tercier, P., 2000. Review and intercomparison of operational methods for the determination of the mixing height, Atmos. Environ., 34, 1001-1027

Sherlock, R.H. and Stalker, E.A., 1940. The Control of Gases in the Wake of Smoke Stacks. *Mech. Eng.* 52, 455-458.

Smith, D.B., 1967. Tracer study in an urban valley (Johnstown, Pennsylvania). M. S. Thesis in Meteorology, Pennsylvania State University, University Park, PA.

Snyder, W.H., 1972. Similarity criteria for the application of fluid models to the study of air pollution meteorology. *Boundary-Layer Meteorol.* 3, p. 113.

Snyder, W.H., 1981. Guidelines for fluid modeling of atmospheric diffusion, Report Number EPA-600/8-81-009, Environmental Protection Agency, Research Triangle Park, NC, 200 pp.

Snyder, W.H., 1985. Fluid modeling of pollutant transport and diffusion in stably stratified flows over complex terrain, *Annu. Rev. Fluid Mech*. 17, 239–266.

Snyder, W.H., Lawson, R.E., 1991. Fluid modelling simulation of stack-tip downwash for neutrally buoyant plumes. *Atmos. Environ.*, 25A, 2837–2850.

Sorbjan, Z., 1986. Local Similarity of Spectral and Cospectral Characteristics in the Stable-Continuous Boundary Layer', *Boundary-Layer Meteorol*. 35, 257.

Sorbjan, Z., 1989. Structure of atmospheric boundary layer, London: Prentice Hall, 317

Steeneveld, G.J., Van de Wiel, B.J.H., Holtslag, A.A.M., 2007. Diagnostic equations for the stable boundary layer height: Evaluation and dimensional analysis, *J. Appl.Meteor, Climate* 46, 212–225.

Stein, A.F., V. Isakov, J. Godowitch, and R.R. Draxler., 2007. A hybrid modeling approach to resolve pollutant concentrations in an urban area, *Atmos. Environ*. 41, pp. 9410-9426.

Stull, R.B., 1983. A heat-flux history length scale for the nocturnal boundary layer. *Tellus*, 35A, 219–230.

Stull, R.B., 1988. An Introduction to Boundary Layer Meteorology. Kluwer Academic Publisher, Boston.

Sutton, O.G., 1947. The problem of diffusion in the lower atmosphere, *QJRMS*, 73, 257-281.

Taylor, G.I., 1921. Diffusion by Continuous movement. *Proc. Lond. Math. Soc. Ser. A*, 20, 196-221.

Taylor, G.I., 1931. Effects of Variation in Density on the Stability of Superimposed Streams of Fluids, *Proc. Roy. Soc. (Lond.), Ser. A* 132, 499–523.

Thompson, R.S., 1993: Building amplification factors for sources near buildings: A wind tunnel study, *Atmos. Environ.*, 15, 2313-2325.

Townsend, A.A., 1956. The Structure of Turbulent Shear Flow , Cambridge University Press, Cambridge , England ,pp. 315.

Van Ulden, A.P., 1978. Simple estimates for vertical diffusion from sources near the ground, *Atmos. Environ*. 12:2125-2129. doi: 10.1016/0004-6981(78)90167-1.

Van Ulden, A.P., Holtslag, A. A. M., 1985. Estimation of Atmospheric Boundary Layer Parameters for Diffusion Applications. *J. Appl.Meteor*. 24(11):1196-1207.

Vardoulakis, S., Valiantis, M., Milner, J., ApSimon, H., 2007. Operational air pollution modelling in the UK--Street canyon applications and challenges. *Atmos. Environ.*, 41, 4622-4637.

Venkatram, A., 1980a. Estimating the Monin-Obukhov length in the stable boundary layer for dispersion calculations, *Boundary-Layer Meteorol*., 19, 481-485

Venkatram, A., 1980b, Dispersion from an Elevated Source in a Convective Boundary Layer, *Atmos. Environ*. 14, 1-10.

Venkatram, A., 1984. The uncertainty in estimating dispersion in the convective boundary layer. *Atmos. Environ*. 18, 307–310.

Venkatram, A., 1992. Vertical dispersion of ground-level releases in the surface boundary layer. *Atmos. Environ.*, 26A, 947-949.

Venkatram, A., 1999. Applying a framework for evaluating the performance of air quality models. Proceedings of the Sixth International Conference on Harmonisation within Atmospheric Dispersion Modeling for Regulatory Applications, Rouen, France, 11-14 October, 1999.

Venkatram, A., 2004. The role of meteorological inputs in estimating dispersion from surface releases, *Atmos. Environ.* 38. 2439-2446.doi: 10.1016/j.atmosenv.2004. 02.005

Venkatram, A., 2008. Computing and displaying model performance statistics. *Atmos. Environ.*, 24:6862–6868

Venkatram, A., Cimorelli, A.J., 2007. On the role of nighttime meteorology in modeling dispersion of near surface emissions in urban areas. *Atmos. Environ.* 41(4):692-704.

Venkatram, A., Isakov, V., Pankratz, D. and Yuan, J., 2005. Relating plume spread to meteorology in urban areas. *Atmos. Environ*. 39(2):371-380.

Venkatram, A., Isakov, V., Pankratz, D., Heumann, J., Yuan, J., 2004b. The analysis of data from an urban dispersion experiment. *Atmos. Environ.*, 38 (22), 3647-3659.

Venkatram, A., Isakov, V., Yuan, J., Pankratz, D., 2004a. Modeling Dispersion at Distances of Meters from Urban Sources. *Atmos. Environ.*, 38 (28), 4633-4641.

Venkatram, A., Paine, R., 1985. A model to estimate dispersion of elevated releases into a shear-dominated boundary layer, *Atmos. Environ.*, 19, 11, 1797-1805, doi: 10.1016/0004-6981(85)90006-X.

Venkatram, A., Princevac, M. 2008, Using measurements in urban areas to estimate turbulent velocities for modeling dispersion. *Atmos. Environ.*, 42 (16), 3833–3841.

Vutukuru, S., Carreras-Sospedra, M., Brouwer, J., Dabdub D., 2011. Future impacts of distributed power generation on ambient ozone and particulate matter concentrations in the San Joaquin Valley of California. *J. Air & Waste Manage. Assoc.* 61, (2011) 1319-1333. doi: 10.1080/10473289.2011.603990

Walker, D.A., 1987. A fluorescence technique for measurement of concentration in mixing liquids. *Journal of Physics*, 20: 217-24

Weil, J.C., 1988. Plume Rise, In: Venkatram, A. and Wyngaard, J.C., Editors, 1988. Lectures in Air Pollution Modeling. *Am. Met. Soc.*, Boston, MA, 119–166.

Wilhelm, M., Ritz, B., 2003. Residential proximity to traffic and adverse birth outcomes in Los Angeles County, California, 1994-1996, *Environmental Health Perspectives*, 111, 207-216

Woods, A.W., 1997. A note on non-Boussinesq plumes in an incompressible stratified environment. *J. Fluid Mech*. 345, 347–356.

Wyngaard, J. C., 1973, On Surface Layer Turbulence, Workshop on Micrometeorology, *Am. Met. Soc.*, Boston, Mass., pp. 101-149.

Yamada, T., 1979. Prediction of the nocturnal surface inversion height. *J. Appl.Meteor.*, 18, 226–531.

Yee, E., Gailis, R.M., Hill, A., Hilderman, T., Kiel, D., 2006. Comparison of wind-tunnel and water-channel simulations of plume dispersion through a large array of obstacles with a scaled field experiment. *Boundary-Layer Meteorol.* 121, 389–432.

Yu, T.W., 1978. Determining height of the nocturnal boundary layer. *J. Appl.Meteor.*, 17, 28–33

Zilitinkevich, S.S., 1972. On the Determination of the Height of the Ekman Boundary Layer, *Boundary-Layer Meteorol.*, 3, 141–145.

Zilitinkevich, S.S., Baklanov, A., 2002. Calculation of the Height of the Stable Boundary Layer in Practical Applications, *Boundary-Layer Meteorol*.,105, 389-409.

Zilitinkevich, S.S., Baklanov, A., Rost, J., Smedman, A.S., Lykosov, V., Calanca, P., 2002. Diagnostic and Prognostic Equations for the Depth of the Stably Stratified Ekman Boundary Layer, *QJRMS,* 128, 25–46.

APPENDIX A: DEVELOPMENT AND APPLICATION OF METHODS TO ESTIMATE THE AIR QUALITY IMPACT OF URBAN LOW-LEVEL BUOYANT SOURCES OVER MULTIPLE LENGTH SCALES[§]

A1. Introduction

The air quality in an urban area is affected by a large number of sources, such as vehicles, distributed over the urban area. Thus, the contribution of sources within meters from an urban receptor might be comparable to that of sources outside the local area of interest. In principle, an air quality model can be used to estimate the contributions of all the urban sources to concentrations at a receptor. However, the large number and variety of sources in an urban area necessitates computational resources that can become impractical even with current computers, especially when it is necessary to conduct sensitivity studies over long averaging times. The current approach to this problem is to use models applicable to several scales so that sources at different distances from the area of interest can be treated with different levels of source aggregation. The concentration at a receptor has three components: a regional contribution computed from a long-range transport model with a grid spacing of the order of tens of kilometers, an urban "background" contribution from sources aggregated over kilometer sized grids, and a local contribution from models that estimate concentrations at meters from a receptor.

This chapter focuses on a model that estimates urban "background" concentrations of NO_x, NO_2, and O_3, averaged over a scale of the order of kilometers. These species can

[§] The following work represents an extension to the work done by Dr. Qiguo Jing at the University of California, Riverside. Part of this appendix is also presented in Dr. Jing's Ph.D. dissertation.

be estimated from photochemical models such as CMAQ (Byun and Schere, 2006) and UCI-CIT model (Carreras et al., 2004), but their application becomes a computational burden if concentrations are required over a year. The simple urban background model (UBM) developed by Berkowicz (2000) addresses this problem through two simplifications: a straight-line steady dispersion model and chemistry based on photo-stationarity neglecting the role of hydrocarbons. The model presented here is intermediate between comprehensive photochemical models and the simple UBM. It treats unsteady meteorological conditions with trajectories that reflect space and time varying winds, and it reduces the computational requirements of photochemical models by separating transport and chemistry using a method described in Venkatram et al. (1998). The model is evaluated with data from measurements made in Los Angeles.

A2.The Lagrangian model

The model, based on that proposed by Venkatram and Cimorelli (2007), computes the concentrations at a receptor by following the history of an air parcel that reaches a receptor of interest every hour. The history of the air parcel is traced back 24 hours through back trajectories calculated using surface winds measured at meteorological stations. To facilitate the use of the model, the meteorological inputs are taken directly from the surface input files used by AERMOD (Cimorelli et al., 2005).

The air parcel has horizontal dimensions of 5 km by 5 km, and a height that depends on the local mixed layer height. Emissions are injected into the box and mixed through its volume as the box moves over the urban area, which is described with a

gridded emission inventory of NO_x and VOC. The concentrations are stepped from the (i - 1)th to the i^{th} time step through

$$C_i = C_{i-1} \min\left(\frac{z_{i-1}}{z_i}, 1\right) + \frac{\Delta m_i}{z_i}, \quad \text{(A.1)}$$

where z_i is the mixed layer height. The term within the parenthesis on the right hand side of the equation ensures that the concentration does not increase when the mixed layer decreases during a time step.

The mass of pollutant injected per unit surface area of the air parcel is $\Delta m_i = q_i(\vec{r}, \tau) f_h \Delta t$, where $q_i(\vec{r}, \tau)$ is the emission density at the location of the parcel, $\vec{r}$, injected at time, τ, from the initiation of the trajectory, and Δt is the time step of the trajectory calculation.

The incremental concentration during the last hour of the air parcel's path is computed with a steady state dispersion model that accounts for incomplete vertical mixing,

$$\Delta C_i = \sqrt{\frac{2}{\pi}} \frac{q}{\sigma_w} \ln\left(1 + \frac{\sigma_w \Delta t}{h}\right), \quad \text{(A.2)}$$

where σ_w is the standard deviation of the vertical velocity fluctuations, and h is the initial vertical spread of surface emissions. The equation is modified (Venkatram and Cimorelli, 2007) if the pollutant is well mixed through the boundary layer during the last time step before the parcel reaches the receptor.

In addition to concentrations, the model also calculates the effective age of each species in the box (Venkatram et al. 1994, 1998). The effective age of a molecule is the

time taken for the molecule to travel from source to receptor. We can build upon this simple idea to formulate a conservation equation for species age that accounts for complex flows and emissions in an Eulerian grid model. This equation allows the calculation of age in addition to concentration of a species at every receptor.

In this simple Lagrangian model, the formulation for the species age, A_i, reduces to

$$A_i = A_{i-1}\left(1 - \frac{\Delta m_i}{m_i}\right) + \Delta t\left(1 - \frac{1}{2}\frac{\Delta m_i}{m_i}\right). \quad \text{(A.3)}$$

In the absence of fresh emissions, that is $\Delta m_i = 0$, we obtain the expected result: $A_i = A_{i-1} + \Delta t$. Note that fresh emissions always decrease the effective age of the species within the parcel.

Then, the chemical transformation of this species is estimated by reacting it with other species in a box with initial concentrations corresponding to those in the absence of chemistry. The time period for chemical calculations is specified by the end time corresponding to the time of interest and a start time, which is the end time minus the species age. The chemical calculation is performed over the maximum of the ages of the species in the air parcel. The chemistry accounts for the variation of photolysis rates with time of day.

The chemistry uses the Carbon Bond IV mechanism in which the volatile organic compounds (VOC) are assumed to be a mixture typical of ambient measurements made in Los Angeles; the VOC is distributed among 8 surrogate species and one inert species.

A3. Evaluation of BACKGROUND model

The model is applied to estimating NO_x, NO_2, and O_3 concentrations in the South Coast Air Basin (SoCAB) of Los Angeles, depicted in Figure A.1 The left panel of the figure shows the NO_x emissions developed by Samuelsen et al. (2005) for the SoCAB. The right panel shows the assumed diurnal variation of NO_x emissions, which roughly corresponds to traffic volume. The background ozone is taken to be 20 ppb. VOC emissions are also obtained from the Samuelsen et al. (2005) for the SoCAB. Model estimates are compared with NO_x concentrations measured at 21 monitoring stations operated by CARB, which are numbered in the left panel of Figure A.1. A comparison between the daily (24hr) NO_x and VOC emissions in the SOCAB are shown in Figure A.2.

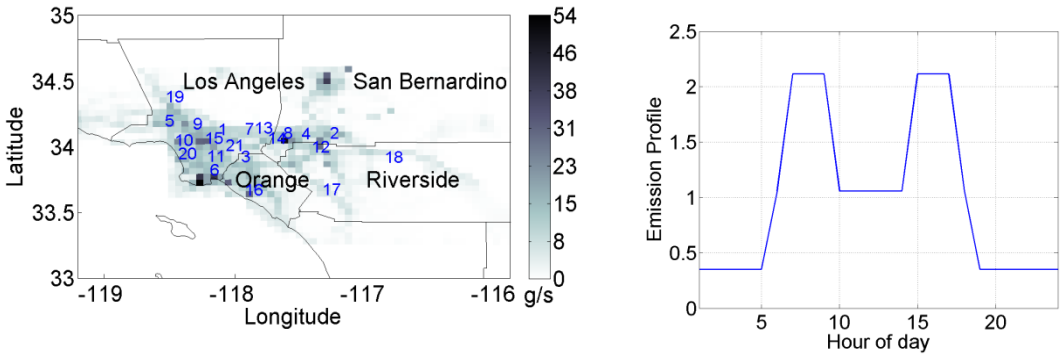

Figure A.1: Gridded NO_x emissions and monitoring stations located in the South Coast Air Basin, Los Angeles. The right panel shows the assumed temporal profile of NO_x emissions (from Jing, 2011).

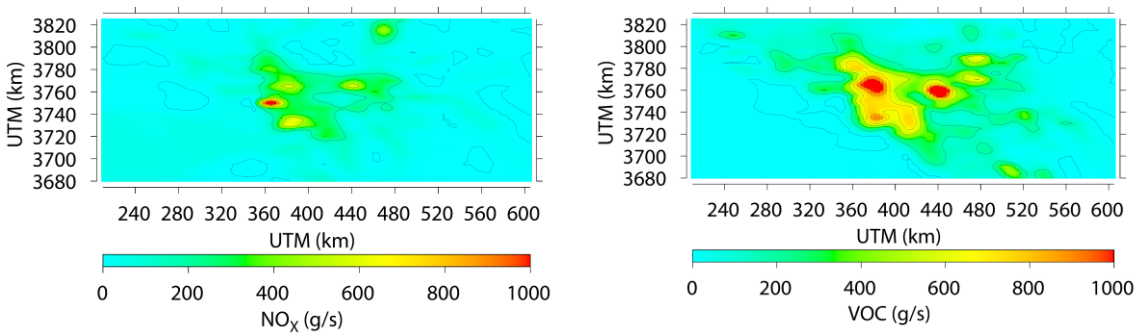

Figure A.2: Daily (24-hr) NO_x (left panel) and VOC (right panel) emissions (g/day).

The model was run with surface meteorological data corresponding to 2007, measured at 26 meteorological stations operated by the South Coast Air Quality Management District. Model performance is described in terms of the geometric mean and standard deviation, m_g, s_g of the ratio of the estimated to the observed concentrations (Venkatram et al. 2005). FAC2 refers to the fraction of the model estimates within a factor of two of the corresponding observations.

First, we examined the performance of the UBM (Berkowicz, 2000) and lagrangian model describing the monthly (September) averaged background concentrations over 21 receptors for NO_x, NO_2, and O_3 (Figure A.3). As it can be seen, the UBM model substantially overestimates the NO_x (top left panel) and NO_2 (middle left panel) concentrations while it underestimates the O_3 (bottom left panel) concentrations as indicated by value of m_g. However, as it is illustrated by the right panels of Figure 3, the lagrangian model shows a reasonably well performance describing the background concentrations since both NO_x and NO_2 predictions are within a factor of two with a little bias of 10 - 13 % and O_3 concentrations shows almost same performance as the UBM does.

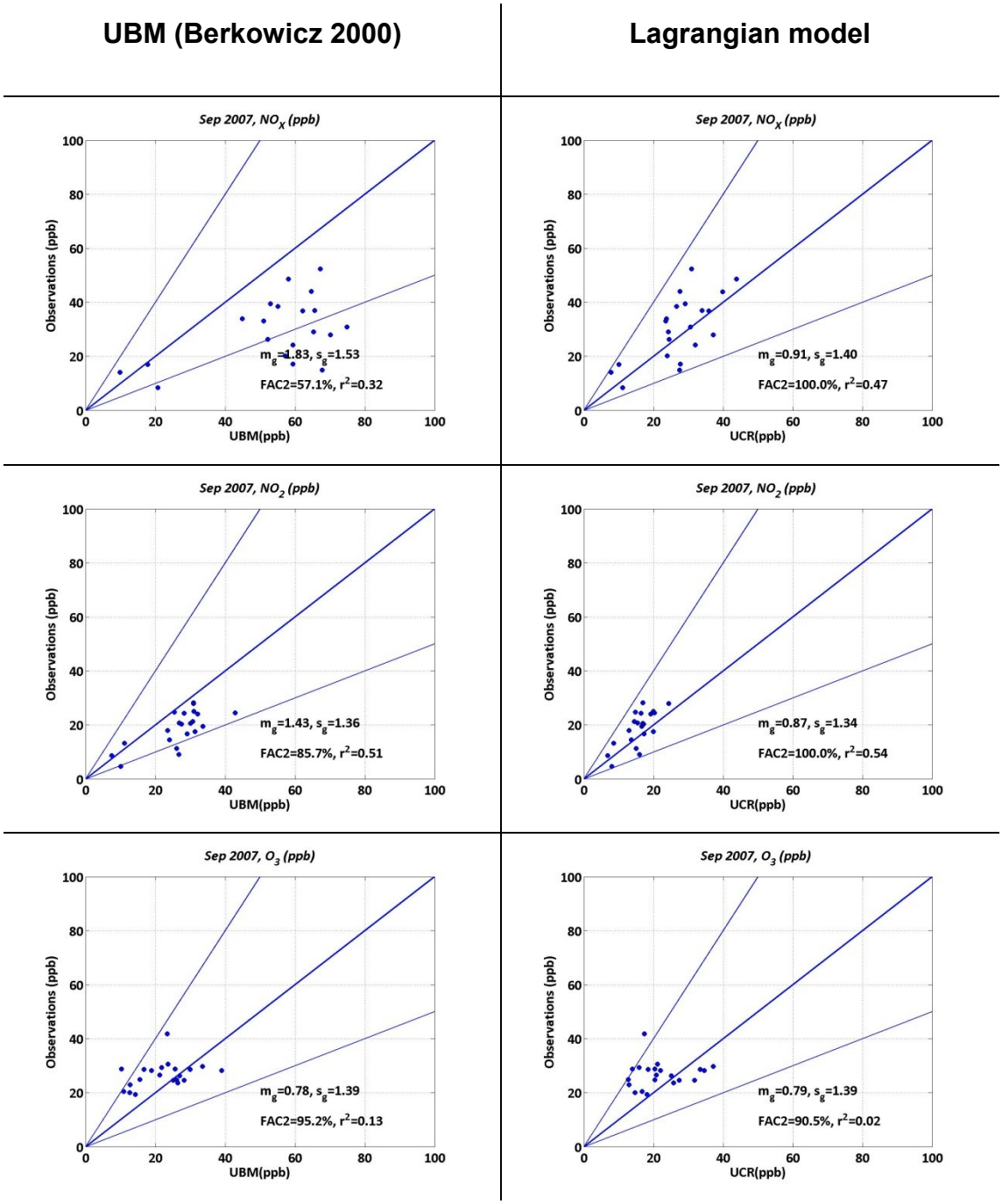

Figure A.3: Comparison of modeled and measured monthly averaged NO_x , NO_2 , and O_3 concentrations at 21 sites in the SoCAB. Both UBM (Berkowicz 2000) and Lagrangian model are tested.

Next, we examined the performance of the lagrangian model by considering two sites, one on the west and the other located in the east of the Los Angeles basin. The top

two panels of Figure A.4 show that the modeled NO_2 and NO_x concentrations, averaged over a month, are well correlated with the corresponding observations. However, the model overestimates the NO_2 and NO_x during the winter and fall months at the San Bernardino site as seen in Figure A.4. The bottom panels compare the modeled and observed maximum daily ozone concentrations at these stations. Although the scatter is not small, the model shows little bias as indicated by m_g values close to unity.

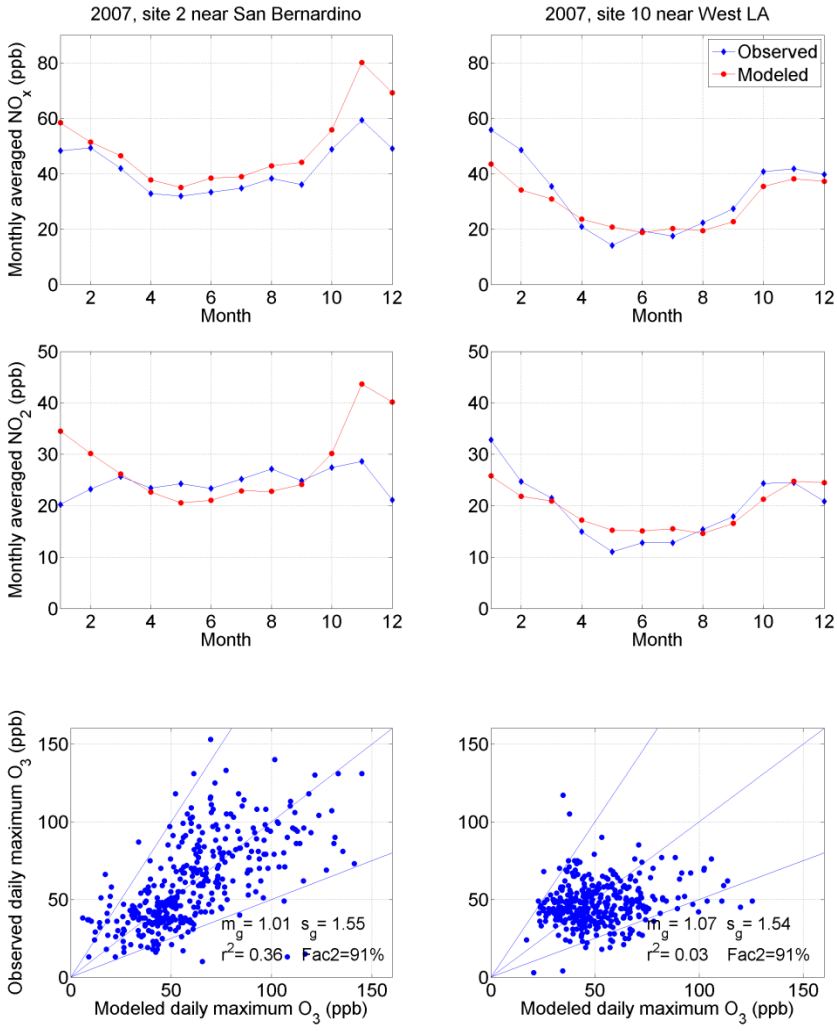

Figure A.4: Monthly averaged NO_x, NO_2, and daily maximum ozone concentrations compared with observations at two sites in the SoCAB (from Jing, 2011)

Figure A.5 shows that the model overestimates NO_2 and NO_x concentrations in the early morning hours at the San Bernardino site. This might be related to the uncertainty in estimating the mixed layer height during these hours. It could also be associated with the assumed temporal profile of NO_x emissions.

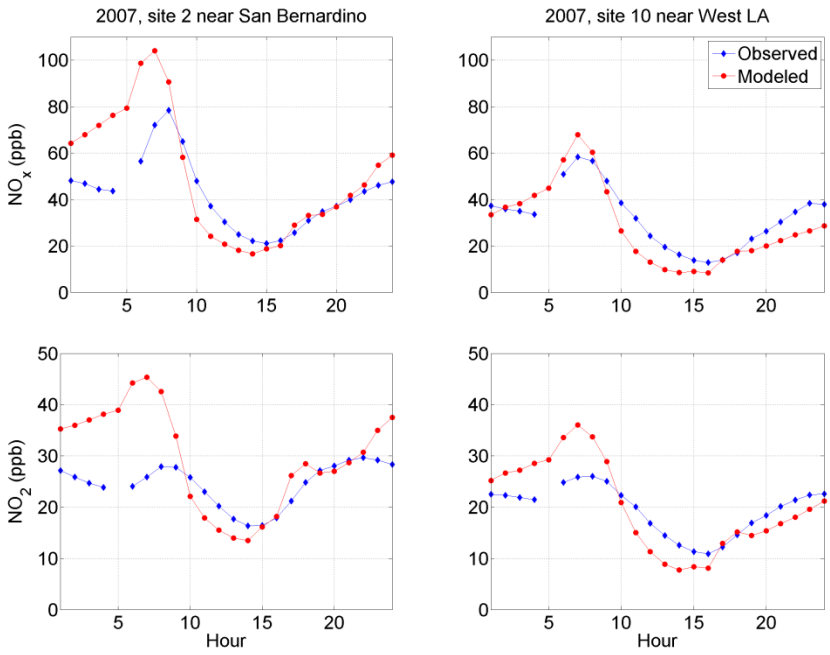

Figure A.5: Averaged daily variation of NO_x and NO_2 compared with observations at two sites in the SoCAB (from Jing, 2011)

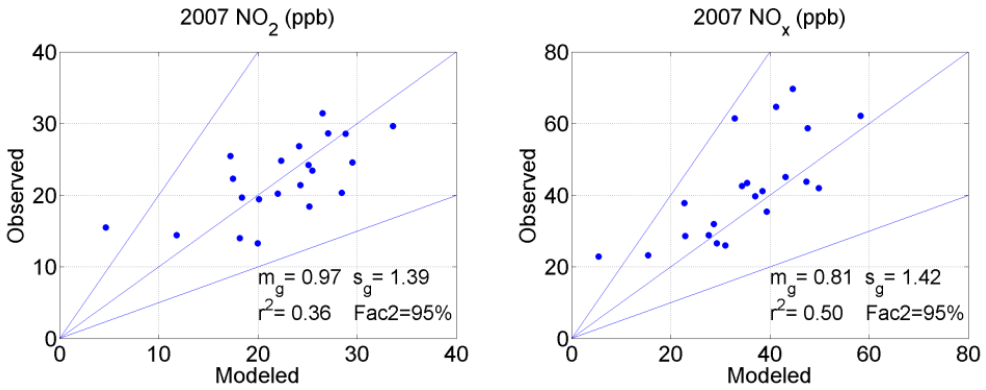

Figure A.6: Comparison of modeled and measured annually averaged NO_2 and NO_x concentrations at 21 sites in the SoCAB (from Jing, 2011)

Figure A.6 indicates that the model provides a satisfactory description of the spatial variation of the concentrations of these species across the 21 stations in the SoCAB.

UCI-CIT Model

The University of California, Irvine - California Institute of Technology (UCI-CIT) model is a regional atmospheric transport model used to predict the air quality of Southern California. The UCI-CIT model solves numerically mass conservation equations for modeled species on a computational grid to obtain spatially and temporally resolved concentrations of gas and aerosol species of interest (Dabdub 2008). Atmospheric gas-phase chemistry is modeled using the Caltech Atmospheric Chemical Mechanism (CACM) (Griffin et al., 2002).

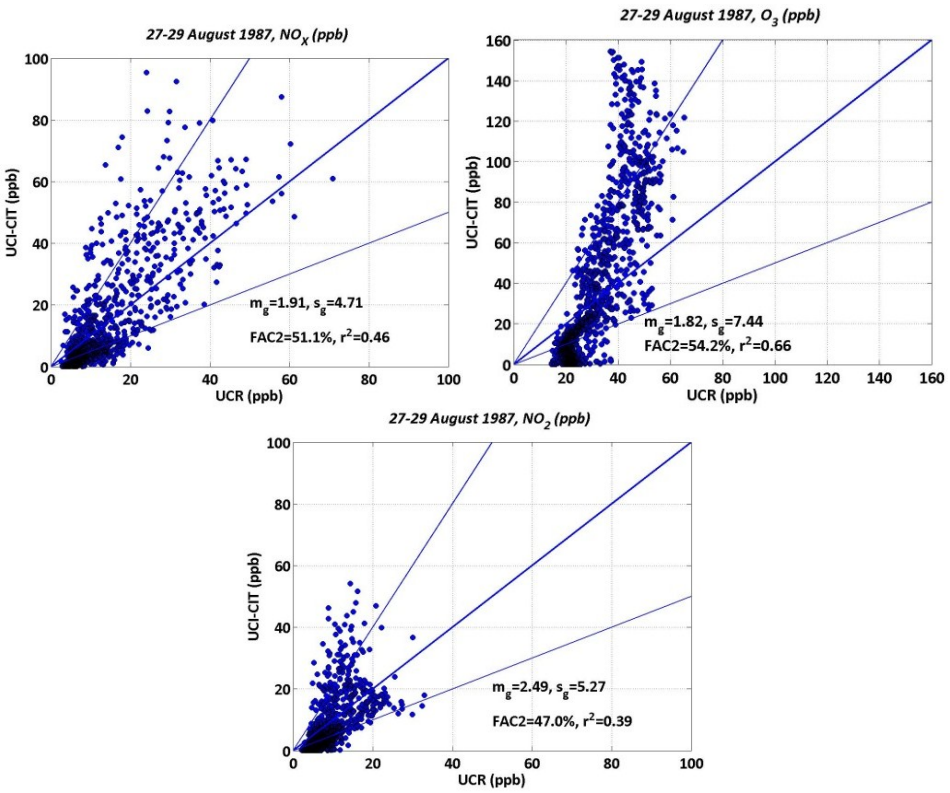

Figure A.7: Averaged (72-hour) concentrations of NO_x, NO_2, and O_3 for 994 stations in the SOCAB from 27 -29 August 1987.

In addition to the background model proposed in this report, the performance of UCI-CIT model was also evaluated for the three consecutive days from August 27-29, 1987. Results from the UCI-CIT model were obtained for 994 stations located in SOCAB. These results were compared with those obtained from the Lagrangian model (Figure A.7). As it can be seen in Figure A.7, UCI-CIT model tends to over predict the NO_x and NO_2 concentrations. In addition, O_3 concentrations predicted by UCI-CIT vary from 0 to 160 ppb while those predicted by UCR are varying from a minimum of 20 to a maximum of 60 ppb showing a smaller variation in concentrations.

Generic Reaction Set (GRS) Chemistry Module

In addition to Carbon Bond IV mechanism, which is a relative complex chemistry model, we implemented a scheme referred to as the GRS chemistry module. This module is an empirical approximation of all the processes that lead to production of radicals (RP) from the volatile organic compounds (VOC) through photo oxidation. Using these radicals, *NO* is converted to NO_2, and causes the net production of O_3. This module reduces the complicated chemistry reaction in the atmosphere to seven reactions among seven species as follow:

$$ROC + h\nu \rightarrow RP + ROC \quad \text{(R1)}$$

$$RP + NO \longrightarrow NO2 \quad \text{(R2)}$$

$$NO_2 + h\nu \rightarrow NO + O_3 \quad \text{(R3)}$$

$$NO + O_3 \rightarrow NO_2 \quad \text{(R4)}$$

$$RP + RP \rightarrow RP \quad \text{(R5)}$$

$$RP + NO_2 \rightarrow SGN \quad \text{(R6)}$$

$$RP + NO_2 \rightarrow SNGN \quad \text{(R7)}$$

where

ROC= reactive organic compounds

RP = radical pool

SGN=stable gaseous nitrogen product

SNGN= stable non-gaseous nitrogen product

These reaction and the corresponding reaction rates are defined as:

R1. Radical production from photo-oxidation of ROC

$k_1 = 0.0067\ k_3\ f(T)$ where $f(T) = \exp\left(-1000\left[\frac{1}{T} - \frac{1}{316}\right]\right)$

R2. Oxidation of nitric oxide by radicals

$k_2 = 3.58\times10^6\ T^{-1}$

R3. Photolysis of nitrogen dioxide to nitric oxide

$k_3 = \exp\left(-\frac{0.575}{sin(\theta)}\right)$ where θ is the sun elevation angle.

R4. Nitric oxide-ozone titration reaction

$k_4 = 9.24 \times 10^5\ T^{-1} \exp\left(-\frac{1450}{T}\right)$

R5. Radical pool sink through recombination to stable products

$k_5 = 10200$

R6. Sink for nitrogen dioxide to stable gaseous nitrates

$k_6 = 120$

R7. Sink for nitrogen dioxide to stable non-gaseous nitrates

$k_7 = 120$

Solving these set of stiff differential equations numerically; we implemented this model into the lagranigian transport model and predicted the NO_x, NO_2, and O_3 concentration for 21 receptor in SOCAB (Figure A.1) for September 2007 (Figure A.8).

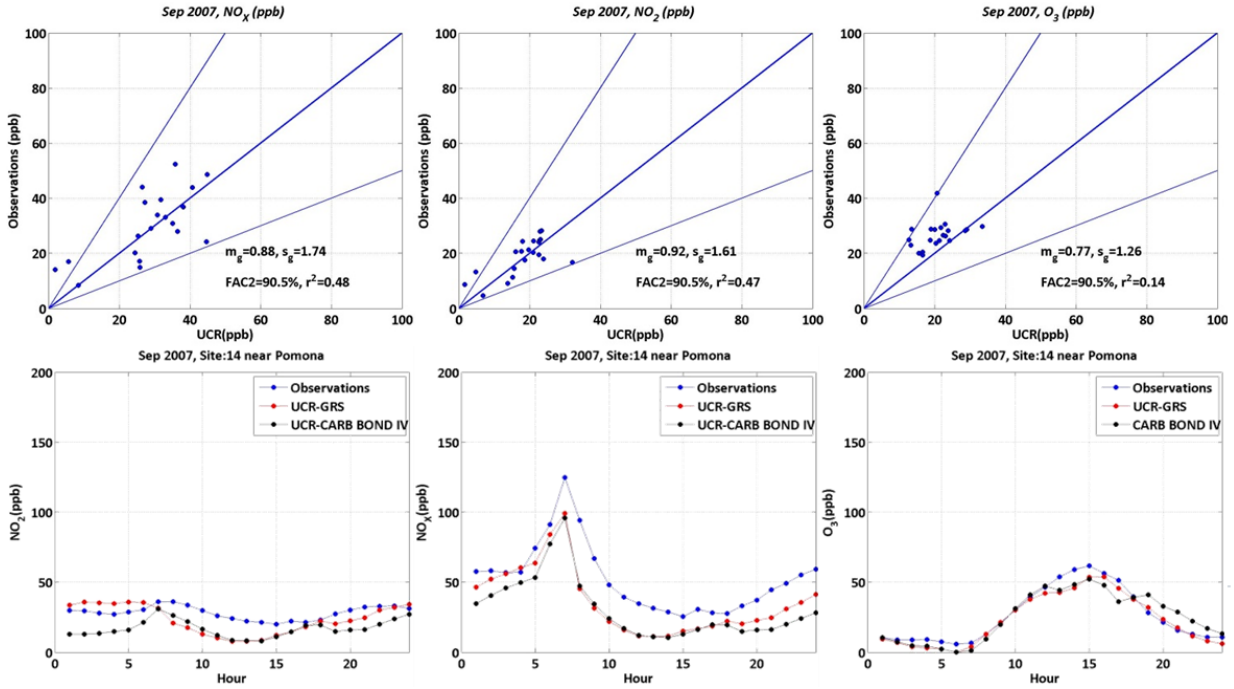

Figure A.8: Monthly averaged concentrations predicted using the GRS chemistry module over 21 receptor in SOCAB (top panel). Comparison between the observations, transport model with GRS and Carbon Bond IV chemistry module (bottom panel).

As it can be seen, despite the simplicity of the GRS chemistry module, it performs reasonably well comparing to Carbon Bond IV model, which has been used earlier. Therefore, this suggests that the most important factor affecting the concentrations is transport scheme rather than the chemistry itself.

A4. Investigating the impact of Distributed Power Generators on the concentrations in SOCAB

Following the evaluation of the background model proposed in this report, the concentrations of the NO_x, NO_2, and O_3 in the presence and absence of the DGs (under EHP scenario from Samuelson et al., 2005) were predicted using meteorology from 27 - 29 August 1987. The increase/ decrease in pollutant concentrations were calculated and compared with those obtained from the UCI-CIT (Figure A.9).

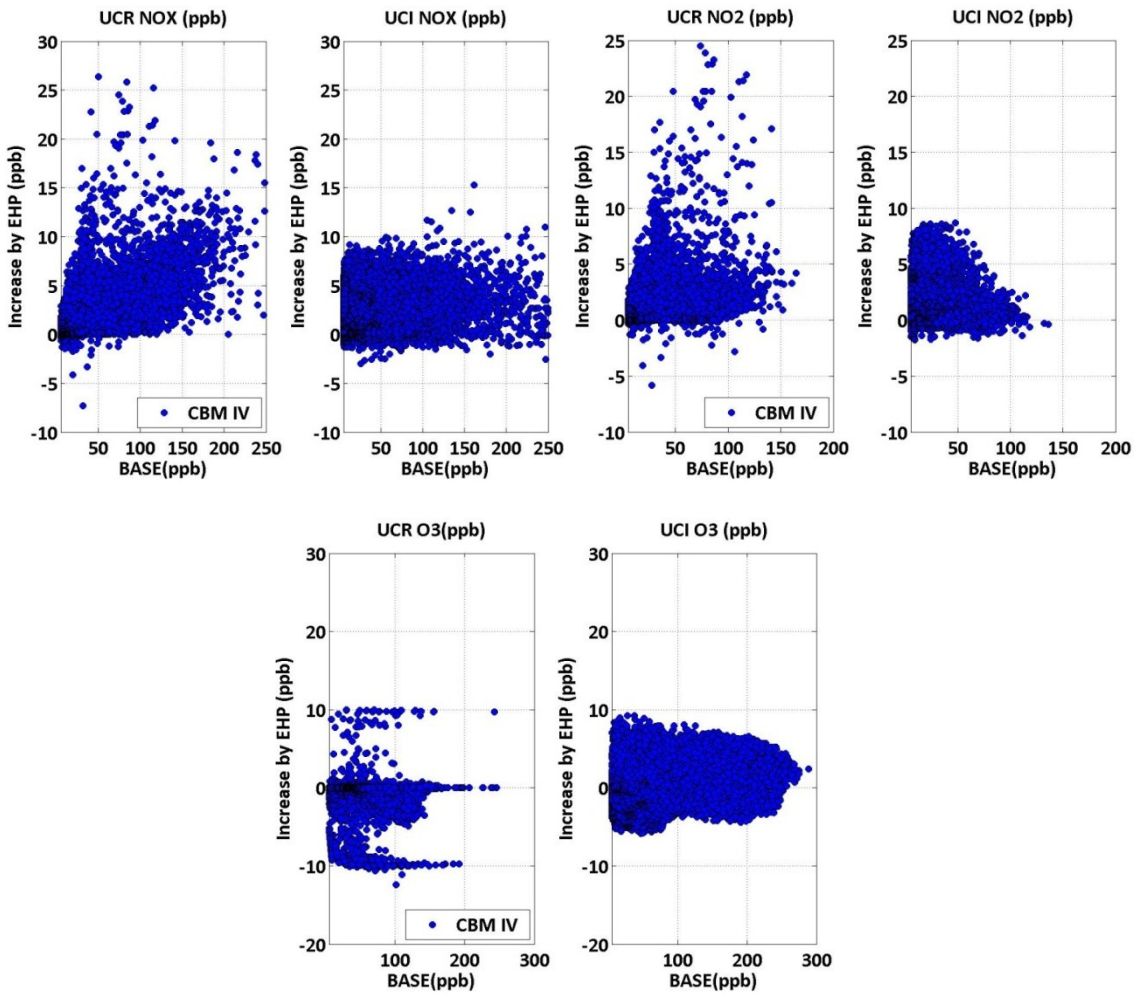

Figure A.9: The impact of DGs on the concentrations of NO_x, NO_2, and O_3 under EHP scenario.

As it can be seen, both models (UCI-CIT on the right panel and UCR on the left panel) show negligible increases (<10ppb for NO_x and O_3 and <20ppb for NO_x) in background concentrations associated with the EHP. The predicted impact of DGs on NO_x and NO_2 by the UCI-CIT model is slightly lower than the UCR model. As it can be seen in the bottom panel of Figure A.9, O_3 concentrations are predicted to be substantially decreased by the UCR model, which illustrates the limitations on the production of NO_2 by the reaction of NO and O_3 due to the lack of available O_3. The

impacts of DGs on concentrations at different locations are more clearly shown in Figure A.10. The emission color-map is added for better interpretations of concentration increase/decrease.

One of the main reasons for the extra small impact of DGs is their relatively small emissions comparing to base emissions. The comparison between base emissions and the increase in emissions are shown in Figure A.11. As it is shown, the average increase in emission is almost less than 40 g day^{-1} for NO_x, and less than 10 g day^{-1} for VOC emissions, which shows the negligible impact of DGs on total NO_x and VOC emission in SOCAB.

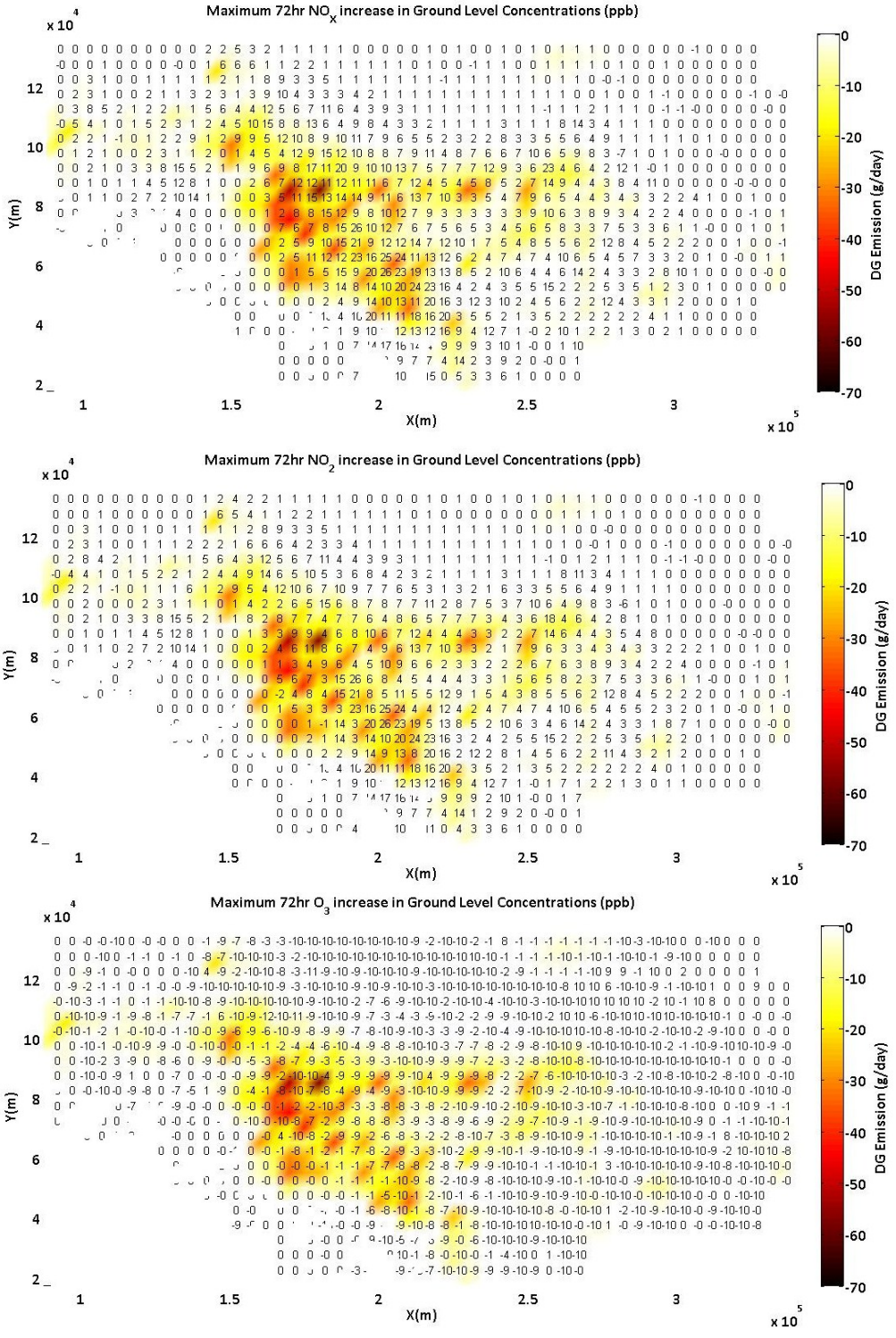

Figure A.10: Maximum increase/decrease in ground level concentrations of NO_x, NO_2, and O_3 under EHP scenario with ***CBM IV*** as the chemistry module.

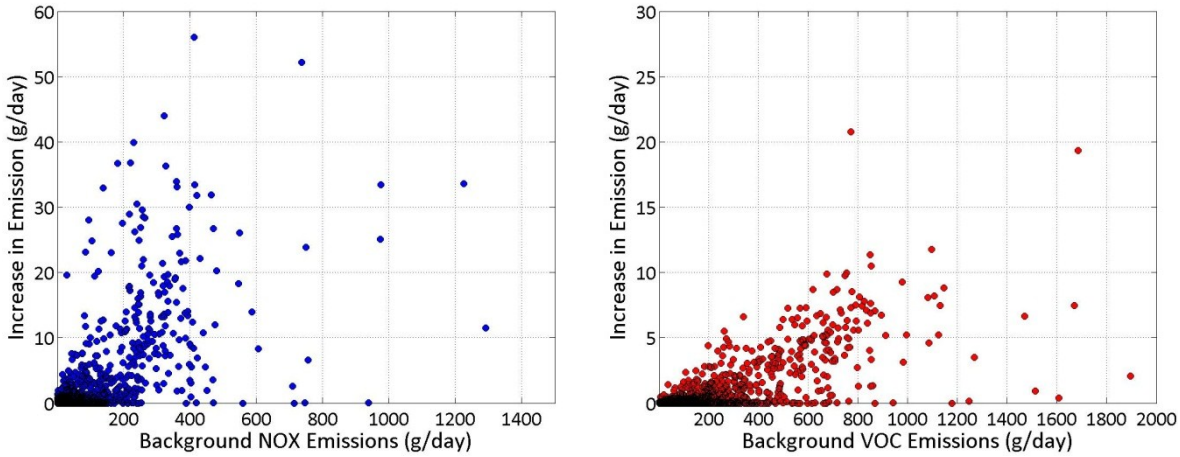

Figure A.11: increase in total daily emissions associated with surface sources and DGs (under EHP Scenario) comparing to the background (Base) emissions for NO_x (left panel) and VOC (right panel).

Although these models are showing the relatively small impact of DGs on background concentrations, the short-range impact of these sources are not considered in these prediction. The impact of DGs on the background concentrations were also investigated using the GRS chemistry model, in order to observe the sensitivity of the DG impacts on chemistry module that has been used. Results from this analysis are shown in Figure A.12.

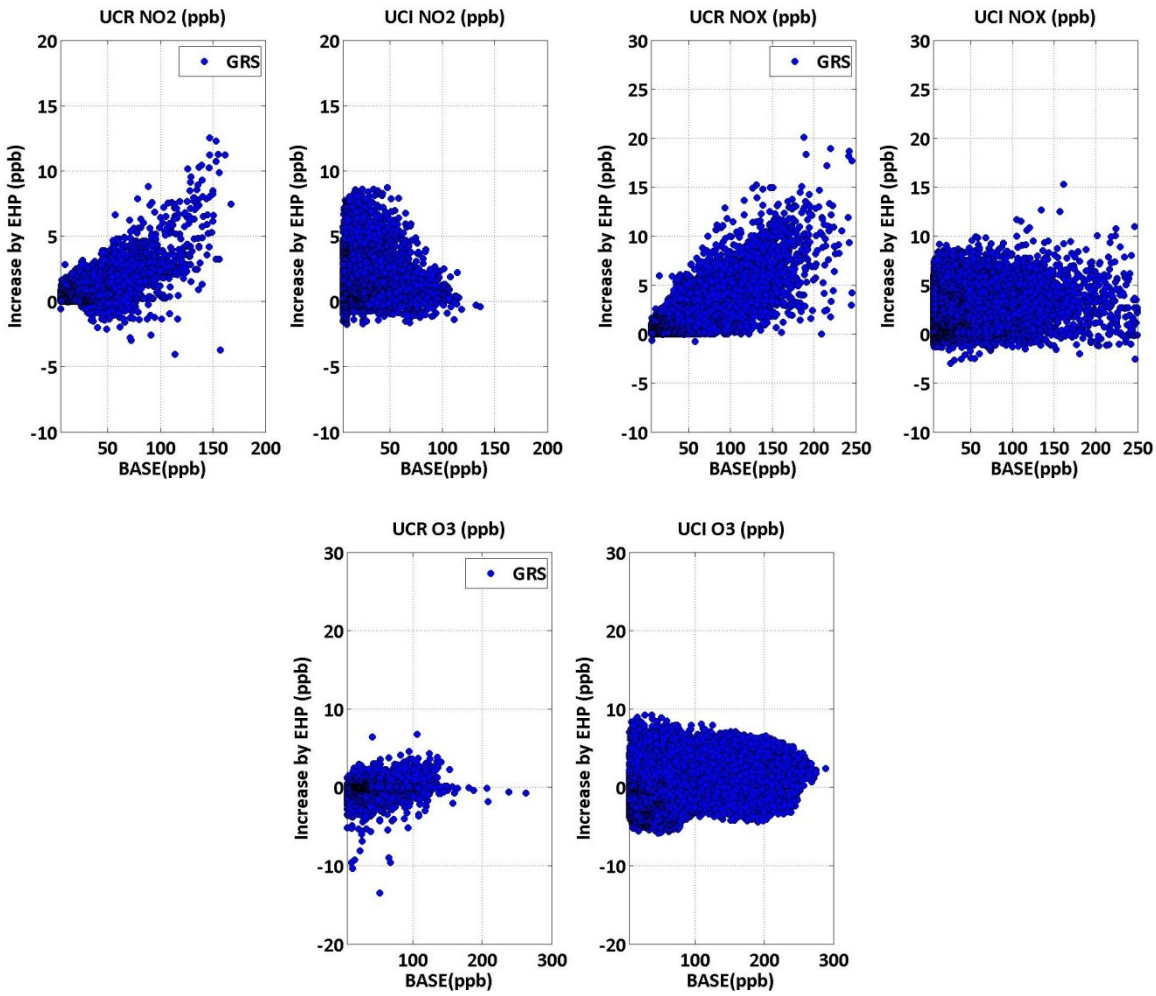

Figure A.12: The impact of DGs on the concentrations of NO_x, NO_2, and O_3 under EHP scenario using GRS chemistry set.

As can be seen, significant differences on the impact of DGs on O_3 concentrations can be seen when the chemistry module is changed from CBM IV to GRS , although the concentration prediction from both chemistry models are in good agreement (Figure A.13). However, similar to CBM IV, GRS chemistry model show an increase in NO_2 concentrations which in most cases is higher than what UCI-CIT model predicts. The reason to this higher impact can be explained through the higher impact of NO_x predicted

by lagrangian model which mainly goes back to the approach behind the transport model which plays the major role in determining the NO_x concentrations.

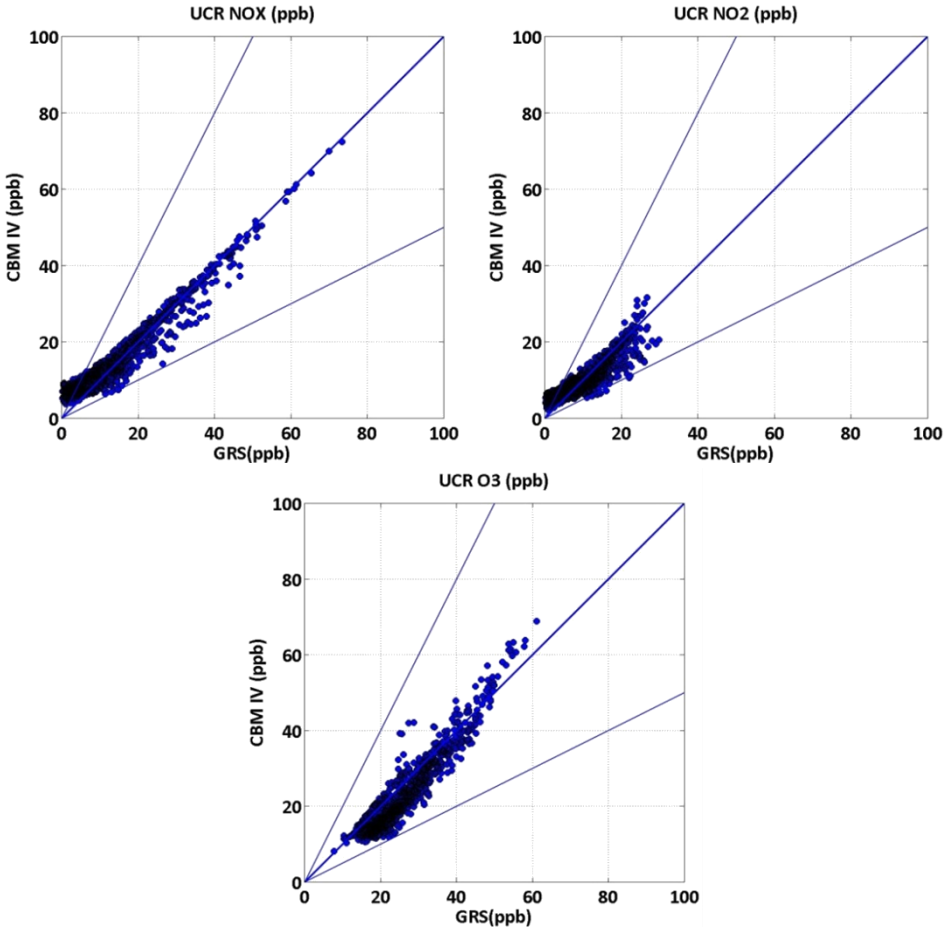

Figure A.13: Comparison of different chemistry modules (GRS vs. CBM IV) in predicting the concentrations of NO_x, NO_2, and O_3 under base scenario.

A5. Hybrid Modeling

Following the modeling of the background concentrations, the combined short-range and long-range impact of DGs on ground level concentration, can be predicted through a hybrid model consisting of AERMOD (Cimorelli et al., 2005) as a short-range dispersion model with the back-ground model explained in previous section.

Using AERMOD, the hourly maximum ground level concentrations associated with DGs at each grid is calculated. In this set of calculation, the ground level concentration is only affected by DGs inside the grid of interest, and any DG outside this grid does not have any impact. The spatial resolution of 50 m is used for prediction of ground level concentrations in each grid point. Following these calculations, the maximum hourly concentration is selected in each grid point. Following a sub-grid scale chemistry method proposed by Hess and Cope (1989) for photochemical modeling, O_3 and NO_2 concentrations are predicted using the background concentrations which has been calculated earlier through the background model and then will be added to the background concentrations in that grid point for combined short and long range impact analysis. The model suggested by Hess and Cope (1989) assumes that hydrocarbons impacts at the source are negligible. Thus, considering only NO_x and O_3 the chemistry can be simplified as,

$$NO_2 + h\nu \rightarrow^{k1} NO + O \quad \text{(R1)}$$

$$O + O_2 + M \rightarrow^{k2} O_3 + M \quad \text{(R2)}$$

$$O_3 + NO \rightarrow^{k3} NO_2 + O_2 \quad \text{(R3)}$$

where $h\nu$ is the solar radiation energy and k_1, k_2 and k_3 are the reaction rates. Considering the nitrogen and excess oxygen balance as,

$$NO_x(t) = NO_2(t) + NO(t) = D(t)NO_x(0) + [1 - D(t)]NO_x^b \quad \text{(A.4)}$$

$$O_x(t) = NO_2(t) + O_3(t) = D(t)[NO_2(0) + O_3(0)] + [1 - D(t)](NO_2^b + O_3^b) \quad \text{(A.5)}$$

where $NO_x(0)$ is the concentration at the source, superscript b denotes the background values and dilution $D(t)$ is defined as,

$$D(t) = \pi r_s^2/[4\pi\sigma_y\sigma_z] \quad \text{(A.6)}$$

where r_s is radius of the stack. Hence, assuming that the O_2 , NO and O_3 are in photo-stationary equilibrium, one can writes that,

$$NO_2 = \left(\frac{k_3}{k_1}\right)[NO][O_3] \quad \text{(A.7)}$$

Solving equations (A. 4 - 7),

$$NO_2(t) = 0.5\left[\left(a + b + \frac{k_1}{k_3}\right)^2 - 4ab\right]^2 \quad \text{(A.8)}$$

$$NO(t) = a - NO_2(t) \quad \text{(A.9)}$$

$$O_3(t) = b - NO_2(t) \quad \text{(A.10)}$$

where,

$$a = D(t)NO_x(0) + [1 - D(t)]NO^b \quad \text{(A.11)}$$

$$b = D(t)NO_2(0) + [1 - D(t)]\left(NO_2^b + O_3^b\right) \quad \text{(A.12)}$$

However, the main unknown in these expressions is the amount of dilution. The σ_y and σ_z defined in equation (A. 6) are the instantaneous plume spread (σ_r) which can be modeled following Plume Volume Molar Ratio Method (PVMRM) for modeling the conversion of NO_x to NO_2 in AERMOD

$$\sigma_{ra} = \frac{a_1\varepsilon^{\frac{1}{2}}t^{\frac{3}{2}}}{1+a_2t/T_{Lr}} \quad \text{(A.13)}$$

where a_1 is a constant (= 0.57), a_2 = 0.62 a_1, t is the plume travel time (= x/U), and T_{Lr} is a Lagrangian time scale for relative dispersion defined as

$$T_{Lr} = a_{r1}\frac{z_i}{\sigma_w} \quad \text{(A.14)}$$

where a_{r1} = 0.46, z_i is the mixing height, and σ_w is the standard deviation of vertical component of turbulent velocity. The turbulence dissipation rate, ε, is calculated as follows, based on Weil (1996):

$$\varepsilon = b\sigma_w^2/T_{Lr} \quad \text{(A.15)}$$

where b is a constant (= 0.78).

Using this instantaneous plume spread, we calculated the weighted average dilution rate over different sources. Since the method suggested by Hess and Cope (1989) provides the instantaneous concentrations, we had to scale these concentrations, to the 1-hr averaged values, obtained by AERMOD. Hence, we calculated the NO_2 to NO_x ratio and obtained the 1-hr averaged NO_2 concentrations, by multiplying this ratio to the 1-hr averaged NO_x concentrations calculated from AERMOD. Following this method, the impact of DGs in each grid on the NO_2 concentrations can be calculated.

It has to be noted that the background concentration for that specific grid is associated with all sources including DGs, except the DG sources inside that specific grid. Thus, the short range transport model prediction will add the concentrations associated with DGs inside that grid point. Results from the short range transport model without the chemistry (only NO_x) concentrations are shown in Figure A.14. As can be seen in Figure A.14, the maximum 72hr concentrations is mostly about 3ppb, while in

one location it exceeds to 5 ppb. Thus, as it was expected the impact of short range dispersion on the ground level concentration is almost negligible comparing to the impact of DGs on background concentration. The result from this analysis is shown in Figure A.15. As it can be seen, the NO_2 has very similar pattern to the NO_x contribution, since the NO_2 to NO_x ratio were close to 1.0 (Figure A.16). The reason for this behavior is the significantly small values of dilution which entrain high amount of background O_3 into the plume, causing the fast conversion of NO to NO_2.

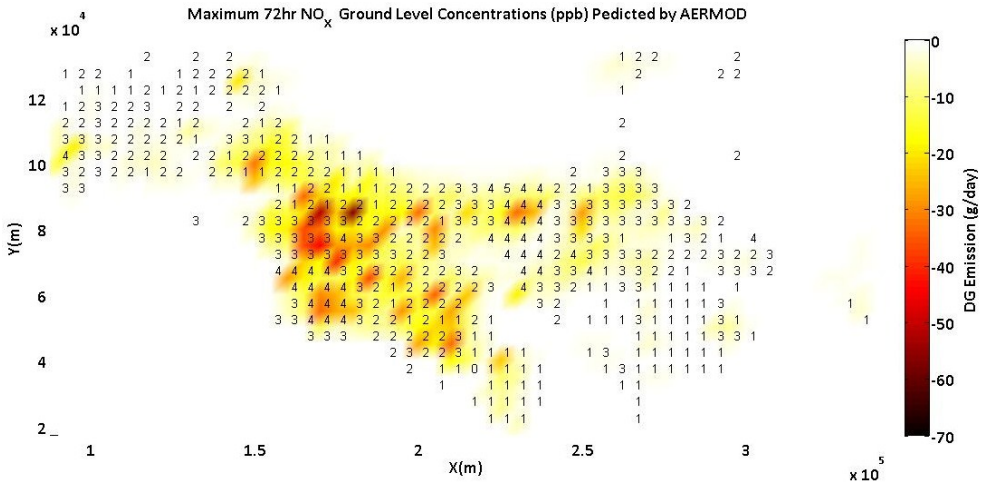

Figure A.14: Maximum 72hr NO_x ground level concentrations (ppb). The color-map shows only DGs emissions at different locations, while the text number shows concentrations in ppb.

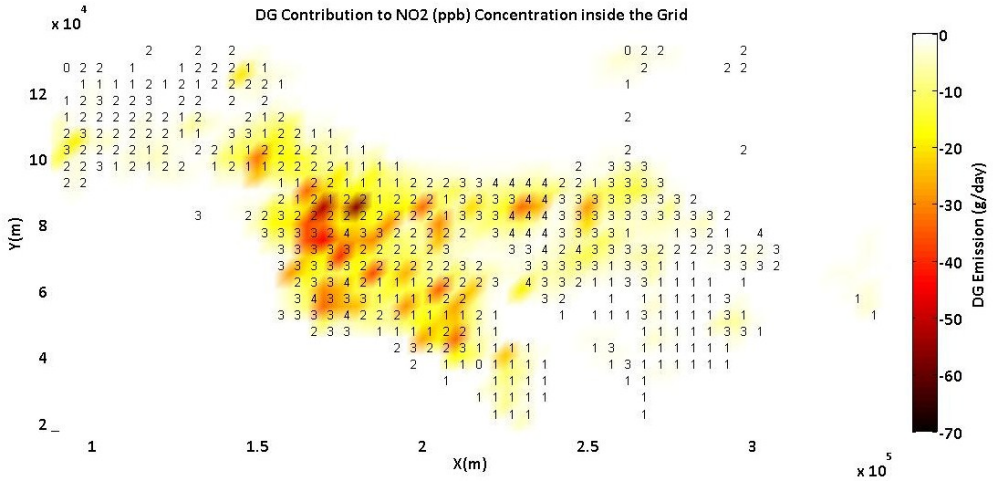

Figure A.15: The contribution of DGs to the maximum increase/decrease in ground level concentrations of NO_2 at each grid point.

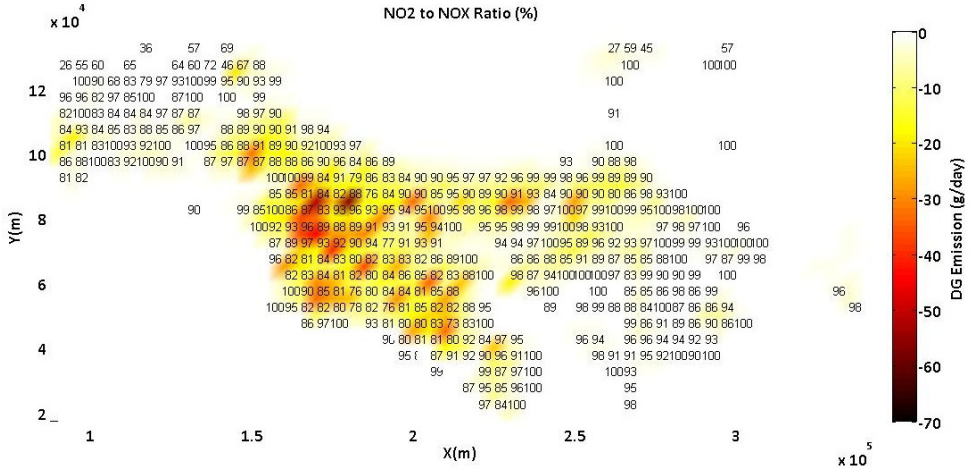

Figure A.16: the ratio of NO_2 to NO_x from Hess and Cope (1989) model.

Following this analysis, we calculated the overall impact of DGs on ground level concentrations of NO_x, NO_2, and O_3. These results are shown in Figure A.17 in color-map since the difference with those shown in Figure A.12 are relatively small and perhaps it would be very difficult to recognize the difference through the scatter plots. in order to clarify this, a comparison on the impacts solely predicted by the lagrangian model with

GRS as the chemistry module, with those obtained from the hybrid model is shown in Figure A.18.

As it can be seen the hybrid model shows slightly higher NO_x increase, due to the relatively higher short range impact of DGs that is included in this model. However, the predicted impacts on NO_2 using the hybrid model is slightly lower than the lagrangian model. The reason to this effect can be explained through the weaker potential of plume model in converting the NO_x to NO_2 (probably due to the less availability of O_3) compared to that of the lagrangian model. Thus, despite higher NO_x concentrations predicted by hybrid model, less NO_2 contribution is observed. Since the focus of hybrid modeling is on the NO_2, this analysis does not include the impact on O_3 concentrations.

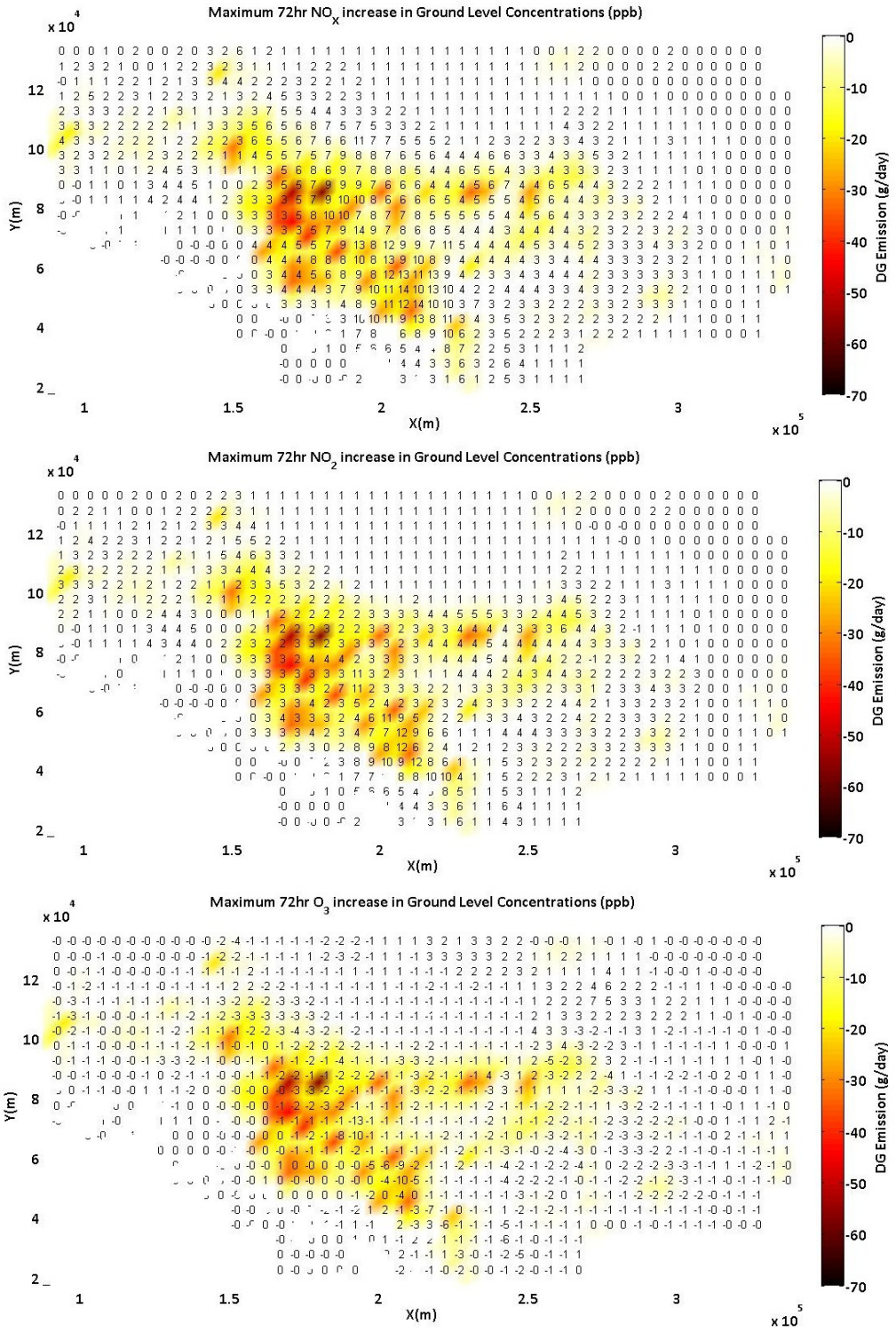

Figure A.17: Maximum increase/decrease in ground level concentrations of NO_x, NO_2, and O_3 under EHP scenario calculated using the ***Hybrid model*** with ***GRS*** as the base chemistry module for the Background concentration calculations.

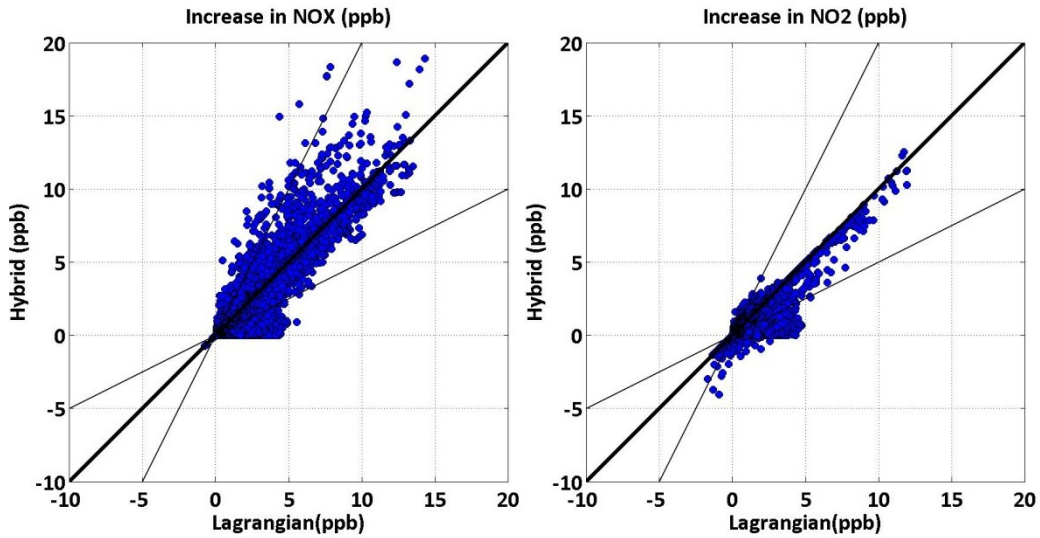

Figure A.18: Comparison between the impact on NO_x and NO_2 predicted by lagrangian model to those obtained from the hybrid model.

A6. Summary and Conclusion

Air pollution in urban areas, is mostly affected by sources located in relatively short and long distances from the receptor. In this dissertation, our main focus was on the short range impact of stationary sources such as distributed power generators located inside urban area. However, it needs to be noted, that the sources located far from the receptor (> 5 km) can have significant impact on the air quality in urban area and their combined contribution with sources in close vicinity to the receptor is unknown. Unlike short dispersion models at which the effect of chemistry can be neglected as a result of relatively short travel times, in these models, chemistry plays a major role in determining the concentration of major pollutants such as NO_2 and O_3. Therefore, we initiated this study to develop appropriate models that can be used for this purpose. We have formulated a simple Lagrangian model that can be used to estimate background

concentrations of NO, NO_2, and O_3 in an urban area. The model can provide hourly concentrations of these species over time periods of a year, which is required in exposure studies. The model achieves its computational efficiency by separating transport and chemistry using the concept of species age. Evaluation with measurements made in SoCAB during 2007, indicates that the model can provides adequate descriptions of the spatial and temporal behavior of NO_x and NO_2. Model estimates of maximum hourly ozone concentrations are unbiased relative to observations but the 95% confidence interval($\approx s_g^2$) of the ratios of observed to estimate concentrations is over a factor of two. This model has also been compared with the UCI-CIT grid model. The comparison shows that UCI-CIT model predict substantially higher concentrations, and the variation of O_3 concentrations is unrealistically higher than that from the lagrangian model. Unlike the lagrangian model, the UCI-CIT model were not evaluated against the 2007 observations in SoCAB, due to the relatively high computational requirements for running this model over a period of one year. Therefore, over this study we mainly focused on the lagrangian model rather than UCI-CIT.

The lagrangian background model were combined with a short range transport model such as AERMOD (Cimorelli et al., 2005) to understand the relative impact of DGs on the ground level concentration of NO, NO_2 and O_3. Using the emission inventory developed by Samuelson et al. (2005), the concentrations of NO, NO_2 and O_3 under two different scenarios were tested. The first scenario, known as “base” scenario, reflects the effect of basic ground level sources (such as mobile sources) on the ground level concentrations. The second scenario uses the emission inventory assuming extra high

penetration of DGs in SoCAB. This scenario is known as EHP. In modeling the ground level concentrations under second scenario, two different approaches were used: 1) the background model was solely used to predict the impact of DGs on the ground level concentrations, 2) the lagrangian model were combined with AERMOD to predict the impact of DGs. This approach is known as hybrid modeling, where combination of a short range and long range photochemical transport models are used to predict the relative impact of sources located at different multiple length scales from the receptor. A schematic of this method is shown in Figure A.19.

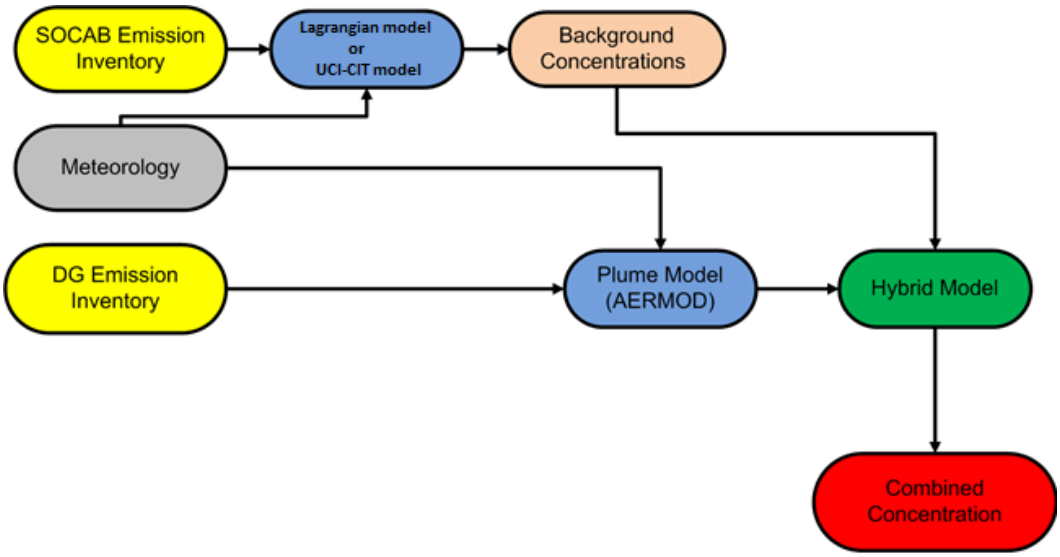

Figure A.19: Schematic of the hybrid model

The hybrid model used the background concentrations from either lagrangian model or the UCI-CIT to predict the conversion of NO_x to NO_2 inside the plume. The plume species concentrations obtained from this method are added to those from the background sources (both base and DGs) to predict the total concentration of species at the receptor. Following these two approaches, it has been seen that the contribution of DGs to the

ground level concentrations of NO_x, NO_2 and O_3 is less than 10% of the base concentrations. The reason to this low impact is the relative small increase in the total emission associated with DGs under EHP scenario. Also, it has been observed that the hybrid model shows higher impact of DGs on NO_x with lower impact on NO_2 compared to the background model. Following this study, the answer to the question raised at the beginning of this dissertation is mostly cleared. DGs impact on the air quality in SOCAB is relatively small, since their contribution to the total emission is much smaller than those from the other (base) sources.

References

Berkowicz, R., 2000: A Simple Model for Urban Background Pollution. *Environmental Monitoring and Assessment,* 65, 259-267.

Brandt, J., Christensen, J.H., Frohn, L.M., Berkowicz, R., 2003: Air pollution forecasting from regional to urban street scale--implementation and validation for two cities in Denmark. Physics and Chemistry of the Earth, Parts A/B/C 28, 335-344.

Byun, D., Schere, K.L., 2006: Review of the Governing Equations, Computational Algorithms, and Other Components of the Models-3 Community Multiscale Air Quality (CMAQ) Modeling System. *Applied Mechanics Reviews* 59, 51-77.

CARB, 2011: California air quality data for the years 1980-2009. Air Resources Board, Sacramento, CA (http://www.arb.ca.gov/aqd/aqdcd/aqdcddld.htm).

Carreras, M., Medrano, M., Samuelsen, G.S., Brouwer, J., Rodriguez, M., Dabdub, D., 2004: Urban air quality impacts of distributed generation, Proceedings of ASME Turbo Expo, 14-17 June, Vienna, Austria.

Cimorelli, A.J., Perry, S.G., Venkatram, A., Weil, J.C., Paine, R., Wilson, R.B., Lee, R.F., Peters, W.D., Brode, R.W., 2005. AERMOD: A dispersion model for

industrial source applications. Part I: general model formulation and boundary layer characterization. *Journal of Applied Meteorology*, 44(5), 682-693.

Jing, Q., 2011. Air Quality Impact of Distributed Generation of Electricity, Dissertation (PhD), University of California, Riverside.

Samuelsen, S., Dabdub, D., Brouwer, J., Medrano, M., Rodriguez, M., Carreras-Sosedra, M., 2005: Air quality impacts of distributed generation. California Energy Commission, PIER Energy-Related Environmental Research, CEC-500-2005-069-F.

Venkatram, A., Karamchandani, P., Pai, P., Goldstein, R., 1994: The development and application of a simplified ozone modeling system (SOMS). *Atmos. Environ.* 28, 3665-3678.

Venkatram, A., Du, S., Hariharan, R., Carter, W., Goldstein, R., 1998: The concept of species age in photochemical modeling. *Atmos. Environ.* 32, 3403-3413.

Venkatram, A., Isakov, V., Pankratz, D., Yuan, J., 2005. Relating plume spread to meteorology in urban areas. *Atmos. Environ.*, 39, 371-380.

Venkatram, A., Cimorelli, A.J., 2007: On the role of nighttime meteorology in modeling dispersion of near surface emissions in urban area. *Atmos. Environ.,* 41, 692-704.